Spray Aerosols From Saltwater to Freshwater Breaking Waves

Charbel Harb

Dissertation submitted to the Faculty of the
Virginia Polytechnic Institute and State University
in partial fulfillment of the requirements for the degree of

Doctor of Philosophy
in
Civil Engineering

Hosein Foroutan, Chair
Gabriel Isaacman-VanWertz
Linsey C. Marr
David G. Schmale III
Mark A. Stremler

August 2nd, 2022
Blacksburg, Virginia

Keywords: Breaking waves, bubbles, spray aerosols, bioaerosols, atmospheric microplastics

Spray Aerosols From Saltwater to Freshwater Breaking Waves

Charbel Harb

(ABSTRACT)

While sea spray aerosols (SSAs) generation by oceanic breaking waves continues to be an active research area, lake spray aerosols (LSAs) production by freshwater breaking waves is an emerging research field. Recent studies have linked LSAs to regional cloud processes and the aerosolization of freshwater pathogens and pollutants. Yet, differences in spray aerosol ejection between freshwater and saltwater and their impact on the water-to-air dispersal of microorganisms and pollutants are poorly understood. The goals of this dissertation work were to understand mechanistic differences between spray aerosol generation in freshwater and saltwater, develop a representation of LSA emissions in atmospheric models and evaluate their impact on regional aerosol loading, and compare the aerosolization of bacteria and microplastics by SSAs and LSAs. Experiments in a breaking-waves analogue tank revealed that the subsurface bubble plume in saltwater is characterized by more submillimeter bubbles than that in freshwater, and hence, saltwater surface foams were more persistent and were comprised of more submillimeter surface bubbles. Consequently, the average number concentration of generated SSAs was eight times higher than that of LSAs. Using these measurements, the developed LSA emission parametrization revealed that freshwater emissions were, at least, an order of magnitude lower than saltwater emissions for the same wave-breaking conditions. When implementing this emission parameterization to simulate LSA emissions from the Laurentian Great Lakes, LSAs did not contribute significantly to regional aerosol loading ($< 2\%$), yet their impact on coarse-mode aerosols was more significant with up to a 19-fold increase in some areas. Furthermore, modeled LSAs reached up to 1000 km inland and were incorporated in the lakes' cloud layer. Despite the generation of more spray aerosols in saltier waters, cumulative salt additions in the freshwater–saltwater continuum (0-35 gkg^{-1}) led to a nonmonotonic increase in freshwater bacterial aerosolization abundance, which exhibited a peak at lower oligohaline conditions (0.5-1 gkg^{-1}). However, the aerosolization of microplastics by SSAs was one order of magnitude higher than that by LSAs. Overall, this dissertation work showed that LSA emissions are intrinsically different from SSA emissions, which influences their role in transferring microorganisms and pollutants at the air-water interface.

Spray Aerosols From Saltwater to Freshwater Breaking Waves

Charbel Harb

(GENERAL AUDIENCE ABSTRACT)

When waves break, they entrain large volumes of air in the form of subsurface bubbles. These bubbles rise to the surface and pop ejecting small droplets into the air, also known as spray aerosols. The droplets ejected from saltwater breaking waves are referred to as sea spray aerosols (SSAs) and are extensively studied due to their important role in Earth's atmosphere. However, the ejection of lake spray aerosols (LSAs) from freshwater breaking waves is far less understood. With recent studies linking freshwater breaking waves to regional cloud processes and the transfer of aquatic pathogens to the air, a better understanding of LSAs formation and how it compares to SSAs production was needed. The goals of this dissertation work were to understand the differences between spray aerosol generation in freshwater and saltwater, develop a representation of LSA emissions in atmospheric models and assess their contribution to atmospheric aerosols, and contrast the role of LSAs and SSAs in transferring bacteria and microplastics to the air. Experiments in a spray aerosol generation tank revealed that saltwater breaking waves generate more submillimeter bubbles at the subsurface level than freshwater breaking waves and that the generated surface foam is more persistent and is comprised of smaller bubbles in saltwater. Consequently, SSA generation in the experimental tank was eight times higher than LSA generation. When implementing these results in an atmospheric model to simulate LSA emission from the surface of the Laurentian Great Lakes, it was found that the regional aerosol population was not significantly affected. However, LSA particles were transported inland up to 1000 km and reached cloud level which hints at possible implications on public health and regional climate. Despite a higher generation of aerosols by breaking waves in saltier waters, the abundance of freshwater bacteria that was dispersed to the air by spray aerosols did not increase monotonically in response to a gradual increase in freshwater salinity. Yet, microplastics transfer to the air by SSAs was an order of magnitude higher than that by LSAs. The results of this dissertation work highlight the important differences between the generation of spray aerosols by breaking waves in freshwater and saltwater and their corresponding roles in the water-to-air dispersal of microorganisms and pollutants.

To my parents and brother:
Emil, Sayde, and Rabah.

Acknowledgments

I am indebted to several individuals for providing me with both professional and personal support throughout my Ph.D. journey, and without whom, this dissertation work would not have been possible. First, I would like to express my profound gratitude to my advisor Dr. Hosein Foroutan who took it upon himself to recruit me as his first Ph.D. student. I attribute my successes throughout this journey to his insightful guidance and continuous support. I thank him for encouraging me to be ambitious and giving me the freedom to tailor my Ph.D. research, for helping me in determining my career goals, and for always being patient and approachable. It was truly inspiring to watch us grow together from that first meeting we had four years ago.

I would also like to express my gratitude to my committee members for their guidance and support. I'd like to thank Dr. Linsey Marr for allowing me to use her laboratory equipment to conduct my experiments, and for providing research and professional guidance. I am also grateful to her for giving me the opportunity to work on testing homemade masks in March 2020, which was hopefully a small contribution to the global response to the Covid-19 pandemic. It was truly inspiring to work with Dr. Marr on this project and see its direct impact on the community. I have benefited greatly, both professionally and personally, from this experience. I'd also like to extend my gratitude to Dr. David Schmale for giving me access to his lab equipment and inviting me to participate in field campaigns. These campaigns gave me a new perspective on research which I'm sure will be valuable in my scientific career. I'm also grateful to Dr. Gabriel Isaacman-VanWertz and Dr. Mark Stremler for their perceptive comments on my research.

My gratitude also goes to the faculty, staff, and fellow graduate students in the EWR program. The technical support and assistance provided by Dr. Weinan Leng, Dr. Stephen DeVilbiss, Dr. AJ Prussin, and Ms. Regina Hanlon were essential for my research. I am also

grateful to my colleagues Jin Pan, Nishan Pokhrel, and Xinyue Huang for being wonderful collaborators and friends. I am also fortunate to have worked with two great undergraduate students, Nora AlAmri and Jennie Lee, who provided me with the opportunity to be a mentor and helped me with my research. My gratitude also goes to the members of the AIRFlowS lab for their support and insightful comments on my research.

Lastly, I would like to thank my parents and brother for believing in me, for providing continuous support and unconditional love, and for encouraging me to pursue my dreams wherever they take me. I am forever grateful to you.

Contents

List of Figures

List of Tables

Chapter 1

Introduction

The formation of waves and their subsequent breaking on the water surface has intrigued humankind since time immemorial, with raging sea waves inciting anticipation and fear among early seafarers engaged in fishing, trading, and maritime exploration. The Glossary of Meteorology of the American Meteorological Society defines the breaking of ocean surface waves as "a complex phenomenon in which the surface of the wave folds or rolls over and intersects itself. In the process it may mix (entrain) air into the water and generate turbulence. The causes of wave breaking are various, for example, through the wave steepening as it approaches a beach, through an interaction with other waves in deep water, or through the input of energy from the wind causing the wave to steepen and become unstable" [1].

The study of breaking waves dates back to the early work of Airy [2] and Stokes [3] who laid the foundations of waves and tides physics. It was not until the Second World War that a more concerted effort emerged to understand and predict breaking waves to improve the belligerent's naval warfare capabilities [4]. Early observational data of wind generated waves were provided by Sverdrup and Munk [5] and Sverdrup and Munk [6], followed by a more thoretical framework developped by Miles [7] and Phillips [8]. By the mid 1960's, the factors responsible for the formation of the wind wave spectrum have been identified, however predicting the evolution of this spectrum required more field measurements and laboratory studies as well as advances in computational power [4]. Subsequent studies by Melville [9], Duncan and Longuet-Higgins [10], and Duncan [11], who investigated breaking waves created by a hydrofoil, provided important insights on breaking waves regimes and evolution, and

precipitated several articles on the topic [12]. Starting in the 1990's, several review articles discussing breaking waves and their secondary effects were published, and the interested reader is referred to them and the references therein. Specifically, Banner and Peregrine [13] presented a comprehensive review of field measurements and laboratory studies of breaking waves. Melville [14] reviewed the effect of breaking waves on air-sea interaction, and King et al. [15] reviewed air entertainment in breaking waves. Perlin et al. [12] presented a review on breaking waves geometry, breaking-onset criteria, and energy dissipation in deep and intermediate waters, while the review of Veron [16] discussed bubble bursting and droplet generation from breaking waves bubbles. More recently, Deike [17] reviewed the role of wave breaking, and the associated entrained bubbles and ejected droplets, in mediating mass transfer at the air-sea interface.

Nowadays, wave breaking has developed into an important research field with applications in naval and coastal engineering including ship hydrodynamics [18], coastal structures [19], and energy generation [20]. More pertinent to this dissertation is the role of breaking waves in air-sea interactions [14], and particularly how they can generate atmospheric particles [16, 17].

1.1 Breaking waves and atmospheric particles

When waves break on the water surface, they entrain large volumes of air in the form of subsurface bubbles. These bubbles rise to the surface and burst ejecting tiny droplets into the air. The dipersal of droplets into the air by bursting bubbles was first identified by Jacobs [21] who postulated that aerosols are produced by the pinch-off of an upward jet following the breaking of a surface bubble. Later, Knelman et al. [22] identified a second and more efficient mechanism of droplet ejection from bursting bubbles whereby tiny water droplets are dispersed during the shattering of the bubble cap. The presence of such mechanisms that transfer water droplets into the air indicated that breaking waves, and the ensuing bursting bubbles, can be an important source of aerosols into the atmosphere, especially from the oceans.

1.1.1 Sea spray aerosols

Sea spray aerosols (SSAs) are comprised of tiny water droplets ejected from breaking waves in saltwater (i.e., oceans and seas) due to wind action [16]. Aerosols emitted from the ocean surface were first identified by Jacobs [21] who termed them at the time as "atmospheric chlorides". The release of SSAs into the atmosphere occurs via three main pathways: film drops, jet drops, and spume drops (Fig. 1.1). Spume drops are large water droplets (diameter > 140 μm) that are torn of the wave crest at sufficiently high wind speeds (7-11 ms^{-1}), and usually fall back to the water surface in the matter of seconds [16]. Of more relevance to atmospheric processes are film and jet drops due to their much smaller size (diameter < 100 μm)[16] and hence higher atmospheric residence times. Contrary to spume drops, film and jet drops are generated from the burst of surface bubbles. Film drops are expelled during the shattering of the bubble cap following a hole nucleation on the cap surface. Jet drops are ejected following the shattering of the bubble cap, whereby the resulting cavity collapses emitting a series of droplets vertically upward [16]. The size of emitted SSAs spans several orders of magnitudes and ranges from a few nanometers to at least several millimeters. This wide size range influences the atmospheric residence time of SSAs, which varies from seconds and minutes for larger particles to days for smaller particles [16, 23].

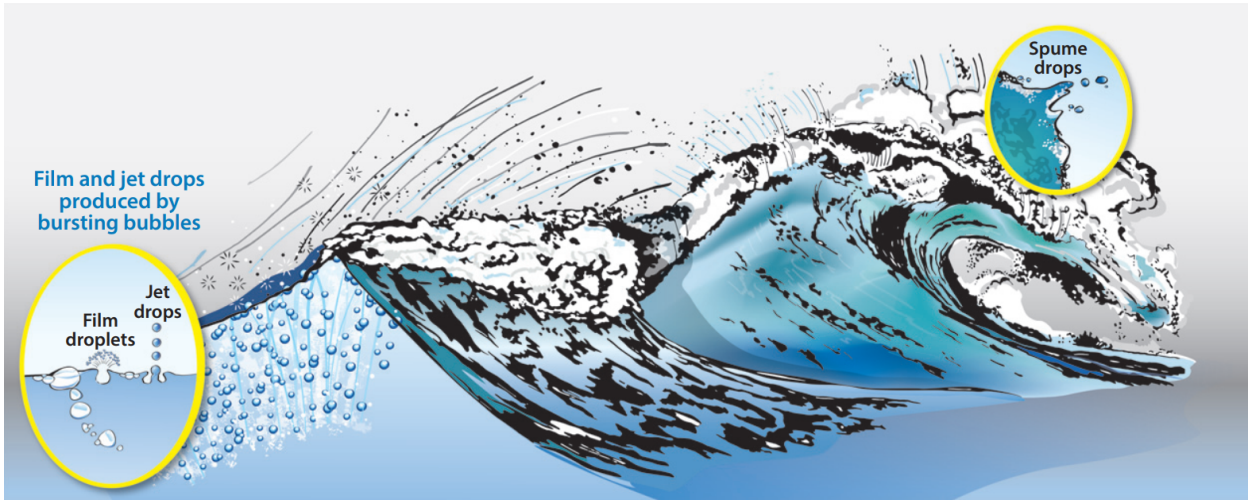

Figure 1.1: **Spray aerosol ejection pathways.** Ejection pathways of spray aerosols emitted from breaking waves. Adapted from Veron [16].

On a global scale, SSA emissions are estimated to be on the order of 10^{12} to 10^{14} kg per year [24], making them, along with mineral dust emissions, the dominant source of aerosol

mass flux to the atmosphere from non-anthropogenic sources [23]. The ubiquity of SSAs in the atmosphere, therefore, allows them to play an important role in atmospheric processes by partaking in atmospheric chemical reactions [25], cloud formation [26], and scattering of incoming solar radiation [27]. Perhaps one of the most important ways in which SSAs influence Earth's climate is in their direct and indirect effects on Earth's radiative budget. The direct effects pertain to the ability of SSAs to scatter light especially above the world's oceans. The estimated upward scattering of sunlight by SSA particles varies between 0.08 and 6 Wm^{-2}, which leads to a net cooling effect on Earth's climate [23, 27]. The indirect radiate forcing effects have to do with the ability of SSAs to seed clouds especially in remote ocean regions unattained by continental particles [28]. SSAs are efficient cloud condensation nuclei (CCN) due to their hygroscopicity and can influence marine clouds drizzle formation and albedo even at low concentrations of few particles per cubic centimeter [26, 29]. These direct and indirect radiative forcing effects have even led to proposing the injection of SSAs into the tropical marine boundry layer, known as marine cloud brightening (MCB), as a climate intervention strategy with low ecological impact aiming to offset the effects of global warming [30, 31, 32].

Because of these important geophysical and geochemical roles, SSAs have been the subject of research for several years leading to an extensive body of literature about the topic [27]. For more details, the interested reader is refereed to the excellent monograph by Lewis and Schwartz [27] containing a comprehensive review of SSAs production and their behavior, transport, and removal from the atmosphere, as well as the factors controlling these processes. Other resources include the review of O'Dowd and de Leeuw [33] containing information about the chemical implications of SSAs, the review of De Leeuw et al. [23] which is another excellent review of SSA production flux, the review of Veron [16] which covers the exchange of heat and momentum between SSAs and the atmosphere, and the review of Alsante et al. [34] covering the role of SSAs in the air-sea exchange of microorganisms.

1.1.2 Lake spray aerosols

Lake spray aerosol (LSA) is a term that refers to spray aerosols emitted from freshwater breaking waves, namely, from lakes [35]. LSA particles were first detected during an aerosol sampling campaign above the Laurentian Great Lakes in North America in the summer

of 2009 [36]. It was not until the study of May et al. [35] that the properties of LSAs were examined using a laboratory LSA generator. The results of that study indicated that bubble formation and aerosol generation from freshwater and saltwater breaking waves are drastically different. Only a handful of studies about LSA followed, mostly spurred by the discovery of cyanobacterial derivatives in LSAs ejected from freshwater with harmful algal bloom occurrences [37, 38].

Although the same bubble-bursting mechanism is behind SSA and LSA generation, the physical characteristics of air entrainmnet in freshwater and saltwater are different [39, 40, 41]. These differences are likely driven by disparate water compositions in the two environments. The major ions in the calcareous Great Lakes, for instance, are Ca^{2+} and CO_3^{2-}[42], whereas major ions in seawater are Na^+ and Cl^- [43]. Furthermore, the inorganic ions concentrations in the Great Lakes are 2-5 order of magnitude lower than those in seawater [35]. Meanwhile, total organic carbon (TOC) concentrations are comparable to the concentrations of inorganic ions in the Great Lakes, whereas TOC concentrations in saltwater are often much smaller than inorganic ions concentrations [35]. These intrinsic differences in water composition lead to distinctive disparities between bubble evolution characteristics in freshwater and saltwater breaking waves. A general trend emerges whereby entrained subsurface bubbles in seawater are smaller, more numerous, and have higher subsurface residence times than those in freshwater [41, 44, 45]. These differences at the subsurface level are reflected on the surface, with early observations of foam coverage in seawater and freshwater suggesting that foam patches are more persistent in seawater than in freshwater [44, 46]. As for spray aerosol ejection, May et al. [35] showed that produced LSA concentrations are up to 67% lower than SSA concentrations. Moreover, the LSA size distribution was mostly bimodal as opposed to the unimodal size distribution of SSAs [35]. To generate these LSAs, the setup employed by May et al. [35] consisted of four circular plunging jets in an 18 L acrylic box. It is important to note that this LSA generator has been evaluated using bubble size distribution measurements in saltwater, and hence, it is not clear if it can also reproduce the correct sizes of bubbles found in freshwater breaking waves. Therefore, one should keep in mind that current LSA experimental studies, including the dissertation work herein, employ laboratory setups that are designed and evaluated using SSA data due to the absence of data from in situ freshwater breaking waves.

In general, the study of LSAs is still a nascent research field as compared to the relatively

well-established SSA research field. Given the aforementioned difference in spray aerosol ejection characteristics between freshwater and saltwater, it is important to consider LSA emissions as a standalone process from SSA emissions. Treating the two emissions separately is especially relevant in atmospheric models, although currently, only SSA emissions are considered. However, it was recently found that LSA particles can be incorporated in clouds [47] and that they can transfer pathogenic microbes across the atmosphere [37, 38, 48]. Therefore, there is a paramount need to include LSAs in atmospheric simulations to understand their larger scale impacts on regional climate and public health.

1.1.3 Spray aerosols in atmospheric models

Due to their important role in Earth's aerosol load and atmospheric processes, atmospheric model simulation of SSAs is an active research area. Since wind is the major meteorological factor driving SSAs emission and a common parameter in atmospheric models, the model representation of SSA emission is mostly dependent on wind speed [23, 27]. Monahan et al. [49] put forth the first SSA emission parameterization (hereinafter source function) as a function of wind speed at a reference height of 10 m (i.e., 10-m wind speed), enabling the inclusion of SSA emissions in atmospheric models. The parameterization used the whitecap method [23, 27], which combines knowledge of whitecap (foam) formation as a function of wind speed (usually at 10 m) determined from ship or satellite imagery [50, 51, 52] with size resolved SSA emission flux per whitecap unit area from laboratory experiments [49, 53]. The whitecap method is the most widely used method in SSA source function development [23], yet other methods such as the steady state dry deposition method, the statistical wet deposition method, and other micrometeorological methods have been used in some studies to determine SSA production flux [23, 27]. While wind speed is a major determinant of SSA emission flux, other environmental factors such as temperature [54, 55, 56], salinity [35, 53], and biological activity [54, 57] have also been shown to influence SSA emission flux. In particular, the inclusion of sea surface temperature (SST) in SSA parametrizations has been shown to significantly improve model skill in predicting global SSA emission flux [58].

While the bulk of research in this area has focused on SSA emission parameterization, only one study [59] attempted to model LSAs emission to the atmosphere, but employing an SSA parametrization [60] since an LSA source function was unavailable at the time. Due to

significant differences in spray aerosol emission characteristics between marine and freshwater environments [35], the contribution of LSA to aerosol loading in this study [59] is likely to be overestimated. More recently, Amiri-Farahani et al. [61] attempted to improve the Chung et al. [59] simulation by using a corrected version of the Geever et al. [60] SSA emission parameterization by scaling to the laboratory measurements of May et al. [35]. However, only correcting for the number emission flux might not be sufficient as the same wind conditions over freshwater and saltwater are likely to induce different wave breaking conditions [44]. Therefore, a better understanding of LSA emissions using modeling studies warrants the development of an LSA source function, which is still lacking to date.

1.1.4 The complex composition of spray aerosols

Spray aerosols are more than just a simple mixture of salts with water. In fact, an SSA particle has such a complex composition that its characteristics have been compared to those of a cell [62]. For instance, similar to a cell membrane, an SSA particle is coated by a membrane of fatty acids and other lipids which affects its hygroscopicity [62]. In the interior, other similarities exit including the presence of internal lipid vesicles and bacterial derivatives [62, 63].

Over the past several years, studies have shown that SSA particles can contain a diverse array of proteins, enzymes, and organic compounds including sugars and fatty acids [64]. These organic compounds in SSAs are enriched with respect to seawater with the smallest SSA particles exhibiting the highest enrichment levels [64]. An examination of individual SSA particles using cryogenic transmission electron microscopy also revealed that SSAs can host entire microorganisms including bacteria and viruses [63]. One of the earliest studies reporting the presence of microorganisms in SSAs was that of Baylor et al. [65] who found viral enrichment factors of 200 in aerosol droplets created by the surf. Single bubble experiments by Blanchard and Syzdek [66] confirmed microorganisms enrichment in SSAs revealing a bacterial enrichment factor ranging from 10 to 20. The study of Hejkal et al. [67] was one of the earliest studies to report differences in the ability of bacterial species to be aerosolized by bursting bubbles, but only three marine bacterial species were considered due to the inherent limitation of the culture-based technique used in that study. The emergence of DNA-based techniques including targeted amplicon sequencing paved the way for the full

characterization of aerosolized microbial communities, with the study of Michaud et al. [68] confirming that certain bacterial and viral taxa are preferentially aerosolized with respect to others, and that bacteria are transferred to SSAs more efficiently than viruses.

Besides their organic and biological content, SSAs can host anthropogenic pollutants and are, hence, a vector for their water-to-air dispersal. The role of SSAs in transferring aquatic pollutants at the air-sea interface is an emerging area with important implication on climate and public health. Examples of pollutants that were found to be enriched in SSAs include particulate and gaseous compounds from oil spills [69], perfluoroalkyl acids (PFAAs) [70], and microplastics (MPs) [71].

Unlike SSAs, LSAs composition and their role in the water-to-air dispersal of freshwater microorganisms and pollutants are not well understood. To date, only two works examined the biological content of LSAs, but were restricted to cyanobacterial aerosolization from freshwater with HABs occurrence [37, 38]. Looking at the whole microbial communities, it is expected that the community structure in SSAs and LSAs is different. This difference is expected because salinity is not only a determinant of the physical characteristics of spray aerosol ejection (Sect. 1.1.2) but also of the structure of waterborne bacterial communities [72]. Similarly, the ability of SSAs and LSAs to disperse aquatic pollutants into the air is also probably different due to the aforementioned differences in spray aerosol ejection properties between freshwater and saltwater (Sect. 1.1.2).

1.2 Research objectives

It is evident from the introductory material in section 1.1 that spray aerosol research is centered around SSAs. Therefore, the overall goal of this dissertation work is to understand mechanistic differences between spray aerosol ejection in freshwater and saltwater, transfer this knowledge to large-scale atmospheric models, and understand its impacts on the water-to-air dispersal of microorganisms and emerging pollutants. Specific research objectives include:

1. Evaluate the characteristics of air entrainment in breaking waves for salinities ranging from freshwater to saltwater.

2. Develop an LSA emission parameterization, implement it in an atmospheric chemical transport model, and investigate effects of aerosols from freshwater breaking waves in regional simulations.

3. Investigate the effect of a freshwater-to-saltwater salinity gradient on bacterial aerosolization by breaking waves.

4. Compare the aerosolization of microplastics from freshwater and saltwater breaking waves.

1.3 Organization of the dissertation

Chapter 2, "Salinity and air entrainmnet in breaking waves", addresses research objective 1. In this chapter, a laboratory water tank with a plunging sheet is used to simulate bubble formation in breaking waves. Water salinity in the tank is systematically increased from freshwater to marine conditions and the characteristics of the subsurface bubble plume and the resulting surface foam patch at each salinity treatment are monitored using digital cameras. The effect of increasing water salinity on the sizes of bubbles in the subsurface bubble plume as well as the longevity and sizes of bubbles in the surface foam patch are discussed.

Chapter 3, "A lake spray aerosol emission parameterization", addresses research objective 2. In this chapter, the same water tank setup is used to develop an LSA emission parameterization for use in atmospheric models. The parametrization was developed using measurements of foam area and the corresponding LSA emission flux from experiments with synthetic freshwater in the tank. The developed parameterization was then implemented in the Community Multiscale Air Quality (CMAQ) model to assess the impact of freshwater emissions on regional aerosol loading in the Great Lakes region which contains the largest inland body of unfrozen freshwater on Earth. The LSA emission parameterization was compared to an SSA emission parameterization developed using the same procedure as well as several other SSA emission parameterizations from literature. Model simulation results revealed the impact of LSA emissions on regional aerosol number and mass concentrations in the surface and cloud layer above the Great Lakes basin.

Chapter 4, "Freshwater salinization impact on aerosolized bacteria", addresses research ob-

jective 3. In this chapter, cumulative salt additions in the freshwater-marine continuum were administered to a freshwater sample added to the tank. At each salinity treatment, waterborne and the corresponding airborne bacterial samples were collected and analyzed for abundance and diversity. The effect of increasing freshwater salinity on the abundance of waterborne bacterial aerosolization is explored. Differences between the diversity of bacterial communities in water and air at each salinity treatment are also discussed as well as the enrichment of different bacterial families in the aerosol phase across the salinization gradient.

Chapter 5, "Microplastics aerosolization by breaking waves", addresses research objective 4. In this chapter, fluorescent polystyrene microplastic spheres with a uniform 2-μm diameter are aerosolized in the tank using synthetic freshwater and saltwater solutions. The microplastics-laden LSAs and SSAs are collected on filters and examined using a fluorescent microscope. The abundance of polystyrene microplastics aerosolization by LSAs and SSAs is compared and the implications of these experiments on microplastics aerosolization by freshwater and oceanic breaking waves are briefly discussed.

Chapter 6 concludes this dissertation by providing the outcomes of each research objective stated in Sect. 1.2, broader impacts of the research, and recommendations for future work.

Chapter 2

Salinity and air entrainmnet in breaking waves

2.1 Abstract

The evolution of air bubbles after breaking waves plays an important role in gas and particle exchange between water bodies and the atmosphere. To improve our understanding of the impacts of salinity on this process, we systematically investigate the effect of salt concentrations ranging from 0 to 40 g/kg on the volume and size distributions of subsurface bubble plumes and surface foams in a laboratory breaking wave analog. Our experimental setup utilizes an intermittent plunging sheet to simulate breaking waves, while two synchronized digital cameras were used to monitor the temporal evolution of bubble plumes and surface foams. We first highlight the importance of plunging sheet intermittency on surface foam evolution. We then show that increasing salinity enhances the entrainment of submillimeter bubbles but has a less significant effect on larger supramillimeter bubbles. We observed that

the foam area in saltier waters is consistently higher than that in freshwater throughout the foam decay phase. Furthermore, our investigation of surface bubble sizes shows that salinity has a more distinct effect on smaller (sub 2 mm) than on larger bubbles. This suggests that salinity may have a more pronounced impact on jet than on film drops ejection mechanisms. Finally, we conclude that the change in salinity within the typical oceanographic range is likely not a major factor for bubble-mediated interactions at the water surface during breaking waves. However, even low-salt concentrations greatly alter air entrainment characteristics in freshwater systems.

2.2 Plain language summary

When sea waves break, they entrain large volumes of air in the form of bubbles. These bubbles rise up to the surface and burst, ejecting gas and small droplets into the air. This ejection mechanism plays an important role in air quality and climate dynamics. The effect of water salinity on this process is still not well understood. We used an intermittent plunging waterfall inside a laboratory tank and digital cameras to monitor the evolution of bubbles within and at the surface of water. We found that the jet intermittency affects the foam evolution on the surface following the wave-breaking event. Increasing water salinity led to an increase in the entrained bubbles number, and potentially the air volume injected by the breaking waves. We also observed a larger and more persistent foam patch in more saline water than in freshwater. The size of the surface bubbles in the foam patch was also affected by the salinity indicating that the latter affects the bubble-bursting mechanism on the surface. We conclude that water salinity has a measurable effect on the air volume and bubble sizes injected by breaking waves and should be accounted for in future air-sea interactions studies.

2.3 Introduction

Air entrainment by breaking waves plays an important role in air-sea interactions. Subsurface bubble plumes generated during breaking events rise to the surface and burst, enhancing gas and particle transfer at the air-water interface [16, 23, 27, 73]. Upon bursting, surface bubbles

eject droplets into the atmosphere in two forms: film and jet drops. Film drops are expelled during the shattering of the bubble cap following a hole nucleation on the cap surface. Jet drops are created following the shattering of the bubble cap, whereby the resulting cavity collapses emitting a series of droplets vertically upward [16]. Due to this difference in the ejection mechanisms, film drops are generally less than 1 μm in radius and are more representative of the surface film composition, whereas jet drops radii are usually in the supramicrometer range and their composition is more representative of the bulk water [16]. Accordingly, the terminal fall velocity of film drops is lower than that of jet drops resulting in them having higher atmospheric residence times. Furthermore, entrained bubbles contribute to the formation of whitecaps — highly reflective patches at the water surface that consist of the subsurface bubble plumes and surface foam generated by breaking waves. Next to being a medium for gas and particle transfer at the air-water interface, whitecaps also influence the global radiative balance by increasing the ocean's surface albedo [74].

Water properties that affect air entrainment from breaking waves include temperature, gas saturation, surfactant concentrations, and salinity [39, 75, 76, 77, 78]. Among these, temperature effects on air entrainment are fairly well studied [56, 76]. However, the interplay between salinity and surfactant concentrations in the water and their effect on surface and subsurface bubbles during wave-breaking events is still not well understood. In particular, our understanding of the systematic effect of water salinity on subsurface bubble plumes and surface foams is still lacking. Several factors suggest that it is important to account for salinity variations when studying air entrainment mechanisms in water bodies. Other than the intrinsic differences in salinity between freshwater and saltwater bodies, the world's oceans, which constitute the largest portion of water bodies on the globe, are not uniformly saline. Although the salinity in the open ocean is mostly between 33 and 37 g/kg, it drops down to 7 g/kg in the Baltic Sea and goes up to around 40 g/kg in the Red Sea [27]. Additionally, with the increasing repercussions of global warming, the gap in salinity between the most and the least salty regions in the oceans is increasing [79, 80]. Furthermore, there is an increased interest in the mechanisms of air entrainment from breaking waves in freshwater surfaces. Recent studies have suggested that breaking waves and the subsequent spray aerosols in freshwater lakes can be a vessel for the transfer of harmful algal bloom toxins from the lakes into the surrounding residential areas [37, 81]. Yet, few studies have investigated aerosolization from breaking waves in freshwater bodies as compared to the large body of literature

on aerosolization from seawater [35] Accordingly, understanding the effect of water salinity on air entrainment and whitecap coverage helps to better characterize air-water interactions and their implications on the climate and air quality.

Previous studies on the effect of salinity on subsurface bubble plumes from air entrainment focused on the contrast between freshwater and seawater [40, 44, 45, 82, 83]. While Anguelova and Huq [39] investigated the effect of different salinity values on the transient void fraction by using a continuous plunging jet, no previous systematic studies have been reported on the effect of salinity on bubble size distributions following active air entrainment. In an early experiment on whitecap coverage, Monahan and Zietlow [44] found that saltwater bubble clouds are characterized by an abundance of small bubbles as compared to freshwater bubble clouds. Due to their reduced buoyancy, the smaller bubbles increased the lifetime of entrained bubble plumes in saltwater. This observation was interpreted as a possible explanation for the higher whitecap coverage in seawater over freshwater for similar wind conditions in previous field measurements [46]. To further explain these field observations, a later study also showed an increase in small bubbles number with increasing salt concentration [41]. This behavior was attributed to increased resistance to coalescence in saltwater as compared to freshwater [84]. The smaller subsurface bubbles in saltwater persist longer and can extend the lifetime of surface whitecaps. However, it has also been argued that bubble breakup in more saline water results in smaller bubbles than that in freshwater, which was linked to the differences observed in the bubble populations between freshwater and saltwater [85]. An increase in bubble population of all sizes in saltwater as compared to freshwater was also reported in a laboratory wave channel for two different depths [82]. Similarly, bubbles in seawater were observed to be smaller, more numerous, and having higher subsurface residence time than those in freshwater [45]. Contrary to Haines and Johnson [45], who argued that there is a shift to smaller bubbles in seawater bubble plumes, Wu [86] argued based on the measurements of Cartmill and Su [82] that more air is entrained in seawater and that the number of bubbles of all sizes is greater in seawater than in freshwater. Moreover, using an intrusive probe for bubble detection, Chanson et al. [87] also reported that finer bubbles are created beneath seawater plunging jets than in freshwater. The authors also reported that less air volume and smaller bubbles are present in freshwater as compared to saltwater. In contrast, Loewen et al. [83] found no significant difference in bubble size distributions between fresh and seawater. Their observation was for bubbles greater than 0.8

mm in diameter beneath laboratory waves generated by a mechanical wave paddle. As noted previously by Blenkinsopp and Chaplin [40], the disparity in the insights provided by several previous investigations suggests that the exact effect of salinity on bubble entrainment in breaking waves needs further investigation.

The aforementioned studies on the effect of water salinity on air entrainment from breaking waves have focused almost exclusively on underwater bubble plumes [39, 40, 41, 45, 82, 83, 88]. However, surface interactions at the air-water interface occur mostly via the foam patches created at the water surface following the rise of the bubble plumes [23, 27]. Nevertheless, few studies have investigated the differences in surface foam characteristics for different water salinity values [44, 75, 89]. The lifetime of surface foam is affected by various water properties including salinity, temperature, and surfactant concentrations. In the absence of significant amounts of surfactants, the timescale of decay of surface foam is comparable to that of bubble plume degassing. However, the presence of an appropriate amount of surfactant can extend the lifetime of surface foam beyond that of the degassing plume [76, 77]. Increasing water temperature has a less marked effect on the lifetime of surface foam. A study of surface foam decay in a tank with a plunging water sheet showed an 8 % difference between the temperature extremes of 6 °C and 30 °C for filtered seawater [76]. As for the effect of salinity, early observations of whitecap coverage in seawater and freshwater surfaces suggested that foam patches are more persistent in seawater than in freshwater [46]. This observation was later confirmed when experiments in a whitecap simulation tank showed that surface foam coverage decays slower in saltwater than in freshwater [44]. In a later study on the effect of salinity on the thickness of surface foam, the authors reported a noticeable influence on foam thickness decay for salinities between 0 and 16 g/kg but not for salinities between 20 and 36 g/kg [89].

Due to the difficulty of reproducing air entrainment from breaking waves in small-scale laboratory systems, researchers have used different experimental setups to generate subsurface bubbles including porous glass tubes [41, 53], overturning buckets [45, 88], continuous jets [35, 56], intermittent water sheets [90, 91], and wave channels [83, 92, 93]. The validity of such setups to faithfully reproduce air-water interactions from breaking waves depends on their ability to replicate the in situ bubbles and aerosols size distributions [90, 94]. Various challenges hamper the correct reproduction of breaking waves' bubble plumes in simple laboratory setups. In plunging breakers found in the ocean, air entrapment occurs by the

formation of an air tube between the jet tip and the impact surface, and the subsequent splashing events occurring in the break zone. The plunging jet tip and the flow at the impact surface have almost the same velocity and the jet tip does not penetrate the wave face. The preceding mechanism is in contrast with a laboratory plunging jet where the water jet penetrates the static surface and entraps craters of air [95]. Moreover, the lifetime of bubble plumes in such laboratory setups are shorter than those found in the ocean [94]. Despite these disparities in air entrainment mechanisms, it has been shown that intermittent plunging sheets can replicate the correct bubble size distribution found in ocean's breaking waves [90].

In this study, we systematically explore the effect of water salinity values ranging from 0 to 40 g/kg on subsurface bubble plumes and surface foams in a laboratory breaking wave analog. This investigation will help in assessing whether salinity variations have considerable effects on air bubbles evolution after breaking waves and whether they should be accounted for in future air-water interaction studies.

2.4 Methods

A laboratory water tank with a controllable plunging sheet is used to simulate air entrainment from breaking waves. The design and operation of the tank follow closely the Marine Aerosol Reference Tank (MART) system [90]. The setup consists of a polycarbonate tank (100 cm $\times$ 54.6 cm $\times$ 61 cm) and two concentric tubes mounted inside the tank (Fig. 2.1a). The outer and inner tubes have inner diameters of 78 and 21 mm, respectively. The concentric tube setup allows water to drip from regularly spaced holes at the bottom of the inner tube and accumulate in the outer tube. A slot (200 mm x 3 mm) on the outer tube side allows the accumulated water to exit as a uniform sheet (Fig. 2.1a). Water inside the system is continuously recirculated using 25 mm tubing from the bottom of the tank into the concentric tubes by a 1/3 HP self-priming utility pump (AMT 2851-96). The intermittency of the water sheet is controlled by a solenoid valve (Parker 2-way normally closed skinner valve) mounted on the pump discharge port and connected to a time delay relay (Macromatic TR-53122-07). A flow meter (Dayton 32ZN69) is mounted at the inner tube inlet to monitor the flow (Fig. 2.1a). This system is chosen for the experiments because it generates subsurface bubble

plumes that have similar characteristics to air bubbles trapped beneath breaking waves in the ocean [90]. The large volume of the water tank also allows the submerged bubble plume to penetrate and evolve freely without interference from the tank walls.

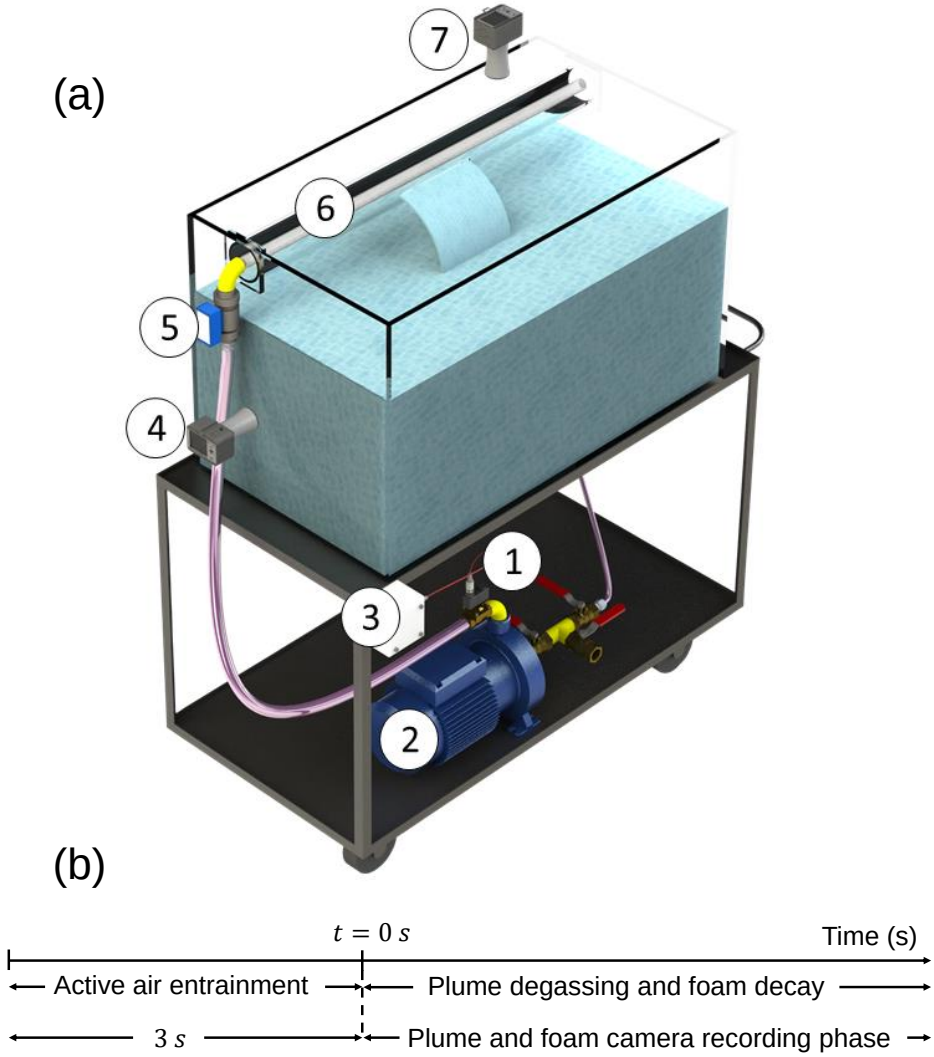

Figure 2.1: **The components of the intermittent plunging sheet system and timeline of data acquisition. (a)** The intermittent plunging sheet system and its components: (1) Solenoid valve, (2) Centrifugal pump, (3) Time relay control box, (5) Digital Flowmeter, and (6) Concentric tubes. Also shown are the two camera positions: (4) Bubble plume camera and (7) Surface foam camera. **(b)** Timeline of data acquisition following active air entrainment from the plunging sheet.

Water salinity is varied by adding an appropriate amount of artificial sea salt (Instant Ocean

Sea Salt) to tap water. The temperature and salinity of the water during the experiments are measured using an Extech EC170 salinity/temperature meter. We used artificial sea salt instead of pure NaCl because although the latter is the major compound in sea salt [27], other ionic compounds (e.g., Mg^{2+} and SO_4^{2-}) have been shown to alter bubble shattering characteristics of pure NaCl solutions [85]. Hence, there is a concern on the ability of studies using NaCl as a proxy to sea salt to reproduce the correct bubble size distribution and drops production found in the ocean [27].

Before each set of experiments, the tank is cleaned with soap and left to dry. We filled the tank with 240 L of tap water providing a water depth of 44 cm. At this water depth, the vertical distance between the slot and the water surface is approximately 10 cm. Once filled, we left the water in the tank to sit until it reaches room temperature and gas saturation [96]. After the addition of salt to the water, we ran the recirculation system for several minutes to achieve a homogeneous salinity in the water volume. Before the start of each experiment, we measured and recorded the temperature and salinity values. The water outflow rate from the slot during active air entrainment is 21 L/min and remains constant throughout the experiments.

Subsurface bubble plumes are photographed using a Nikon D750 DSLR camera (shutter speed 1/640 s, f-stop 18, and ISO 1600). The plume camera's focal length is 120 mm, providing a pixels density of 31.62 pixels/mm. The Nikon D750 is operated at three frames per second (fps). Subsurface bubble plumes are monitored inside a rectangular 12.6 $\times$ 18.9 cm window with its top and left edge located at a depth of 11 cm from the water surface and at 8.5 cm from the closest tank wall, respectively (Fig. 2.2a). Surface foam patches are captured using an overhead Nikon D5300 DSLR camera (shutter speed 1/320 s, f-stop 5, and ISO 1600). The foam camera's focal length is 60 mm, providing a pixel density of 105.38 pixels/cm. The Nikon D750 is mounted horizontally facing the tank side wall whereas the Nikon D5300 is mounted vertically facing the water surface from the top (Fig. 2.1a). Lighting for subsurface bubbles photography is provided by two 500-W tungsten bulbs illuminating a diffuser sheet that is glued to the tank back wall facing the bubble plume camera. Accordingly, subsurface bubbles in the photographs appear as dark shadows against a bright background (see first column in Fig. 2.2b). Surface foams are illuminated by two 80-W LED bars positioned at the tank sides. A black antireflective cardboard is glued to the tank bottom to provide a dark background for foam photographs. This lighting

configuration results in a bright foam area against a dark background in foam photographs (see second column in Fig. 2.2b).

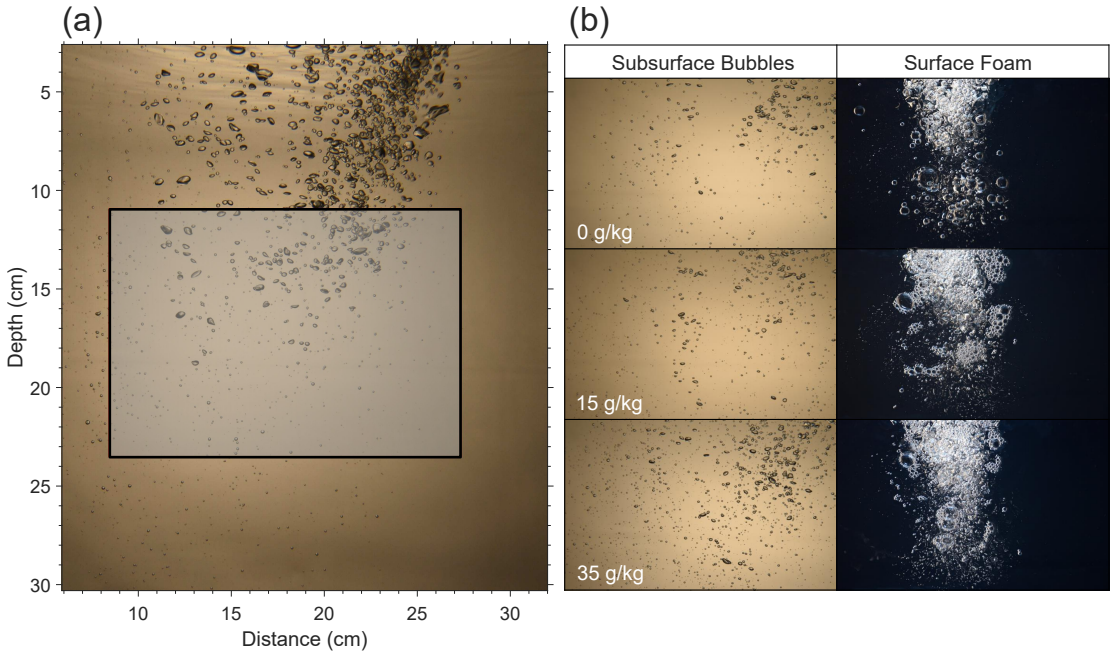

Figure 2.2: **The subsurface imaging window and examples of acquired bubbles and foam images at various water salinities. (a)** The imaging window of the plume camera at the bottom of the evolving bubble plume. Shown on the y-axis is the distance from the mean water level and the x-axis represents the distance from the closest tank wall. **(b)** Sample images of subsurface bubbles and surface foams at water salinity values of 0, 15, and 35 g/kg.

The two cameras are triggered simultaneously by sensing the electric signal from the solenoid valve. Shooting starts at the instant the sheet stops hitting the water surface (Fig. 2.1b) and this time is defined as the reference time for the experiments. Subsurface bubble sizes and numbers as well as surface foam patch areas are determined by an algorithm executed in the image processing software ImageJ [97]. The algorithm first subtracts the background from the images and then uses a threshold to create a binary image that separates the subsurface bubbles (or foam patches) from the background (see Fig. A.1 in Appendix A). Watershed segmentation is used to isolate highly clustered subsurface bubbles in the initial moments after air entertainment cessation that are characterized by high-void fractions (see Fig. A.1a). The unprocessed pictures were scaled by taking photos of a precision ruler placed at the water surface for the foam images and at the tank midplane (piercing the

bubble plume) for the subsurface bubble images. Unlike surface foam areas which were determined using an automated threshold technique (Fig. A.1b), foam cells (i.e., surface bubbles) were manually identified using the ImageJ software (Fig. A.1c).

Two sets of experiments are carried out in this study. In the first set, we fixed the air entrainment time to 3 s and varied the plume degassing time between 0 and 5 s by appropriately setting the dials on the time delay relay. The salinity of the water during the experiments is almost 0 g/kg and the water temperature varied between 19.6 °C and 20.5 °C. In the second set, air entrainment was fixed at 3 s and we allowed the plume to degas for 8 s (fixed) to replicate wave conditions in the ocean [76]. Synthetic sea salt is then added in increments providing absolute salinity values of 0, 5, 10, 15, 20, 25, 30, 35, and 40 g/kg. The water in the tank is kept the same for all experimental runs to ensure that unwanted surfactants effects (that might have been introduced to the water by soap residue from the cleaning process) are the same across all measurements. The water temperature during the salinity experiments varied between 19.0 °C and 22.2 °C.

2.5 Results and discussion

2.5.1 The effect of plunging sheet intermittency

Many previous experimental studies have used continuous water jets as an analog of air entrainment from breaking waves [15, 35, 56, 98]. While Stokes et al. [90] incorporated an intermittent plunging sheet, no previous studies have systematically investigated the effect of the air entrainment intermittency on bubble clouds characteristics. Continuous air entrainment from an impinging jet can be associated to the acoustically active phase of wave breaking [92]. Yet, it has been shown that breaking events in the ocean are characterized by two distinct phases: the acoustically active phase during which bubbles are formed followed by a quiescent phase during which the fully formed bubble plume evolves and rises to the surface. Comparing air entrainment from a continuous jet to that of an intermittent jet is important since continuous bubbling might affect the size of ejected aerosols at the air-water interface. The concern is that continuous bubbling might hinder the bursting of small bubbles on the water surface during the quiescent phase, thus affecting the film and jet

drop contribution to the produced aerosols [99]. To investigate this hypothesis, we ran a series of experiments with different jet intermittency values by changing the relay delay time (Fig. 2.3).

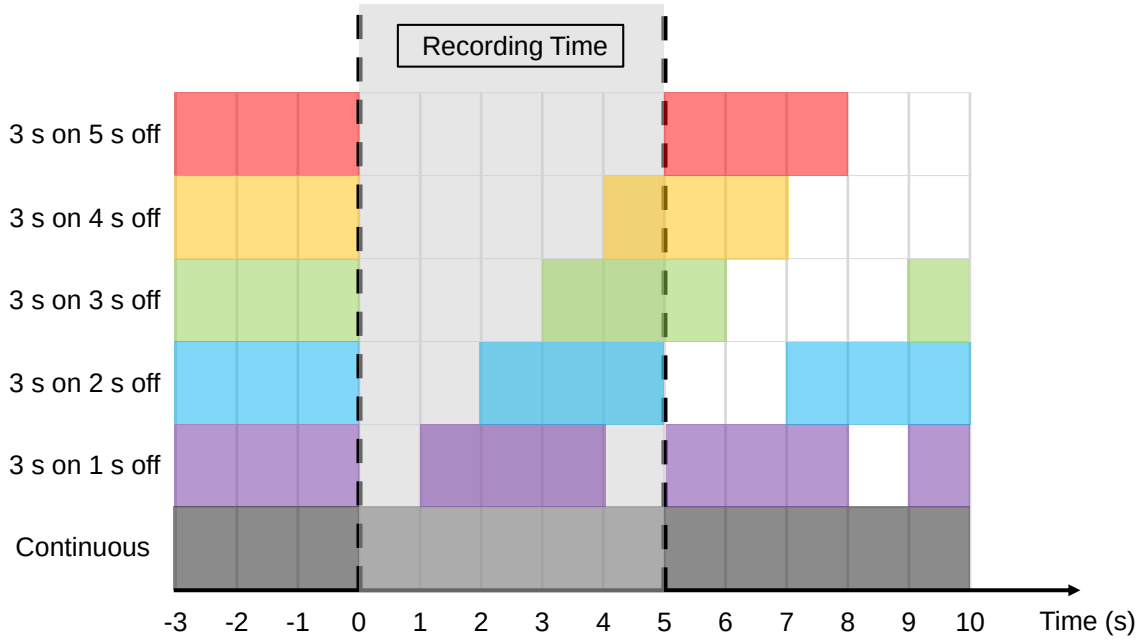

Figure 2.3: **Timeline of the plunging sheet intermittency experiments.** Timeline of the six plunging sheet intermittency experiments. By setting the dial of the time delay relay, we fixed the active air entrainment time to 3 s in all experiments and varied the solenoid valve shutoff time between a minimum of 0 s (continuous hitting) at the bottom row and a maximum of 5 s at the top row. For all experiments, the bubble plume camera recorded for a period of 5 s starting from the cessation of active air entrainment ($t = 0$ s).

As mentioned earlier, the two cameras are triggered simultaneously at the time the plunging sheet stops hitting the surface, and this time is termed time zero in Fig. 2.3. Once triggered, the cameras recorded for a period of 5 s for all six experimental cases. The evolution of underwater bubble size distributions at 1-s time intervals for each intermittency case is depicted in Fig. 2.4. By increasing the shutoff time between consecutive air entrainment events, the number of bubbles of all sizes decreases due to buoyancy and dissolution. This loss of bubbles is manifested with an increase in the slopes of bubbles both greater and smaller than the Hinze scale [92]. Bubbles greater than the Hinze scale are fragmented due to the action of turbulent and shear flow, whereas bubbles smaller than the Hinze scale are

stabilized against breakup by the action of surface tension [92]. Therefore, the Hinze scale is defined as the radius of the smallest bubbles that fragment beneath a breaking wave. As also shown by Deane and Stokes [92], the physical mechanisms of yield or resistance to fragmentation described earlier act on two scales in the subsurface bubble size distribution, resulting in two slopes that are separated by the Hinze scale. Visual inspection of the slope change in the bubble size distributions in Fig. 2.4 indicates that the Hinze scale is initially ∼1 mm, but changes with time. Bubbles that are greater than the Hinze scale rise first to the surface, which explains the faster slope increase for this range of bubble sizes (Fig. 2.4). Smaller bubbles persist longer underwater and their slope variation is slower than that of the bigger bubbles. A close examination of the bubble size distributions also reveals that supramillimeter bubbles are completely lost between 3 and 4 s following active air entrainment (Figs. 2.4c to 2.4e), whereas submillimeter bubbles linger in considerable numbers even 5 s following active air entrainment cessation (Fig. 2.4e).

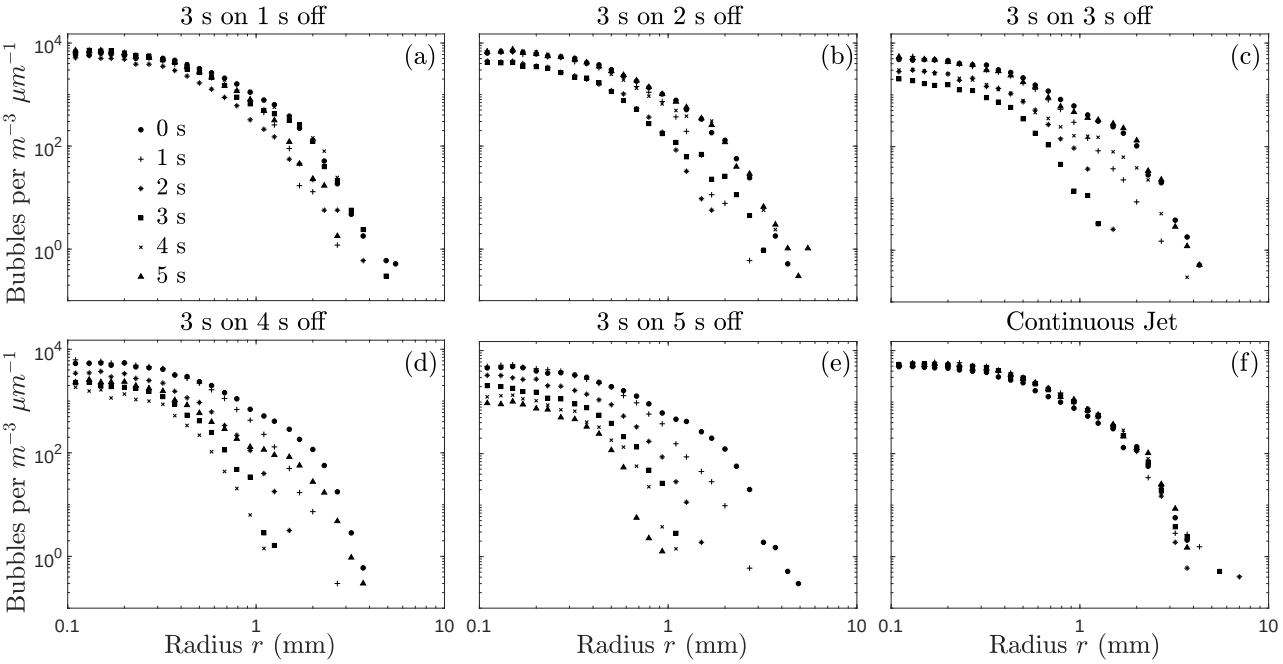

Figure 2.4: **Temporal evolution of subsurface bubble size distributions for the intermittency experiments.** Temporal evolution of subsurface bubble size distributions at 1 s intervals for the intermittency experiments of Fig. 2.3. The plots correspond to **(a)** 1 s, **(b)** 2 s, **(c)** 3 s, **(d)** 4 s, and **(e)** 5 s of solenoid valve shutoff time. Plot **(f)** is for the continuous plunging sheet case. The bubble density in each bin size is the average of 10 independent experiments.

The temporal evolution of the normalized bubbles number ($\frac{N}{N_0}$, where N_0 is the number of bubbles in the imaging window at time $t = 0$ s) for bubbles with radii smaller and greater than 1 mm (Figs. 2.5a and 2.5b, respectively) and the corresponding time derivatives (Figs. 2.5c and 2.5d) are explored for the 5-s plume degassing time case (3 s on 5 s off). After 5 s from air entrainment cessation, the imaging window still contains around 13 % of the initial submillimeter bubbles N_0 (Fig. 2.5a). In contrast, supramillimeter bubbles are completely lost 3 s following air entrainment cessation (Fig. 2.5b). There is a peak in the rate of loss of submillimeter bubbles at time $t = 1$ s (Fig. 2.5c) and at $t = 0.33$ s for supramillimeter bubbles (Fig. 2.5d), which indicates that the most significant variations in bubble numbers in our system occur within 1 s following the cessation of active air entrainment. The rate of change of the normalized submillimeter bubbles number approaches zero asymptotically at a much slower rate than that of the normalized supramillimeter bubbles number. In fact, the rate of change of the normalized supramillimeter bubbles number is almost zero at time $t = 2$ s (Fig. 2.5d), whereas that of the normalized submillimeter bubbles number levels off at -0.06 s^{-1} after $t = 3.5$ s (Fig. 2.5c). The implication of the preceding analysis is that submillimeter bubbles persist for a longer time in water and keep on feeding the surface foam for even longer than 5 s in our system. The first few seconds of plume evolution following breaking waves are associated with the highest gas exchange rate as the largest bubbles rise to the surface [73]. The rest of the smaller bubbles form the background bubble population found in the ocean [100]. The bubbles that persist at $t = 5$ s and later have mostly radii less than 0.5 mm (Fig. 2.4e) which are believed to result exclusively in jet drops when they burst at the water surface [27, 99, 101]. But most importantly, there are no supramillimeter bubbles rising and settling at the surface after $t = 3$ s (Fig. 2.5b), which allows the smaller bubbles to evolve and burst freely on the water surface. The conditions investigated in Fig. 2.5 are relevant to low-frequency wave-breaking events where the effect of background bubble population is considerable.

For high-frequency wave-breaking events under high-wind conditions or in the surf zone, the effect of the transient bubble population becomes important as consecutive wave breaking thwarts the free evolution of the bubble plume. Such conditions can be associated with the case of continuous air entrainment (Fig. 2.4f) where the bubble size distribution is almost constant over time and there is no noticeable loss in small bubbles due to the continuous injection of bigger bubbles. Accordingly, there is no evident coalescence effect on

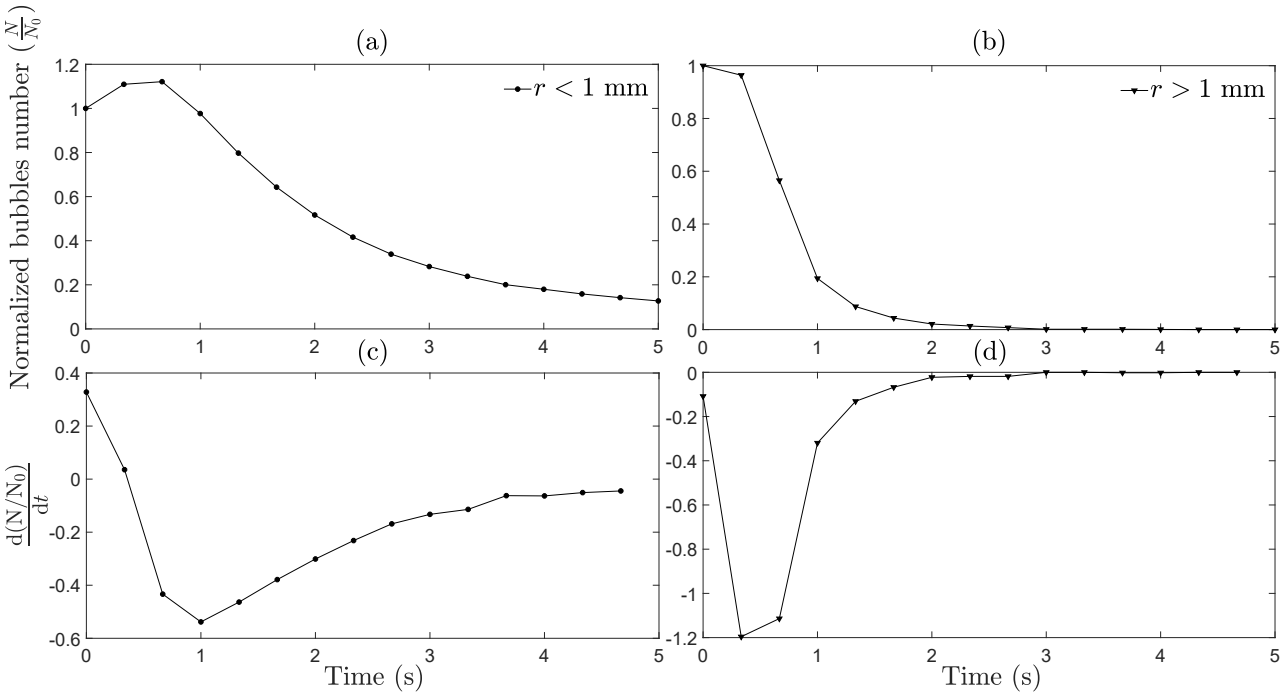

Figure 2.5: **Time evolution and rate of change of the population of submillimeter and supramillimeter subsurface bubbles during plume degassing.** Time evolution of the normalized bubbles number $(\frac{N}{N_0})$ with radius (r) **(a)** less than 1 mm and **(b)** greater than 1 mm in the 3 s on 5 s off experiment. Figures 2.5**(c)** and 2.5**(d)** show the corresponding time rate of change $(\frac{d(N/N_0)}{dt})$ of the normalized submillimeter and supramillimeter bubbles, respectively. The normalized bubbles number in Figs. 2.5**(a)** and 2.5**(b)** is averaged over 10 independent plunging events for each time step (0.33 s).

the subsurface bubble plume. In fact, some investigators have ruled out the importance of underwater bubble coalescence/fragmentation [85, 102] due to hydrodynamic repulsion between approaching bubbles. However, the effect of continuous bubbling may be more pronounced on the surface foam. Unlike rising bubbles, the mechanisms of bubble evolution and coalescence in the surface foam are far more complicated. Adjacent bubbles in a foam patch experience liquid drainage and coarsening, which alters the initial size distribution input from rising bubbles that reach the surface [103, 104]. Hence, continuously feeding the water surface with big bubbles might prevent fine bubbles from evolving and bursting freely. Accordingly, the contribution of film drops that are ejected from the unconstrained bursting of submillimeter bubbles at the surface might be restricted. Indeed, a previous study showed that the shape of the aerosol size distribution for seawater enhanced with organic materials is altered when using a continuous jet as compared to a pulsed jet [105].

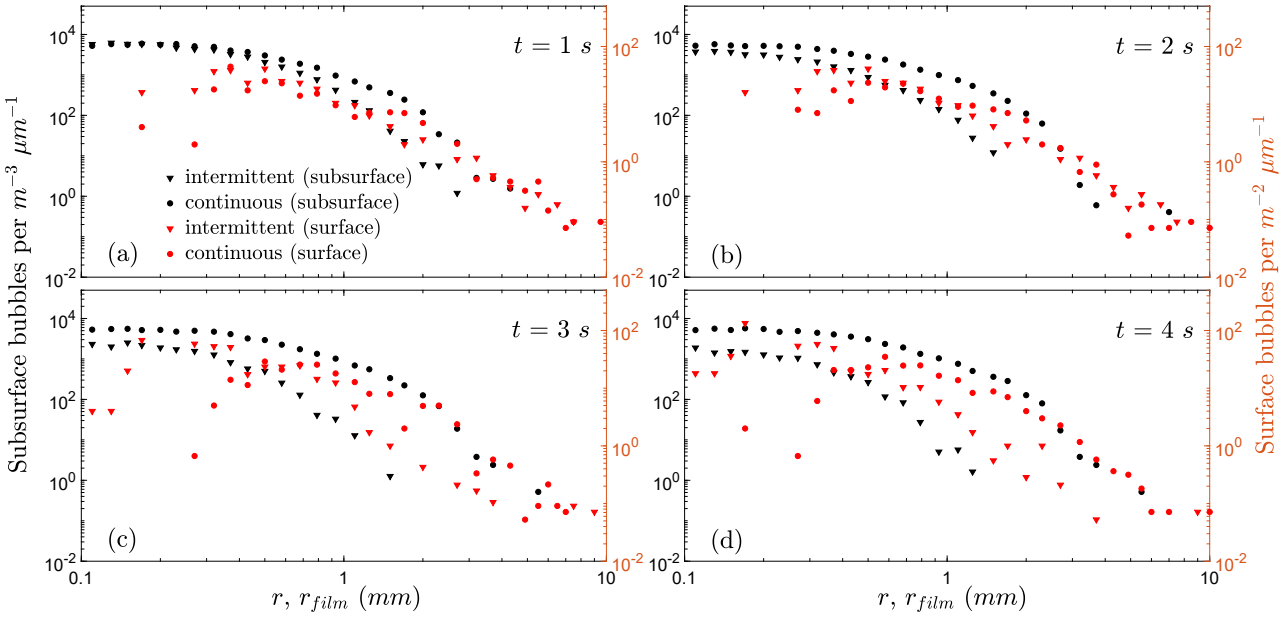

Figure 2.6: **Subsurface and surface bubble size distributions following active air entrainment in the continuous and intermittent water sheet experiments.** Subsurface (black) and surface (red) bubble size distributions for times **(a)** $t = 1$ s, **(b)** $t = 2$ s, **(c)** $t = 3$ s, and **(d)** $t = 4$ s following active air entrainment. Circles correspond to the continuous water sheet data and triangles correspond to the intermittent water sheet data. The left axis (black) corresponds to the subsurface bubble size distribution and has units of density per unit volume of water per micrometer increment in bubble radius. The right axis (red) corresponds to the surface bubble size distribution and has units of density per unit area of water surface per micrometer increment in bubble film radius. The x-axis corresponds to both the subsurface bubble radii (r) and the surface film radii (r_{film}).

To further understand the effect of air entrainment intermittency on the free decay of a surface foam, we measured the sizes of the bubbles within the surface foam for a continuous water sheet as well as for an intermittent (3 s on 5 s off) sheet case (Fig. 2.6). Most of the literature in oceanography studies focuses on the subsurface bubble size distribution with few investigators reporting on bubble size distributions in the surface foam [56]. We report our results on the size distribution of surface bubbles as number of bubbles per unit area of water surface per micrometer increment in bubble film radius [56]. Note that the radius of a bubble settling on the water surface is called film radius and is generally different in size from the corresponding subsurface bubble radius (Lewis and Schwartz [27]; their Fig. 31; Salter et al. [56]). At times $t = 1$ s (Fig. 2.6a) and $t = 2$ s (Fig. 2.6b), the surface bubble size distributions are almost the same for the intermittent and continuous water

sheet cases. For the intermittent case, the film radius of surface bubbles is greater than the radius of the submerged bubbles at all times. This difference in bubble sizes between subsurface and surface bubbles stems from the effect of coalescence and coarsening in surface foams that alters the surface bubble size distribution. For instance, at time $t = 2$ s (Fig. 2.6b), the greatest subsurface bubble radius is less than 2 mm, whereas surface bubbles are present with a film radius up to 8 mm. A considerable difference in the surface bubble size distributions between the intermittent and the continuous water sheet cases starts to be noticeable at times $t = 3$ s (Fig. 2.6c) and $t = 4$ s (Fig. 2.6d). There is a noticeable increase in sub 0.3-mm bubbles in the intermittent case after 3 s of active air entrainment cessation (Figs. 2.6c and 2.6d). In contrast, these small bubbles are almost not present in the continuous case. Moreover, following 4 s of active air entrainment cessation (Fig. 2.6d), very few supramillimeter bubbles remain on the surface in the intermittent case as compared to the continuous case. The presence of very fine bubbles accompanied by the absence of supramillimeter bubbles, in the intermittent water sheet case, allows fine bubble to evolve freely on the water surface without any interactions with the bigger bubbles. In contrast, the presence of a persistent layer of big bubbles in the foam generated by a continuous water sheet (Figs. 2.6a to 2.6d) might lead the fine subsurface bubbles to be trapped below the foam layer [105]. Furthermore, even if they reach the water surface, sub 0.3-mm bubbles are likely to coalesce with bigger bubbles emerging from continuous air entrainment. Based on the evidence above, our results support the hypotheses that continuous air entrainment prevents smaller bubbles from evolving freely on the water surface and leads to spray aerosol production that is more biased toward film drops.

2.5.2 Salinity effect on air entrainment in the plunging sheet

2.5.2.1 Subsurface bubble plume characteristics

In this section, we investigate the effect of water salinity on air entrainment in the wave-breaking analog tank. Following our observations in Sect. 2.5.1 on the implications of the plunging sheet intermittency on subsurface bubble plumes and surface foam characteristics, we chose an intermittent (3 s on 8 s off) water sheet case for the salinity study. As mentioned in the Sect. 2.3, previous studies on the effect of salinity on air entrainment focused on

comparing freshwater and seawater. No systematic study on the effect of different salinities on bubble plume characteristics (especially size distribution) has been reported [27], except a single study on void fraction dependence on salinity [39]. We start our investigation by comparing the bubble size distribution of freshwater and synthetic seawater containing 35 g/kg of salt in our experiments against available data from the literature (Figs. 2.7a and 2.7b). The shapes of the distributions for both freshwater and seawater imply that the bubble generation mechanism has a considerable effect on the subsurface bubble plume characteristics. For seawater (Fig. 2.7a), the bubble size distribution in the present study, in the MART system [76] , and in a wave channel [92], are characterized by two distinct slopes. The two slopes are less noticeable in the lake spray aerosol (LSA) generator [35]. This discrepancy may be attributed to the small size of the tank used in the LSA generator (only 18 L) as well as the manual bubble detection technique [35]. The bubble size distribution in our experiment is in very good agreement with that in Deane and Stokes [92] and Callaghan et al. [76] for submillimeter bubbles. However, the corresponding supramillimeter bubble size distributions show some discrepancy. The bubble size distribution in our experiment and in the MART system [76] are in good agreement even for supramillimeter bubbles. This agreement is expected since our system is basically identical to the MART system and the experimental conditions for the two distributions are almost similar (see Fig. 2.7 caption). Yet, the slopes of supramillimeter bubble size distribution in both systems are steeper than that of the wave channel. This difference in slopes is expected since the wave channel data are averaged over the acoustic phase, whereas the present and the Callaghan et al. [76] studies correspond to the quiescent phase (see Sect. 2.5.1). Nonetheless, even when comparing the plunging sheet bubble size distribution during the acoustic phase (i.e., at time $t = 0$ s) to the distribution in the wave channel, the slope of supramillimeter bubbles is still slightly steeper in the plunging sheet setup. Accordingly, we expect that bigger bubbles are entrained beneath an oceanic wave than in our setup. Given that bubbles bigger than the Hinze scale are created during the cavity (air tube) collapse [92], a flow feature that is not reproducible in a plunging water sheet, it seems that our setup cannot reproduce the sizes and the numbers of the biggest bubbles formed under an oceanic wave (up to 1 cm in radius according to Deane and Stokes [92]). Note that despite the different locations of imaging windows used in the present study (Fig. 2.2a) and in the Callaghan et al. [76] study (the top part of their analysis window is located 3 cm below the water surface as shown in their

Fig. 2), there is a good agreement between the bubble size distributions evaluated in the two studies. This consistency indicates that our choice of the imaging window does not have a significant effect on the subsurface bubble size distribution measurements. In the case of freshwater (Fig. 2.7b), there is a higher discrepancy between the bubble size distributions available in the literature. Unlike for seawater, the freshwater bubble size distribution in a tipping trough [88] is bimodal at 0.3 and 1-2 mm, respectively. There is also a peak in the LSA generator bubble size distribution for both synthetic and Lake Michigan freshwater [35] at around 0.3 mm (Fig. 2.7b). In contrast, the freshwater distribution in the wave channel [83] and in the plunging sheet of our system have no distinguishable modes. Moreover, there is a good agreement between the slopes of supramillimeter bubbles in the plunging sheet and in the wave channel [83]. Furthermore, in a similar experimental setup to Deane and Stokes [92] and Loewen et al. [83], Leifer and De Leeuw [106] and Leifer et al. [107] identified nine distinct plume categories distributed among two main groups in experiments in a wind-wave channel using unclean freshwater. The first group represents plumes termed as "diffuse" whereas the second group is constituted of plumes termed as "dense" based on the ability of the plumes to obscure the background. Although dense plumes exhibited multimodal distributions unlike the two slopes distribution in diffuse plumes, the subsurface bubble size distribution was characterized by two slopes when all nine plume categories were combined [106, 107]. Accordingly, the two slopes that characterize bubble size distribution in seawater-breaking waves [92] are also present in freshwater [106, 107], which conforms with the freshwater bubble size distribution of our setup shown in Fig. 2.7b. Figure 2.7c shows the ratio of 35 g/kg saltwater bubble size distribution (D_{35}) to freshwater bubble size distribution (D_0) at the instant of active air entrainment cessation ($t = 0$ s). In the submillimeter bubble radii range, the percent increase in the population of saltwater subsurface bubbles over the corresponding population of freshwater bubbles ranges between 53% and 117% at bubble radii of 0.32 and 0.79 mm, respectively. In contrast, the ratio in the supramillimeter range is more sporadic with values above unity for bubbles with radii up to 1.7 mm and below unity in the 1.7- to 2.3-mm bubble radii range.

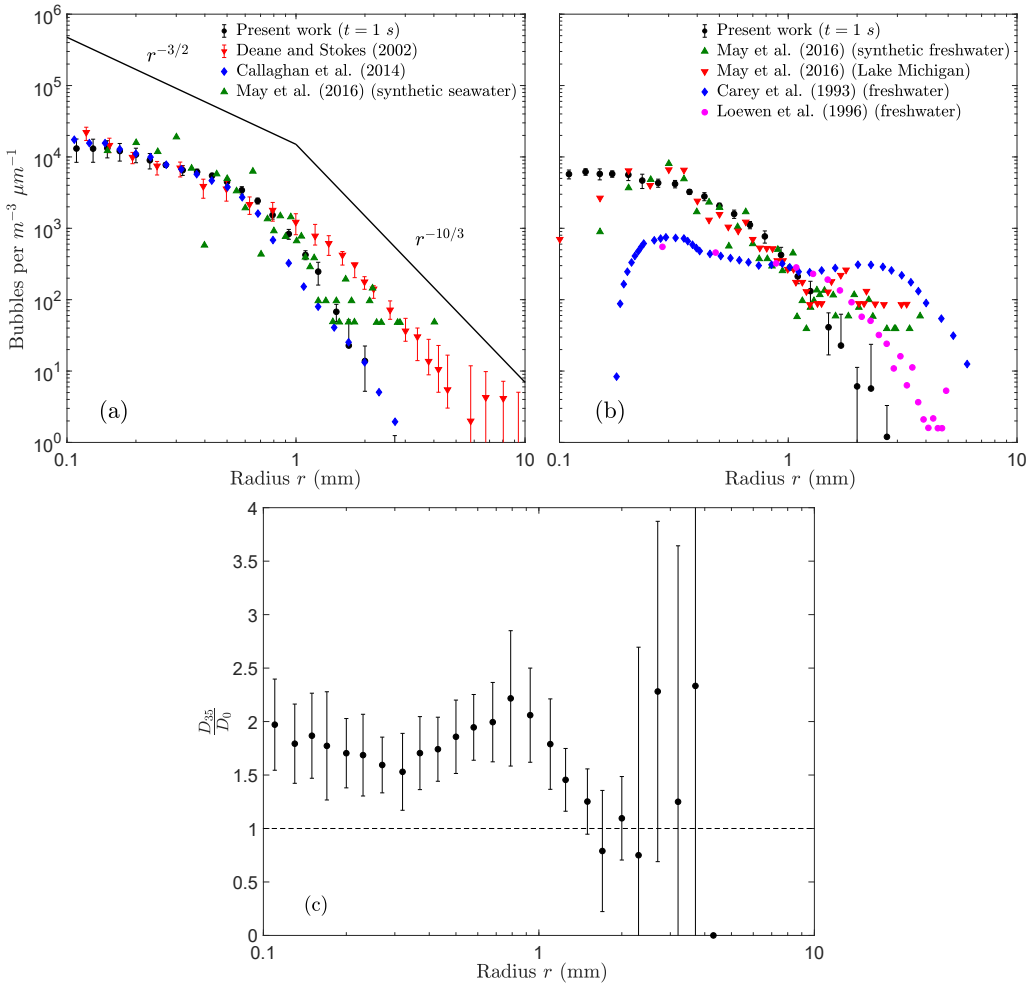

Figure 2.7: **Subsurface bubble size distribution in seawater and freshwater compared to other measurements from literature and the ratio of saltwater-to-freshwater bubble size distributions.** Bubble size distribution in **(a)** seawater and **(b)** freshwater. Panel **(a)** shows the bubble size distribution at a salinity of 35 g/kg and a temperature of 20.3 °C in this study at time $t = 1$ s. Also shown are previously measured bubble size distributions in unfiltered seawater with a salinity of 33 g/kg at 20 °C in a MART system also at time $t = 1$ s [76], synthetic seawater in a lake spray aerosol (LSA) generator during active air entrainment [35], and seawater in a wave flume during active wave breaking [92]. The lines are the theoretical -3/2 and -10/3 power scaling laws for bubbles smaller and greater than the Hinze scale, respectively [92]. Panel **(b)** shows the bubble size distribution for freshwater at 19.0 °C at time $t = 1$ s. Also shown are previously measured bubble size distributions in synthetic and Lake Michigan freshwater [35], in freshwater in a wave channel [83], and in freshwater with a tipping trough [88]. In the determination of subsurface bubble size distributions, the line of sight of the plume camera spanned the tank length (1 m) and this dimension was used to calculate the total water volume in the camera's field of view. The bubble size distributions in panels (a)-(b) are scaled to coincide at the Hinze scale [90]. **(c)** The ratio of saltwater (35 g/kg) to freshwater (0 g/kg) bubble size distributions at time $t = 0$ s.

The bubble size distributions at 1-s intervals starting from air entrainment cessation ($t = 0$ s) for salinity values of 0, 10, 20, 30, and 40 g/kg are depicted in Fig. 2.8. Although not shown in Fig. 2.8, the standard deviation of the data points in the submillimeter range is within 10 % to 15 % of the average value, yet the uncertainty increases to more than 100 % in the supramillimeter range. Increasing salinity leads to a pronounced and monotonic increase in bubbles with radii between 0.1 and 0.5 mm at time $t = 0$ s (see Fig. 2.8a and Fig. A.2a). This increase is consistent with the results of May et al. [35]; their Fig. 7, who observed an increase (2-3 orders of magnitude) in the density of bubbles with radii smaller than 0.3 mm during active air entrainment in the LSA generator. However, the increase in bubble density for sub-0.3 mm bubbles is less pronounced in our system, with the maximum difference between freshwater and the most saline water (40 g/kg) not exceeding a ratio of two at time $t = 0$ s. Unlike the significant increase in bubble population in the submillimeter range, the density of supramillimeter bubbles is almost constant over the investigated salinity range (see Figs. 2.8 and Fig. A.2b). Since increasing salinity enhances the submillimeter bubble population in the bubble plume, the gap between the bubble size distributions at different salinity values increases with time, driven by the reduced buoyancy of the profusion of tiny bubbles in saltier waters (Figs. 2.8b to 2.8f). One possible explanation for the increase in small bubbles density in higher salinities is the enhanced coalescence inhibition in more salty waters [41, 84, 108, 109]. Another explanation is the ion specific shattering of big bubbles into smaller bubbles in saltier waters [85]. However, the increased coalescence inhibition is based on observation of bubbling from a glass frit [84]. Air entrainment by a plunging sheet is intrinsically different from glass frits bubbling, and such an explanation might not apply to air entrainment from water jets and breaking waves. Additionally, it has been suggested that the effect of bubble coalescence in underwater bubbles is minimal [85, 102, 106] due to the hydrodynamic repulsion between approaching bubbles. Hence, further investigations on the effect of salinity on the physical mechanisms of air entrainment in a breaking wave (see Deane and Stokes [92]) can help in elucidating the increase in bubble population in the plume observed with increasing salinity. Monitoring changes in the plunging sheet roughness (see Callaghan et al. [76], Kiger and Duncan [95], Zhu et al. [110]) and the Hinze scale during systematic salinity experiments can provide great insights on the change in air entrainment volume and subsurface bubble size distribution with salinity.

To more closely investigate the effect of water salinity on bubble size distribution, we divided

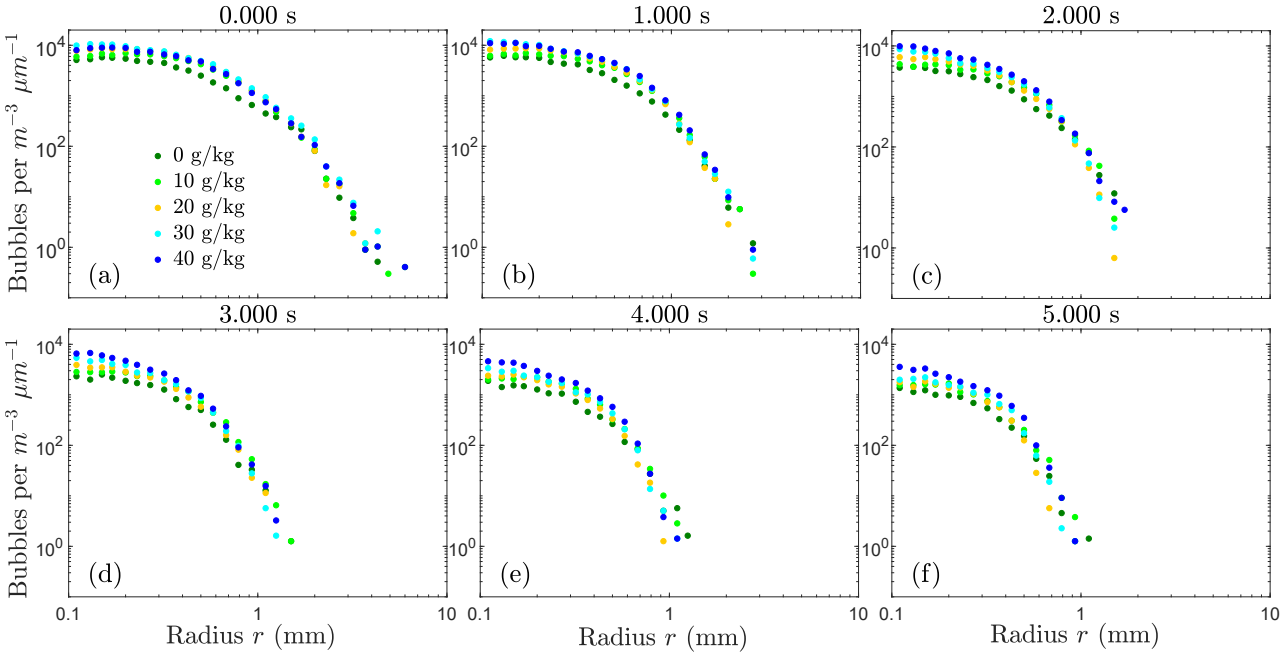

Figure 2.8: **Time evolution of subsurface bubble size distributions for different water salinities.** The time evolution of bubble size distributions for different salinities ranging from 0 to 40 g/kg in 10 g/kg increments. Each data point is the result of an ensemble average over 10 plunging events for each bin size.

the bubble radii between 0.1 and 5.0 mm into six bins and determined the time evolution of the normalized total bubbles number (Figs. 2.9a, 2.9d, and 2.9g), the void fraction α (Figs. 2.9b, 2.9e, and 2.9h), and the fraction of total air volume (Figs. 2.9c, 2.9f, and 2.9i) in each bin. There is an increase in bubble population in all six bins (average increase of 65 %) in the highest salinity water (40 g/kg) over the freshwater (0 g/kg) experiment at time $t = 0$ s (Fig. 2.9a). The greatest increase of 92 % in bubble population occurs for bubbles with radii between 0.5 and 0.8 mm (Fig. 2.9a). Moreover, the bubble population plots (Figs. 2.9a, 2.9d, and 2.9g) suggest that increasing salinity results in a systematic increase in bubble populations especially for submillimeter bubbles. On the other hand, supramillimeter bubbles do not exhibit a clear correlation with salinity (see Fig.A.2b and the supramillimeter bins in Figs. 2.9a, 2.9d, and 2.9g). Likewise, previous experiments in a wave channel also showed no significant differences between freshwater and seawater in the entrainment of bubbles with radii greater than 0.8 mm [83]. However, caution should be exercised when interpreting the data pertaining to supramillimeter bubbles due to the high uncertainty associated with this range in the plunging sheet setup (Figs. 2.7a to 2.7c and

2.9a, 2.9d, and 2.9g; see also Stokes et al. [90]; their Fig. 4) as compared to a wave channel. To associate the bubble population results to the air entertainment volume, the total air volume inside the imaging window is computed by integrating the subsurface bubble size distribution (see Fig.A.3). Evaluating the total air volume at time $t = 0$ s indicates that there is an increase of 52 % in the total volume of air entrained in the 40 g/kg saline water over freshwater (see Fig. A.3a). Although nonmonotonic, there is a general increasing trend in the total entrained air volume between the two salinity extremes at time $t = 0$ s. Therefore, we may speculate that more air is entrained in more saline water. However, the reader should keep in mind that the air volume was computed starting from a depth of 11 cm (Fig. 2.2a), and accordingly, the densest near-surface part of the bubble plume is not incorporated in the air volume calculations. Although our speculation on the increase of air entrainment with salinity is inconclusive due to the limitation in the location of the imaging window, an increase in air entrainment volume in seawater over freshwater was also observed in a wave channel experiment [82, 86], and in the LSA generator [35].

The distribution of the void fraction α over the six bins indicates that at time $t = 0$ s, bubbles of radii greater than 0.5 mm contribute around 75 % to the total void fraction (Figs. 2.9b and 2.9c). As the degassing of the bubble plume continues, the peak in volume fraction contribution shifts to smaller radii with bubbles less than 0.5 mm contributing to around 55 % of the total air volume at time $t = 4$ s (Fig. 2.9i). The void fraction at $t = 0$ s increases systematically with salinity for all submillimeter bubbles (Fig. 2.9b), which is consistent with the systematic increase of submillimeter bubble population with salinity reported earlier. For later times (Figs. 2.9e and 2.9h), there is also a noticeable difference in the void fraction in each bin size, even though most of the entrained air is lost with the degassing of the larger bubbles. The preceding analysis suggests that the background bubble population that remains after the degassing of the initial bubble plume is higher in more saline water than in freshwater (Figs. 2.9e and 2.9h). The enhancement of background bubble population in saltier water stems from the abundance of tiny bubbles that characterizes saltwater. Due to their reduced buoyancy, these submillimeter bubbles extend the lifetime of the bubble plume, which enhances the background bubble population in saltwater over freshwater.

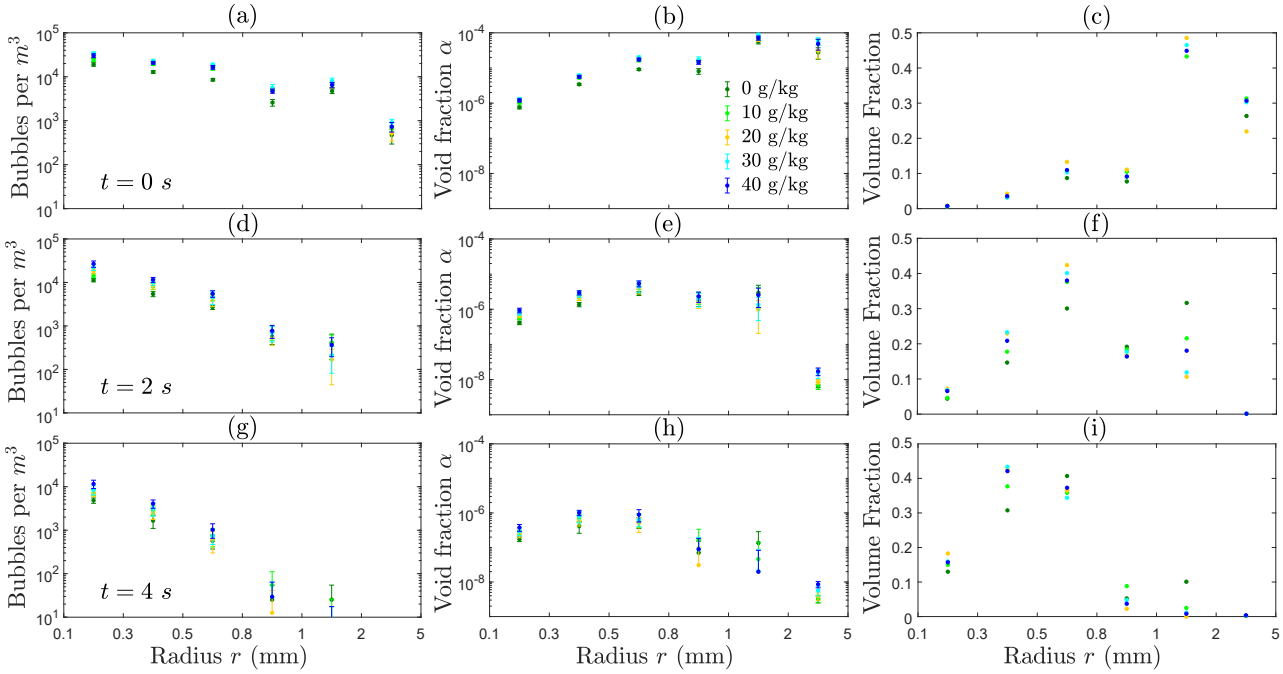

Figure 2.9: **Time evolution of the bubble concentration, void fraction, and fraction of total air volume in six subsurface bubble size bins for various water salinities.** Time evolution of the normalized bubbles number (bubbles per m^3 of water volume in the imaging window) divided into six bins (**a**, **d**, and **g**). The corresponding void fraction α (air volume occupied by the bubbles divided by the water volume in the imaging window) in each bin size, calculated by assuming spherical bubble shapes (**b**, **e**, and **h**). Also shown is the contribution of each bin size (expressed in volume fraction) to the total air volume (**c**, **f**, and **i**). The values are the result of an ensemble averaging over 10 independent trials for each salinity value and the error bars in the first and second columns are ± 1 standard deviation.

2.5.2.2 Surface foam characteristics

The temporal decay of surface foam area A following cessation of active air entrainment for all salinity values (0-40 g/kg) is depicted in Fig. 2.10a. Increasing water salinity leads to a systematic increase in foam persistence time with the most noticeable increase in foaming enhancement occurring between salinity values of 0 and 5 g/kg, as well as between 5 and 10 g/kg. Although there is an increase in foam persistence for water salinities between 20 and 40 g/kg, the foam decay curves are relatively similar. These results are consistent with a previous study that found no significant differences in foam thickness for oceanographically relevant salinities [89]. To further investigate the effect of water salinity on the decay char-

acteristics of surface foam, we modeled the temporal decay of surface foam with a simple exponential model [44]:

$$A(t) = A_0\, e^{-t/\tau} \tag{2.1}$$

where A_0 is the area at the start of the areal decay (at time $t = 0$ s) and τ is a decay timescale (see Table 2.1). The maximum foam area (A_0) increases nonmonotonically with salinity, with the maximum foam area increasing by 32.7 % with a 30 g/kg addition of salt to freshwater. We can infer from the increasing trend in A_0 that more foam persists at the water surface at the end of active air entrainment in more saline waters. The decay time is a quantitative measure of the persistence of foam patches on the water surface. A higher decay time indicates more persistent foams, whereas lower decay times indicate less persistent foams. Similarly to the A_0 values, the decay times also show a nonmonotonic increase with salinity, with the lowest value occurring for freshwater and the highest at a salinity of 35 g/kg. Accordingly, there is a quantifiable effect of water salinity on surface foam persistence: foams persist longer in saline water than in freshwater. To further quantify the increase in foam persistence in more saline water, the foam area for water salinities of 10, 20, 30, and 40 g/kg normalized to that of freshwater (0 g/kg) are depicted in Fig. 2.10c. Increasing water salinity results in an orderly increase in areal ratio with time. The percent increase in foam area over freshwater (averaged over the 5-s data collection period) is 78%, 90%, 97%, and 103 % for salinity values of 10, 20, 30, and 40 g/kg, respectively. One explanation for the increased foaming effect observed in more saline water is the increased number of subsurface bubbles with increased salinity (Figs. 2.8 and 2.9). As described by Scott [41], the increased number of slowly rising submillimeter bubbles in more saline water extends the lifetime of surface foam. Indeed, sub-500-microns bubbles are more persistent in more saline water (Figs. 2.8d to 2.8f), and they accordingly replenish the surface foam for a longer time. Nevertheless, surface foam evolution is not only affected by replenishing from the subsurface bubble plume but also by physical mechanisms affecting its persistence on the water surface. Since salinity has a minute effect on viscosity [27], the thin-film drainage of foam cells is not expected to be affected significantly by variations in salinity due to viscosity variations [111]. However, the reduction in surface tension expected in our tap water experiments [39] may reduce the drainage pressure [101, 112] and decrease viscous drainage on the bubble cap. Furthermore,

Table 2.1: The coefficients of exponential decay fit (Eq. (2.1)) for all salinity values.

Salinity (g/kg)	$A_0\,(cm^2)$	$\tau\,(s)$
0	114.0 (107.7, 120.4)	1.66 (1.53, 1.82)
5	138.0 (129.9, 146.2)	1.89 (1.73, 2.08)
10	145.5 (136.6, 154.4)	2.14 (1.95, 2.37)
15	145.9 (137.5, 154.4)	2.24 (2.05, 2.47)
20	145.9 (136.8, 155.1)	2.28 (2.07, 2.54)
25	142.4 (132.2, 152.6)	2.48 (2.22, 2.81)
30	151.3 (139.6, 163.1)	2.32 (2.06, 2.66)
35	143.5 (133.0, 154.0)	2.54 (2.27, 2.90)
40	145.3 (133.1, 157.5)	2.48 (2.18, 2.88)

Note. The fitting starts at time $t = 0$ s. Columns 2 and 3 show the area (A_0) at the start of the decay ($t = 0$ s) and the foam decay time (τ), respectively. The 95 % confidence intervals are displayed between parentheses for each fit coefficient.

recent studies have shown a replenishing upward flow (Marangoni flow) from the bubble base to its apex induced by surface tension gradients after addition of salt to freshwater [113]. This flow is induced by the evaporative effects on the bubble cap, and it counteracts the viscous drainage from the bubble cap to the bulk water. A reduced viscous drainage coupled with a replenishing upward flow on the bubble cap extends its lifetime, although the latter is also affected by interactions of the bubble with the surrounding foam cells. Further investigations on the effect of salinity on foam cells drainage and coalescence/coarsening mechanisms could help in elucidating the increased foam persistence in more saline water. A particular attention should be drawn to small-salt concentrations (5-10 g/kg) since they greatly enhance the lifetime of surface foam (Fig. 2.10a).

The time rate of change of the foam area ($\partial A/\partial t$) for freshwater and an oceanographic salinity of 35 g/kg is shown in Fig. 2.10b. The maximum rate of decrease of foam area is 64 and 48.5 cm^2/s for 0 and 35 g/kg salinities, respectively. The negative peak in areal decay occurs 0.2 s earlier in freshwater than in the 35 g/kg saltwater. Following the peaks in the areal rate of change, the foam area loss in saltwater is higher than that in freshwater (more negative derivative value as shown in Fig. 2.10b), yet the foam coverage in more saline water remains higher than that in freshwater at any instant during the surface foam decay (Figs.

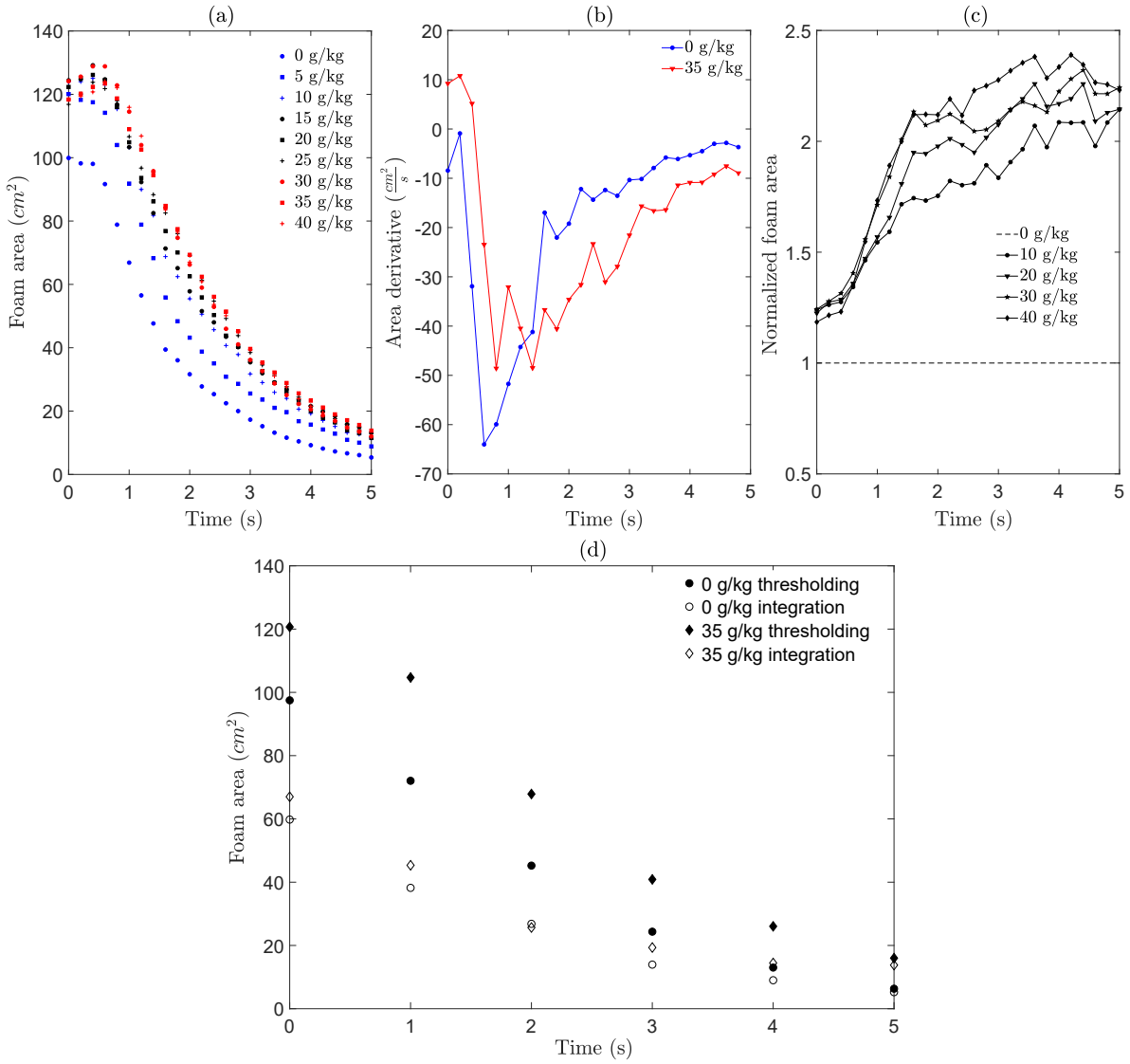

Figure 2.10: **Characteristics of the time evolution of surface foam area for various water salinities and the decay of surface foam area calculated via thresholding and by integration of the surface bubble size distribution.** **(a)** Temporal evolution of surface foam area A for water salinity values increasing from 0 to 40 g/kg in 5 g/kg increments. **(b)** Temporal evolution of the rate of change of surface foam area $\partial A/\partial t$ with time for freshwater (0 g/kg) and saltwater (35 g/kg). **(c)** Temporal evolution of the surface foam area at salinities of 10, 20, 30, and 40 g/kg normalized to the foam area of freshwater (0 g/kg). The data in Figs. 2.10a to 2.10c are obtained by the thresholding algorithm described earlier and the data points are average values over 10 independent plunging events for each water salinity. **(d)** The decay of surface foam area in freshwater and 35 g/kg saltwater calculated via thresholding and by integration of the surface bubble size distribution.

2.10a, 2.10c, and 2.10d). Hence, despite the higher loss of foam cells in saltwater, surface foam remains more persistent in saltwater than in freshwater. The higher rate of foam cells loss in saltwater also indicates that more surface bubbles are lost by bursting, which can increase droplets emission from the surface with increasing salinity.

Next to the thresholding method described earlier (see Sect. 2.4, Text S1, and Fig. A.1b), we determined the total foam area by integrating the surface bubble size distribution $n(r_{film}, t)$ (see Fig. A.1c) using :

$$A(t) = \int_{r_{film,1}}^{r_{film,2}} \pi\, r_{film}^2\, n(r_{film}, t)\, dr_{film} \tag{2.2}$$

Where, r_{film} is the bubble film radius and $r_{film,1}$ and $r_{film,2}$ are the lowest and highest surface bubbles film radii in the foam, respectively. Figure 2.10d shows the temporal evolution of the surface foam area calculated using Eq. (2.2) and by binarizing the image using a thresholding algorithm for freshwater and a 35 g/kg saltwater. The maximum foam areas computed using the thresholding technique are ∼70% higher than those computed by integrating the surface bubble size distribution. Moreover, the percent increase in maximum foam area in saltwater over freshwater at time $t = 0$ s is 23.8% and 12.1% using the thresholding and integration methods, respectively. The overestimation of the foam area using the thresholding method could be an artifact of the image binarization algorithm. Since the threshold method is based on differences in the pixels intensity of the image, excessive light scattering from highly clustered swarms of surface bubbles might hinder the accuracy of the algorithm. For instance, a closer look at the binary foam image in Fig. A.1b reveals that areas not covered by foam patches do contribute to the total foam area, possibly due to light scattering from nearby foamy patches. Moreover, unlike the integration method that exclusively resolves surface bubbles, subsurface bubble plumes might have contributed to the foam areas evaluated by the thresholding method. Despite this inherent drawback in the thresholding method, the same threshold algorithm was applied to all the foam images across the different experimental runs, which renders the extracted foam decay properties at different salinity values in Figs. 2.10a to 2.10c internally consistent.

To further investigate the effect of salinity on the time evolution of foam cells, we quantified surface bubbles film radii in freshwater and saltwater (see Sect. 2.5.1). The surface bubbles

size distributions (red curves) for freshwater (0 g/kg) and a typical oceanic salinity of 35 g/kg for times $t = 0$ s, $t = 1$ s, $t = 2$ s, $t = 3$ s, $t = 4$ s, and $t = 5$ s are shown in Fig. 2.11. Also shown are the subsurface bubble size distributions (blue curves) at each time. At times $t = 0$ s (Fig. 2.11a), $t = 1$ s (Fig. 2.11b), and $t = 2$ s (Fig. 2.11c), there is a noticeable increase in the number of surface bubbles in saltwater as compared to freshwater for bubbles less than 2 mm in radius. Surface bubbles with film radii greater than 2 mm are comparable in number for the two salinities at times $t = 0$ s (Fig. 2.11a) and $t = 1$ s (Fig. 2.11b) and they are more numerous in freshwater at time $t = 2$ s (Fig. 2.11c). Following 3 s from the cessation of active air entrainment, few bubbles with film radii greater than 1 mm, for both salinities, persist on the water surface (Figs. 2.11d to 2.11f). Moreover, surface bubbles with film radii down to 0.1 mm are more numerous in saltwater than in freshwater at times $t =$ 3 s (Fig. 2.11d), $t = 4$ s (Fig. 2.11e), and $t = 5$ s (Fig. 2.11f). The overall increase in surface bubble concentration in more saline water suggests that more droplets from bubble bursting are emitted from saltwater following wave breaking as compared to freshwater. This result agrees with the aerosol size distribution of freshwater and saltwater in an LSA generator (May et al. [35], Fig. 4a), albeit the considerable increase in dry particles emission in saltwater reported in the aforementioned study is probably due to the higher ionic content in saltwater as compared to freshwater (May et al. [35], Fig. 1).

Next to the increase in the total number of droplets emitted in saltwater, we can infer the contribution of film drops and jet drops to the spray aerosol production during the foam area decay from the size distributions of surface bubbles. Based on the review of Lewis and Schwartz [27]; Fig.26, and the experimental study of Lhuissier and Villermaux [101], bubbles with film radii less than 1-1.5 mm produce almost exclusively jet drops, whereas bigger bubbles produce almost exclusively film drops. Overall, the increase in surface bubbles population in more saline water is for bubbles with radii up to a couple of millimeters and down to the detection limit of the overhead camera (Fig. 2.11). This result suggests that more jet drops emission is expected in more saline water. Given that no noticeable differences in supra 2-mm surface bubbles population are observed in our experiments between saline water and freshwater during the foam decay (Fig. 2.11), we conclude that the film drop emissions would not be as highly associated to salinity as jet drop emissions.

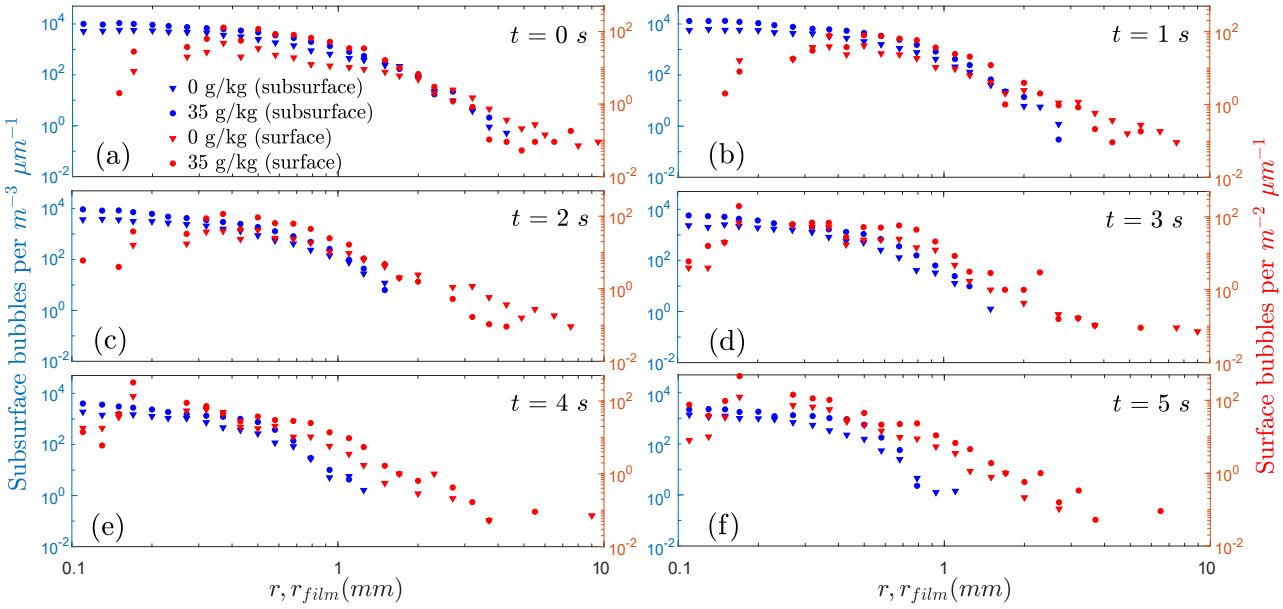

Figure 2.11: **Time evolution of subsurface and surface bubble size distributions in freshwater and saltwater.** Subsurface bubble size distributions (left axis) and surface bubble size distributions (right axis) for water salinities of 0 and 35 g/kg at times **(a)** $t = 0$ s, **(b)** $t = 1$ s, **(c)** $t = 2$ s, **(d)** $t = 3$ s, **(e)** $t = 4$ s, and **(f)** $t = 5$ s.

2.6 Conclusions

In this study, we systematically explored the effect of water salinity on subsurface bubble plumes and surface foams in an intermittent plunging sheet setup. Our experiment on the effect of plunging sheet intermittency on air entrainment highlights the disparities in bubble plume characteristics and surface bubbles sizes in systems that use continuous jets as opposed to systems that use intermittent jets. In the intermittent sheet case, the surface bubbles size distribution is highly variable with time after air entrainment cessation, which influences the bubble-mediated interactions at the water surface. Bubble film radii at the water surface shift to smaller sizes as the surface foam evolves indicating that the contribution of film and jet drops varies during foam decay. Our results confirm the concerns put forward by many previous researchers [56, 91, 99, 105], who argued that continuous air entrainment could lead to a biased aerosols emission from the surface foam. Accordingly, we suggest that it is important to allow enough time for the bubble plumes and surface foams to evolve following active air entrainment in future experimental studies dealing with aerosolization from aquatic environments. Such a recommendation is especially relevant to the contribution

of the background bubble population to air-sea processes under low frequency wave-breaking events. However, if the breaking events are highly frequent in time and space, the continuous air entrainment case could better describe the in situ evolution of surface foams.

Increasing water salinity leads to an evident effect on the sizes and numbers of entrained subsurface bubbles. Contrary to the supramillimeter bubbles population that is almost independent of salinity, submillimeter bubbles exhibited a systematic increase with increasing salinity. Regarding the effect of salinity on the total entrained air volume, our analysis was restricted to a deep section of the bubble plume and missed the near-surface section that holds the majority of the entrained air. Despite this limitation, we speculate that breaking waves inject more air in the water column in saltwater than in freshwater.

As for the surface foam, our results indicate that there is a systematic and distinct increase in the area and lifetime of surface foam with increasing salinity. Next to the increased foaming in more saline water, surface bubbles in freshwater and saltwater showed distinct disparities. Considering surface bubbles of all sizes, there is a noticeable increase in surface bubble population with increasing salinity, which suggests that more droplets are ejected from more saline water as compared to freshwater. More specifically, bubbles with film radii up to a couple of millimeters are more numerous in saline water as compared to freshwater. We did not observe any noticeable difference in the population of surface bubbles with radii greater than 2-3 mm with increasing salinity. The surface bubbles characteristics hint that changing water salinity has a more pronounced effect on jet drops than on film drops.

With the lack of a comprehensive study on the variation of air entrainment from breaking waves with salinity, our study provides insights on the changes in air-water interactions due to variations in salinities in different bodies of water. Both the increase in surface bubbles number and their residence time with increasing salinity indicate that the latter has a considerable effect on bubble mediated interactions at the air-water interface. Yet, the extent of the salinity effect on water foaming is dependent on the salt concentration. Although a systematically varying salinity did not have a considerable effect on foam decay for oceanographically relevant salinities (say 30-40 g/kg), even low-salt concentrations drastically enhance the foaming characteristics of freshwater. This result raises concern on the use of saltwater models to predict bubble-mediated air-water interactions in freshwater bodies (see, e.g., Chung et al. [59]).

2.7 Acknowledgments

We acknowledge the College of Engineering at Virginia Tech for supporting this research. We would also like to thank two anonymous reviewers for their insightful comments that ultimately strengthened the quality of this manuscript. All data presented herein are available at https://doi.org/10.7294/ZGR9-9G86. The authors declare no conflict of interest.

Chapter 3

A lake spray aerosol emission parameterization

Reprinted (adapted) with modifications from Harb, C., & Foroutan, H. (2022). Experimental development of a lake spray source function and its model implementation for Great Lakes surface emissions. *Atmospheric Chemistry and Physics Discussions*, 1-32.

3.1 Abstract

Lake spray aerosols (LSAs) are generated from freshwater breaking waves in a similar mechanism to their saltwater counterparts, sea spray aerosols (SSAs). Unlike the well-established research field pertaining to SSAs, studying LSAs is an emerging research topic due to their potential impacts on regional cloud processes and their association with the aerosolization of freshwater pathogens. A better understanding of these climatic and public health impacts requires the inclusion of LSA emission in atmospheric models, yet a major hurdle to this inclusion is the lack of a lake spray source function (LSSF), namely, an LSA emission parameterization. Here, we develop an LSSF based on measurements of foam area and the corresponding LSA emission flux in a marine aerosol reference tank (MART). A sea spray source function (SSSF) is also developed for comparison. The developed LSSF and SSSF are then implemented in the Community Multiscale Air Quality (CMAQ) model to simulate par-

ticle emissions from the Great Lakes surface from 10 to 30 November 2016. Measurements in the MART revealed that the average SSA total number concentration was eight times higher than that of LSA. Over the 0.01-10 μm aerosol diameter size range, the developed LSSF was around one order of magnitude lower than the SSSF and was around two orders of magnitude lower for aerosols with diameters between 1 and 3 μm. Model results revealed that LSA emission flux from the Great Lakes surface can reach $\sim 10^5$ $m^{-2}s^{-1}$ during an episodic event of high wind speeds. These emissions only increased the average total aerosol number concentrations in the region by up to 1.65%, yet, their impact on coarse-mode aerosols was much more significant with up to a 19-fold increase in some areas. The increase in aerosol loading was mostly near the source region, yet LSA particles were transported up to 1000 km inland. Above the lakes, LSA particles reached the cloud layer, where the total and coarse-mode particle concentrations increased by up to 3% and 98%, respectively. Overall, this study helps quantify LSA emission and its impact on regional aerosol loading and the cloud layer.

3.2 Introduction

In a similar mechanism to sea spray aerosols (SSAs) generation in saltwater [27], lake spray aerosols (LSAs) can be produced by the entrainment of air bubbles by freshwater breaking waves and the subsequent bubble bursting process on the water surface [35]. LSAs were first detected above the surface of the Laurentian Great Lakes in North America during an aircraft sampling campaign in summer 2009 [36], and have since become an emerging research topic [35, 47, 59, 81, 114]. Unlike SSAs which constitute a major fraction of the global aerosol mass input into the atmosphere (10^{12}-10^{14} kg y^{-1}; Textor et al. [24]) and play a key role in Earth's climate by affecting cloud properties and scattering light [27], the role of LSAs in atmospheric processes is not well understood. While oceans cover around 70% of Earth's surface, freshwater lakes cover a significantly smaller area and are for the most part limited in fetch. Therefore, the impact of LSAs on atmospheric processes might be constrained to regional scales. Nonetheless, recent research has shown that LSA emission might pose a risk to respiratory health by being a vector for the water-to-air dispersal of biological material from freshwater bacteria [115], including cyanobacterial toxins from harmful algal blooms (HABs) [37, 38, 48], and hence might pose a risk to respiratory health. Moreover, LSAs have

been sampled in the cloud layer above the Great Lakes surface [47], which indicates possible implications on cloud process and hence regional climate.

Although breaking waves in saltwater and freshwater might look identical at first glance, looking more closely at the bubble formation and bursting mechanisms reveals important differences between the two environments. At the subsurface level, the entrained bubble plume in saltwater is characterized by a higher void fraction and is comprised of smaller and more numerous bubbles than that in freshwater [39, 40, 41, 116]. These differences have been ascribed to enhanced bubble coalescence in freshwater due to lower ionic content, which constrains the formation of the tiny bubble clouds observed in saltwater [84, 108]. Disparities in bubble formation between freshwater and saltwater are manifested at the surface level, whereby saltwater whitecaps (foams) have been observed to be bigger and more persistent than their freshwater counterparts for the same wave breaking conditions [44, 116]. Furthermore, saltwater whitecaps are comprised of a profusion of tiny surface bubbles, whereby those in freshwater contain bigger bubbles [116]. Surface bubble size influences the spray aerosol ejection pathway, which can occur either during the shattering of the bubble cap or after the ensuing cavity collapse. The former mechanism, known as film drop formation, occurs mostly in bubbles with a radius greater than 0.5-1 mm, while the latter, known as jet drop formation, occurs mostly in bubbles with a radius smaller than 0.5 mm [16, 17, 27]. Therefore, the smaller surface bubbles observed in saltwater whitecaps might enhance jet drop production in saltwater as compared to freshwater [116]. These distinct air entrainment characteristics have important implications on the abundance and size of ejected SSAs and LSAs. Laboratory experiments revealed that the ejection abundance of SSA is more than three times higher than that of LSA [35, 115], and that the size distribution of freshly emitted SSAs is unimodal with an accumulation mode at 110 nm whereby that of LSAs is bimodal with an ultrafine mode at 46 nm and an accumulation mode at 180 nm [35]. The aforementioned mechanistic differences in SSA and LSA production imply that they should be represented independently in general circulation models (GCMs) and chemical transport models (CTMs).

Due to their important role in Earth's climate, the inclusion of SSAs in GCMs and CTMs is an active research area [24, 117]. Several SSA emission parameterizations, hereinafter sea spray source functions (SSSFs), have been proposed using both laboratory experiments and field measurements [23, 27]. These SSSFs essentially compute the number of SSA particles

released per unit ocean area per unit time [33]. The major driver of SSA emissions is wind stress. Therefore, most SSSFs are formulated as a function of wind speed typically at reference height of 10 m (u_{10}) which is a common meteorological parameter in models [23, 27]. However, it has been found that SSSFs that rely solely on wind speed fail to predict measured SSA concentrations [58, 118]. Therefore, some SSSFs have been expanded to also include oceanic parameters such as sea surface temperature (SST) [53, 58, 119, 120], water salinity [120], and wave state [121], which led to better reproduction of observed SSA concentrations.

A lake spray source function (LSSF), on the other hand, is still lacking to date which hampers our understanding of the atmospheric burden of LSAs. Chung et al. [59] conducted the first ever modeling study of LSA emission from the surface of the Great Lakes using the mesoscale Weather Research and Forecasting model with online Chemistry (WRF-Chem). They reported up to a 20% increase in regional aerosol numbers above the lakes surface during July 2004 when LSA emissions were enabled. However, it should be noted that they adopted an SSSF [60] to represent LSA emissions which is a significant source of uncertainty in that study [59]. To improve on this simulation and understand the effect of LSAs on thermodynamic equilibrium in the Great Lakes region, Amiri-Farahani et al. [61] conducted WRF-Chem simulations and found that calcium rich LSA particles lead to a 37% increase in particulate nitrate and a 16% decrease in particulate ammonium above the Great Lake surface. They used a corrected version of the Geever et al. [60] SSSF by scaling to the laboratory measurements of May et al. [35]. However, only correcting for the number emission flux when adapting an SSSF for LSA emissions might not be sufficient, since the same wind speed over freshwater and saltwater does not induce the same wave breaking conditions. With these two studies being the only LSA modeling studies to date, it is clear that more modeling work is needed to better understand the effect of LSAs on atmospheric processes, specifically in the Great Lakes region. Such studies would be much improved if an LSSF was made available to the community, rather than having to use corrected versions of SSSFs.

Here, we develop the first LSSF starting from laboratory experiments using the widely adopted marine aerosol reference tank (MART; Stokes et al. [90]), which is now considered the de facto experimental method for generating realistic spray aerosols [122]. We also use the MART to develop an SSSF for comparison. To test the developed LSSF, we use the Community Multiscale Air Quality (CMAQ) model to simulate LSA emissions from the

surface of the Great Lakes. With a combined surface area of 244,000 km^2, these lakes form collectively the largest inland body of unfrozen freshwater on Earth [123]. The Great Lakes basin is home to 48.5 million people (2011 figures; Méthot et al. [124]) and is considered to be a critical component of the economic health of central North America since it supports a wide array of commercial, industrial, and recreational activities [125]. Therefore, the Great Lakes were chosen for these simulations due to their sheer size (sometimes referred to as "inland seas"; Sterner et al. [126]), their proximity to major population centers in central North America, and their susceptibility to high wind speeds and wave breaking [36, 44, 114].

3.3 Methods

3.3.1 Water samples collection and preparation

A solution of synthetic freshwater, based on Lake Michigan ionic concentrations [35, 42], was produced by dissolving anhydrous inorganic salts (Fisher Scientific; $CaCO_3 \geq 99\%$, $MgSO_4 \geq 99\%$, $NaCl \geq 99\%$, $KCl \geq 99\%$) in ultrapure water ($\sim$ 18.2 MΩ.cm, Picopure®) to achieve the following concentrations: 1 mM Ca^{2+}, 1 mM CO_3^{2-}, 0.4 mM Mg^{2+}, 0.4 mM SO_4^{2-}, 0.3 mM Na^+, 0.3 mM Cl^-, and 0.02 mM K^+. This water sample was used to develop the LSSF.

Synthetic seawater was prepared by dissolving artificial sea salt (Instant Ocean® Spectrum Brands, Blacksburg, VA, USA) in ultrapure water ($\sim$ 18.2 MΩ.cm, Picopure®) with a 35 g/kg mixing ratio corresponding to a typical marine salinity. This water sample was used to develop the SSSF.

To investigate LSA production from natural freshwater with organic contents, two freshwater samples (180 L each) were also collected from the surface of Claytor Lake (Pulaski County, VA, USA) using pre-autoclaved 20 L HDPE carboys (Fig. B.1). To contrast seasonality and biological activity, the first sample was collected in the fall on 31 October 2020 whereas the second sample was collected in the summer on 9 August 2021. During sampling, water temperature and salinity were measured using an Extech EC170 (Extech Instruments, Nashua, NH, USA) salinity-temperature meter and are reported in Table B.1. The collected water samples were then immediately transported to the laboratory to be used within 24 hours after collection.

3.3.2 Experimental development of the source functions

3.3.2.1 Aerosol generation and size distribution measurements

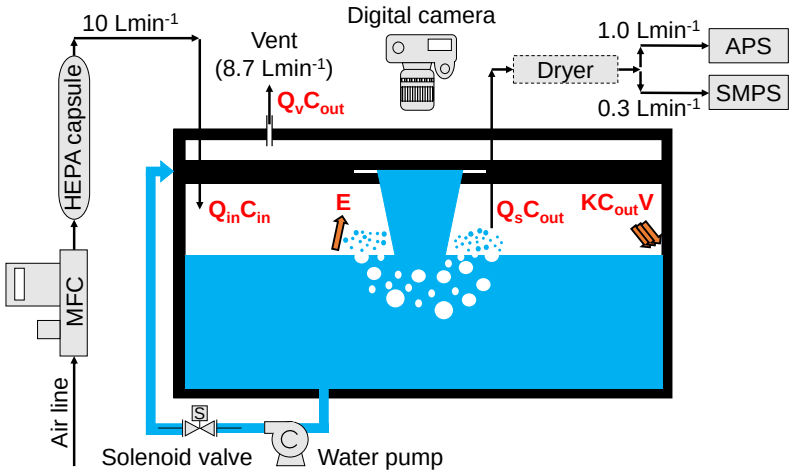

Figure 3.1: **A schematic of the experimental setup used in this study.**

Spray aerosols were generated using a custom-built MART (Stokes et al. [90]; see Fig. 3.1). In short, the setup is comprised of a polycarbonate tank (100 cm x 54.6 cm x 61 cm) with two concentric tubes at the top of the tank that allow water to exit as a uniform sheet (Fig. 3.1). A 1/3 HP self-priming utility pump (AMT Pumps, Royersford, PA, USA) allows the water to circulate in the system. Water sheet intermittency can be controlled by a Parker skinner valve (Parker Hannifin, Madison, MS, USA) mounted on the pump discharge port and connected to a Macromatic TR-53122-07 time delay relay (Macromatic, Menomonee Falls, WI, USA). More details about the setup construction and operation can be found in Harb and Foroutan [116]. Similar to the MART [90, 127], the setup used in this study has been shown to reproduce the correct physical characteristics of air entrainment and spray aerosol generation found in oceanic breaking waves, and has been previously used to generate laboratory SSAs and LSAs [115, 116].

To generate spray aerosols from the water samples described in Sect. 3.3.1, a total volume of 147 L from each water sample was added to the MART providing a water depth of 27 cm. The water sheet was operated continuously for 4 h at a flow rate of 24.5 Lmin^{-1} to maximize aerosol production. It is important to note that continuous air entrainment might lead to biases in the size of ejected spray aerosols if surface foam evolution is suppressed [116], yet the

size of the tank was large enough to minimize the interaction between surface bubble rafts and tank walls (see Fig. B.2 in the supplement). Prior to aerosol size distribution measurements, the headspace was flushed with HEPA-filtered air until the background particle concentration was less than 10 cm^{-3}. Nascent spray aerosols ejected from the generated foam patch were sampled ∼2 cm above the water surface, and then directed to a scanning mobility particle sizer (SMPS 3936, TSI, Shoreview, MN, USA) and an aerodynamic particle sizer (APS 3321, TSI, Shoreview, MN, USA) (Fig. 3.1) to determine particle size distribution. It is a common practice to include a dryer upstream of the aerosol sizing instrumentation to measure dry particle size [35, 90, 94], however, there is concern about supermicron particle losses in such setups [56]. To examine these losses, two aerosol size distribution measurements were taken in the experiments with synthetic freshwater and saltwater solutions. In the first measurement, aerosols were directly sampled by the aerosol sizing instrumentation (SMPS and APS) without drying. In the second measurement, aerosols were dried using a diffusion dryer (TSI 3062, TSI, Shoreview, MN, USA) installed directly upstream of the aerosol sizing instrumentation (Fig. 3.1). Experiments with the Claytor Lake water samples were carried out without a dryer. Therefore, six experiments were carried out in total. More details about these experiments can be found in Table B.2.

The SMPS was operated at a sampling flow rate of 0.3 $Lmin^{-1}$ and a scan rate of 5 min, providing a size distribution of particles with electrical mobility diameter (d_{em}) between 14 and 700 nm. The APS was operated at a sampling flow rate of 1.0 $Lmin^{-1}$ and a scan rate of 5 min, providing a size distribution of particles with aerodynamic diameter (d_a) between 0.5 and 20 μm. The inlet flow rate of clean air was maintained at 10 $Lmin^{-1}$ using an Aalborg GFCS-010013 mass flow controller (Aalborg Instruments & Controls, Orangeburg, NY, USA) and a vent in the tank lid allowed excess air flow (8.7 $Lmin^{-1}$) to escape (Fig. 3.1). In order to obtain a single aerosol size distribution spanning the SMPS and APS measurement ranges, the d_{em} and d_a size distributions were merged into a single physical diameter (d_p) size distribution using a procedure described elsewhere [35, 90, 128]. Electrical mobility diameters measured by the SMPS were converted to physical diameters by assuming spherical particle geometry:

$$d_p = d_{em} \tag{3.1}$$

Aerodynamic diameters measured by the APS were converted to physical diameters using the following relation:

$$d_p = \frac{d_a}{\sqrt{\frac{\rho_{eff}}{\rho_0}}} \tag{3.2}$$

In Eq. (3.2), ρ_0 is equal to unit density (1 gcm^{-3}) and ρ_{eff} is an effective density assigned to particles sized by the APS. For both LSAs and SSAs, ρ_{eff} was considered to be equal to 1.5 g/cm^3 [37, 129] assuming considerable aerosol liquid content since the relative humidity RH in the tank headspace was mostly greater than 90% throughout the experiments (B.2). When stitching, particle bins in the overlapping size range of the SMPS and APS were removed due to uncertainties in particle counting efficiency [90].

3.3.2.2 Foam area determination

To monitor the evolution of the foam patch area generated inside the MART, a Nikon D750 camera was used to take photographs of the water surface during active air entrainment in the synthetic freshwater and saltwater solutions. Due to condensate accumulation on the inside of the tank walls, it was not possible to capture foam photographs concurrently with aerosol size distribution measurements. Therefore, these photographs were taken in subsequent air entrainment experiments. The same water flow conditions described in Sect. 3.3.2.1 were used, and each experiment lasted for approximately 2 h with the camera (Fig. 3.1) programmed to capture a single photograph every 10 min.

To determine the foam patch area, photographs were analyzed using the image processing software ImageJ [97]. Foam areas were identified manually and were sized after scaling the photographs using pictures of a precision ruler placed on the water surface. An example of a processed surface foam image is shown in Fig. B.2.

3.3.2.3 Source functions derivation

The continuous whitecap method (CWM; Monahan and Callaghan [130]) was used to determine source function formulations from the experiments with synthetic freshwater (here-

inafter simply LSSF) and synthetic saltwater (hereinafter simply SSSF). In brief, the CWM infers the production flux of spray aerosols from measurements of size-depended spray aerosol production scaled by unit whitecap area. An inherent assumption in this method is that a whitecap area has the same production rate of spray aerosols regardless of its generation method (e.g., in situ breaking wave or laboratory water sheet) [23, 130]. Using this approach, the source function formulation reads:

$$\frac{\partial F}{\partial r}(u_{10}, r) = W(u_{10}).\frac{\partial F_{wc}}{\partial r}(r) \tag{3.3}$$

In Eq. (3.3):

- $\partial F/\partial r$ ($\mathrm{m^{-2}s^{-1}\mu m^{-1}}$) is the rate of spray aerosol generation, per unit area of water surface, per unit increment of spray droplet radius r.

- W ($\mathrm{m^{-2}m^{-2}}$) is the whitecap coverage defined as the area of whitecap foam per unit area of water surface. W is usually parameterized as a function of u_{10} [51]. For our formulations, we adapted the commonly used Monahan and Muircheartaigh [52] parameterization for saltwater whitecap coverage. To account for reduced foaming in freshwater as compared to saltwater, and in the absence of a freshwater whitecap parameterization to date, a factor α was introduced to the saltwater parameterization of Monahan and Muircheartaigh [52]. Following the proposition of Monahan [131], α was defined as the ratio of foam exponential decay time constant (τ) in freshwater to that in saltwater, and was calculated using previously published τ values in freshwater and saltwater measured using the MART (Harb and Foroutan [116], their Table 1). Interestingly, the calculated α value of 0.65 from these MART experiments is in excellent agreement with the 0.66 value calculated by Monahan [131] from their whitecap simulation tank experiments [44]. Therefore, the corrected whitecap coverage W reads ($\alpha = 1$ for saltwater, and $\alpha = 0.65$ for freshwater) :

$$W(u_{10}) = \alpha(3.84 \times 10^{-6} u_{10}^{3.41}) \tag{3.4}$$

- $\partial F_{wc}/\partial r$ ($\mathrm{m^{-2}s^{-1}\mu m^{-1}}$) is the number of aerosol particles produced per unit whitecap area per unit time as a function of spray droplet radius r. $\partial F_{wc}/\partial r$ was determined

experimentally by dividing the measured steady state, size-resolved, number emission rate of spray aerosols inside the MART headspace E by the foam (whitecap) area on the water surface A, as follows:

$$\frac{\partial F_{wc}}{\partial r}(\mu m^{-1}s^{-1}m^{-2}) = \frac{E(\mu m^{-1}s^{-1})}{A(m^2)} \tag{3.5}$$

In Eq. (3.5), A was determined from the foam imaging experiments described in Sect. 3.3.2.2, whereas E was determined by considering a mass-balance (Eq. (3.6) and Fig. 3.1) inside the MART headspace under the assumption of well-mixed conditions [132, 133].

$$\frac{\mathrm{d}(C_{out}V)}{\mathrm{d}t} = Q_{in}C_{in} - Q_vC_{out} - Q_sC_{out} + E - kVC_{out} \tag{3.6}$$

Under steady state conditions, defined as the period with less than 20% variation in total aerosol number concentration in the MART headspace, the left-hand-side of Eq. (3.6) becomes zero, and E can be calculated from Eq. (3.7).

$$E = -Q_{in}C_{in} + Q_vC_{out} + Q_sC_{out} + kVC_{out} \tag{3.7}$$

In Eqs. (3.6) and (3.7), Q_{in} is the inlet flowrate of HEPA-filtered air, C_{in} is the concentration of spray aerosols in the inflow (equal to zero), Q_v is the flow rate of excess air that is vented, C_{out} is the measured size-resolved number concentration of spray aerosols in the headspace, Q_s is the sampling flowrate of the aerosol sizing instrumentation (SMPS+APS), V is the headspace volume, and k is the wall loss coefficient (Fig. 3.1). k was determined experimentally by arresting water flow and spray aerosol generation in the tank (i.e., E= 0), and then measuring the decay of C_{out} with time. Wall losses were assumed to be a first-order exponential decay process and k was calculated by fitting an exponential function to the measured C_{out} decayed over time. More details about the wall loss coefficient determination can be found in Sect. B.1 and Fig. B.3 in the supplement.

A common convention is to report a source function formulation in terms of the particle radius at a reference relative humidity of 80% [23]. Therefore, the measured particle radius was converted to the value it would have at an RH=80% (i.e., r_{80}) using the correction proposed by Zhang et al. [134, Eq. (2)]. The experimentally determined source functions,

now expressed as $\partial F/\partial r_{80}$, were then fitted and formulated as the sum of two lognormally distributed modes, as follows:

$$\frac{\partial F}{\partial r_{80}}(u_{10}, r_{80}) = \alpha(3.84 \times 10^{-6} u_{10}^{3.41}) \sum_{i=1}^{2} \frac{N_i}{\sqrt{2\pi}\ln(\sigma_i)} \exp(-\frac{1}{2}\frac{(\ln r_{80} - \ln \mu_i)^2}{(\ln \sigma_i)^2}) \tag{3.8}$$

In Eq. (3.8), u_{10} is expressed in meters per second, r_{80} is expressed in micrometers, and N_i, σ_i, and μ_i are the number production flux, the geometric standard deviation, and the geometric mean of the i-th mode, respectively.

3.3.3 Model implementation

To test the developed LSSF, LSA emissions from the surface of the Great Lakes system in North America were considered. The Community Multiscale Air Quality (CMAQ) model version 5.3 (CMAQv5.3; Appel et al. [135]) was used for this purpose. The simulation time period (10 to 30 November 2016 with a 9 day spin-up) was chosen to coincide with the season of minimal to no lake ice cover [136] and high wind speeds over the surface of the lakes [137]. Simulations were performed using CMAQv5.3 benchmark test case of the Conterminous United States (CONUS) [138]. In brief, this test case employs a 12-km uniform horizontal grid covering the CONUS, parts of northern Mexico and southern Canada, and the eastern Pacific and western Atlantic oceans, with 35 vertical layers expanding up to 50 hPa. Meteorological inputs are provided by a WRFv3.8 simulation and were processed using the Meteorology-Chemistry Interface Processor (MCIPv5.0; Appel et al. [135], Otte and Pleim [139]). The physics parameterizations used in the WRFv3.8 simulation include the Morrison double-moment microphysics scheme [140], the Rapid Radiative Transfer Model for General circulation models (RRTMG) radiation scheme [141], the Kain–Fritsch convective parameterization [142], the Pleim-Xiu land-surface model [143, 144], and the Asymmetric Convective Mixing 2 planetary boundary layer model [145]. Baseline anthropogenic emissions were provided by the 2016beta Emission Modeling Platform inventory (EMP; http://views.cira.colostate.edu/wiki/wiki/10197). Boundary conditions were provided from a hemispheric CMAQ (HCMAQ) simulation with a 108 x 108 km polar stereographic grid covering the northern hemisphere, 44 vertical layers, and meteorological fields

Table 3.1: Summary of the three emission scenarios: BASE, LAKE, and SEA.

Simulation	Ocean emissions	Great Lakes emissions
BASE	SSSF	None
LAKE	SSSF	LSSF
SEA	SSSF	SSSF

from WRFv3.8. Science configurations used in CMAQv5.3 include the updated M3dry model for deposition, the CB06r3 chemical mechanism and AERO7 aerosol model for atmospheric chemistry, and the KMT version 2 (KMT2) and the KMTBR modules for cloud chemistry [135]. More details about CMAQv5.3 settings and evaluation can be found in Appel et al. [135].

The current spray aerosols emission scheme in CMAQv5.3 only allows for SSA emission from the surface of saltwater bodies (i.e., eastern Pacific and western Atlantic oceans in the domain considered herein). The SSA scheme uses the Gong [146] source function with $\theta = 8$ for online SSA emission flux calculations with a linear SST dependence following the Ovadnevaite et al. [121] parameterization [147]. For the purpose of this study, the Gong [146] source function was replaced by our synthetic saltwater source function, with the SST dependence kept the same. Concurrently, spray aerosol emissions from the Great Lakes surface were enabled and were evaluated for three emission scenarios. In the BASE scenario, no LSA emissions from the Great Lakes surface were considered (default CMAQv5.3 configuration for the CONUS). In the LAKE and SEA simulations, LSA emissions from the Great Lakes surface were enabled using the developed LSSF and SSSF, respectively, with no lake surface temperature (LST) dependence. In both of the latter scenarios, spray aerosols emitted from the Great Lakes surface were modeled as chemically-inert dry particles with a density of 1.5 gcm^{-3} [37, 129]. The emission scenarios evaluated in this study were designed to assess the contribution of LSA emissions to regional aerosol loading in the Great Lakes basin (LAKE scenario), and the overestimation of LSA emissions brought about by considering the Great Lakes as saltwater bodies and using an SSSF (SEA scenario) (see e.g., Chung et al. [59]). A brief summary of these emission scenarios is shown in Table 3.1.

3.4 Results and Discussions

3.4.1 Spray aerosol size distribution

The average size distributions of spray aerosols generated in the MART headspace during the last 2 h of active air entrainmnet in each experiment are shown in Fig. 3.2a. A close-up of the average aerosol size distributions from the freshwater solutions (i.e., synthetic and Claytor Lake freshwater) is shown in Fig. 3.2b. It is obvious from these two figures that the abundance of spray aerosols generation in saltwater is significantly higher than that in freshwater, with an average SSA and LSA total number concentrations (wet) of 822 and 102 cm^{-3}, respectively. The higher generation of spray aerosols in saltwater compared to that in freshwater concurs with previous observations [35, 115], and can be attributed to higher void fractions and whitecap formation following wave breaking in saltier waters [39, 41, 116]. The shape of the SSA and LSA size distributions are also distinct. In saltwater (Fig. 3.2a), the size distribution of wet SSAs exhibits two distinct modes at 0.09 and 2.3 μm, whereas that of dry SSAs exhibits a single mode at $\sim$0.2 μm with the second supermicron mode being suppressed. While the dry SSA size distribution agrees well with previous laboratory measurements in the MART [90, 127], the second distinct supermicron mode observed for wet SSAs has not been previously reported. We speculate that this second mode is a "jet drop" mode [53, 115], and is not detected when using a dryer due to tubing losses which will be discussed later in the text. In freshwater (Fig. 3.2b), on the other hand, the LSA size distributions from both synthetic or Claytor Lake freshwater are characterized by a single dominant mode at $\sim$0.1 μm. The subtle variation in LSA size distributions between synthetic and natural lake water could be due to low biological activity in the water samples collected from Claytor Lake in October and August. However, high biological content in lake water has been observed to significantly increase LSA production abundance [38]. Therefore, lakes with high seasonal variability in biological content, in particular those with algal bloom occurrences, might exhibit large temporal variations in LSA emissions abundance.

To the best of our knowledge, only one laboratory study [35] attempted to investigate differences between LSA and SSA production to date. Figure 3.2c shows the LSA size distribution in synthetic freshwater (wet and dry) plotted along with LSA size distributions from synthetic and Lake Michigan freshwater produced by an LSA generator [35]. The LSA generator, a

small water tank (∼18 L) with four circular water jets, is inherently different from the MART system used in this study. Therefore, it is not valid to comment on differences in the magnitude of number concentrations between the two studies and, hence, the comparison is limited to the shape of the size distributions. Comparing the LSA size distribution from synthetic freshwater in both studies reveals a unimodal distribution in the MART at ∼0.15 and ∼0.09 μm for dry and wet LSAs, respectively. In the LSA generator, on the other hand, the LSA size distribution is bimodal with a minor mode at 0.08 μm and a major mode at 0.3 μm. It is likely that these disparities are due to different LSA generation methods as the synthetic freshwater solution is identical in both studies. The size distribution of LSAs generated from Lake Michigan freshwater in the LSA generator, in contrast, is mostly unimodal at 0.18 μm, which is close to the major mode (at ∼0.15 μm) observed in wet LSAs produced from synthetic freshwater in the MART.

To better comment on the relative magnitude of LSA and SSA production in the two studies, Fig. 3.2d compares the SSA-to-LSA number size distribution ratio (hereinafter referred to as SSA-to-LSA ratio) measured from synthetic freshwater and saltwater solutions in the MART (wet and dry) to that measured in the LSA generator (dry) of May et al. [35]. The SSA-to-LSA ratio for wet aerosols in the MART and that for dry aerosols in the LSA generator show good agreement up to 0.1 μm, with values ranging from 4 to 9. Meanwhile, the SSA-to-LSA ratio for dry aerosols in the MART exhibited higher values of up to 37 in this size range. In the 0.1-10 μm particle size range, noticeable disparities are observed between the SSA-to-LSA ratios. In the accumulation mode (0.1-0.5 μm), the SSA-to-LSA ratio for wet aerosols in the MART is not reliable due to uncertainties in the measurement efficiency of the SMPS in this size range (see Fig. 3.2a), therefore, we limit this discussion to supermicron particles (i.e., D_p >1 μm). While the SSA-to-LSA ratios for dry aerosols in MART and dry aerosols in the LSA generator drop significantly after for D_p >1 μm, this ratio for wet aerosols in the MART exhibits a peak of 900 at ∼2.3 μm, which is driven by the distinct supermicron mode in the wet SSA size distribution shown in Fig. 3.2a. It is worth noting that the SSA-to-LSA ratio in the LSA generator has been employed by Amiri-Farahani et al. [61] to determine an LSSF by scaling the Geever et al. [60] SSSF, which underscores its importance in comparing the magnitude of LSA and SSA production fluxes at different aerosol particle sizes.

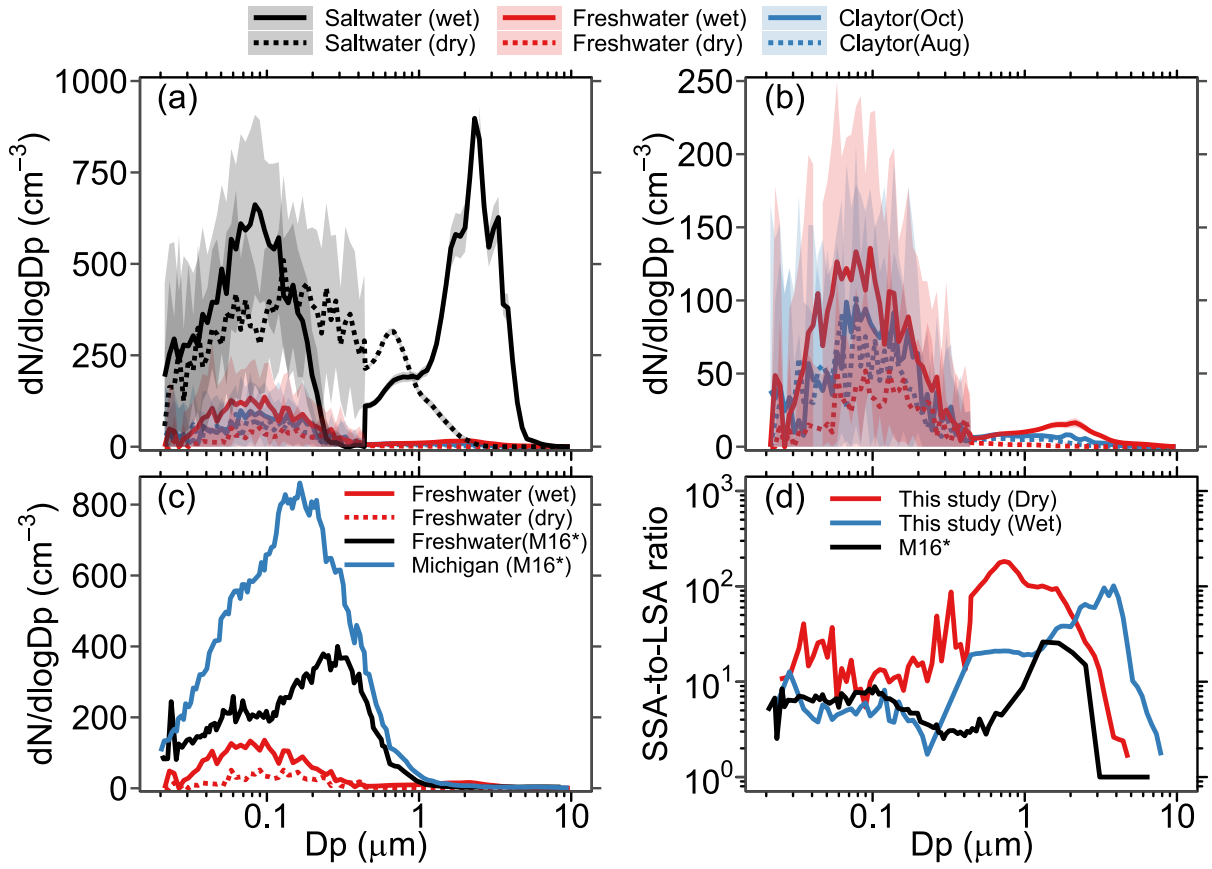

Figure 3.2: **Aerosol size distributions from this work and comparisons with other measurements from literature.** **(a)** Average aerosol size distribution generated in the MART using the synthetic freshwater, synthetic saltwater, and Claytor Lake water samples collected in October and August. Shaded areas represent ± 1 standard deviation. "dry" and "wet" denote measurements made with and without a dryer, respectively. **(b)** A close-up of the average aerosol size distributions from the synthetic and Claytor Lake freshwater solutions. **(c)** LSA size distribution from synthetic freshwater (wet and dry) plotted along with LSA size distributions from synthetic and Lake Michigan freshwater from May et al. [35]. **(d)** Ratio of SSA-to-LSA aerosol size distributions produced in the MART (wet and dry) and that produced in the LSA generator of May et al. [35].
* M16 denotes May et al. [35]

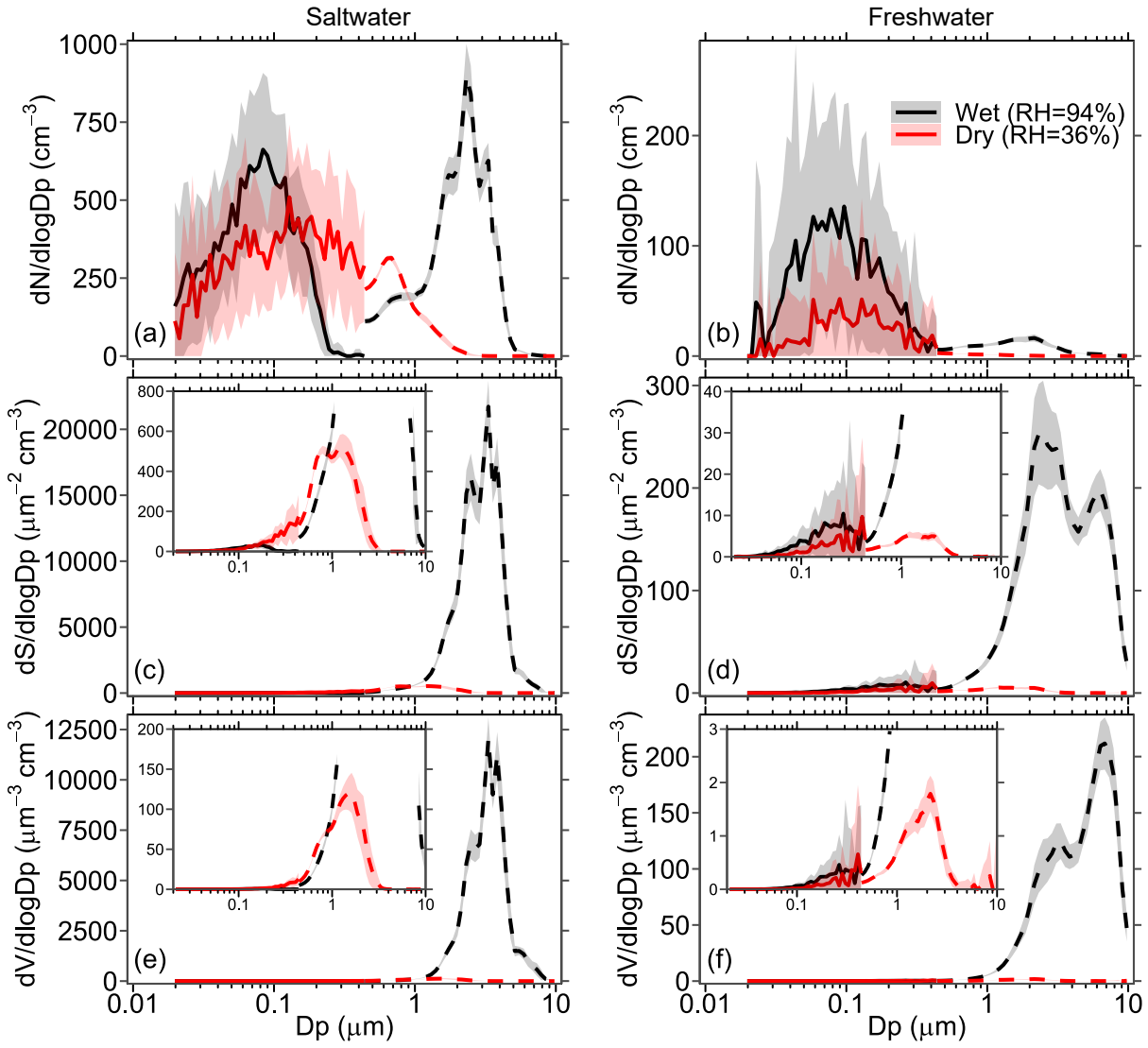

Figure 3.3: **The number, surface area, and volume size distributions of dried and wet aerosols.** The synthetic saltwater and freshwater average aerosol **(a,b)** number , **(c,d)** surface area , and **(e,f)** volume size distributions of dry and wet aerosols, corresponding to sampling with and without a dryer, respectively. Shaded areas represent ± 1 standard deviation. Insets show a close-up of the dry surface area and volume size distributions.

The effect of including a dryer upstream of the aerosol sizing instrumentation on the aerosol size distributions, especially on the SSA size distribution, is evident in Fig. 3.2a. To further analyze this effect, Fig. 3.3 shows the synthetic saltwater and freshwater average aerosol number (a,b), surface area (c,d), and volume (e,f) size distributions of wet and dry aerosols, corresponding to sampling with and without a dryer, respectively. As mentioned previously,

the dryer at our disposal was a TSI 3062 diffusion dryer, with two Swagelok® 90°-elbows at the inlet and outlet ports. As it turned out, drying the particles before sampling was not trivial, and led to considerable tubing losses, particularly in the supermicron size range. In saltwater (Fig. 3.3a), the supermicron mode is completely lost when drying the particles and some losses are also observed for submicron particles where the peak shifts from 0.09 to 0.2 μm. The loss in submicron particles is more evident in freshwater where the number concentration peak of 136 ($\pm$93) cm^{-3} at 0.1 μm for wet aerosols is reduced by more than half to 51 ($\pm$92) cm^{-3} at 0.13 μm when drying the particles. The issue of particle loss when including a dryer in the sampling line was raised previously by Salter et al. [56], who estimated a 50 % loss for particles with dry diameter greater than 5 μm using the von der Weiden et al. [148] procedure. Using this same approach, we attempted to estimate particle losses in a greatly simplified tubing configuration of the TSI 3062 diffusion dryer (see Sect. B.2 and Fig. B.4a in the supplement). We find that in the submicron size range, particle loss was less than 10%, yet this loss increases exponentially for supermicron particles reaching more than 50% for particles with a diameter greater than 5 μm (Fig. B.4b). Hence, it is likely that particle losses in the dryer were even more considerable, especially in the supermicron size range, which explains the loss of the supermicron peak in the SSA size distribution when drying the particles (Fig. 3.3a). Yet, in the absence of a dryer, there is a discontinuity in the wet aerosol size distribution in the overlapping size range between the SMPS and APS (Fig. 3.3a). Moreover, there is a sharp decrease in the wet aerosol number concentrations in the upper size range of the SMPS (i.e., D_p ~0.13-0.40 μm). This sharp decrease might be associated with our observation of water accumulation in the impactor inlet in the absence of a dryer, which might reduce the impactor cut-off size. Therefore, caution is required when interpreting results in this size range. Losses in surface area and volume concentrations are even more severe, since supermicron particles are especially relevant for these quantities. Indeed, the peak in surface area concentration for D_p¿1 μm drops from 22000 ($\pm$ 2000) to 520 ($\pm$ 70) μm^{-2}cm^{-3} in saltwater and from 250 ($\pm$ 50) to 5.4 ($\pm$ 0.8) μm^{-2}cm^{-3} in freshwater. Similarly, the peak in volume size distribution drops from 12000 ($\pm$ 1000) to 120 ($\pm$ 30) μm^{-3}cm^{-3} in saltwater, and from 210 ($\pm$ 20) to 1.8 ($\pm$ 0.3) μm^{-3}cm^{-3} in freshwater. Given these considerable losses, source function development in the following section (Sect. 3.4.2) are based on wet aerosol measurements from synthetic freshwater and saltwater solutions.

Table 3.2: Lognormal parameters for the present LSSF and SSSF. Refer to Eq. (3.8).

	LSSF	SSSF
α	0.65	1
N_1	6.4106×10^{7}	1.0452×10^{8}
N_2	1.2140×10^{5}	2.3646×10^{6}
μ_1	0.0137	0.0167
μ_2	0.5852	0.6815
σ_1	2.4623	2.6022
σ_2	1.5694	1.4096

3.4.2 Source function development

Using the procedure described in Sect. 3.3.2.3, we developed an LSSF and an SSSF from wet aerosol measurements in the MART using the synthetic saltwater and freshwater solutions, respectively. The lognormal parameters for each formulation (see Eq. (3.8)) are given in Table 3.2. These source functions are plotted in Fig. 3.4a for u_{10} = 10 ms^{-1}. Due to the aforementioned (Sect. 3.4.1) uncertainty in the SMPS counting efficiency of wet aerosols in the accumulation mode size range (corresponding to $r_{80} \sim$ 0.1-0.2 μm), data points in this size range were excluded from the SSSF fit. Figure 3.4a reveals that the SSA emission number flux is one order of magnitude higher than that of LSA for r_{80}¡0.2 μm, and almost two orders of magnitude higher for r_{80}=0.2-2 μm. Unlike the accumulation mode which is similar between the LSSF and the SSSF (0.72 vs 0.77 μm), the Aitken mode of the SSSF centered at 0.042 μm is greater than that of the LSSF, which is centered at 0.031 μm. This Aitken mode in the LSSF compares well with the Aitken mode (0.025-0.035 μm) measured above the Great Lakes surface [36].

The developed LSSF and SSSF are compared to a collection of common SSSFs from literature in Fig. 3.4b. It is worth noting that some source functions shown in this figure are reported as a function of dry particle diameter (D_{dry}) (e.g.,Mårtensson et al. [53], Salter et al. [119], Clarke et al. [149]), while others (e.g.,Gong [146]) are reported in terms of particle radius at RH=80% (r_{80}). For the sake of consistency, we converted the latter parameterizations (denoted by an asterisk in the legend) to become a function of dry particle diameter D_{dry} by

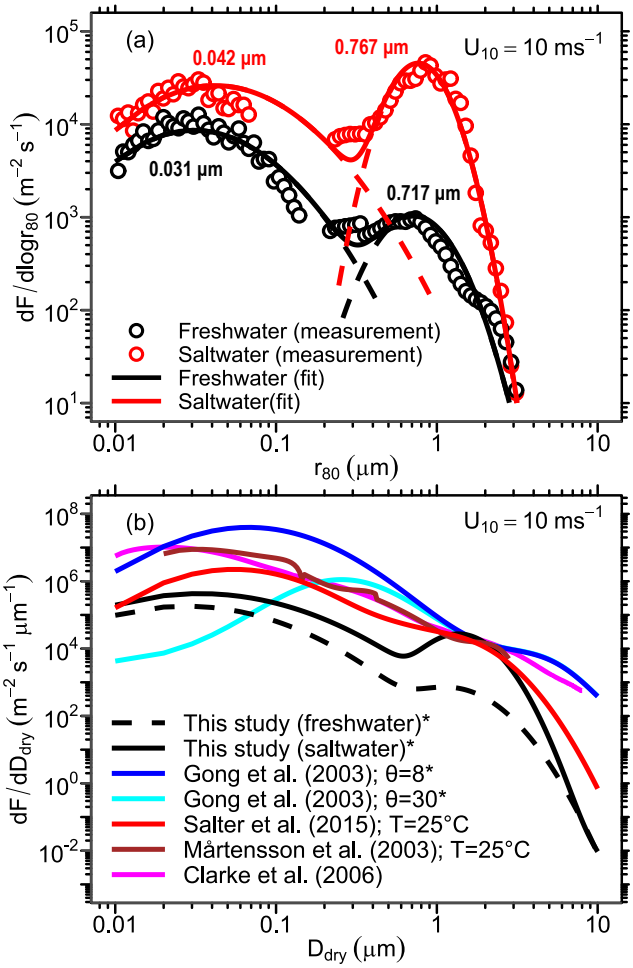

Figure 3.4: **The developed LSA and SSA source functions and their comparison with other source functions from literature. (a)** The developed LSSF (freshwater) and SSSF (saltwater) plotted for $u_{10} = 10$ ms^{-1}. Data points represent the measured emission parameterizations using the MART setup, solid curves represent the lognormal distribution fit, and dashed lines represent each lognormal mode. **(b)** Comparison between the present LSSF and SSSF and a collection of common SSSFs from literature for $u_{10} = 10$ ms^{-1}. Note the change in axes between panels **(a)** and **(b)**.
* Corrected from their original formulation as a function of r_{80} by assuming $r_{dry} = r_{80}/2$

assuming $r_{dry} = r_{80}/2$, a common rule of thumb [16, 33]. We start by comparing the SSSFs to assess the validity of our method for developing sound estimates of SSA emission fluxes. It is evident from Fig. 3.4b that there is a general agreement between all SSSFs in the supermicron size range. In the submicron size range, however, there is some disagreement between the SSSFs which span up to 3 orders of magnitude in the ultrafine range (D_{dry} <0.1 μm). Yet,

all SSSFs exhibit a distinct accumulation mode at around 0.1 to 0.2 μm. The discrepancy in the SSSFs magnitudes in the submicron size range can be attributed to different methods for developing the emission parameterization in each study. The Gong [146] parameterization, for instance, is a mathematical extension of the Monahan et al. [49] parameterization to diameters below 0.2 μm. This extension, nevertheless, is just an adjustable mathematical formulation (using a parameter θ) for setting the shape of the source function for the sub-0.2 µm size range, and lacks therefore a scientific rationale for its development [33]. The Clarke et al. [149] source function is developed based on ambient measurements of SSAs generated from the surfzone, and hence, might overestimate SSA emission from open ocean breaking waves. Meanwhile, the Mårtensson et al. [53], the Salter et al. [119], and the present SSSF are developed using measurements of laboratory generated SSAs. However, the method in which SSAs were generated in each study is different, with the Mårtensson et al. [53] study employing a small chamber (2 L) with a glass frit, the Salter et al. [119] study using a larger cylindrical tank (170 L) with a circular water jet, and the present study using the ∼300 L MART with a thin water sheet. Moreover, the current SSSF and the Mårtensson et al. [53] source functions use the Monahan and Muircheartaigh [52] formulation for whitecap coverage dependence on wind speed, whereas the Salter et al. [119] source function employs a formulation of the air entrainment flux dependence on wind speed modified from Long et al. [150].

To further assess the validity of the here derived source functions, we estimate the emission mass flux as a function of wind speed using the different source function formulations shown in Fig. 3.4b. We compare these estimates to field measurements of submicron SSA emission mass flux (PM_1), obtained using an aerosol mass spectrometer (AMS), which estimates the mass of particles with a vacuum aerodynamic diameter D_{va}=0.5-1 μm, or D_{dry}=r_{80}=0.029–0.580 μm [151, 152, 153]. Assuming spherical particles, we use Eq. (3.9) and Eq. (3.10) to estimate the mass flux from source functions expressed in terms of particle radius at RH=80% ($\overline{F}_{80}$) and from source functions expressed in terms of dry particle diameter ($\overline{F}_{dry}$), respectively:

$$\overline{F}_{80} = \frac{4}{3}\pi\rho_{80}\int_{r_{80,1}}^{r_{80,2}} \frac{dF}{r_{80}} r_{80}^3 dr_{80} \tag{3.9}$$

$$\overline{F}_{dry} = \frac{1}{6}\pi\rho_{dry}\int_{D_{dry,1}}^{D_{dry,2}} \frac{dF}{dD_{dry}} D_{dry}^3 dD_{dry} \tag{3.10}$$

Where, ρ_{80} and ρ_{dry} denote the wet (RH=80%) and dry particle density, and are assumed to be equal to 1.5 and 2.16 g/cm^3, respectively. The limits of integration were chosen to be $r_{80,1}$=$D_{dry,1}$=0.029 μm and $r_{80,2}$=$D_{dry,2}$=0.580 μm to match the measurement range of the AMS instrument. Figure 3.5 shows the calculated mass fluxes compared against the PM_1 measurements of Ceburnis et al. [151, 152] on a (a) linear, and (b) logarithmic y-axis. As expected, the emission mass flux computed from the present LSSF is, at least, one order of magnitude lower than that computed from the SSSFs at any wind speed (Fig. 3.5b). Furthermore, this comparison revealed that the present SSSF and that of Salter et al. [119] agree relatively well with the field measurements. Meanwhile, the Gong [146], Mårtensson et al. [53], and Clarke et al. [149] SSSFs overestimate the measured PM_1 flux (Fig. 3.5b) as previously reported in several studies [119, 152, 153]. Furthermore, as discussed in the De Leeuw et al. [23] review, these SSSFs also appear to overpredict submicron number emission flux, as shown in Fig. 3.4b, and hence fail to agree with SSA number concentrations measured in the marine boundary layer. This overprediction is likely to become more drastic at even higher wind speeds (>12 ms^{-1}), as suggested by Fig. 3.5a, which raises concern about the skill of many CTMs and GCMs that use such source functions for their SSA emission schemes [23, 24].

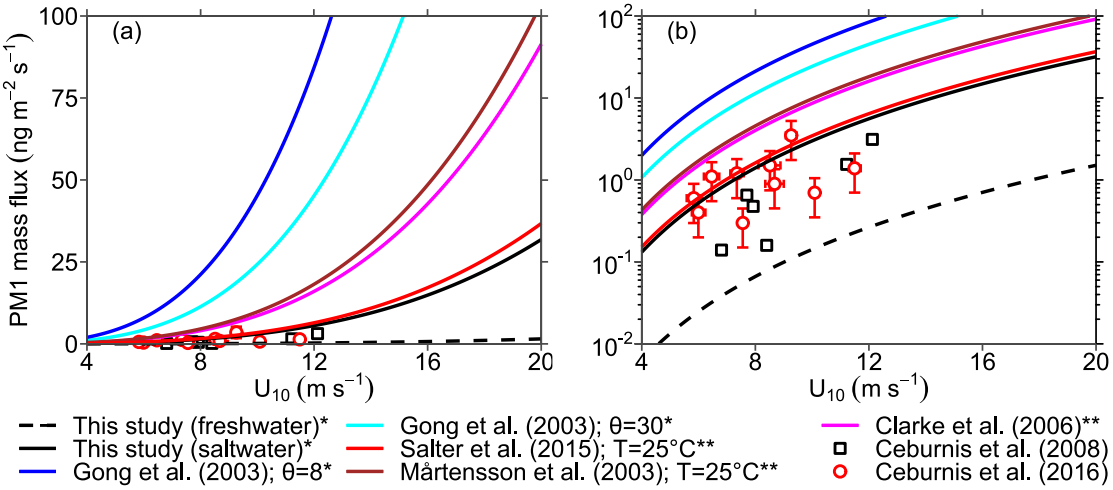

Figure 3.5: **Aerosol mass fluxes from this work compared to measurements from literature.** The calculated mass fluxes from the source functions shown in Fig. 3.4b compared with PM_1 mass flux measurements from Ceburnis et al. [151, 152] on a **(a)** linear, and **(b)** logarithmic y-axis.
* Computed using Eq. (3.9)
** Computed using Eq. (3.10)

3.4.3 Model simulation

As described in section 3.3.3, we implemented the newly developed LSSF in the CMAQ model to assess LSA emission from the Great Lakes surface for the emission scenarios shown in Table 3.1. We start this discussion by exploring the LSA emission abundance during significantly windy conditions over the Great Lakes surface. Figure 3.6 shows the modeled number emission flux of LSA particles during an episode of very high 10-m wind speeds (19 November 2016, 15:00:00 UTC) for the LAKE and SEA scenarios. During this time, winds were generally northwesterly over Lakes Superior and Michigan and southwesterly over the remaining lakes, with wind speeds ranging from a high of 17 to 21 ms^{-1} over most of Lakes Superior and Michigan, and a low of 5 to 9 ms^{-1} over Lake Ontario (Fig. 3.6a). A clear dependence of LSA number emission flux on wind speed, as anticipated, can be seen in Figs. 3.6b and 3.6c. The highest emissions are from the surface of Lakes Superior and Michigan and range between 7×10^4 and 1×10^5 m^{-2} s^{-1} in the LAKE scenario, and between 3×10^5 and 5×10^5 m^{-2} s^{-1} in the SEA scenario. Meanwhile, emissions from Lake Ontario, for instance, were up to two orders of magnitude lower, ranging from 1×10^3 to 7×10^3 m^{-2}

s^{-1} in the LAKE scenario and 4×10^3 to 3×10^4 m^{-2} s^{-1} in the SEA scenario. The results of Fig. 3.6 reveal that the LSA emission flux is highly sensitive to wind conditions, increasing exponentially with higher wind speeds as shown in Fig. 3.5a. Furthermore, using an SSSF to represent LSA emissions (i.e., the SEA scenario) can overestimate the actual number emission flux by up to one order of magnitude.

While looking into episodic events of very high wind speeds highlights the extent of LSA emission from the Great Lakes surface, a more holistic understanding requires studying long-term averaged emissions. Figure 3.7 shows the time-averaged total (a,d), accumulation-mode (b,e), and coarse-mode (c,f) number emission fluxes of particles from the Great Lakes surface for the entire simulation period using the LAKE and SEA scenarios. In the LAKE scenario, the total number emission flux ranges from 7×10^3 to 1.3×10^4 m^{-2} s^{-1} (Fig. 3.7a). For comparison, the average emission rates in the simulation of Amiri-Farahani et al. [61] for the month of November 2015 were on the order of 10^6 m^{-2} s^{-1}, which are two orders of magnitude higher than the results of this simulation despite their use of an improved LSSF formulation. Particle emission in the LAKE scenario is dominated by the accumulation mode (94% contribution), with coarse-mode particles only contributing to 6% (3×10^2 to 7.5×10^2 m^{-2} s^{-1}) of total emissions (Figs. 3.7b and 3.7c). In the SEA scenario, on the other hand, the average total aerosol number emission flux ranges from 3×10^4 to 6.5×10^4 m^{-2} s^{-1} (Fig. 3.7d), which leads to a significant 4-fold overestimation of actual emissions. Accumulation-mode particles also contribute the most (62%) to this emission (Fig. 3.7e), yet, coarse-mode particles also contribute significantly (38%) (Fig. 3.7f) unlike their low contribution in the LAKE scenario. The contribution of each particle size mode to particle emissions in Fig. 3.7b, c, e, and f mirror their relative magnitudes in Fig. 3.4, whereby the coarser particle mode in the SSSF is of comparable magnitude to the finer particle mode, whereas it is one order of magnitude lower in the LSSF.

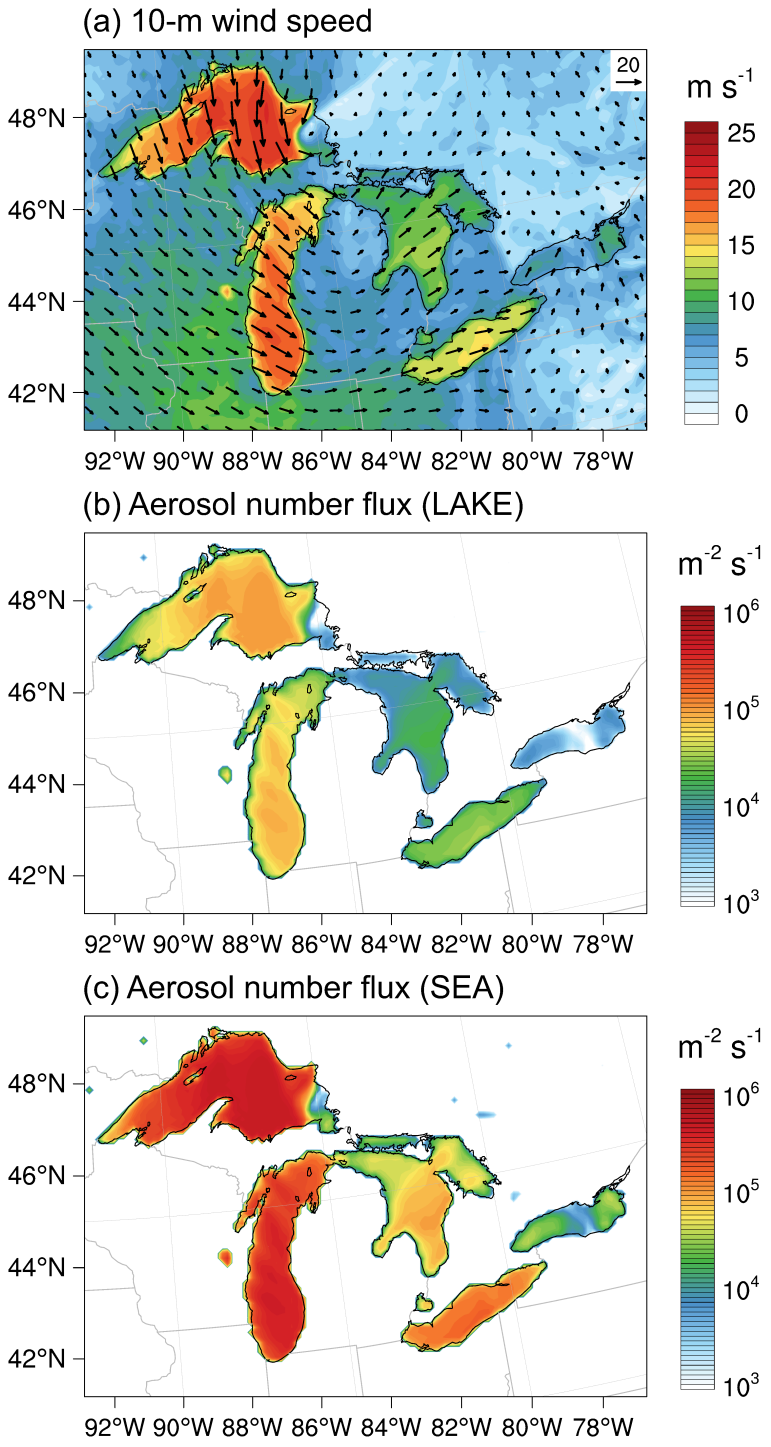

Figure 3.6: **Modeled aerosol number emission flux from the Great Lakes surface on a windy day for different emission scenarios.** **(a)** The 10-m wind speed and the corresponding aerosol number emission flux from the Great Lakes surface in the **(b)** LAKE and **(c)** SEA scenarios on 19 November 2016, 15:00:00 UTC.

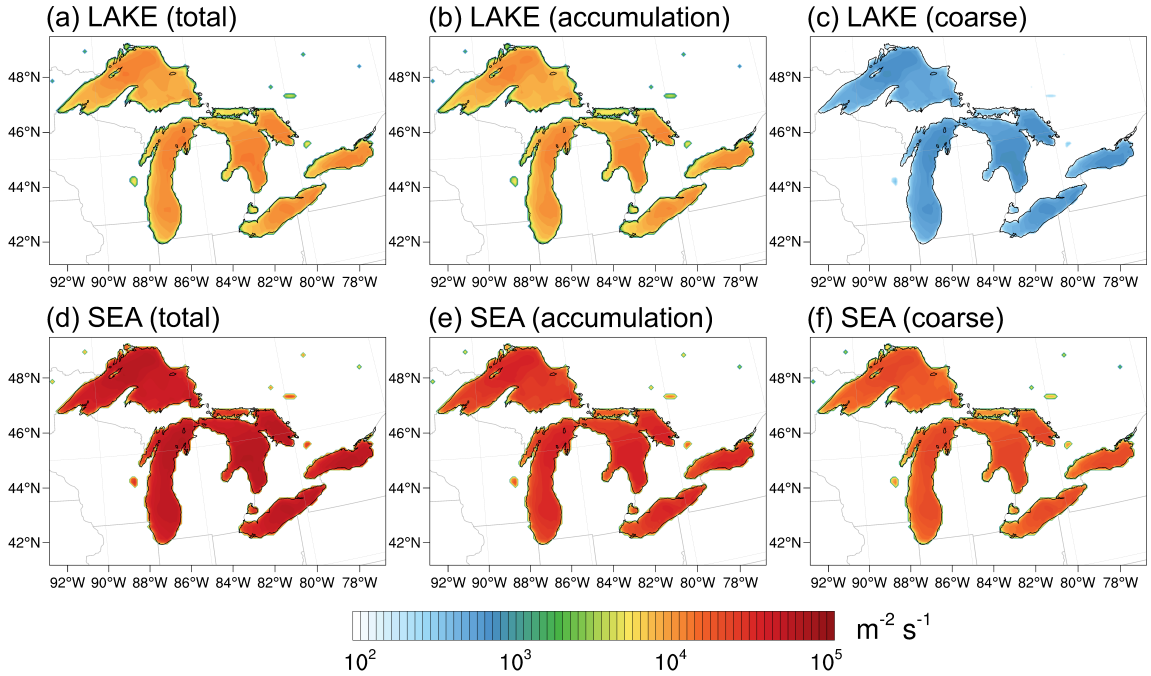

Figure 3.7: **Modeled aerosol number emission flux from the Great Lakes surface averaged over the simulation period for different emission scenarios.** Average (10-30 November 2016) **(a,d)** total, **(b,e)** accumulation-mode, and **(c,f)** coarse-mode aerosol number emission flux in the LAKE and SEA scenarios.

In the remainder of this section, we discuss the implication of spray aerosol emissions from the Great Lakes surface on regional aerosol number and mass concentrations. It is important to reiterate that these spray aerosols are essentially considered to be chemically-inert particles with a density of 1.5 gcm^{-3} (see Sect.3.3.3). Such a consideration facilitates the tracking of these particles in the atmosphere without chemical processing. However, the chemistry involving LSA particles is important as it has been shown that these particles can alter thermodynamic equilibrium in the Great Lakes region, leading to an increase in particulate nitrate and a decrease in particulate ammonium [61]. Therefore, without a realistic chemical speciation, the results of this simulation only provide a preliminary estimate of the impact of particle emission from the Great Lakes surface on regional aerosol loading.

Figure 3.8 shows the total, accumulation-mode, and coarse-mode surface-layer aerosol number concatenations in the BASE scenario averaged over the simulation period (a-c) and their corresponding percent increase in the LAKE (d-f) and SEA scenarios (g-i). In the absence of surface emissions from the Great Lakes (i.e., BASE scenario), regional aerosol loading in the

Great Lakes basin is dominated by anthropogenic emissions from the Chicago and Toronto metropolitan areas. In these regions, total number concentrations reach more than 1000 cm^{-3}, while average concentrations above the Great Lakes surface are mostly smaller than 500 cm^{-3} (Fig. 3.8a). Looking at the contribution of each mode reveals a clear dominance of accumulation-mode particles on regional aerosol population. Meanwhile, aerosol number concentrations in the coarse mode are three orders of magnitude lower than those in the accumulation mode, reaching $\sim$2 cm^{-3} in the Chicago and Toronto metropolitan areas and $<$l cm^{-3} above the Great Lakes surface (Figs. 3.8b and 3.8c). When enabling LSA emissions from the Great Lakes surface (i.e., LAKE scenario), the increase in the average total (and accumulation-mode) aerosol number concentrations is mostly in the source region (i.e., above the lakes surface), with up to 1.65% in northwestern Lake Superior and $<$0.25% average increase above other parts of the lakes (Figs. 3.8d and 3.8e). A much more prominent increase can be seen for coarse-mode particles, for which the percent increase can reach up to 1900% in northwestern Lake Superior and ranges from 5 to 150% over other parts of the lakes (Fig. 3.8f). This apparent increase can be attributed to low preexisting aerosol concentrations ($<$l cm^{-3}) in the source region, especially over the remote northern lakes (Fig. 3.8c), coupled with discernible LSA emissions in the coarse mode from the lakes on the order of 10^2 m^{-2} s^{-1} (Fig. 3.7c). Enabling SSA emissions from the Great Lakes surface (i.e., SEA scenario), on the other hand, leads to a more noticeable increase in regional aerosol loading. Average total number concentrations increase by up to 7.5% in northwestern Lake Superior (Figs. 3.8g and 3.8h), which is lower than the maximum increase of 20% reported by Chung et al. [59] over the same region. Over other parts of the lakes, the increase in average total aerosol number concentrations ranges from 0.5 to 1.2%. Furthermore, the percent increase in coarse-mode aerosol number concentrations is much more significant and ranges between 90% in western Lake Erie and up to 64000% in northwestern Lake Superior. Inland, coarse-mode aerosol number concentrations reach more than 10% in regions up to $\sim$1000 km northeast of the lakes (Fig. 3.8i). Altogether, using an SSSF led to around one order of magnitude overestimation of LSA contribution to regional aerosol numbers.

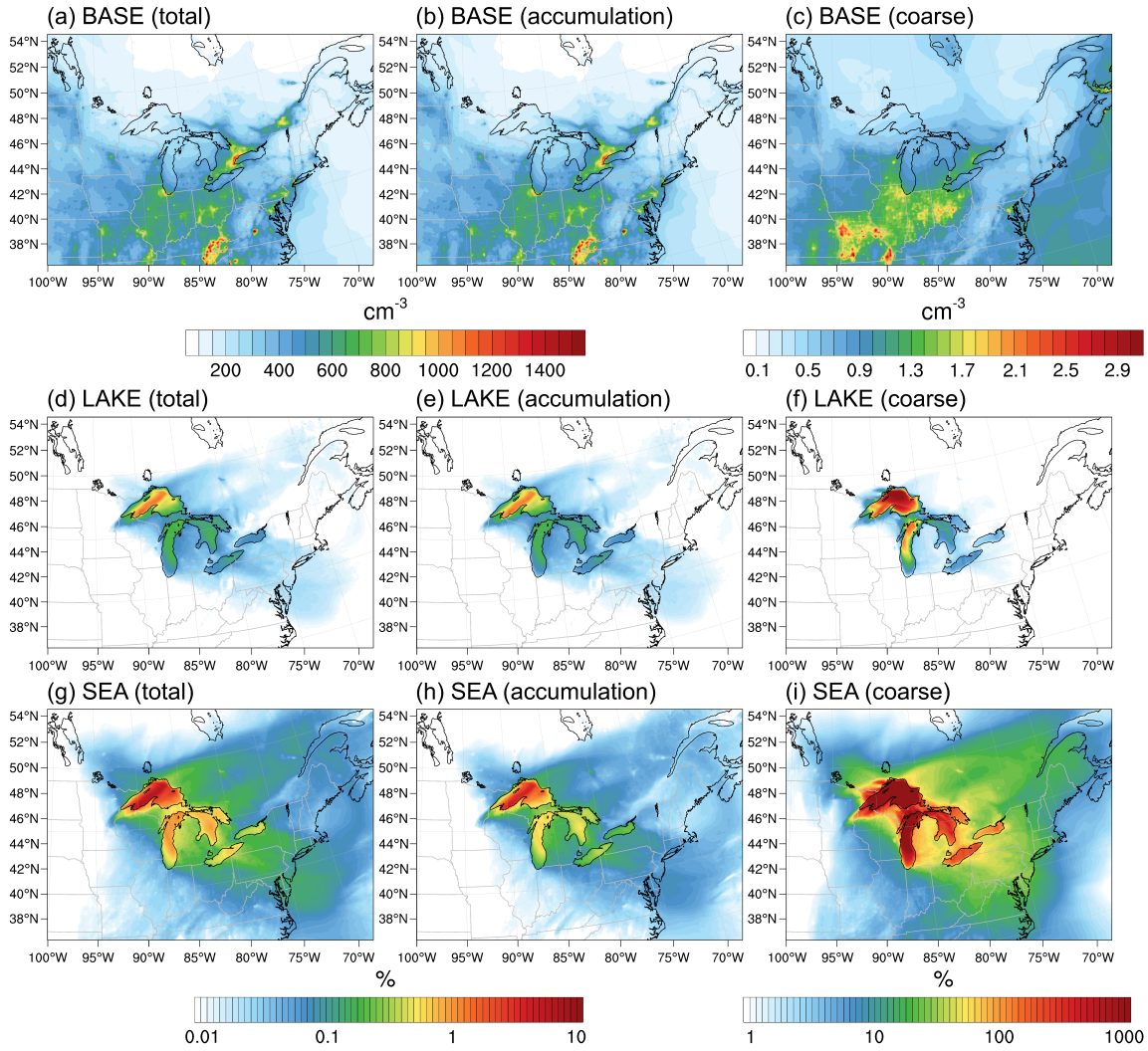

Figure 3.8: **Modeled surface-layer aerosol number concentration averaged over the simulation period for different emission scenarios.** Average (10-30 November 2016) **(a-c)** total, accumulation-mode, and coarse-mode surface-layer aerosol number concentrations in the BASE scenario, and their corresponding percent increase in the **(d-f)** LAKE and **(g-i)** SEA scenarios. Notice the different colormap for coarse-mode number concentrations.

Figure 3.9 shows the average total, accumulation-mode, and coarse-mode surface-layer aerosol mass concatenations of particles emitted from the surface of the Great Lakes in the LAKE (a-c) and SEA scenarios (d-f). In the LAKE scenario, the average mass concentration is highest in the source region (50 to 175 ngm^{-3}) and can reach more than 10 ngm^{-3} inland up to ∼1000 km east and northeast of the Lakes (Fig. 3.9a). This inland transport of LSA particles supports previous field observations of LSA contribution to the aerosol population

in a rural site in northern Michigan located >25 km from the nearest Great Lakes source [37]. Looking more closely at the contribution of each mode reveals that coarse-mode particles dominate the mass concentration ($\sim$ 98%) (Fig. 3.9c), as expected, whereby the contribution of accumulation-mode particles is only $\sim$2% (less than 4 ngm^{-3}) and is mostly constrained to the source region (Fig. 3.9b). In the SEA scenario, the average mass concentration reaches up to 5160 ngm^{-3} in the source region and 300 ngm^{-3} inland with significantly greater spatial coverage (Fig.3.9d). As with the LAKE scenario, the average mass concentration is also dominated ($\sim$ 99%) by coarse-mode particles (Fig. 3.9f), whereby the contribution of accumulation-mode particles is only $\sim$1% (less than 50 ngm^{-3}) (Fig. 3.9e). Overall, it can be seen from Fig. 3.9 that the mass concentration of particles emitted from the Great Lakes surface is overestimated by more than one order of magnitude when using an SSSF instead of an LSSF.

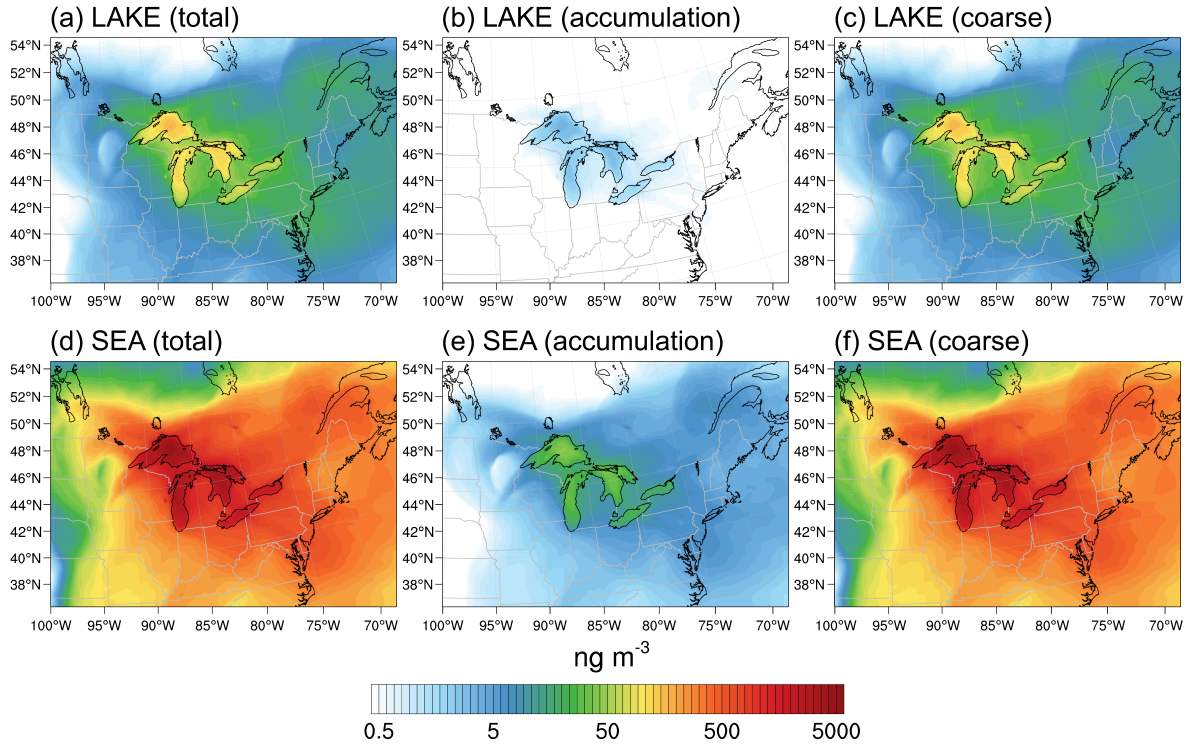

Figure 3.9: **Modeled surface-layer aerosol mass concentration averaged over the simulation period for different emission scenarios.** Average (10-30 November 2016) total, accumulation-mode, and coarse-mode surface-layer aerosol mass concentrations of particles emitted from the Great Lakes surface in the **(a-c)** LAKE and **(d-f)** SEA scenarios.

To put these mass emissions into perspective, Fig. 3.10 shows regional PM_1, $PM_{2.5}$, and PM_{10} surface-layer concentrations in the BASE scenario averaged over the simulation period (a-c) and their corresponding percent increase in the LAKE (d-f) and SEA scenarios (g-i). In the BASE scenario, PM_1, $PM_{2.5}$, and PM_{10} concentrations above the Great Lakes surface were highest over the southern parts of Lake Michigan and Lake Erie where they were about 7, 9, and 15 μgm^{-3}, respectively, and were lowest in the remote northern lakes, specifically over northwestern Lake Superior where they were about 3,4, and 6 μgm^{-3}, respectively (Figs. 3.10a to 3.10c). PM concentration hotspots can be clearly seen in the Chicago and Toronto metropolitan areas where PM_1, $PM_{2.5}$, and PM_{10} average concentrations reach 15, 20, and 28 μgm^{-3}, respectively. When LSA emissions from the surface of the Great Lakes are enabled (i.e., LAKE scenario), PM_1 and $PM_{2.5}$ increase by up to 4% and 14% in northwestern Lake Superior, respectively, driven by low preexisting PM concentrations in that area (Figs. 3.10d and 3.10e). The average percent increase in PM_{10} is rather more significant reaching 99 % over northwestern Lake Superior (Fig. 3.10f). Overall, the increase in PM concentrations in the LAKE scenario is mostly in the source region with some increase inland specifically in the vicinity of the lakes. On the other hand, SSA emissions (i.e., in the SEA scenario) result in up to 47%, 400%, and 3200% average increase in PM_1, $PM_{2.5}$, and PM_{10} concentrations in the source region, respectively (Figs. 3.10g to 3.10i). Therefore, using an SSSF to represent LSA emissions resulted in one order of magnitude overestimation of Great Lakes surface emission contribution to regional PM concentrations. Interestingly, it can also be seen from Fig. 3.10 that the effect of surface emissions from the Great Lakes can extend far beyond the source region and into the Atlantic Ocean. For instance, the PM_{10} average concentrations over the western Atlantic Ocean increased by up to 5 % and 40 % in the LAKE (Fig. 3.10f) and SEA (Fig. 3.10i) emission scenarios, respectively. These increases in faraway regions stem from an episodic event of high particle emissions from the Great Lakes surface on 20-21 November 2016, followed by atmospheric transport to the western Atlantic Ocean which is otherwise an area with low preexisting PM concentrations (Figs. 3.10a to 3.10c). Therefore, emissions from the Great Lakes surface can extend further inland during episodic events of very high wind speeds—a feature that is concealed when averaging over several weeks.

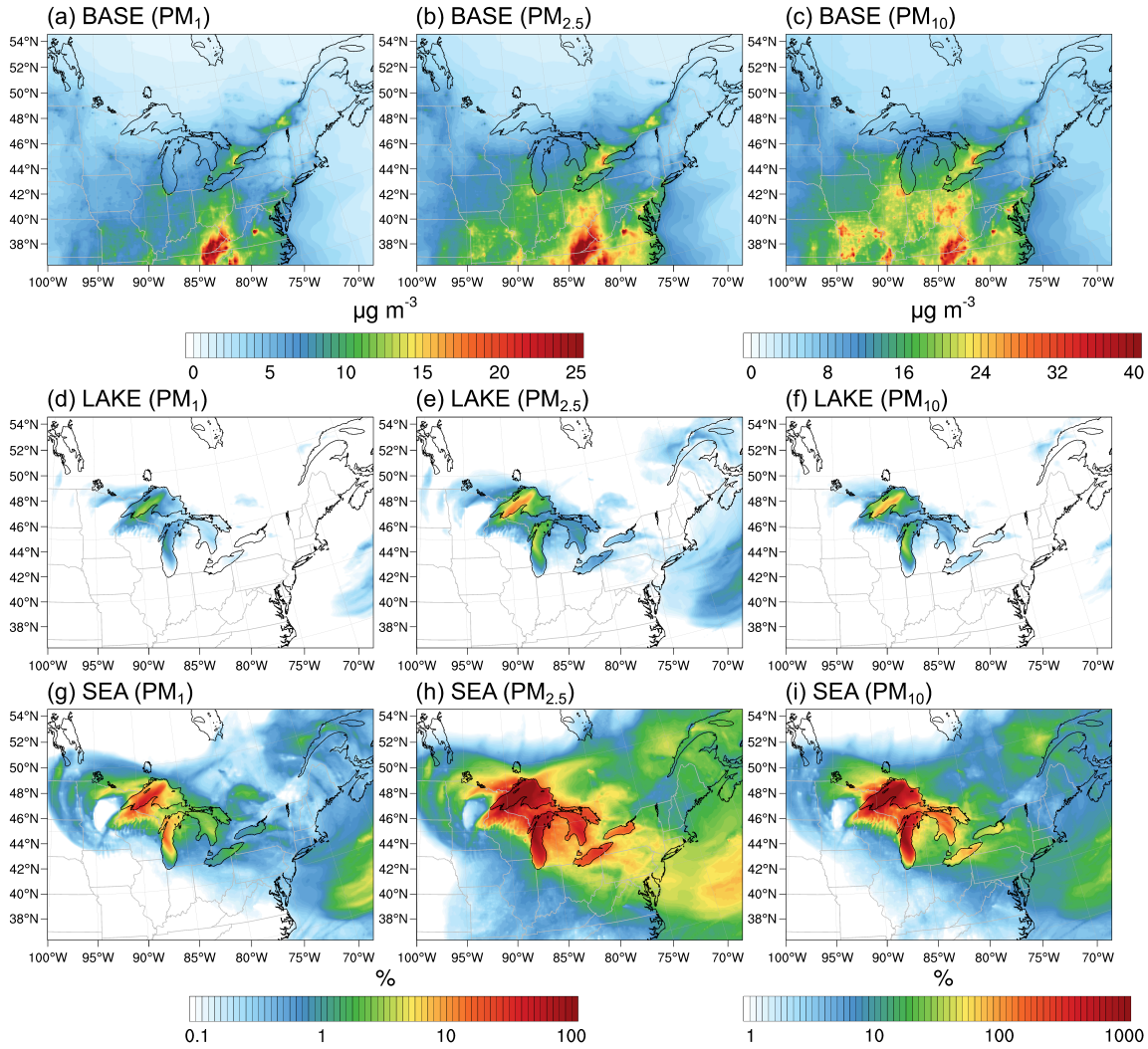

Figure 3.10: **Modeled PM_1, $PM_{2.5}$, and PM_{10} surface-layer concentrations averaged over the simulation period for different emission scenarios.** Average (10-30 November 2016) **(a-c)** PM_1, $PM_{2.5}$, and PM_{10} surface-layer concentrations in the BASE scenario, and their corresponding percent increase in the **(d-f)** LAKE and **(g-i)** SEA scenarios. Notice the different colormap for PM_{10} concentrations.

We conclude this section by examining the vertical reach of particles emitted from the Great Lakes surface and their potential to reach the cloud layer. However, the reader should keep in mind that a more comprehensive assessment of the potential impact of LSAs on cloud processes, specifically the associated changes in cloud condensation nuclei (CCN) and ice nucleating particles (INPs), requires the use of an online-coupled model [154]. Figure 3.11 shows vertical cross-sections (slices) of the percent increase in total aerosol number

concentration in the LAKE (a,c,e,g) and SEA (b,d,f,h) scenarios during an episodic event of high wind speed on 19 November 2016, 15:00:00 UTC. Also shown is the model estimated location of cloud bottom and top layers for reference. It is clear from this figure that emitted spray aerosols can reach several kilometers above the water surface, and into the cloud layer, which concurs with previous field measurements showing LSA particles incorporation into Great Lakes clouds [47]. In the LAKE scenario, the highest percent increase in vertical aerosol number concentration is ∼5% up to 1000 m above ground level and occurs in the middle of slice 2, which falls into the central region of the Great Lakes (Fig. 3.11c). Moving further north or south from the midst of the lakes (i.e, slices 1, 3, and 4) reduces the influence of surface emissions on vertical aerosol number concentrations, with the percent increase in aerosol number concentrations above 100 m being mostly smaller than 1% (Figs. 3.11a, 3.11e, and 3.11g). In the cloud layer, this percent increase ranges from less than 1% and up to 3%. In the SEA scenario, on the other hand, the contribution of the Great Lakes to vertical aerosol number concentration becomes noticeably higher (Figs. 3.11b, 3.11d, 3.11f, and 3.11h), reaching 26% up to 1000 m above ground level in slice 2. In the cloud layer, the percent increase of aerosol number concentration ranges from less than 1% and up to 13%. Therefore, using an SSSF led to around 4-fold overestimation of LSA contribution to vertical aerosol number concentrations.

Given the small contribution (<3%) of LSA particles to the aerosol number concentration in the cloud layer (Fig. 3.11), it might seem that LSA emissions from the Great Lakes surface have a limited influence on regional cloud processes. However, the size of the ejected spray aerosol plays a major role in its ability to act as seed particle for cloud drops, with recent studies indicating that the majority of INPs originating from SSAs are supermicron in scale [155, 156]. It is likely that these results translate to LSA particles, therefore, Fig. 3.12 shows the same data presented in Fig.3.11 but for coarse-mode particles. It is evident from this figure that the increase in coarse-mode particles in the LAKE scenario is significant. In slice 2, for instance, these particles increase by up to 144% up to 1000 m above ground level (Fig. 3.12c). When moving away from the midst of the Lakes (Figs. 3.12a, 3.12e, and 3.12g), the increase in coarse particles above 100 m is still significant and ranges from 5% to 100%. In the cloud layer, and across all slices, the increase in coarse-mode particle concentrations is significant and ranges from less than 1% all the way up to 98%. When considering the unrealistic scenario of SSA emissions from the Great Lakes surface (i.e.,

SEA scenario), there is a drastic percent increase in coarse-mode particle concentrations, with values exceeding 100 % across all slices (Figs. 3.12b, 3.12d, 3.12f, and 3.12h). Given that freshwater is considered an important INP reservoir [157] and that clouds are highly sensitive to the presence of even low INPs concentrations [158], the significant increase of up to 98% in coarse-mode particles in the cloud layer indicates that LSA emissions from the Great Lakes might play an important role in regional cloud ice formation and precipitation. Future modeling studies incorporating LSA chemical speciation and aerosol-cloud interaction are needed to shed more light on this role.

3.5 Conclusions

In this paper, we developed the first LSSF by simulating air entrainment in synthetic freshwater using a MART system. To compare freshwater and saltwater emissions, we also developed an SSSF in the same setup. Over the 0.01-10 μm particle diameter size range, the measured total SSA number concentration was on average eight times higher than that of LSA. There were no significant differences in LSA generation between the inorganic synthetic freshwater and Claytor Lake freshwater which might be due to low organic content in the collected Claytor Lake samples. However, it was observed that organic material might enhance LSA generation in freshwater [38]. Therefore, actual LSA emissions from the Great Lakes might deviate from what is predicted in this study especially in spring and summer seasons when the lakes exhibit higher concentrations of organic material [159]. We also show that drying the spray aerosols prior to sampling is not trivial, and leads to considerable particle losses especially in the supermicron size range. Losses in the aerosol surface area and volume size distributions, which are highly dependent on supermicron particle number concentration, are even more manifest. Therefore, it is important to take such losses into account in any experimental setup that incorporates diffusion dryers. The LSSF and SSSF developed from these experiments reveal that, at the same wind speed, LSA emissions are almost one and two orders of magnitude lower than SSA emissions for r_{80} <0.2 μm and r_{80} ~0.2-2 μm, respectively. Under the assumption of dry particles with a density of 1.5 gcm^{-3}, the emission mass flux computed from the present LSSF is at least one order of magnitude lower than that computed from the SSSFs at any wind speed.

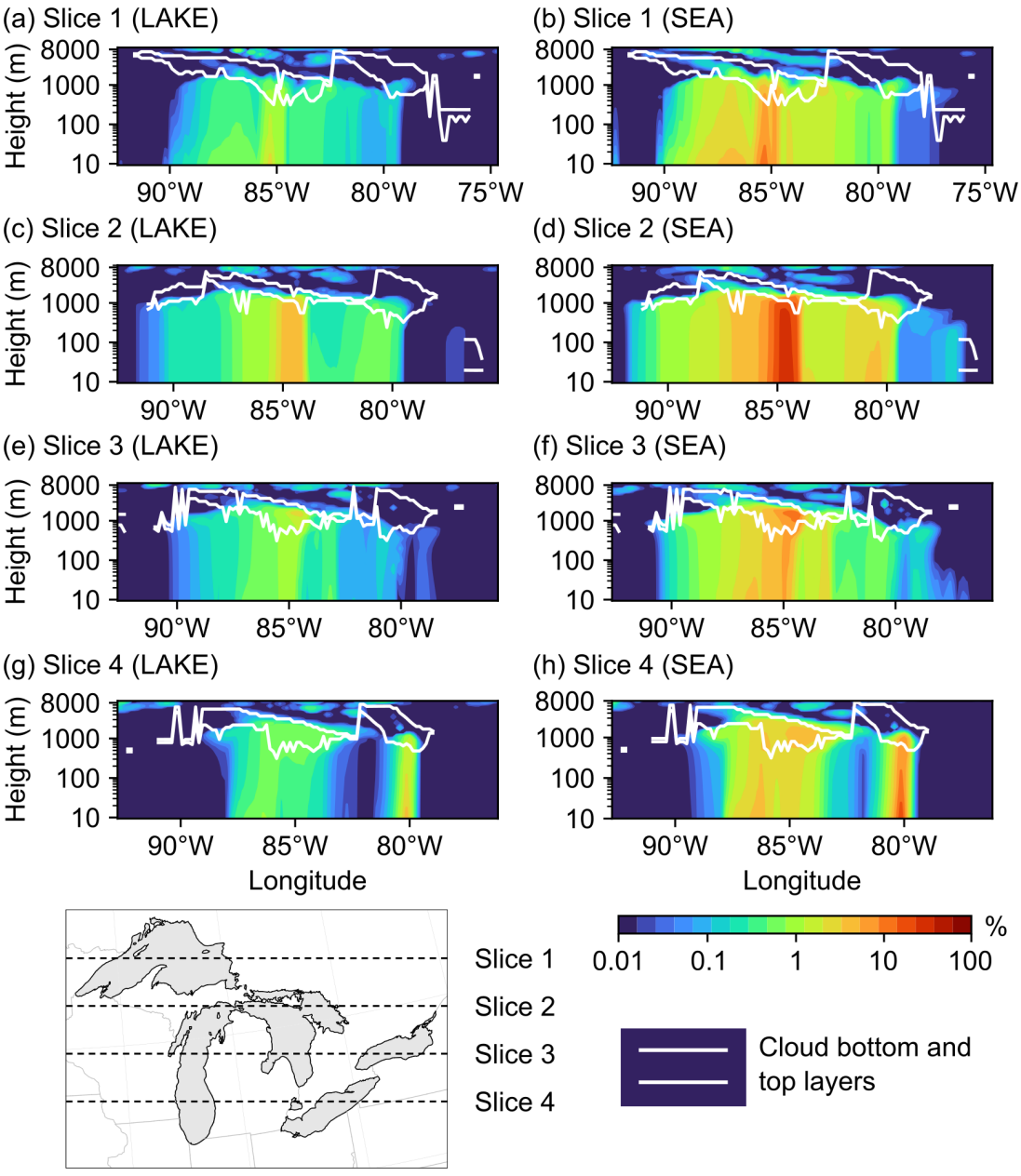

Figure 3.11: **Modeled percent increase in the total vertical aerosol number concentration above the Great Lakes surface for different emission scenarios.** Percent increase in the total vertical aerosol number concentrations in 4 cross-sections (slices) spanning the Great Lakes basin from north to south in the **(a-c-e-g)** LAKE and **(b-d-f-h)** SEA scenarios on 19 November 2016, 15:00:00 UTC. Also shown are the model estimated cloud bottom and top layers in each slice.

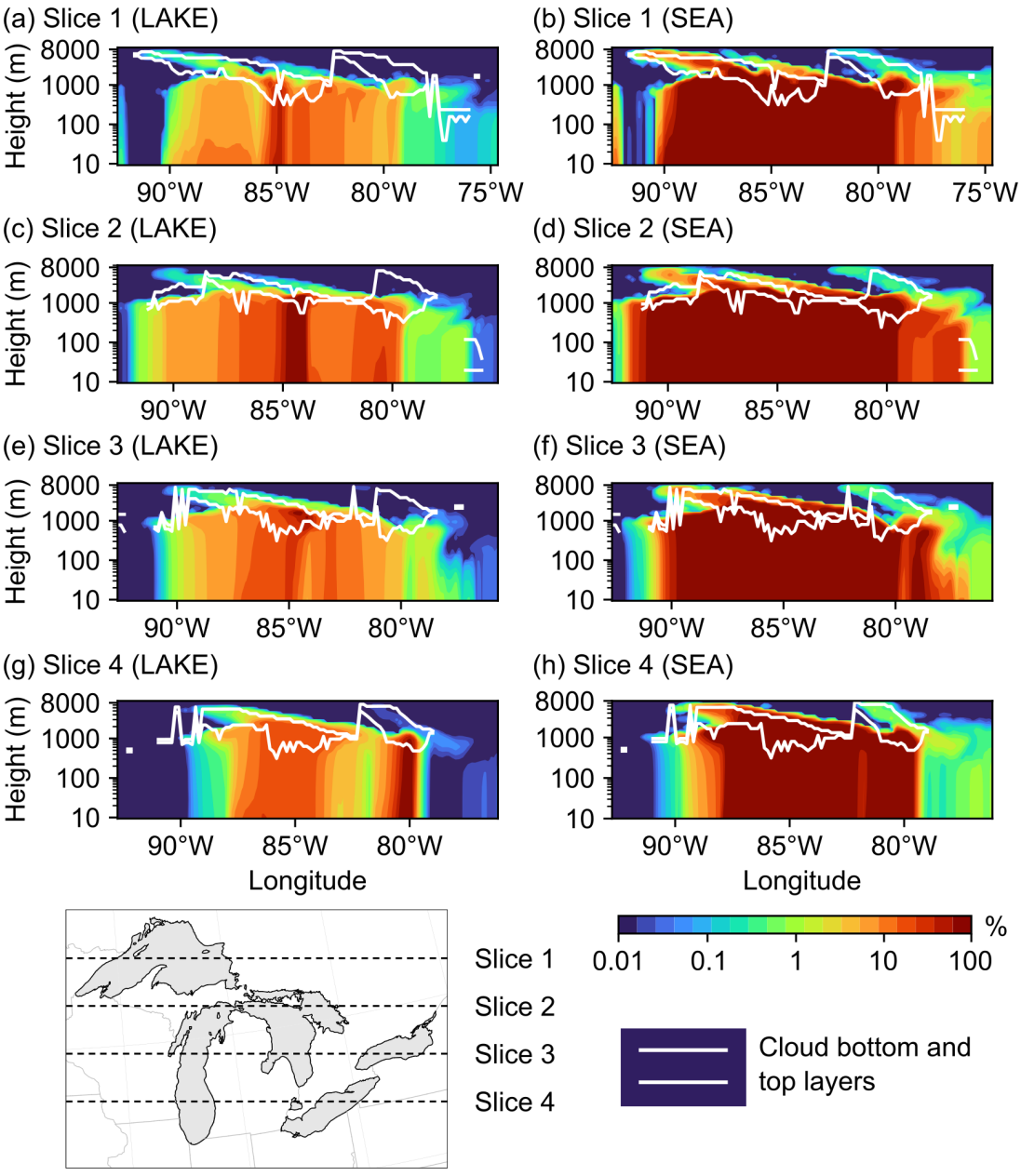

Figure 3.12: **Same as Fig.3.11 but for coarse-mode particles**

We also implemented the developed LSSF and SSSF in the CMAQ model to examine spray aerosol emissions from the Great Lakes surface during 10 to 30 November, 2016. During an episode of very high wind speeds on 19 November 2016 at 15:00:00 UTC, LSA emissions from the Great Lakes surface reached up to 10^5 m^{-2} s^{-1}. The impacts of these emissions on regional aerosol number and mass concentrations were also assessed under the assumption of

chemically-inert particles with a fixed density of 1.5 gcm^{-3}. While total aerosol number concentrations increased only by up to 1.65%, coarse-mode particle concentrations exhibited a significant 19-fold increase over northwestern Lake Superior. Looking at the mass concentration of emitted LSA particles reveals that it is dominated by coarse-mode particles and that these particles are mostly concentrated in the source region, yet they can get transported further inland up to ∼1000 km from the nearest Great Lakes source. This inland transport of coarse LSAs can have significant implications on the respiratory health of affected communities, since the enrichment of LSA particles in biological material increases with particle diameter greater than 0.5 μm [37]. LSA emissions also led to a significant increase in PM_{10} concentrations in the region, which rose by up to 117% above the Great Lakes surface. Looking at the vertical distribution of aerosol number concentrations, our simulation shows that LSA particles reached the cloud layer, yet they only resulted in a slight (<5%) increase in total aerosol number concentrations above the lakes. However, coarse-mode particles exhibited a more significant increase of up to 144% in the layer extending up to a 1000 m above ground level, and up to a 98% increase in the cloud layer. Given the importance of supermicron particles for ice nucleation [155, 156], this marked increase in coarse particles as a result of LSA emissions hints at possible implications on regional cloud processes.

This study highlights the errors brought about by using a SSSF to represent freshwater LSA emissions. For the case of Great Lakes emissions, for instance, using an SSSF resulted in around one order of magnitude overestimation of LSA contribution to regional aerosol numbers and mass concentrations. Although this study laid the groundwork for future modeling studies involving LSA emissions from freshwater, it is important to note that the LSSF developed herein does not incorporate other lake conditions such as LST and biological activity. These factors are especially relevant for the Great Lakes which experience significant seasonal LST changes [160] and episodic events of algal bloom occurrences [161]. Moreover, the simulation conducted here was only based on a three-week period in November 2016, and misses LSA chemistry and LSA-cloud interaction representations. Therefore, future avenues of research include incorporating LST and biology effects into the developed LSSF, increasing the simulation period to explore seasonal emission patterns, and incorporating LSA chemistry and LSA-cloud interaction representations to better understand the effects of LSAs on regional aerosol loading and cloud processes. The inclusion of LSA chemical speciation in the simulation will also allow for evaluating model results against PM observations

from regulatory air-quality networks in the region.

3.6 Acknowledgements

Part of this work was performed in shared facilities at the Virginia Tech National Center for Earth and Environmental Nanotechnology Infrastructure (NanoEarth), a member of the National Nanotechnology Coordinated Infrastructure (NNCI), supported by NSF (ECCS 1542100 and ECCS 2025151). We thank Brett Gantt from the U.S. Environmental Protection Agency for assistance with the CMAQ sea spray aerosol emission scheme. We also thank Xinyue Huang from Virginia Tech for helping with setting up the CMAQ model and Nora AlAmiri from Virginia Tech for helping with water samples collection and foam images processing.

Chapter 4

Freshwater salinization impact on aerosolized bacteria

4.1 Abstract

Increases in the salt concentration of freshwater result in detrimental impacts on water quality and ecosystem biodiversity. Biodiversity effects include freshwater microbiota, as increasing salinity can induce shifts in the structure of native freshwater bacterial communities, which could disturb their role in mediating basal ecosystem services. Moreover, salinity affects the wave breaking and bubble-bursting mechanisms via which water-to-air dispersal of bacteria occurs. Given this dual effect of freshwater salinity on waterborne bacterial communities and their aerosolization mechanism, further effects on aerosolized bacterial diversity and abundance are anticipated. Cumulative salt additions in the freshwater-euhaline continuum (0-35 g/kg) were administered to a freshwater sample aerosolized inside a breaking wave analogue tank. Waterborne and corresponding airborne bacteria were sampled at each salin-

ity treatment and later analyzed for diversity and abundance. Results demonstrated that the airborne bacterial community was significantly different (PERMANOVA; $F_{1,22} = 155.1$, $r^2 = 0.38$, $p < 0.001$) from the waterborne community. The relative aerosolization factor (r-AF), defined as the air-to-water relative abundance ratio, revealed that different bacterial families exhibited either an enhanced (r-AF $>> 1$), neutral (r-AF ~ 1), or diminished (r-AF $<< 1$) transfer to the aerosol phase throughout the salinization gradient. Going from freshwater to euhaline conditions, aerosolized bacterial abundance exhibited a nonmonotonic response with a maximum peak at lower oligohaline conditions (0.5-1 g/kg), a decline at higher oligohaline conditions (5 g/kg), and a moderate increase at polyhaline-euhaline conditions (15-35 g/kg). Our results demonstrate that increases in freshwater salinity are likely to influence the abundance and diversity of aerosolized bacteria. These shifts in aerosolized bacterial communities might have broader implications on public health by increasing exposure to airborne pathogens via inhalation. Impacts on regional climate, related to changes in biological ice-nucleating particles (INPs) emission from freshwater, are also expected.

4.2 Introduction

Despite only accounting for approximately 2.5% of water on Earth [162], freshwater is essential for human welfare. Freshwater resources are used in potable water production, energy generation, irrigation, industry, and recreation [163]. Anthropogenic stressors such as fertilizer runoff from agricultural activities, land alteration, resource extraction, and roadway de-icing have led to the emergence of freshwater salinization [164, 165, 166]. Salinization has negative impacts on water quality [167, 168, 169] and biodiversity [170, 171, 172], including shifts in the composition of aquatic bacterial communities [170, 171, 173]. Yet, the effect of changes in freshwater salinity on aerosolization of bacterial communities during wave breaking remains unexplored despite its potential impacts on regional climate and public health. Studies have shown that aerosolized bacteria in the atmosphere can act as cloud condensation nuclei (CCN) [174] and ice-nucleating particles (INPs) [175] influencing cloud properties and hence the climate. Airborne bacteria are considered one of the most active naturally occurring INPs in the atmosphere [175], since certain genera express an ice-nucleating protein [176] allowing them to form ice crystals at relatively warm temperatures [175]. Moreover, aqueous pathogenic strains in freshwater systems have been shown to be aerosolized and

transmitted to humans via inhalation [38, 48, 177, 178], which poses a risk on human respiratory health. Therefore, it is important to characterize the species of freshwater bacteria that become airborne and their aerosolization response to changes in freshwater salinity.

Freshwater salinization has both an instant impact on spray aerosol generation from breaking waves [35, 116] and a more prolonged effect by altering aquatic bacterial community structure [170, 171, 173]. Aqueous bacterial communities can be aerosolized by the action of breaking waves and the ensuing bubble-bursting mechanism [66, 67, 68, 179, 180]. As they rise to the surface, entrained air bubbles can scavenge suspended bacterial cells in the bulk water mainly by interception [181, 182, 183, 184], with bubble-to-cell size ratio playing a major role in scavenging (collision) efficiency [183]. Once settled at the surface, bacteria-laden surface bubbles burst, ejecting tiny "film drops" during the shattering of the bubble cap and bigger "jet drops" during the ensuing cavity collapse [16]. Both film [66] and jet [184, 185] drops are capable of aerosolizing bacteria via the bubble-bursting mechanism. Moreover, it is suggested that these two ejection mechanisms disperse microbes to the air from different regions in the water column, with film drops aerosolizing microbes from the surface microlayer and jet drops from the bulk water [99]. Salinity has important effects on the wave breaking mechanism and the resulting spray aerosol ejection. As salinity increases, the concentration of smaller bubbles in the entrained bubble plume increases [35, 116], surface foams become bigger and more persistent [116], and smaller surface bubbles emerge, which might enhance jet drops ejection in saltier waters [116]. Furthermore, increasing salinity leads to an enhancement in spray aerosol production from bursting surface bubbles [35]. Yet, the implications of these mechanistic changes on the abundance and diversity of aerosolized bacteria remain unclear.

Salinity is also a major environmental determinant of bacterial community composition [72]. Broad salinity changes have been shown to significantly influence aquatic bacterial communities across the freshwater-estuarine-marine continuum. A general trend emerges [186, 187, 188, 189, 190] where increasing salinity is associated with an increase in α-proteobacteria and γ-proteobacteria, and a decrease in β-proteobacteria. In a mesocosm experiment, freshwater bacterial community composition also shifted from more limnic to more marine genera in response to salt additions [173]. Despite the shifts in the composition of waterborne bacterial communities being relatively well documented, potential parallel shifts in airborne community composition have not been studied yet. Further, shifts in bacterial community composition across salinity gradients were accompanied by shifts in

functional performance including community production, respiration, and growth efficiency [190]. Indeed, when confronted with a moderately brackish salinity (4 g/kg), the growth efficiency of freshwater bacteria decreased, while respiration and growth rate increased [191]. Similarly, the growth of freshwater bacteria was stimulated at a low brackish salinity of 2 g/kg, yet cell mortality started to emerge after exposure to higher brackish salinities (10 and 20 g/kg) with significant mortality reported beyond a salinity of 20 g/kg [192]. Cell death in this study [192] occurred over a relatively low timescale of hours, whereas longer residence times (days) were required for bacterial community shift from a mixture of allochthonous communities to a native estuarine community along an estuarine salinity gradient [193]. It remains unclear whether these salinity-induced shifts in growth and cell-activity in water-borne bacteria are reflected in the abundance of aerosolized bacteria.

The incorporation of bacteria in droplets from bursting bubbles has been studied before in lab-scale setups [66, 67, 68, 179, 180, 194, 195]. Most previous studies have focused on a single bubble [66, 67, 184, 185] or specific strains of bacteria [66, 67, 179, 184] and have employed a culture-based technique [66, 67, 180, 195]. However, culture-based techniques do not provide the ability to fully characterize microbial communities, including the large proportion of unculturable taxa. More recently, DNA-based approaches, including targeted amplicon sequencing, have become the standard approach for analyzing microbial diversity and community structure [196]. Modern sequence-based community analysis has been recently applied to investigate microbial aerosolization from saltwater, uncovering taxon-specific transfer potential to the aerosol phase [68, 180, 194]. However, recent microbial aerosolization studies focused exclusively on saltwater [68, 180, 194, 197] although aerosolized microorganisms were also detected above freshwater [198, 199]. While some studies examined the incorporation of harmful *Cyanobacteria* strains in lake spray aerosols (LSAs) [37, 38, 200], no previous studies investigated freshwater bacterial community aerosolization from a holistic perspective. Furthermore, the effect of increases in salinity on the aerosolization of freshwater bacterial communities is not well understood.

The specific objective of this study was to understand the effect of increasing freshwater salinity on the abundance and diversity of aerosolized bacterial communities. Given the dual effect of salinity on the wave breaking mechanism and freshwater bacterial community structure, we hypothesized that increasing freshwater salinity increases the abundance and alters the diversity of aerosolized communities. A laboratory water tank was used to sim-

ulate bacterial aerosolization from breaking waves. Salinity treatments extending beyond freshwater conditions (<0.5 g/L) to oligohaline (0.5-5.0 g/L), mesohaline (5-18 g/L), and euhaline (30-40 g/L) conditions [201] were administered to a freshwater sample. Paired waterborne and airborne bacterial communities were sampled at each salinity treatment and were subsequently analyzed for total bacterial abundance and community structure.

4.3 Materials and methods

4.3.1 Freshwater sample collection, aerosol generation, and salinization timeline

Freshwater samples were collected on November 2, 2019 between 9:30 and 11:30 AM from Pandapas Pond (37.28°N, 80.47°W) in Blacksburg, Virginia (Fig. 4.1A). A total of 160 L of surface water (5-15 cm) was collected using preautoclaved 20 L HDPE carboys. The water samples were then immediately transported to the lab to be used within 2 h after collection.

Spray aerosols were generated using a laboratory water tank (100 cm × 54.6 cm × 61 cm) with a controllable water sheet [116] (Fig. 4.1B). In brief, water is circulated from the bottom of the tank to a concentric tube system above the water surface by means of a centrifugal pump (AMT Pumps, Royersford, PA). Water then uniformly exits from a slot at the outer surface of the concentric tubes and crashes into the water surface below entraining air bubbles that later rise and burst at the surface generating spray aerosols (Fig. 4.1B). A solenoid valve (Parker Hannifin, Madison, MS) connected to a time delay relay (Macromatic, Menomonee Falls, WI) is installed at the centrifugal pump outlet to control the intermittency of the water sheet. The tank is designed based on the Marine Aerosol Reference Tank (MART) system [90] and has been shown [116] to reproduce the size distribution of subsurface bubbles generated by in situ breaking waves [92]. Moreover, aerosolization experiments in the tank using tap water treated with a typical marine salinity of 35 g/kg resulted in a spray aerosol size distribution with a distinct accumulation mode peak around 120 nm (Fig. C.5C), which is comparable to the peak observed in the MART system (∼160 nm) [127] and other measurements in marine environments [23]. More details on the construction, operation, and performance of the tank can be found in Harb and Foroutan [116].

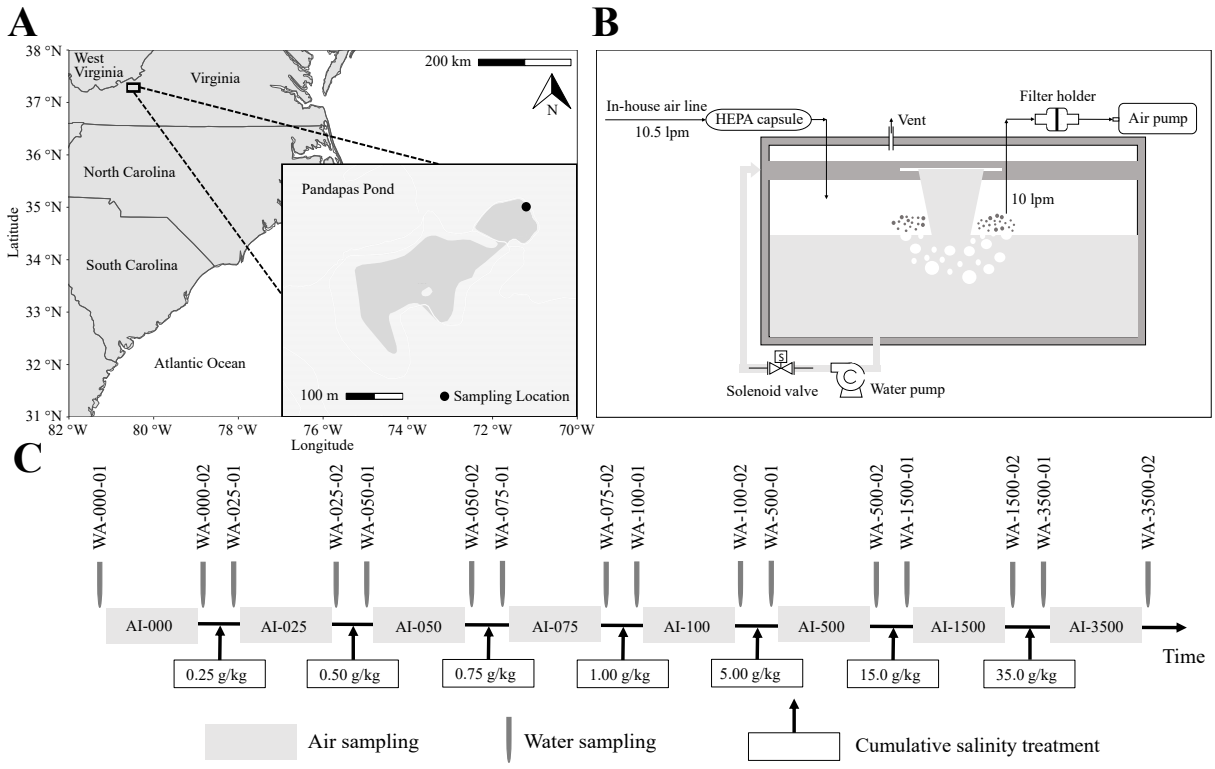

Figure 4.1: **Freshwater sampling location in Pandapas Pond, experimental setup, and salinization timeline. (A)** Regional map of the Eastern US showing the location of Pandapas Pond in Virginia. The inset is a close-up map of the pond showing the sampling location on the northeastern bank. **(B)** Schematic of the experimental setup. **(C)** Salinization timeline showing the steps of air and water sampling. More information on sample nomenclature, sampling times, and sample volumes are available in Appendix C, Tables C.1 and C.2.

Prior to the experiments, the tank was flushed with 5% isopropyl alcohol (99%)/deionized water solution for 5 h and the tank walls were wiped with 70% ethanol. The tank was then filled with 147 L of collected Pandapas Pond water and the water sheet was then turned on continuously by adjusting the knobs on the time delay relay. The measured water depth and flowrate in the tank were 27 cm and 24.5 L/min, respectively. Sweep air passed through a high-efficiency particulate air (HEPA) filter was injected into the tank's headspace at 10.5 L/min. Nascent spray aerosols were drawn from the headspace (1-3 cm above the water surface) using an SKC Leland Legacy pump (SKC Ltd., Dorset, U.K.) operating at 10 L/min (Fig. 4.1B). A vent in the tank's lid allowed excess air to discharge from the headspace.

Salinity treatments of 0.25 (freshwater); 0.50, 0.75, 1, 5 (oligohaline); 15 (mesohaline); and

35 (euhaline) g/kg were applied to the water volume inside the tank by adding incremental amounts of Instant Ocean Sea Salt (Instant Ocean Spectrum Brands, Blacksburg, VA) over a period of 56 h (Fig. 4.1C, Tables C.1 and C.2). All experiments were carried out at room temperature (∼20 °C). Salt additions were administered in quick succession and over a relatively short period of time to limit bacterial community succession at each salinity treatment. That way, we attempted to accentuate the effect of instant salinity changes on the aquatic bacterial community as opposed to allowing enough time for community succession as performed in previous aerosolization studies [68].

4.3.2 Bacterial sampling and DNA extraction

Water samples were collected from the location of sheet impact with the water surface using preautoclaved 1 L HDPE bottles (see Table C.1 for water sampling times and volumes). A water sample was taken at the start and end of each air sampling period (Fig. 4.1C). Collected samples were then filtered on mixed cellulose ester (MCE) membranes with 47 mm diameter and 0.22 μm pore size (Merck KGaA, Darmstadt, Germany). Membrane filtration through 0.22 μm pore size has been shown to have a generally high collection efficiency of waterborne freshwater bacteria (>96%); however, certain slender spirillum-shaped bacteria exhibited favored passage through the membrane filters [202].

Aerosols were collected on MCE membranes with 47 mm diameter and 3 μm pore size (Merck KGaA, Darmstadt, Germany) mounted in a URG-2000-30RAF filter holder (URG, Chapel Hill, NC) (Fig. 4.1B). Laboratory experiments have shown that 3 μm pore size filters have excellent collection efficiency of 0.9 μm airborne bacteria (∼100%) [203], but MCE membranes were not tested in this study. We encountered a clogging problem with the 3 μm MCE membranes during air sampling due to the high relative humidity (RH ≈ 90%) in the tank's headspace. Accordingly, two membranes were used in series at each salinity treatment to increase the sampled bacterial load (see Table C.2 for the total sampled air volume at each salinity treatment). The air samples were then combined for subsequent targeted amplicon sequencing. Prior to each salt addition, we opened the tank lid and flushed the headspace (∼185 L) at 10.5 L/min with clean sweep air for at least 30 min before a resumption of sampling.

Before DNA extraction, membrane filters were stored in a -20 °C freezer for up to 9 days. DNA from filtered aerosol samples was extracted using a DNeasy PowerSoil Kit (Qiagen, Hilden, Germany) with the following modifications to the manufacturer's protocol to elevate DNA yield: we cut the filter with a presterilized and disposable scalpel into sections and transferred all of the cuttings into a 5 mL bead tube (DNeasy PowerWater Kit, Qiagen, Hilden, Germany). The bead tube with filter sections was homogenized with solution C1 as instructed by the protocol. Before adding solution C2, we added 100 μL of RLC buffer, 3 μL of lytic enzyme, and 20 μL of Proteinase K (all provided by Qiagen, Hilden, Germany) to the sample and incubated it at 65 °C for 15 min. Samples then went through the purification process in accordance with the protocol, and the purified DNA was eluted twice in 25 μL of solution C6 (10 mM Tris), resulting in 50 μL of elution in total. DNA from filtered water samples was extracted using a DNeasy PowerWater Kit (Qiagen, Hilden, Germany) following the manufacturer's protocol.

4.3.3 Microbial analyses

Bacterial community structure was characterized via targeted amplicon sequencing. Amplification and sequencing of extracted DNA were performed by the Genomics Sequencing Center at Virginia Tech (Blacksburg, VA 24061). The V4-V5 region of the 16S rRNA gene was amplified by polymerase chain reaction (PCR) using the 515F/926R primer pair [204, 205]. DNA sequencing was performed on an Illumina MiSeq platform with 350 base pair, paired end sequencing. Prior to sequencing, the pooled sample was spiked with ∼25% PhiX (Illumina). Post sequencing, the 16S rRNA gene amplicon sequences were processed using QIIME2 [206]. Raw sequence reads were quality filtered using DADA2 [207], allowing for a maximum estimated error of 2. The resulting amplicon sequence variants (ASVs) were then frequency filtered, removing those that were present only once in the data set or occurred in only one sample. A pretrained Naïve Bayesian classifier [208] for 16S sequences was used with the Silva reference database (Silva 132 release [209]), bound by the 515F/926R primer pair, to taxonomically classify ASVs. Finally, ASVs classified as chloroplast, mitochondria, or unassigned at the Domain level were removed and the final data set was rarefied to the sample with the lowest number of total reads (40937).

4.3.4 Statistical analysis of microbiome and qPCR data

Differences among bacterial communities were analyzed based on ASV relative abundances using the Phyloseq package [210] in RStudio (version 1.2.1335 [211]). A two-way permutational MANOVA (PERMANOVA) was used to test for interactive effects of media (i.e., water vs air) and salinity on bacterial community structure. A permutational test of multivariate dispersion (PERMDISP2 [212]) was used to detect significant differences in dispersion, which can result in false-positive PERMANOVA results.

Total bacterial abundance in each sample was enumerated by quantitative PCR (qPCR) of the 16S rRNA gene (forward primer (1369F): 5'-CGGTGAATACGTTCYCGG-3'; reverse primer (1496R): 5'-GGWTACCTTGTTACGACTT-3') following a previously published protocol [213]. Prior to the qPCR experiments, the DNA extracts were stored in a -20 °C freezer for 5 months. The qPCR reactions occurred in 96-well plates and two separate plates were completed. Each well contained 10 μL of qPCR reactions, including 400 nM of each primer, 1 $\times$ SsoFast EvaGreen Supermix (Bio-Rad, Hercules, CA), and 1 μL of DNA extract or molecular grade water as a negative control. The qPCR program consisted of 98 °C for 2 min, and then 40 cycles of 98 °C for 5 s and 55 °C for 5 s [213] and was run on the CFX96 Touch Deep Well Real-Time PCR System (Bio-Rad, Hercules, CA). A representative subset of samples was chosen to identify the optimal dilution factor for all samples, including three from the air samples and seven from the water samples. We analyzed the serial dilutions of the subset samples, and the results revealed that 1:10 dilution generated the highest yield, indicating this dilution factor was sufficient for inhibitor reduction. Serially diluted 16S gBlock DNA fragments (IDT, Coralville, IA) served as the standards in each qPCR run, ranging from 1 to 10^7 gene copies/μL. The quantification limit was set at 100 gene copies/μL based on the lowest amplified standard with an efficiency higher than 80% and R^2 higher than 0.99 for both plates (Figs. C.1A and C.1B). All standards, negative controls, and samples were run in triplicates.

To estimate absolute abundances of bacterial families based on qPCR, ASVs were aggregated first at the family level for each sample to calculate relative abundances. Families with fewer than 1000 total reads were aggregated and categorized as "Others." Absolute abundances of bacterial families in each sample were then estimated by multiplying the respective relative abundance by the 16S gene copy (gc) number from qPCR for each sample [214]. Statistical

analyses including analysis of variance (ANOVA) and Tukey's range test were applied to assess differences in the ratio of gc number concentration in air to that in water at each salinity treatment.

4.4 Results and discussion

4.4.1 Diversity and abundance of aerosolized bacterial communities

Principal coordinate analysis (PCoA) of the water and air samples at each salinity treatment are shown in Fig. 4.2A. Air and water bacterial communities separated into two statistically distinct clusters along the x-axis (PERMANOVA; $F_{1,22} = 155.1$, $r^2 = 0.38$, $p < 0.001$). Bacterial community structure was also significantly different among salinity treatments, separating by salinity along the y-axis (PERMANOVA; $F_{7,8} = 23.9$, $r^2 = 0.41$, $p < 0.001$). There was also an interactive effect of media type (i.e., water vs air) and salinity (PERMANOVA; $F_{7,8} = 10.8$, $r^2 = 0.19$, $p < 0.001$). Despite the quick succession in salt additions (Fig. 4.1C), we cannot be certain that the shift in waterborne community composition was due to salinity alone, as no control experimental setup without salinity treatments was available to account for bacterial community succession over time. However, changes in salinity across this range have been found to significantly alter bacterial community composition across the freshwater-marine continuum [72, 187, 189, 191, 215]. In parallel to these shifts in the waterborne bacterial community, our results also show that the airborne bacterial community structure was also different at each salinity treatment.

Shannon diversity index values for air and water samples at each salinity treatment are shown in Fig. 4.2B. At salinity treatments of 0 and 0.25 g/kg (freshwater), bacterial diversities in air and water were comparable. While salinity did not impact Shannon diversity of water samples, air samples became significantly less diverse than water samples at salinity treatments beyond freshwater conditions (greater than 0.25 g/kg). This pattern suggests that either a subset of the water microbiome is aerosolized at higher salinities or that the aerosolized communities are dominated by certain taxa more than the original waterborne communities. In the air samples, as salinity increased from 0.5 to 35 g/kg (i.e., beyond

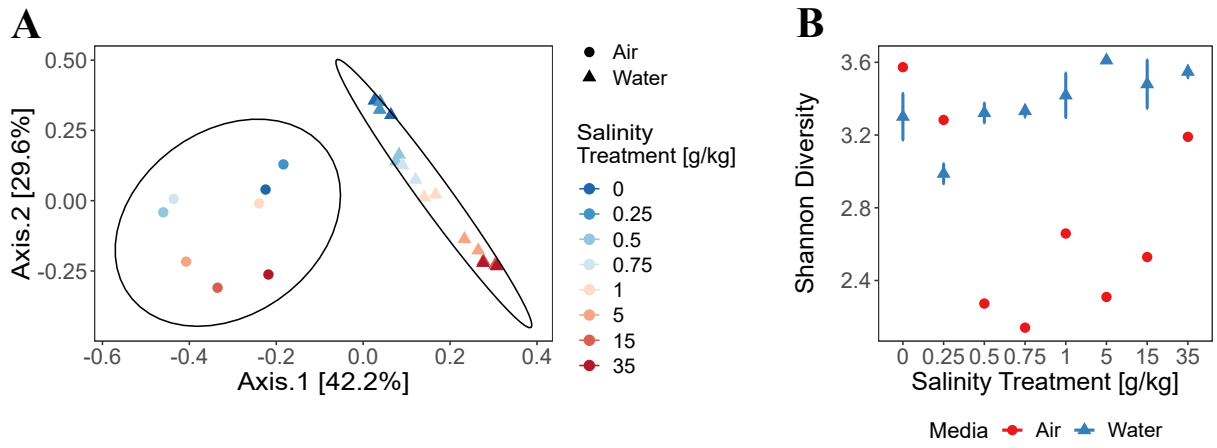

Figure 4.2: **Principal coordinate analysis (PCoA) and Shannon diversity index for the water and air samples at each salinity treatment. (A)** Principal coordinate analysis (PCoA) on the water (duplicates) and air (no replication) samples at each salinity treatment. **(B)** Shannon diversity index for water (duplicates) and air samples (no replication) vs salinity treatment. Bars (for water samples) represent the standard error of duplicates.

freshwater conditions), Shannon diversity index showed an increasing trend but was still consistently less diverse than that of the water samples. The U-shaped trend in the Shannon diversity index of air samples suggests that freshwater salinity treatments in the oligohaline range (0.5-5 g/kg) may lead to the aerosolization of a less diverse bacterial community than salinity treatments in the freshwater (0, 0.25 g/kg) and polyhaline-euhaline (15, 35 g/kg) ranges. If we factor out salinity treatments, grouping all samples together by media (Fig. C.6) shows that bacterial diversity is lower in air samples than in water samples (Welch's two-sample t-test, $p = 0.01$).

Total bacterial abundances, based on 16S gene copy (gc) concentrations, are shown in water and air at each salinity treatment in Fig. 4.3. The gc number concentrations in water varied throughout the salinization gradient between a minimum of 7.27×10^{11} ($\pm 2.4 \times 10^{11}$) gc/m^3 for untreated water and a maximum of 2.41×10^{12} ($\pm 3.56 \times 10^{10}$) gc/m^3 for a mesohaline salinity treatment of 15 g/kg. In air, gc number concentrations exhibited greater variations across the salinity range with the highest concentration of 5.09×10^{7} ($\pm 0.51 \times 10^{7}$) gc/m^3 measured at an oligohaline salinity treatment of 1 g/kg, whereas the lowest concentration of 0.34×10^{7} ($\pm 0.11 \times 10^{7}$) gc/m^3 occurred at a freshwater salinity treatment of 0.25 g/kg. The measured gc number concentrations in air are within the same order of magnitude

with concentrations of bacterial cells in freshly emitted sea spray aerosols (SSAs) in a wave flume [68], yet they are 3 orders of magnitude higher than the more diluted atmospheric concentrations measured in marine air [216]. The measured gc number concentrations in the tank's headspace are also at least 3 orders of magnitude higher than *Cyanobacteria* concentrations [199, 217] measured in the near-surface air layer (20-30 cm) above freshwater lakes in New Hampshire, Greenland, and Antarctica, as well as colony-forming unit (CFU) concentrations [198] measured 50 m above a freshwater lake in Virginia. These discrepancies are expected since the laboratory experimental setup prevents atmospheric dilution observed in field experiments.

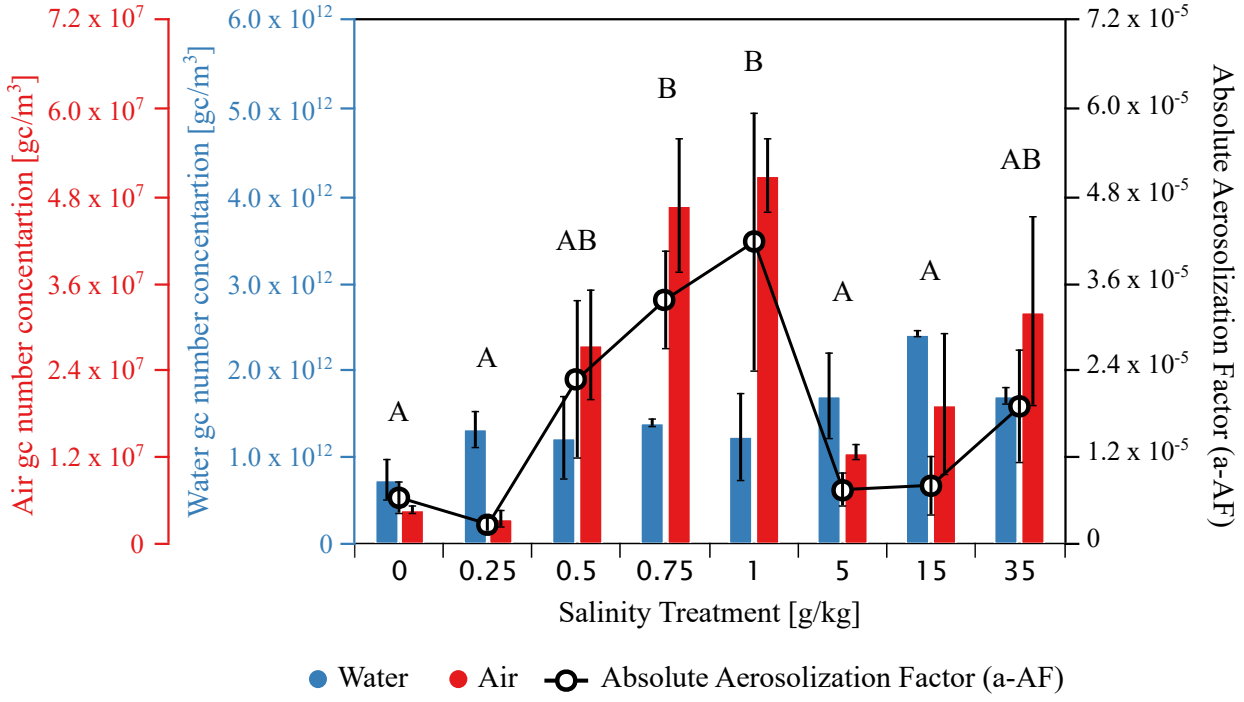

Figure 4.3: **Bacterial gene copy number concentrations in water and air, and the air-to-water gene copy number concentration ratio at each salinity treatment.** Total bacterial gene copy (gc) number concentration in air (red) and water (blue) at each salinity treatment. The black curve shows the absolute aerosolization factor (a-AF) at each salinity treatment. The a-AF is defined as the ratio of gc number concentration in air to that in water. Error bars represent ±1 standard deviation (SD) of triplicates. Note that SD values for air gc number concentrations also account for the sample volume uncertainties in Table C.2. a-AF values not sharing the same letter (i.e., A vs B) are significantly different (Tukey's HSD test, $p < 0.05$).

To quantify the fraction of aquatic bacterial gc number that is aerosolized at each salinity

treatment, we define the absolute aerosolization factor (a-AF) as the ratio of gc number concentration in air to that in water (Fig. 4.3). The a-AF values were positively correlated with the gc number concentrations in air and did not exhibit a monotonic trend throughout the salinization gradient. In particular, a-AF values increased distinctly going from freshwater (0, 0.25 g/kg) into lower oligohaline conditions (0.5-1 g/kg), then decreased in upper oligohaline-polyhaline conditions (5, 15 g/kg) before increasing again in euhaline conditions (35 g/kg). Analysis of variance (ANOVA) followed by Tukey's HSD test ($p < 0.05$) revealed that a-AF values at salinity treatments of 0.75 and 1 g/kg are significantly higher than those at 0, 0.25, 5, and 15 g/kg, but not significantly higher than a-AF values at 0.5 and 35 g/kg (Fig. 4.3).

4.4.2 Taxon-specific aerosolization trends

Bacterial community structures, presented as relative abundances of 12 bacterial families, in air and water measured across the salinization gradient are shown in Fig. 4.4A. Despite noticeable variations in the aquatic community composition, *Flavobacteriaceae* and *Burkholderiaceae* were the most abundant waterborne families and collectively accounted for at least 35% of the aquatic bacterial community for all salinity treatments. In air, there was a noticeable increase in the relative abundance of the *Chitinophagaceae* family, which accounted for up to 54% of the airborne community at the 15 g/kg salinity treatment. Together with *Flavobacteriaceae*, *Chitinophagaceae* accounted for at least 44% of the aerosolized bacterial families making them the two most abundant airborne families. The considerable increase in the relative abundance of *Chitinophagaceae* in air as compared to water hints at preferential aerosolization of certain bacterial families by the bubble-bursting mechanism.

To further investigate the aerosolization trends of different bacterial families, we computed the relative aerosolization factor (r-AF) of each family, which is defined as the ratio of the family's fraction in air to that in water [68]. The r-AF values of the bacterial families throughout the salinization gradient are shown in Fig. 4.4B. Most families seem to be either consistently enhanced (red) or consistently diminished (blue) in the aerosol phase throughout the entire salinization range. For instance, *Sporichthyaceae*, *Spirosomaceae*, *Burkholderiaceae*, and *Methylophilaceae* were mostly diminished in the aerosol phase, whereas *Caulobacteraceae*, *Chitinophagaceae*, and *Rhodobacteraceae* were consistently enriched in the aerosol phase re-

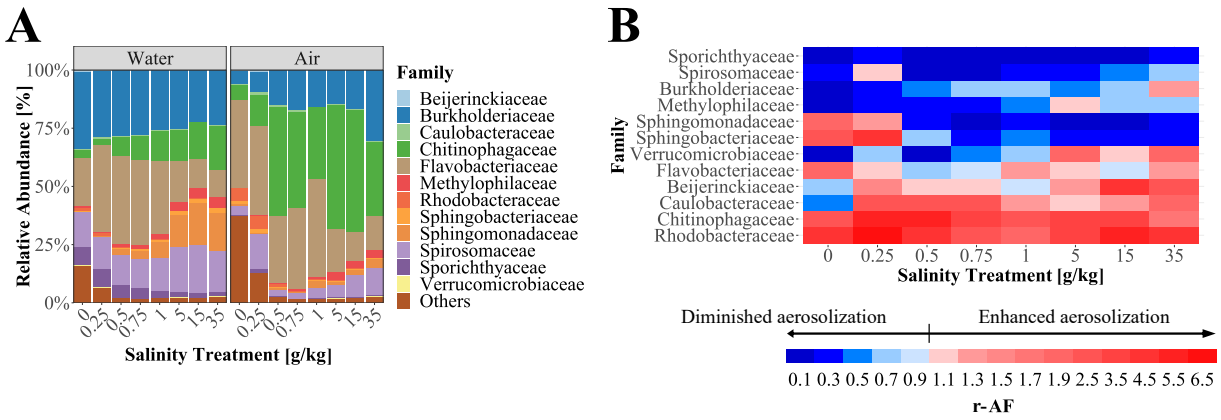

Figure 4.4: **Relative abundances of 12 bacterial families in water and air, and their enrichment in aerosols across the salinization gradient.** **(A)** Relative abundances of 12 bacterial families in water and air at each salinity treatment. **(B)** Heat map of relative aerosolization factor (r-AF) calculated for each bacterial family and at each salinity treatment. r-AF is defined as the ratio of a family's relative abundance in air to that in water. Colors indicate the extent of bacterial family enrichment in aerosols (red = enhanced aerosolization, blue = diminished aerosolization).

gardless of salinity treatment. Other families such as *Flavobacteriaceae* and *Beijerinckiaceae* did not exhibit neither an enhanced nor a diminished trend in the aerosol phase, with their r-AF values close to unity. Comparing r-AF values of freshwater bacteria at a typical marine salinity of 35 g/kg (Fig. 4.4B) to those of marine bacteria across phytoplankton blooms [68], we find similarly diminished aerosolization for *Sphingomonadales* and *Spirosomaceae*, and similar enhanced aerosolization for *Beijerinckiaceae*. However, marine *Rhodobacteraceae* and *Flavobacteriaceae* [68] exhibited neutral and diminished transfer to the aerosol phase, respectively, unlike their freshwater counterparts which exhibited enhanced aerosolization at a salinity treatment of 35 g/kg (Fig. 4.4B). These discrepancies indicate that freshwater bacterial families subjected to marine salinity conditions can exhibit different aerosolization patterns than marine bacterial families. Nonetheless, the observed differences in the potential for water-to-air dispersal among different freshwater bacterial families further corroborate previous findings of taxon-specific aerosolization potential in saltwater [67, 68, 180, 194]. Moreover, our results also suggest that some freshwater bacterial families maintain a consistent aerosolization pattern regardless of salinity treatment.

The total abundances of each bacterial family, estimated by multiplying the total 16S gc number concentrations by relative abundances of each family, in water (Fig. 4.5A) and air

(Fig. 4.5B) were also determined at each salinity treatment. In water, the most abundant families for salinity treatments smaller than 1 g/kg were *Flavobacteriaceae* and *Burkholderiaceae*. However, the gc number concentration of *Flavobacteriaceae* dropped for brackish (5, 15 g/kg) and saline (35 g/kg) treatments, while other families such as *Spirosomaceae*, *Sphingomonadaceae*, and *Chitinophagaceae* became considerably more abundant in this salinity treatment range. These shifts in the absolute abundances of families at different salinity treatments further show that the bacterial community structure in water is significantly different among various salinity treatments (Fig. 4.2A). Concentrations of bacterial families in air (Fig. 4.5B) reveal that *Flavobacteriaceae*, *Chitinophagaceae*, and *Burkholderiaceae* dominated the airborne bacterial community throughout most salinity treatments. Interestingly, the abundances of these three families in air exhibited a distinct increase in the 0.5-1 g/kg salinity treatment range. The dominance of these families relative to others in the lower oligohaline range (0.5-1 g/kg) might be associated with the decrease in Shannon diversity index in airborne bacteria observed in this same salinity range (Fig. 4.2B).

To further evaluate the potential of each bacterial family for airborne dispersal, we computed family-specific a-AF values (Fig. 4.5C). The a-AF values varied significantly among the evaluated bacterial families, further demonstrating the variability in their potential for water-to-air dispersal. The families with the highest a-AF values for most salinity treatments were *Chitinophagaceae*, *Rhodobacteraceae*, and *Caulobacteraceae*, all of which also expectedly exhibited the highest r-AF values (Fig. 4.4B). Due to limitations of ASV taxonomic classification, our ability to determine specific cell wall properties across bacterial families was limited. Yet, differences observed in the aerosolization potential of different bacterial families could be attributed to their cell surface properties. For instance, Gram-negative bacteria were preferentially aerosolized as compared to Gram-positive bacteria in a study involving five bacterial strains [218]. In the same study, no correlation was found between preferential aerosolization and bacterial shape and size [218], yet cell's shapes and roughnesses were shown to influence the capillary forces at the air-water interface [219] and possibly scavenging efficiency by rising subsurface bubbles. Moreover, cell surface hydrophobicity also influences bacterial adhesion to the gas-liquid interface [220] and aerosol enrichment, as it has been found that bacteria with missing hydrophobic cell capsules are correlated with reduced aerosolization [68].

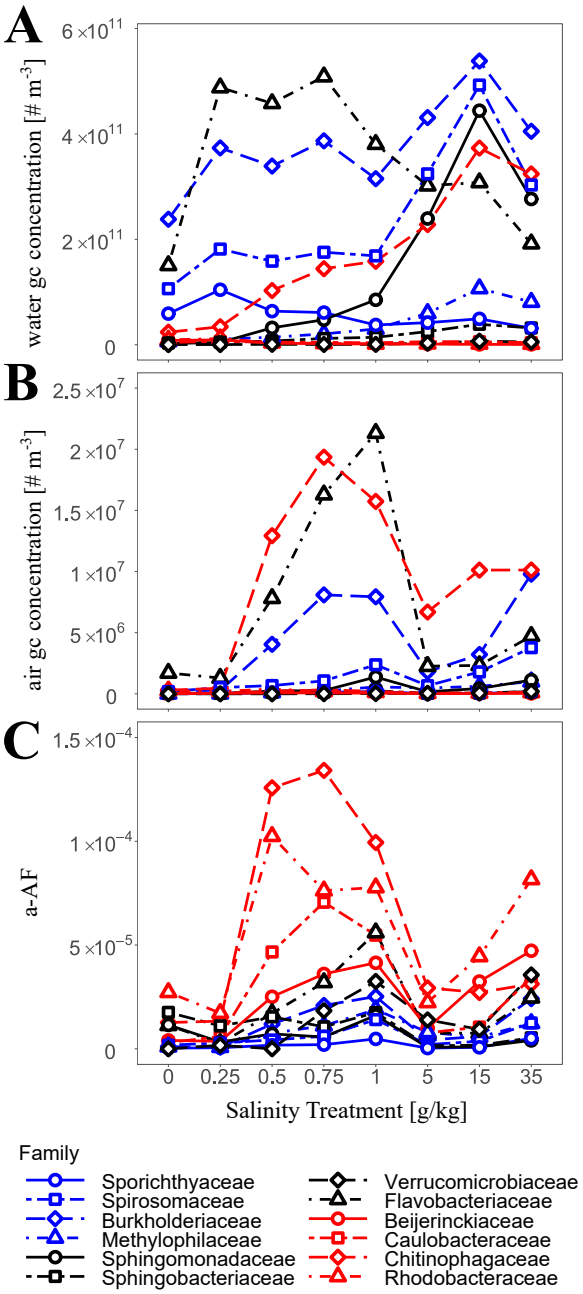

Figure 4.5: **Gene copy number concentrations of 12 bacterial families in water and air , and the air-to-water gene copy number concentration ratio of each family at each salinity treatment.** Gene copy (gc) number concentration of 12 bacterial families in water **(A)** and air **(B)** at each salinity treatment. **(C)** Absolute aerosolization factor (a-AF) of each bacterial family vs salinity treatment. a-AF is defined as the ratio of a family's gc number concentration in air to that in water. The color scheme reflects a classification of the enrichment level of families in the aerosol phase based on their r-AF values (see Fig. 4.4B): blue = diminished aerosolization, black = neutral aerosolization, and red = enhanced aerosolization.

4.4.3 Bubble-bursting mechanism and bacterial aerosolization

To confirm salinity-induced shifts in the bubble-bursting mechanism observed in previous studies [35, 116] and to understand their impacts on bacterial aerosolization, auxiliary experiments were performed in the tank to monitor the response of surface foam evolution and spray aerosol ejection to incremental salt additions. These experiments were carried out at room temperature (∼20 °C) and using laboratory tap water that was filtered after each salt addition (MarineLand Polishing Internal Canister Filter, Spectrum Brands, Blacksburg, VA). Thereby, we attempted to isolate the effect of salinity on the bubble-bursting mechanism from temperature and surfactant effects. More details about these experiments and their results are provided in the Appendix C. In brief, increasing freshwater salinity to oligohaline conditions (up to 5 g/kg) led to the generation of an enhanced and more persistent foam area comprising of smaller and more numerous surface bubbles (Figs. C.5A, C.5B, and C.5D). Similar trends in surface foam size characteristics were also observed with higher salinity treatments spanning the freshwater-euhaline continuum (0-40 g/kg) [116]. Further, incremental salinity treatments up to euhaline conditions (35 g/kg) resulted in a monotonic increase in the total concentration of ejected spray aerosols (Fig. C.5D). This increase occurred in both submicron and supermicron size ranges, which are predominantly associated with film drop and jet drop ejection, respectively (Fig. C.5C). A similar enhancement in submicron spray aerosol production following incremental salt addition was also observed by May et al. [35] in their LSA generator. Finally, we note that previous studies on saltwater have shown that organic material has distinct implications on surface foam evolution [76] and spray aerosol ejection [54, 57, 127, 221]. Future work is needed to examine the extent to which organic material found in pond water, that is otherwise excluded from filtered tap water, affects the response of the bubble-bursting mechanism to increased salinity.

Shifts in the bubble-bursting mechanism in response to increased salinity might have discernable implications on the composition and abundance of aerosolized bacterial communities. Compositional changes in aerosolized bacteria might occur due to a decrease in the size of entrained subsurface bubbles with increasing salinity [116], which alters the bubble-to-cell size ratio [183], and might favor the scavenging of bacteria within a specific size range. Moreover, the abundance of aerosolized bacteria is expected to increase with salinity. More persistent surface foams in saltier waters (Figs. C.5A and C.5D) have been associated with thinner

surface bubbles [222], which might lead to the ejection of droplets with high bacterial enrichment upon burst [181]. Further, the increase in the population of submillimeter surface bubbles with increasing salinity (Fig. C.5B) might enhance the ejection of jet drops [116]. This shift in ejection mechanism might enhance the viability of aerosolized bacteria, as it has been suggested that intact bacterial cells are more likely to be enriched in jet drops than in film drops [48]. Finally, the increase in spray aerosol ejection in saltier waters (Fig. C.5D) might lead to an increase in aerosolized bacterial load, especially in the supermicron size range (Fig. C.5C), where higher levels of enrichment in biological material have been found [37, 105, 127]. Overall, in mechanistic terms, increasing freshwater salinity seems to promote bacterial aerosolization due to enhanced foaming and spray aerosol ejection, particularly in the supermicron range.

4.4.4 Nonmonotonic response of freshwater bacterial aerosolization to increased salinity

While the response of the bubble-bursting mechanism to increased salinity is monotonic (Fig. C.5) and seems to favor bacterial aerosolization with successive salt additions, the abundance of aerosolized freshwater bacteria (i.e., a-AF) increased nonmonotonically and exhibited an optimum at lower oligohaline conditions (0.5-1 g/kg) (Figs. 4.3 and 4.5C). Given salinity effects on bacterial survival, this optimum might be associated with stimulated growth of freshwater bacteria in this salinity range coupled with restricted growth in mesohaline conditions and even death beyond polyhaline conditions [192]. Cell lysis starting at mesohaline conditions (>5 g/kg) might have contributed to the drop in a-AF values beyond a salinity treatment of 1 g/kg (Fig. 4.3), as it has been found that aerosolized bacteria in SSAs are predominantly viable [223]. Changes in bacterial scavenging efficiency [183] by rising subsurface bubbles, in response to increased salinity, might also be associated with the observed nonmonotonic a-AF trend. The scavenging efficiency of rising subsurface bubbles is impacted by at least two factors: (1) bubble-to-cell size ratio [183] and (2) bacterial surface hydrophobicity [224]. Since both bacterial cells [225] and subsurface bubbles [92] span a size range of approximately 2 orders of magnitude, they are expected to equally influence bubble-to-cell size ratio. As salinity increases, subsurface [116] bubbles shift monotonically to smaller sizes. Meanwhile, the size of suspended bacterial cells is also expected to change

due to shifts in community composition (Fig. 4.2A), especially in the oligohaline-mesohaline range (0.5-15 g/kg), where reduced Shannon diversity can be associated with a skew toward a restricted size range. Therefore, the bubble-to-cell size ratio is likely to exhibit a nonmonotonic response to increased salt additions. Furthermore, salinity has been shown to modulate bacterial hydrophobicity [226] and facilitate the attachment of hydrophobic particles onto the air-water interface [227]. Hence, it is likely that scavenging efficiency increased in the lower oligohaline salinity range due to stimulated bacterial growth, optimal bubble-to-cell size ratio, and optimal bacterial cell hydrophobicity, which culminated in a peak in bacterial aerosolization (Figs. 4.3 and 4.5C).

4.4.5 Regional climate and public health implications

Overall, this study suggests that increasing freshwater salinity to euhaline conditions induces shifts in the abundance and diversity of aerosolized waterborne bacteria. Of particular relevance to the freshwater salinization problem are salinity treatments up to 1 g/kg, since they span the salt concentration range observed in freshwater streams [228] and lakes [229]. In this salinization range, increasing salt concentrations resulted in considerable increase in aerosolization abundance (Fig. 4.3), coupled with reduced diversity in aerosolized communities (Fig. 4.2B). These shifts in bacterial aerosolization characteristics might have important implications on public health and regional climate in areas with large freshwater bodies.

Public health implications are probably most relevant in freshwater impacted by salinization from agricultural runoff [230]. Fertilizer runoff from agricultural activities has been linked to the intensification of harmful algal blooms (HABs) in freshwater [231]. Research has shown that HAB toxins can be aerosolized [37, 38, 48] by the bubble-bursting mechanism, which could be a public health concern in case of human exposure to these toxins via inhalation [48]. Furthermore, manure application in agricultural activities is associated with fecal contamination in stormwater runoff [232], which might lead to the introduction of zoonotic pathogens to freshwater. Some of these pathogens can thrive with moderate increases in salt concentrations, as it has been shown that E. coli exhibited increased survival rates when increasing salt concentration in the freshwater salinization range [233]. Our results suggest that the water-to-air dispersal of these pathogenic bacteria might be enhanced with increased anthropogenic salinization, as the abundance of total aerosolized bacteria exhibited a mono-

tonic increase with salinity treatments up to 1 g/kg (Fig. 4.3). However, further research into characterizing the aerosolization response of specific pathogenic bacteria to freshwater salinization is needed to better understand potential public health risks.

Climatic implications of freshwater bacterial aerosolization response to salinization are mainly related to the ability of airborne bacteria to act as INPs [175]. Despite its scarcity on a global scale, freshwater is potentially a significant reservoir of INPs on a regional scale, as it has been found that river water INP concentrations are much greater than those in marine systems [234]. Likewise, the concentrations of INPs dropped sharply as salinity increased going from river to marine conditions [235], and it has been suggested that a large fraction of these INPs are of biological origin. Indeed, bacterial strains of *P. syringae* in a freshwater lake have been found to express an ice nucleation protein [236], which potentially allows them to affect cloud process when aerosolized. The distinct increase in the abundance of aerosolized bacteria in the freshwater salinization range (Fig. 4.3) might enhance the number of airborne bacteria available for ice nucleation above freshwater surfaces. However, it is important to note that bacterial strains exhibit different ice nucleation activities [237]. This taxon-specific ice nucleation potential makes the prediction of freshwater salinization effects on cloud process more difficult, given the shift in airborne community composition (Fig. 4.2A) and reduction in diversity (Fig. 4.2B) associated with salinity treatments in the freshwater salinization range. Moreover, the shift of surface bubbles to jet drop ejection sizes with increased salinity (Fig. C.5B), coupled with an enhancement in supermicron particle dispersal (Fig. C.5C), might enhance freshwater INP emission. Research on SSAs has shown that jet drops generate higher submicron INP concentrations than film drops [99], and that supermicron particles have higher INP concentrations than submicron particles at warmer temperatures [156]. Whether these results can be transferred to LSAs remains an open question and could be of prime importance in uncovering freshwater salinization effects on the cloud process at a regional scale.

4.5 Acknowledgments

This work has been partially supported by the Fralin Life Science Institute at Virginia Tech. Shared facilities were used at the Virginia Tech National Center for Earth and Environmen-

tal Nanotechnology Infrastructure (NanoEarth), a member of the National Nanotechnology Coordinated Infrastructure (NNCI), supported by NSF (ECCS 1542100 and ECCS 2025151).

Chapter 5

Microplastics aerosolization by breaking waves

5.1 Introduction

Plastic pollution is globally ubiquitous causing an unprecedented environmental crisis. Microplastics (MPs), defined as small plastic pieces (< 5 mm in size) [238], have been detected widely in marine environments [239], freshwater systems [240, 241], sediments [242], and soil [243]. The omnipresence of MPs pollution has led to well-documented threats on ecosystems [244] and human health [245], with a recent study reporting the presence of MPs in human blood [246]. Recently, MPs have been detected in the air of metropolitan cities [247], and even above the pristine French Pyrenees which suggests intercontinental atmospheric transport of MPs [248]. However, the sources of these airborne MPs are not well understood which hampers our understanding of their environmental and public health impacts. Yet, there is growing evidence suggesting that breaking waves and the ensuing bubble busting mechanism can be an important source of atmospheric MPs [71].

Since the oceans cover 70% of the Earth surface and are a major reservoir of plastic pollution with an estimated 117 to 320 Mt of plastic litter in marine environments [239], it is evident that any mechanism that can transfer small plastic debris from the ocean surface to the air is an important source of atmospheric MPs. Such a mechanism is indeed omnipresent

on the ocean surface, whereby breaking waves entrains small bubbles in the water column, which rise to the surface and form foamy patches. Upon bursting, these bubbles eject tiny droplets into the air (i.e., SSAs), which range in size from 1 nm to a few millimeters [23] and are enriched with material from the bulk water and surface microlayer [99]. Allen et al. [71] were the first to suggest that breaking waves, via the aforementioned mechanism, can be a source of atmospheric MPs by collecting air samples on a remote beach on the French Atlantic coast. Later, Trainic et al. [249] also identified MPs in ambient aerosol samples collected in the North Atlantic Ocean. A couple of experimental studies followed showing direct evidence of MPs incorporation in SSAs including that of Masry et al. [250] and more recently, that of Yang et al. [251].

While the presence of MPs in SSAs ejected from seawater has been considered, the incorporation of MPs in LSAs ejected from freshwater lakes is yet to be studied despite growing evidence indicating MPs accumulation in freshwater [240]. The abundance of MPs accumulation in freshwater is even comparable to that in seawater [252]. For instance, mean MPs concentrations of 0.35, 2.0, and 4.2 cm^{-3} were observed in the river Seine (Paris, France) [253], the Upper Mississippi and St. Croix Rivers (Minnesota and Wisconsin, USA) [254], and 29 Great Lakes Tributaries (USA) [255], respectively. In the Great Lakes, which are an important source of LSAs (see Chapter 3), Lenaker et al. [256] reported a mean MPs concentration of 0.42 cm^{-3} in Lake Michigan. In Lakes Superior, Huron and Erie, Eriksen et al. [257] reported an average MPs (> 333 μm) concentration of 43,000 km^{-2} with a maximum value of more than 466,000 km^{-2} in Lake Erie. Other studies sampling near more populated regions in Lake Ontario reported even higher MPs (> 335 μm) concentrations of up to 6,680,000 km^{-2} in Lake Ontario [258]. We hypothesize, therefore, that MPs in freshwater lakes can be transferred to the air via LSAs. However, the dissimilar spray aerosol ejection characteristics between freshwater and saltwater (see Chapter 3) will likely lead to differences in MPs enrichment levels between SSAs and LSAs.

In this study, we compare the magnitude of MPs aerosolization from freshwater and saltwater breaking waves. To this end, we employ the MART system to generate laboratory SSAs and LSAs and use 2-μm fluorescent polystyrene (PS) particles as MPs surrogates.

5.2 Methods

The MART was used to simulate spray aerosol ejection from breaking waves (Fig. 2.1). In brief, this 100 cm × 54.6 cm × 61 cm tank is constructed from polycarbonate sheets and can hold up to 300 L of water. A centrifugal pump (AMT Pumps, Royersford, PA) circulates water from the bottom of the tank to a concentric tube system above the water surface, where it exists as a uniform sheet and crashes with the water surface. This waterfall generates bubbles that rise to the surface and burst dispersing spray aerosols into the headspace. More details about the tank construction and performance can be found in Chapter 2. The MART is designed to recreate the correct sizes of bubbles (see Chapter 2 and Prather et al. [127]) and SSAs generated by in situ breaking waves [127].

The seawater and freshwater environments were simulated by preparing synthetic saltwater and freshwater solutions, respectively. Synthetic saltwater was produced by dissolving Instant Ocean Sea Salt (Instant Ocean Spectrum Brands, Blacksburg, VA) in ultrapure water ($\sim$ 18 MΩ.cm, Picopure®) to achieve a mixing ratio of 35 gkg^{-1}. Synthetic freshwater was prepared by dissolving a mixture of anhydrous inorganic salts (Fisher Scientific; $CaCO_3$ $\geq$ 99%, $MgSO_4$ $\geq$ 99%, NaCl $\geq$ 99%, Sigma-Aldrich; K_2CO_3 $\geq$ 99%) in ultrapure water ($\sim$ 18 MΩ.cm, Picopure®) to achieve the following concentrations: 1 mM Ca^{2+}, 1 mM CO_3^{2-}, 0.4 mM Mg^{2+}, 0.4 mM SO_4^{2-}, 0.3 mM Na^+, 0.3 mM Cl^-, and 0.02 mM K^+, which closely mimic the inorganic salts composition of the Great Lakes [35, 42]. As a surrogate for MPs, fluorescent and monodisperse PS particles (Polysciences, Inc., Warrington, PA) with a diameter of 2 μm were added to the tank. PS was chosen for these experiments because it is one of the most common types of plastics found in marine [259] and freshwater environments [241].

Two sets of experiments were conducted using synthetic saltwater and freshwater, respectively. For each water type, two PS MPs additions were administered to a volume of 147 L of water inside the tank to achieve a MPs concentration of 10,000 L^{-1} in the first set (hereinafter, Exp-L) and 100,000 L^{-1} in the second set (hereinafter, Exp-H). It is worth noting that these concentrations are well beyond what is measured in seawater [259] and freshwater [241], yet they were chosen for these experiments to maximize MPs aerosolization into the headspace and, hence, facilitate the comparison between the two environments. The tank was operated in continuous mode (i.e., no intermittent plunging) with a water flowrate of 24

Table 5.1: Description and conditions of the MPs aerosolization experiments in MART

Experiment Set	Experiment Code	Water Type	Description	Water Salinity* (ppt)	Water Temperature* (°C)
Exp-L	Exp-L-F1	Freshwater	10,000 L^{-1}, 1st Exp.	0.08/0.08	25.0/29.4
Exp-L	Exp-L-F2	Freshwater	10,000 L^{-1}, 2nd Exp.	0.08/0.08	24.5/28.9
Exp-L	Exp-L-S1	Saltwater	10,000 L^{-1}, 1st Exp.	28.4/28.4	23.5/28.4
Exp-L	Exp-L-S2	Saltwater	10,000 L^{-1}, 2nd Exp.	28.3/28.4	23.8/28.7
Exp-H	Exp-H-F1	Freshwater	100,000 L^{-1}, 1st Exp.	0.08/0.08	24.0/28.8
Exp-H	Exp-H-F2	Freshwater	100,000 L^{-1}, 2nd Exp.	0.08/0.08	23.0/28.4
Exp-H	Exp-H-S1	Saltwater	100,000 L^{-1}, 1st Exp.	28.4/28.5	23.4/28.5
Exp-H	Exp-H-S2	Saltwater	100,000 L^{-1}, 2nd Exp.	28.4/28,.4	23.7/28.7

* As measured by an Extech EC170 salinity-temperature meter before/after each aerosolization experiment.

$Lmin^{-1}$. The air sampling flowrate was maintained at 4 $Lmin^{-1}$ using a Cole-Parmer 32907-73 mass flow controller (Cole-Parmer, Vernon Hills, IL). Sweep inflow air passed through a high-efficiency particulate air (HEPA) filter was injected into the headspace at a rate of 6 $Lmin^{-1}$ maintained using an Aalborg GFC37 mass flow controller (Aalborg Instruments & Controls, Orangeburg, NY). Excess airflow was vented through the tank lid (Fig. 5.1). Each aerosolization experiment consisted of a 1-hour period of active air entrainment, which was sufficient to reach steady-state aerosol concentration in the headspace, followed by a 3-hour air sampling period. The generated SSAs and LSAs were sampled on 47-mm Polycarbonate Track-Etch (PCTE) membrane filters (Zefon International, Inc, Ocala, FL) mounted inside a URG-2000-30RAF filter holder (URG, Chapel Hill, NC) and connected to the vacuum line (Fig. 5.1). To check for the MPs concentration in the water throughout each aerosolization experiment, a 0.2-L aliquot of tank water was collected at the beginning and end of each aerosolization experiment, and subsequently filtered through the (PCTE) membrane filters. For each water type (i.e., freshwater and saltwater), the aerosolization experiment was conducted twice after each PS MPs addition (i.e., 10,000 or 100,000 L^{-1} target concentrations), which resulted in eight aerosolization experiments in total summarized in Table 5.1.

To detect and enumerate the number of aerosolized PS particles, the filters were scanned using a fluorescent microscope (EVOS® FL Auto Imaging System, Thermo Fisher Scientific Inc., Waltham, MA). The scanned images were then processed using an image processing

software (ImageJ [97]). MPs concentrations in air were calculated by dividing the air filter MPs counts by the total volume of sampled air (i.e., 720 L). MPs concentrations in water were calculated by dividing the water filter MPs counts by the volume of the water aliquot (i.e., 0.2 L).

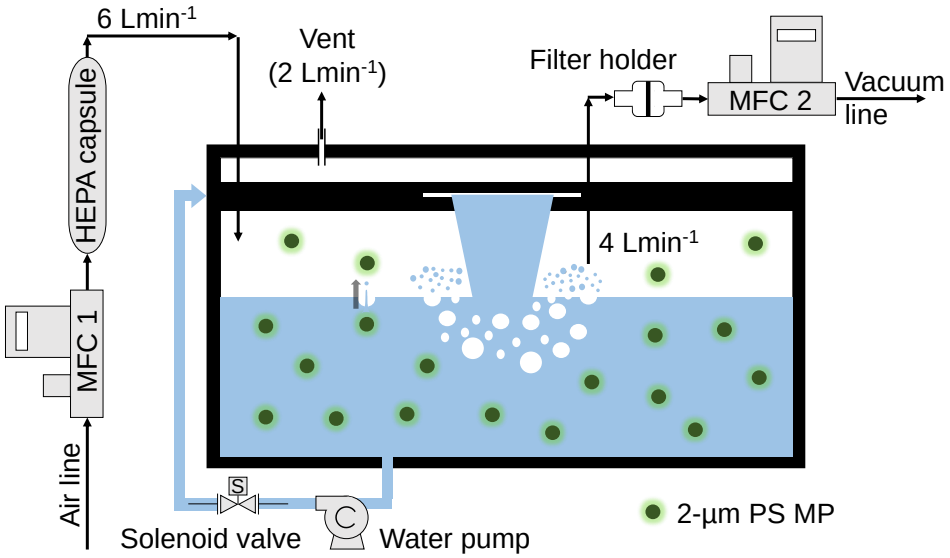

Figure 5.1: **Schematic of the experimental setup.**

5.3 Results and discussions

The PS MPs concentrations in the tank headspace and their corresponding concentrations in water for the eight aerosolization experiments (Table 5.1) are shown in Fig. 5.2a. For both the Exp-L and Exp-H experiments, the measured water concentrations in the synthetic freshwater experiments are closer to the 10,000 and 100,000 L^{-1} target concentrations than those measured in the synthetic saltwater experiments. The drop in the MPs concentration in water for the second experiment is more drastic in saltwater than in freshwater, which is possibly due to higher aerosolization of MPs in saltwater than in freshwater. Indeed, for both Exp-L and Exp-H experiments, the concentration of MPs in the headspace is higher in the saltwater experiments. For the Exp-L experiments, the air concentration of MPs due to LSA generation varied between 4.17×10^{-3} and 1.32×10^{-2} L^{-1}, whereas it varied between 1.81×10^{-2} and 2.84 L^{-1} due to SSA generation. Overall, the exponential fits indicate

that MPs aerosolization in saltwater is at least one order of magnitude higher than that in freshwater.

To quantify the fraction of waterborne MPs that was aerosolized by the bubble-bursting mechanism in freshwater and saltwater, we define the aerosolization factor AF as the air-to-water MPs concentration ratio as follows:

$$AF = \frac{[MPs]_{air}}{[MPs]_{water}} \tag{5.1}$$

In Eq. (5.1), $[MPs]_{air}$ is the concentration of MPs in the generated SSAs or LSAs and $[MPs]_{water}$ is the concentration of MPs in the synthetic saltwater or freshwater solutions. Figure 5.2b shows the AF values for synthetic freshwater and saltwater in the Exp-L and Exp-H experiments. In the Exp-L experiments, the average AF was 1.24×10^{-6} and 1.63×10^{-5} for freshwater and saltwater, respectively. In the Exp-H experiments, the average AF was 1.26×10^{-6} and 4.81×10^{-5} for freshwater and saltwater, respectively. These results reaffirm the one-order-of-magnitude higher MPs aerosolization in saltwater as compared to freshwater. For each water type, the AF values also seem to be similar in the EXP-L and Exp-H experiments, especially in freshwater, which suggests that the concentration of MPs aerosolized by bubble-bursting is proportional to the waterborne MPs concentration. Unlike bacterial cells aerosolization which exhibited a nonmonotonic response to increased salinity (see Chapter 4), the aerosolization of MPs seems to increase with salinity. As discussed in Chapter 4, salinity can alter waterborne bacterial communities which changes their size and surface properties, and hence their scavenging by subsurface bubbles and incorporation into ejected spray aerosols. On the other hand, the size and surface properties of MPs are not likely to be substantially influenced by changes in salinity for the time scale of these experiments. Therefore, the aerosolization response of MPs is only dependent on the response of the spray aerosols ejection mechanism to changing salinity, while that of bacterial cells is also dependent on salinity-induced community shifts.

In summary, this study is the first to show MPs enrichment in LSAs. However, the results indicate that the aerosolization of MPs by freshwater breaking waves is far less efficient than that by oceanic breaking waves. Recently, Yang et al. [260] used laboratory experiments to show that MPs emissions by oceanic breaking waves might not be an important source of

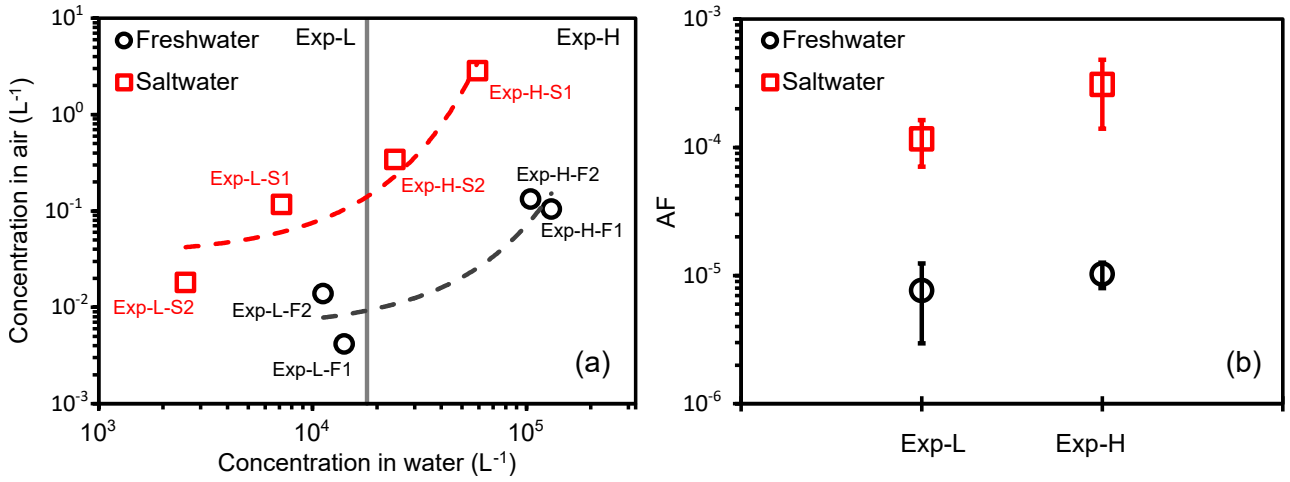

Figure 5.2: **PS MPs concentrations in air versus in water and their air-to-water concentration ratio in the freshwater and saltwater experiments.** **(a)** PS MPs concentrations in the tank headspace plotted against their corresponding concentrations in water for each aerosolization experiment (refer to Table 5.1). Both axes are in logarithmic scale. The dashed curves indicate exponential fits. To aid with visualization, the plot area is divided into two regions containing data points from the Exp-L and Exp-H experiments with target MPs water concentration equal to 10,000 and 100,000 L^{-1}, respectively. **(b)** The average aerosolization factor (AF), defined as the air-to-water MPs concentrations ratio, in the synthetic freshwater and saltwater experiments. Each data point represents an average AF calculated from the two experiments at each target water concentration (i.e., Exp-L and Exp-H). Note that the y-axis is in logarithmic scale. Error bars indicate ± 1 standard deviation (SD).

atmospheric MPs as compared to other sources such as tire wear or agricultural emissions [261]. However, a more recent study by Allen et al. [262] estimated that oceans and seas are a source of ∼43 and ∼38% of atmospheric microplastics and nanoplastics, respectively. Therefore, the contribution of oceans and seas to global atmospheric MPs is still uncertain. As for the contribution of freshwater lakes to global atmospheric MPs, the model simulation results in Chapter 3 show a mostly regional contribution of LSAs to atmospheric aerosols, hence, freshwater breaking waves are most probably a negligible source of global atmospheric MPs. Yet, freshwater emissions of MPs might be important on a regional scale especially in proximity to major population centers where freshwater MPs abundance is comparable and can even exceed the levels found in marine environments [263].

Chapter 6

Conclusions

There are fundamental mechanistic differences in spray aerosol emission characteristics between freshwater and saltwater breaking waves. Yet, our understanding of theses differences and their implications on the water-to-air dispersal of microorganisms and pollutants is lacking. This dissertation work aims to address this knowledge gap and is pivoted around four main components: understanding mechanistic differences in braking waves air entrainmnet characteristics across a salinity gradient, exploring differences in spray aerosol ejection abundance between freshwater and saltwater breaking waves and transferring this knowledge to atmospheric models, examining the effect of a freshwater-saltwater salinity gradient on bacterial aerosolization by breaking waves, and exploring differences in microplastics aerosolization by saltwater and freshwater breaking waves.

The novelty of this work lies in providing new insights on the effect of salinity on bubble evolution and spray aerosol ejection from breaking waves. It also puts forward the first model emission parametrization of spray aerosol ejection from freshwater breaking waves. The work goes further to contrast the ability of freshwater and saltwater breaking waves in aerosolizing waterborne microorganisms and plastic pollutants, which has important public health, climatic, and environmental implications.

6.1 Outcomes of research objectives

6.1.1 Outcomes of research objective 1

Evaluate the characteristics of air entrainment in breaking waves for salinities ranging from freshwater to saltwater.

This work provided some insights into the effect of salinity on subsurface bubble plumes and surface foams generated by breaking waves. Increasing water salinity from freshwater to typical marine conditions led to a systematic increase in the population of submillimeter bubbles in the entrained bubble plume. The abundance of larger supramillimeter bubbles, on the other hand, was almost independent of salinity. On the surface, increasing salinity resulted in a distinct increase in foaming area and persistence. Surface bubbles with radii up to two millimeters were significantly more numerous in saltwater than in freshwater, which suggests that increasing water salinity might have a more pronounced effect on the jet drop than on the film drop ejection pathway (see Fig. 1.1).

Overall, this work showed that the air entrainmnet characteristics are drastically different between freshwater and saltwater breaking waves. The change in the sizes and persistence of surface bubbles are especially relevant to the spray aerosol ejection process — and suggests that saltwater models fail to represent the correct characteristics of LSA emissions from freshwater lakes.

6.1.2 Outcomes of research objective 2

Develop an LSA emission parameterization, implement it in an atmospheric chemical transport model, and investigate effects of aerosols from freshwater breaking waves in regional simulations.

This work introduced an LSA emission parameterization for use in atmospheric models. The study built on the differences in air entrainmnet characteristics between freshwater and saltwater breaking waves described in Chapter 2. These differences translated to the spray aerosol ejection characteristics, whereby the SSA number concentration was eight times higher, on average, than that of LSA over the 0.01-10 μm particle size range. The developed

LSA emission parameterization revealed that for the same wind speed, LSA emissions are at least one order of magnitude lower than SSA emissions. Model results from the CMAQ simulations showed that LSA emissions from the Great Lakes only increased the average total aerosol number concentrations in the region by up to 1.65%. Yet, coarse-mode aerosols exhibited a much more significant 19-fold increase in some areas. While the contribution of LSAs to the regional aerosol loading was mostly in the source regions, they were transported up to 1000 km inland and reached the cloud layer.

Overall, this work highlighted the errors brought about by using an SSA emission parameterization to represent LSA emissions. When considering LSA emissions from the Great Lakes, for instance, there was a one order of magnitude overestimation of predicted freshwater emissions when using an SSA source function.

6.1.3 Outcomes of research objective 3

Investigate the effect of a freshwater-saltwater salinity gradient on bacterial aerosolization by breaking waves.

This work examined the effect of increasing freshwater salinity on the abundance and diversity of bacterial communities aerosolized by freshwater breaking waves. The results showed that the airborne and waterborne bacterial communities were significantly different (PERMANOVA; $F_{1,22} = 155.1$, $r^2 = 0.38$, $p < 0.001$) across the salinization gradient. Increasing water salinity from freshwater to saltwater conditions led to a nonmonotonic response in bacterial aerosolization abundance. The highest fraction of waterborne bacteria was aerosolized at lower oligohaline conditions (0.5-1 gkg^{-1}), followed by a decline at higher oligohaline conditions (5 gkg^{-1}), and a moderate increase at polyhaline-euhaline conditions (15-35 gkg^{-1}). Throughout the salinization gradient, different bacterial families exhibited either a diminished, neutral, or enhanced transfer to the ejected spray aerosols.

Overall, this work showed that although spray aerosol generation increases with salinity, the abundance of aerosolized waterborne bacteria does not follow a similar trend. This result suggests that the aerosolization of bacterial cells is not proportional to the abundance of spray aerosol ejection, as it is the case for inanimate particles such as MPs (See Chapter 5). The complex response of bacterial aerosolization to increased salinity is probably because

the latter also influences waterborne bacterial communities, which in turn has implications on their scavenging efficiency by rising subsurface bubbles and hence their incorporation in spray aerosols.

6.1.4 Outcomes of research objective 4

Compare the aerosolization of microplastics from freshwater and saltwater breaking waves.

This work compared the aerosolization of MPs by oceanic and freshwater breaking waves. The concentration of aerosolized PS MPs in the MART headspace due to SSA generation was around one order of magnitude higher than that due to LSA generation. The fraction of waterborne MPs that were aerosolized by spray aerosols was almost constant across the two water concentrations considered in these experiments (10,000 and 100,000 L^{-1}), in both freshwater and saltwater, which suggests that the bubble-bursting mechanism aerosolizes a fixed fraction of waterborne MPs.

Overall, this work shows that saltwater breaking waves transfer more MPs to the atmosphere than their freshwater counterparts. Increasing water salinity from freshwater to saltwater conditions let to a distinct increase in MPs aerosolization abundance, which diverges from the nonmonotonic response of bacterial cells aerosolization to increased salinity (see Chapter 4). Since the physical characteristics of MPs are not affected by salinity, at least for the short duration of these experiments, the presence of more bubbles and higher spray aerosol ejection in saltwater as compared to freshwater are likely behind the higher aerosolization of MPs by SSAs than by LSAs.

6.2 Broader impacts

Spray aerosols, namely SSAs, have long been thought of as an important component of Earth's atmosphere due to their ability to affect the climate by influencing cloud properties and incoming solar radiation [27]. However, this dissertation work suggests that spray aerosols do not only have climatic implications but even environmental and public health implications.

While the climatic impacts of SSAs are relatively well studied, those of LSAs, if any, are still not well understood. Despite not considering LSA chemical speciation and aerosol-cloud interactions, the model simulations in Chapter 3 show that LSAs can reach the cloud layer above the Great Lakes. If LSA particles are as efficient cloud nuclei as SSAs, which remains to be explored, LSA emissions can have important impacts on regional cloud formation above freshwater Lakes. Some insights into the differences in cloud nucleation potential between LSAs and SSAs can be gleaned from the results of Chapters 2 and Chapter 4. In chapter 2, it is shown that surface bubbles shift to the jet-drop ejection size at higher water salinities, which suggests that the film-jet drop partition is different between LSAs and SSAs. Given that previous studies have shown that jet drops might have a greater influence on cloud formation than film drops [99], it is likely that the cloud nucleation potentials of LSAs and SSAs are considerably different. Furthermore, in Chapter 4, it is not only shown that bacteria can be incorporated in LSAs, but also that water salinity can significantly alter the diversity of aerosolized bacteria. Meanwhile, it is well known that only certain bacterial species, such as *P. syringae*, have surface properties that are conducive to ice nucleation and hence cloud formation [236]. Therefore, the different bacterial species hosted by LSAs and SSAs suggest that they are likely to exhibit different cloud nucleation potentials.

The public health and environmental impacts of spray aerosols have to do with their ability to transfer microorganisms and emerging pollutants such as microplastics from the water to the air. One of the most important pathogenic emissions associated with freshwater are cyanobacterial toxins, which have been shown to be incorporated in LSAs emitted from freshwater with HABs occurrence [37, 38, 48]. The modeling results in Chapter 3 reveal that LSAs from the Great Lakes, which exhibit episodic events of HABs occurrences [161], can be transported thousands of kilometers inland. This transport, therefore, might pose a risk to the respiratory health of communities living not only in the vicinity of the Great Lakes but also much further inland. Besides cyanobacterial toxins from HABs, a plethora of pathogens are introduced into freshwater systems by agricultural and wastewater runoffs [264, 265]. Some of these pathogens are particularly sensitive to changes in water salinity with *E.coli*, for instance, exhibiting higher survival rates in response to small increases in freshwater salt concentration [233]. With the results of Chapter 4 showing that freshwater bacterial aerosolization is greatly enhanced at even low salt concentrations, wastewater and agricultural runoff into oceans and rivers might be hotspots for pathogenic aerosolization.

Furthermore, the experimental results in Chapter 5 reveal that both LSAs and SSAs can transfer emerging pollutants such as microplastics from the water to the air. Atmospheric microplastics constitute a serious public health and environmental concern with recent studies showing their incorporation in human blood samples [246] and lung tissues [266], in addition to the wealth of studies documenting their adverse ecological and environmental effects [244, 267]. Therefore, spray aerosols can exacerbate the threat of aquatic microplastics by resuspending them into the air, which later leads to their transport and deposition back inland, and hence their recycling in the environment.

6.3 Recommendations for future work

This dissertation work did not consider differences in spray aerosol ejection pathways (i.e., film vs jet drops) between freshwater and saltwater. Yet, the results of Chapter 2 suggest that the sizes of surface bubbles, which dictate the drop ejection pathway [27, 101], are significantly different between freshwater and saltwater. Therefore, a future avenue of research is to assess the relative importance of each ejection pathway in freshwater and saltwater breaking waves. Other factors besides water salinity that are also expected to affect bubble sizes in breaking waves, and hence the spray aerosol ejection pathway, include water temperature [76] and biological activity [57]. The effect of organic matter on the spray aerosol ejection pathway is especially interesting because organics reduce surface tension and hence the dynamics of bubble formation and bursting at the water surface. Identifying the influence of these factors on the film-jet drop partition is of paramount importance to its inclusion in atmospheric models. With recent research suggesting that jet drops generate higher INPs concentrations than film drops [99], the inclusion of a film-jet drop partition scheme in spray aerosol emission parameterizations can improve model skill in predicting cloud process [268], especially in remote marine regions with little influence from anthropogenic INPs (e.g., Southern Ocean [269]).

Another avenue of research is to investigate if the droplet ejection pathway is a selection mechanism for the aerosolization of suspended particles from different regions in the water column, namely, surface versus bulk water. Due to physical differences in the ejection mechanism between film drops and jet drops, it has been suggested that film drops are enriched

with material from the surface microlayer whereas jet drops are enriched with material from bulk water [99]. This proposed research can further improve our understanding of bacterial cells (Chapter 4) and MPs (Chapter 5) aerosolization by breaking waves since both bacteria and MPs can reside in different regions in the water column. MPs, for instance, exhibit a density-dependent vertical distribution in the water column, with more dense particles found in the water subsurface, and less dense particles found on the water surface [256, 270]. Furthermore, potentially harmful bacterial species such as *Cyanobacteria* have the ability to regulate their buoyancy using gas vesicles to optimize access to light and nutrient sources [271, 272], which influences their vertical distribution in the water column. Therefore, a better understanding of the efficiency of each ejection pathway (i.e., film vs jet drop) in dispersing them to the air under various vertical distribution conditions is important to characterize their adverse implications on the environment and human respiratory health. It is proposed to carry such an investigation by building a spray aerosol pathway tank (SAPT) that can produce either exclusively film drops, exclusively jet drops, or a mixture of both. The SAPT design can be based on the experimental setup put forth by Wang et al. [99].

The modeling simulation in Chapter 3 was designed to test the newly developed LSA emission parameterization, however several other analyses could be conducted to better understand the effect of LSAs on regional aerosol loading and cloud processes. For instance, the inclusion of LSA chemical speciation [61] will enable the comparison between model PM concentrations and measurements from air quality monitoring sites in the region. Longer simulations covering the whole year can also uncover seasonal patters in LSA emissions. Specifically, it would be interesting to conduct a simulation that takes into account the effect of water temperature on LSA emissions as well as the Great Lakes ice coverage. The results of such a simulation would contrast LSA emissions during late spring and fall when wind speeds are higher and the Lakes are not covered by ice [59] to those during the winter season when a significant area of the Lakes is covered by ice and water temperature is much lower [273]. To better understand the influence of LSAs on regional cloud processes [47], a simulation incorporating aerosol-cloud interactions can also be conducted to provide more information about the changes in regional CCN and INPs concentrations in response to freshwater LSA emissions.

The emission of spray aerosols from the surf zone (i.e., the swell of the sea that breaks upon the shore [274]) and how it differs from open-water spray aerosol emission is another avenue

for future research. The experimental results in Chapter 2 show that the intermittency of air entrainmnet, which distinguishes surf-zone from open-water breaking waves, has distinctive impacts on the void fraction in the bubble plume. Therefore, the size characteristics of spray aerosols emitted from the surf zone might be different than those emitted from open-water braking waves. Moreover, SSA emissions from the surf zone have been shown to be enhanced relative to to those from the open ocean [275]. Incorporating these differences in the model representation of spray aerosol emissions is another direction for future research. Currently, CMAQ is the only atmospheric chemical transport model that distinguishes surf-zone from open-ocean SSA emissions. To increase SSA emissions from the surf zone relative to the open ocean, the CMAQ model treats the surf zone as a 25-m band of 100% whitecap coverage along the shoreline [147]. This representation is obviously simplistic and, hence, more studies are needed to better represent surf-zone emissions in models. Such a model representation is also warranted to better characterize pathogenic aerosolization from coastlines and their impacts on the respiratory health of affected communities. Brevetoxin, for instance, is a neurotoxin produced by the marine dinoflagellate species *Karenia brevis* which are native to the waters of the Gulf of Mexico. These species are associated with yearly HABs, also know as "red tides", occurring on Florida's gulf coast [276]. Due to wave breaking in the surf zone, Brevetoxin can be incorporated in SSAs [277] leading to coughing, shortness of breath, and a suite of other symptoms in the respiratory tract [278].

While this dissertation work was solely focused on spray aerosol ejection from breaking waves, there are other mechanisms that generate bursting surface bubbles in freshwater and saltwater [48]. Such mechanisms include, among others, gas production from microbial activity in sediments [279, 280], recreational boating [281], spillways [282], and aeration basins [283]. While spillways, for instance, generate bubbles in a comparable manner to air entrainment in breaking waves, moving boats can generate bubbles by propeller cavitation, breaking waves due to ship movement, and air entrapment in the boundary layer beneath the hull [284]. Therefore, understanding spray aerosol emission characteristics and patterns from such mechanisms and how they compare to air entrainment in breaking waves is another line of future research.

Bibliography

[1] Wave breaking, Jan 2012. URL https://glossary.ametsoc.org/wiki/Wave_breaking.

[2] George Biddell Airy. *Tides and waves*. B. Fellowes, 1845.

[3] George Gabriel Stokes. On the theory of oscillatory waves. *Transactions of the Cambridge Philosophical Society*, 8:441–455, 1847.

[4] Ian R Young. *Wind generated ocean waves*. Elsevier, 1999.

[5] HV Sverdrup and WH Munk. Wind waves and swell: Principles in forecasting. *Hydrographic Office, US Navy, Misc*, 11:275, 1944.

[6] HV Sverdrup and WH Munk. Breakers and surf : principles in forecasting, 1944.

[7] John W. Miles. On the generation of surface waves by shear flows. *Journal of Fluid Mechanics*, 3(2):185–204, 1957. doi: 10.1017/S0022112057000567.

[8] O. M. Phillips. On the generation of waves by turbulent wind. *Journal of Fluid Mechanics*, 2(5):417–445, 1957. doi: 10.1017/S0022112057000233.

[9] W. K. Melville. The instability and breaking of deep-water waves. *Journal of Fluid Mechanics*, 115:165–185, 1982. doi: 10.1017/S0022112082000706.

[10] J. H. Duncan and Michael Selwyn Longuet-Higgins. An experimental investigation of breaking waves produced by a towed hydrofoil. *Proceedings of the Royal Society of London. A. Mathematical and Physical Sciences*, 377(1770):331–348, 1981. doi: 10.1098/rspa.1981.0127. URL https://royalsocietypublishing.org/doi/abs/10.1098/rspa.1981.0127.

[11] James H. Duncan. The breaking and non-breaking wave resistance of a two-dimensional hydrofoil. *Journal of Fluid Mechanics*, 126:507–520, 1983. doi: 10.1017/S0022112083000294.

[12] Marc Perlin, Wooyoung Choi, and Zhigang Tian. Breaking waves in deep and intermediate waters. *Annual Review of Fluid Mechanics*, 45(1):115–145, 2013. doi: 10.1146/annurev-fluid-011212-140721. URL https://doi.org/10.1146/annurev-fluid-011212-140721.

[13] M L Banner and D H Peregrine. Wave breaking in deep water. *Annual Review of Fluid Mechanics*, 25(1):373–397, 1993. doi: 10.1146/annurev.fl.25.010193.002105. URL https://doi.org/10.1146/annurev.fl.25.010193.002105.

[14] W K Melville. The role of surface-wave breaking in air-sea interaction. *Annual Review of Fluid Mechanics*, 28(1):279–321, 1996. doi: 10.1146/annurev.fl.28.010196.001431. URL https://doi.org/10.1146/annurev.fl.28.010196.001431.

[15] Stephanie M King, Andrew C Butcher, Thomas Rosenoern, Esther Coz, Kirsten I Lieke, Gerrit De Leeuw, E Douglas Nilsson, and Merete Bilde. Investigating primary marine aerosol properties: Ccn activity of sea salt and mixed inorganic–organic particles. *Environmental science & technology*, 46(19):10405–10412, 2012. doi: 10.1021/es300574u.

[16] Fabrice Veron. Ocean spray. *Annual Review of Fluid Mechanics*, 47:507–538, 2015. doi: 10.1146/annurev-fluid-010814-014651.

[17] Luc Deike. Mass transfer at the ocean–atmosphere interface: The role of wave breaking, droplets, and bubbles. *Annual Review of Fluid Mechanics*, 54(1):191–224, 2022. doi: 10.1146/annurev-fluid-030121-014132. URL https://doi.org/10.1146/annurev-fluid-030121-014132.

[18] John Nicholas Newman. *Marine hydrodynamics*. The MIT press, 2018.

[19] Inigo J. Losada, Javier L. Lara, and Manuel del Jesus. Modeling the interaction of water waves with porous coastal structures. *Journal of Waterway, Port, Coastal, and Ocean Engineering*, 142(6):03116003, 2016. doi: 10.1061/(ASCE)WW.

1943-5460.0000361. URL https://ascelibrary.org/doi/abs/10.1061/%28ASCE%29WW.1943-5460.0000361.

[20] D V Evans. Power from water waves. *Annual Review of Fluid Mechanics*, 13(1): 157–187, 1981. doi: 10.1146/annurev.fl.13.010181.001105. URL https://doi.org/10.1146/annurev.fl.13.010181.001105.

[21] Woodrow C. Jacobs. Preliminary report on a study of atmospheric chlorides. *Monthly Weather Review*, 65(4):147 – 151, 1937. doi: 10.1175/1520-0493(1937)65⟨147:PROASO⟩2.0.CO;2. URL https://journals.ametsoc.org/view/journals/mwre/65/4/1520-0493_1937_65_147_proaso_2_0_co_2.xml.

[22] F. Knelman, N. Dombrowski, and D. M. Newitt. Mechanism of the bursting of bubbles. *Nature*, 173(4397):261–261, 1954. ISSN 1476-4687. doi: 10.1038/173261a0. URL https://doi.org/10.1038/173261a0.

[23] Gerrit De Leeuw, Edgar L Andreas, Magdalena D Anguelova, CW Fairall, Ernie R Lewis, Colin O'Dowd, Michael Schulz, and Stephen E Schwartz. Production flux of sea spray aerosol. *Reviews of Geophysics*, 49(2), 2011. doi: 10.1029/2010RG000349.

[24] C. Textor, M. Schulz, S. Guibert, S. Kinne, Y. Balkanski, S. Bauer, T. Berntsen, T. Berglen, O. Boucher, M. Chin, F. Dentener, T. Diehl, R. Easter, H. Feichter, D. Fillmore, S. Ghan, P. Ginoux, S. Gong, A. Grini, J. Hendricks, L. Horowitz, P. Huang, I. Isaksen, I. Iversen, S. Kloster, D. Koch, A. Kirkevåg, J. E. Kristjansson, M. Krol, A. Lauer, J. F. Lamarque, X. Liu, V. Montanaro, G. Myhre, J. Penner, G. Pitari, S. Reddy, Ø. Seland, P. Stier, T. Takemura, and X. Tie. Analysis and quantification of the diversities of aerosol life cycles within aerocom. *Atmospheric Chemistry and Physics*, 6(7):1777–1813, 2006. doi: 10.5194/acp-6-1777-2006. URL https://acp.copernicus.org/articles/6/1777/2006/.

[25] Andrew P. Ault, Timothy L. Guasco, Jonas Baltrusaitis, Olivia S. Ryder, Jonathan V. Trueblood, Douglas B. Collins, Matthew J. Ruppel, Luis A. Cuadra-Rodriguez, Kimberly A. Prather, and Vicki H. Grassian. Heterogeneous reactivity of nitric acid with nascent sea spray aerosol: Large differences observed between and within individual particles. *The Journal of Physical Chemistry Letters*, 5(15):2493–2500, 2014. doi: 10.1021/jz5008802. URL https://doi.org/10.1021/jz5008802. PMID: 26277935.

[26] M.O. Andreae and D. Rosenfeld. Aerosol–cloud–precipitation interactions. part 1. the nature and sources of cloud-active aerosols. *Earth-Science Reviews*, 89(1):13–41, 2008. ISSN 0012-8252. doi: https://doi.org/10.1016/j.earscirev.2008.03.001. URL https://www.sciencedirect.com/science/article/pii/S0012825208000317.

[27] R. Lewis and E. Schwartz. *Sea Salt Aerosol Production: Mechanisms, Methods, Measurements and Models*, volume 152 of *Geophysical Monograph Series*. American Geophysical Union, Washington, D. C., 2004. ISBN 0-87590-417-3. doi: 10.1029/GM152. URL http://www.agu.org/books/gm/v152/.

[28] PK Quinn, DJ Coffman, JE Johnson, LM Upchurch, and TS Bates. Small fraction of marine cloud condensation nuclei made up of sea spray aerosol. *Nature Geoscience*, 10 (9):674–679, 2017.

[29] Graham Feingold, William R. Cotton, Sonia M. Kreidenweis, and Janel T. Davis. The impact of giant cloud condensation nuclei on drizzle formation in stratocumulus: Implications for cloud radiative properties. *Journal of the Atmospheric Sciences*, 56(24):4100 – 4117, 1999. doi: 10.1175/1520-0469(1999)056⟨4100:TIOGCC⟩2.0.CO;2. URL https://journals.ametsoc.org/view/journals/atsc/56/24/1520-0469_1999_056_4100_tiogcc_2.0.co_2.xml.

[30] John Latham. Control of global warming? *Nature*, 347(6291):339–340, 1990.

[31] John Latham. Amelioration of global warming by controlled enhancement of the albedo and longevity of low-level maritime clouds. *Atmospheric Science Letters*, 3(2):52–58, 2002. ISSN 1530-261X. doi: https://doi.org/10.1006/asle.2002.0048. URL https://www.sciencedirect.com/science/article/pii/S1530261X02900484.

[32] Hannah M. Horowitz, Christopher Holmes, Alicia Wright, Tomás Sherwen, Xuan Wang, Mat Evans, Jiayue Huang, Lyatt Jaeglé, Qianjie Chen, Shuting Zhai, and Becky Alexander. Effects of sea salt aerosol emissions for marine cloud brightening on atmospheric chemistry: Implications for radiative forcing. *Geophysical Research Letters*, 47(4):e2019GL085838, 2020. doi: https://doi.org/10.1029/2019GL085838. URL https://agupubs.onlinelibrary.wiley.com/doi/abs/10.1029/2019GL085838. e2019GL085838 2019GL085838.

[33] Colin D O'Dowd and Gerrit de Leeuw. Marine aerosol production: a review of the current knowledge. *Philosophical Transactions of the Royal Society A: Mathematical, Physical and Engineering Sciences*, 365(1856):1753–1774, 2007. doi: 10.1098/rsta.2007.2043. URL https://royalsocietypublishing.org/doi/abs/10.1098/rsta.2007.2043.

[34] Alyssa N. Alsante, Daniel C. O. Thornton, and Sarah D. Brooks. Ocean aerobiology. *Frontiers in Microbiology*, 12, 2021. ISSN 1664-302X. doi: 10.3389/fmicb.2021.764178. URL https://www.frontiersin.org/article/10.3389/fmicb.2021.764178.

[35] Nathaniel W May, Jessica L Axson, Alexa Watson, Kerri A Pratt, and Andrew P Ault. Lake spray aerosol generation: a method for producing representative particles from freshwater wave breaking. *Atmospheric Measurement Techniques*, 9(9):4311–4325, 2016. doi: 10.5194/amt-9-4311-2016.

[36] J. H. Slade, T. M. VanReken, G. R. Mwaniki, S. Bertman, B. Stirm, and P. B. Shepson. Aerosol production from the surface of the great lakes. *Geophysical Research Letters*, 37(18), 2010. doi: https://doi.org/10.1029/2010GL043852. URL https://agupubs.onlinelibrary.wiley.com/doi/abs/10.1029/2010GL043852.

[37] Nathaniel W May, Nicole E Olson, Mark Panas, Jessica L Axson, Peter S Tirella, Rachel M Kirpes, Rebecca L Craig, Matthew J Gunsch, Swarup China, Alexander Laskin, et al. Aerosol emissions from great lakes harmful algal blooms. *Environmental science & technology*, 52(2):397–405, 2017. doi: 10.1021/acs.est.7b03609.

[38] Nicole E. Olson, Madeline E. Cooke, Jia H. Shi, Johnna A. Birbeck, Judy A. Westrick, and Andrew P. Ault. Harmful algal bloom toxins in aerosol generated from inland lake water. *Environmental Science & Technology*, 54(8):4769–4780, 2020. doi: 10.1021/acs.est.9b07727. URL https://doi.org/10.1021/acs.est.9b07727. PMID: 32186187.

[39] Magdalena Anguelova and Pablo Huq. Effects of salinity on bubble cloud characteristics. *Journal of Marine Science and Engineering*, 6(1):1, 2017. doi: 10.3390/jmse6010001.

[40] CE Blenkinsopp and JR Chaplin. Void fraction measurements and scale effects in

breaking waves in freshwater and seawater. *Coastal Engineering*, 58(5):417–428, 2011. doi: 10.1016/j.coastaleng.2010.12.006.

[41] John C Scott. The role of salt in whitecap persistence. *Deep Sea Research and Oceanographic Abstracts*, 22(10):653–657, 1975. doi: 10.1016/0011-7471(75)90002-9.

[42] Steven C. Chapra, Alice Dove, and Glenn J. Warren. Long-term trends of great lakes major ion chemistry. *Journal of Great Lakes Research*, 38(3):550–560, 2012. ISSN 0380-1330. doi: https://doi.org/10.1016/j.jglr.2012.06.010. URL https://www.sciencedirect.com/science/article/pii/S0380133012001384.

[43] Michael E. Q. Pilson. *An Introduction to the Chemistry of the Sea*. Cambridge University Press, 2 edition, 2012. doi: 10.1017/CBO9781139047203.

[44] Edward C Monahan and Carl R Zietlow. Laboratory comparisons of fresh-water and salt-water whitecaps. *Journal of Geophysical Research*, 74(28):6961–6966, 1969. doi: 10.1029/JC074i028p06961.

[45] Meredith A Haines and Bruce D Johnson. Injected bubble populations in seawater and fresh water measured by a photographic method. *Journal of Geophysical Research: Oceans*, 100(C4):7057–7068, 1995. doi: 10.1029/94JC03226.

[46] EDWARD C Monahan. Fresh water whitecaps. *Journal of the Atmospheric Sciences*, 26(5):1026–1029, 1969. doi: 10.1175/1520-0469(1969)026⟨1026:FWW⟩2.0.CO;2.

[47] Nicole E. Olson, Nathaniel W. May, Rachel M. Kirpes, Alexa E. Watson, Kristian D. Hajny, Jonathan H. Slade, Paul B. Shepson, Brian H. Stirm, Kerri A. Pratt, and Andrew P. Ault. Lake spray aerosol incorporated into great lakes clouds. *ACS Earth and Space Chemistry*, 3(12):2765–2774, 2019. doi: 10.1021/acsearthspacechem.9b00258. URL https://doi.org/10.1021/acsearthspacechem.9b00258.

[48] Haley E. Plaas and Hans W. Paerl. Toxic cyanobacteria: A growing threat to water and air quality. *Environmental Science & Technology*, 55(1):44–64, 2021. doi: 10.1021/acs.est.0c06653. URL https://doi.org/10.1021/acs.est.0c06653. PMID: 33334098.

[49] Edward C Monahan, Donald E Spiel, and Kenneth L Davidson. A model of marine aerosol generation via whitecaps and wave disruption. In *Oceanic whitecaps*, pages 167–174. Springer, 1986.

[50] Adrian Callaghan, Gerrit de Leeuw, Leo Cohen, and Colin D. O'Dowd. Relationship of oceanic whitecap coverage to wind speed and wind history. *Geophysical Research Letters*, 35(23), 2008. doi: https://doi.org/10.1029/2008GL036165. URL https://agupubs.onlinelibrary.wiley.com/doi/abs/10.1029/2008GL036165.

[51] Magdalena D. Anguelova and Ferris Webster. Whitecap coverage from satellite measurements: A first step toward modeling the variability of oceanic whitecaps. *Journal of Geophysical Research: Oceans*, 111(C3), 2006. doi: https://doi.org/10.1029/2005JC003158. URL https://agupubs.onlinelibrary.wiley.com/doi/abs/10.1029/2005JC003158.

[52] Edward C. Monahan and IognáidÓ Muircheartaigh. Optimal power-law description of oceanic whitecap coverage dependence on wind speed. *Journal of Physical Oceanography*, 10(12):2094 – 2099, 1980. doi: 10.1175/1520-0485(1980)010⟨2094:OPLDOO⟩2.0.CO;2. URL https://journals.ametsoc.org/view/journals/phoc/10/12/1520-0485_1980_010_2094_opldoo_2_0_co_2.xml.

[53] EM Mårtensson, ED Nilsson, Gerrit de Leeuw, LH Cohen, and H-C Hansson. Laboratory simulations and parameterization of the primary marine aerosol production. *Journal of Geophysical Research: Atmospheres*, 108(D9), 2003. doi: 10.1029/2002JD002263.

[54] Sigurd Christiansen, Matthew E. Salter, Elena Gorokhova, Quynh T. Nguyen, and Merete Bilde. Sea spray aerosol formation: Laboratory results on the role of air entrainment, water temperature, and phytoplankton biomass. *Environmental Science & Technology*, 53(22):13107–13116, 2019. doi: 10.1021/acs.est.9b04078. URL https://doi.org/10.1021/acs.est.9b04078. PMID: 31633921.

[55] S. D. Forestieri, K. A. Moore, R. Martinez Borrero, A. Wang, M. D. Stokes, and C. D. Cappa. Temperature and composition dependence of sea spray aerosol production. *Geophysical Research Letters*, 45(14):7218–7225, 2018. doi: https://doi.org/10.1029/2018GL078193. URL https://agupubs.onlinelibrary.wiley.com/doi/abs/10.1029/2018GL078193.

[56] Matthew E Salter, E Douglas Nilsson, A Butcher, and Merete Bilde. On the seawater temperature dependence of the sea spray aerosol generated by a continuous plunging

jet. *Journal of Geophysical Research: Atmospheres*, 119(14):9052–9072, 2014. doi: 10.1002/2013JD021376.

[57] Peter A. Alpert, Wendy P. Kilthau, Dylan W. Bothe, JoAnn C. Radway, Josephine Y. Aller, and Daniel A. Knopf. The influence of marine microbial activities on aerosol production: A laboratory mesocosm study. *Journal of Geophysical Research: Atmospheres*, 120(17):8841–8860, 2015. doi: https://doi.org/10.1002/2015JD023469. URL https://agupubs.onlinelibrary.wiley.com/doi/abs/10.1002/2015JD023469.

[58] L. Jaeglé, P. K. Quinn, T. S. Bates, B. Alexander, and J.-T. Lin. Global distribution of sea salt aerosols: new constraints from in situ and remote sensing observations. *Atmospheric Chemistry and Physics*, 11(7):3137–3157, 2011. doi: 10.5194/acp-11-3137-2011. URL https://acp.copernicus.org/articles/11/3137/2011/.

[59] SH Chung, BM Basarab, and TM VanReken. Regional impacts of ultrafine particle emissions from the surface of the great lakes. *Atmospheric Chemistry and Physics*, 11 (24):12601–12615, 2011. doi: 10.5194/acp-11-12601-2011.

[60] Michael Geever, Colin D. O'Dowd, Stefan van Ekeren, Robert Flanagan, E. Douglas Nilsson, Gerrit de Leeuw, and Üllar Rannik. Submicron sea spray fluxes. *Geophysical Research Letters*, 32(15), 2005. doi: https://doi.org/10.1029/2005GL023081. URL https://agupubs.onlinelibrary.wiley.com/doi/abs/10.1029/2005GL023081.

[61] Anahita Amiri-Farahani, Nicole E. Olson, David Neubauer, Behrooz Roozitalab, Andrew P. Ault, and Allison L. Steiner. Lake spray aerosol emissions alter nitrogen partitioning in the great lakes region. *Geophysical Research Letters*, 48(12):e2021GL093727, 2021. doi: https://doi.org/10.1029/2021GL093727. URL https://agupubs.onlinelibrary.wiley.com/doi/abs/10.1029/2021GL093727. e2021GL093727 2021GL093727.

[62] Jamie M. Schiffer, Liora E. Mael, Kimberly A. Prather, Rommie E. Amaro, and Vicki H. Grassian. Sea spray aerosol: Where marine biology meets atmospheric chemistry. *ACS Central Science*, 4(12):1617–1623, 2018. doi: 10.1021/acscentsci.8b00674. URL https://doi.org/10.1021/acscentsci.8b00674. PMID: 30648145.

[63] Joseph P. Patterson, Douglas B. Collins, Jennifer M. Michaud, Jessica L. Axson, Camile M. Sultana, Trevor Moser, Abigail C. Dommer, Jack Conner, Vicki H. Grassian, M. Dale Stokes, Grant B. Deane, James E. Evans, Michael D. Burkart, Kimberly A. Prather, and Nathan C. Gianneschi. Sea spray aerosol structure and composition using cryogenic transmission electron microscopy. *ACS Central Science*, 2 (1):40–47, 2016. doi: 10.1021/acscentsci.5b00344. URL https://doi.org/10.1021/acscentsci.5b00344. PMID: 26878061.

[64] Patricia K. Quinn, Douglas B. Collins, Vicki H. Grassian, Kimberly A. Prather, and Timothy S. Bates. Chemistry and related properties of freshly emitted sea spray aerosol. *Chemical Reviews*, 115(10):4383–4399, 2015. doi: 10.1021/cr500713g. URL https://doi.org/10.1021/cr500713g. PMID: 25844487.

[65] E. R. Baylor, M. B. Baylor, Duncan C. Blanchard, Lawrence D. Syzdek, and Curtis Appel. Virus transfer from surf to wind. *Science*, 198(4317):575–580, 1977. doi: 10.1126/science.918656. URL https://www.science.org/doi/abs/10.1126/science.918656.

[66] Duncan C. Blanchard and Lawrence D. Syzdek. Water-to-air transfer and enrichment of bacteria in drops from bursting bubbles. *Applied and Environmental Microbiology*, 43(5):1001–1005, 1982. doi: 10.1128/aem.43.5.1001-1005.1982. URL https://journals.asm.org/doi/abs/10.1128/aem.43.5.1001-1005.1982.

[67] T. W. Hejkal, P. A. LaRock, and J. W. Winchester. Water-to-air fractionation of bacteria. *Applied and Environmental Microbiology*, 39(2):335–338, 1980. doi: 10.1128/aem.39.2.335-338.1980. URL https://journals.asm.org/doi/abs/10.1128/aem.39.2.335-338.1980.

[68] Jennifer M Michaud, Luke R Thompson, Drishti Kaul, Josh L Espinoza, R Alexander Richter, Zhenjiang Zech Xu, Christopher Lee, Kevin M Pham, Charlotte M Beall, Francesca Malfatti, et al. Taxon-specific aerosolization of bacteria and viruses in an experimental ocean-atmosphere mesocosm. *Nature communications*, 9(1):1–10, 2018.

[69] Nima Afshar-Mohajer, Cheng Li, Ana M. Rule, Joseph Katz, and Kirsten Koehler. A laboratory study of particulate and gaseous emissions from crude oil and crude

oil-dispersant contaminated seawater due to breaking waves. *Atmospheric Environment*, 179:177–186, 2018. ISSN 1352-2310. doi: https://doi.org/10.1016/j.atmosenv.2018.02.017. URL https://www.sciencedirect.com/science/article/pii/S135223101830089X.

[70] Bo Sha, Jana H. Johansson, Jonathan P. Benskin, Ian T. Cousins, and Matthew E. Salter. Influence of water concentrations of perfluoroalkyl acids (pfaas) on their size-resolved enrichment in nascent sea spray aerosols. *Environmental Science & Technology*, 55(14):9489–9497, 2021. doi: 10.1021/acs.est.0c03804. URL https://doi.org/10.1021/acs.est.0c03804. PMID: 32859129.

[71] Steve Allen, Deonie Allen, Kerry Moss, Gaël Le Roux, Vernon R. Phoenix, and Jeroen E. Sonke. Examination of the ocean as a source for atmospheric microplastics. *PLOS ONE*, 15(5):1–14, 05 2020. doi: 10.1371/journal.pone.0232746. URL https://doi.org/10.1371/journal.pone.0232746.

[72] Catherine A. Lozupone and Rob Knight. Global patterns in bacterial diversity. *Proceedings of the National Academy of Sciences*, 104(27):11436–11440, 2007. doi: 10.1073/pnas.0611525104. URL https://www.pnas.org/doi/abs/10.1073/pnas.0611525104.

[73] Ralph F Keeling. On the role of large bubbles in air-sea gas exchange and supersaturation in the ocean. *Journal of Marine Research*, 51(2):237–271, 1993. doi: 10.1357/0022240933223800.

[74] R Frouin, SF Iacobellis, and P-Y Deschamps. Influence of oceanic whitecaps on the global radiation budget. *Geophysical research letters*, 28(8):1523–1526, 2001. doi: 10.1029/2000GL012657.

[75] Magdalena Anguelova and Pablo Huq. Effects of salinity on surface lifetime of large individual bubbles. *Journal of Marine Science and Engineering*, 5(3):41, 2017. doi: 10.3390/jmse5030041.

[76] AH Callaghan, MD Stokes, and GB Deane. The effect of water temperature on air entrainment, bubble plumes, and surface foam in a laboratory breaking-wave analog.

Journal of Geophysical Research: Oceans, 119(11):7463–7482, 2014. doi: 10.1002/2014JC010351.

[77] AH Callaghan, GB Deane, and MD Stokes. On the imprint of surfactant-driven stabilization of laboratory breaking wave foam with comparison to oceanic whitecaps. *Journal of Geophysical Research: Oceans*, 122(8):6110–6128, 2017. doi: 10.1002/2017JC012809.

[78] David K Woolf and SA Thorpe. Bubbles and the air-sea exchange of gases in near-saturation conditions. *Journal of Marine Research*, 49(3):435–466, 1991. doi: 10.1357/002224091784995765.

[79] Timothy P Boyer, S Levitus, JI Antonov, RA Locarnini, and HE Garcia. Linear trends in salinity for the world ocean, 1955–1998. *Geophysical Research Letters*, 32(1), 2005. doi: 10.1029/2004GL021791.

[80] Paul J Durack, Susan E Wijffels, and Richard J Matear. Ocean salinities reveal strong global water cycle intensification during 1950 to 2000. *science*, 336(6080):455–458, 2012. doi: 10.1126/science.1212222.

[81] Nathaniel W May, Matthew J Gunsch, Nicole E Olson, Amy L Bondy, Rachel M Kirpes, Steven B Bertman, Swarup China, Alexander Laskin, Philip K Hopke, Andrew P Ault, et al. Unexpected contributions of sea spray and lake spray aerosol to inland particulate matter. *Environmental Science & Technology Letters*, 5(7):405–412, 2018. doi: 10.1021/acs.estlett.8b00254.

[82] John W Cartmill and Ming Yang Su. Bubble size distribution under saltwater and freshwater breaking waves. *Dynamics of atmospheres and oceans*, 20(1-2):25–31, 1993. doi: 10.1016/0377-0265(93)90046-A.

[83] MR Loewen, MA O'Dor, and MG Skafel. Bubbles entrained by mechanically generated breaking waves. *Journal of Geophysical Research: Oceans*, 101(C9):20759–20769, 1996. doi: 10.1029/96JC01919.

[84] U Hofmeier, VV Yaminsky, and HK Christenson. Observations of solute effects on bubble formation. *Journal of colloid and interface science*, 174(1):199–210, 1995. doi: 10.1006/jcis.1995.1383.

[85] David E Slauenwhite and Bruce D Johnson. Bubble shattering: Differences in bubble formation in fresh water and seawater. *Journal of Geophysical Research: Oceans*, 104 (C2):3265–3275, 1999. doi: 10.1029/1998JC900064.

[86] Jin Wu. Bubbles produced by breaking waves in fresh and salt waters. *Journal of Physical Oceanography*, 30(7):1809–1813, 2000. doi: 10.1175/1520-0485(2000)030⟨1809: BPBBWI⟩2.0.CO;2.

[87] H. Chanson, S. Aoki, and A. Hoque. Bubble Entrainment and Dispersion in Plunging Jet Flows: Freshwater vs. Seawater . *Journal of Coastal Research*, 223:664–677, jul 2006. ISSN 0749-0208. doi: 10.2112/03-0112.1.

[88] William M Carey, James W Fitzgerald, Edward C Monahan, and Qin Wang. Measurement of the sound produced by a tipping trough with fresh and salt water. *The Journal of the Acoustical Society of America*, 93(6):3178–3192, 1993. doi: 10.1121/1.405702.

[89] Rodney D Peltzer and Owen M Griffin. Stability of a three-dimensional foam layer in seawater. *Journal of Geophysical Research: Oceans*, 93(C9):10804–10812, 1988. doi: 10.1029/JC093iC09p10804.

[90] MD Stokes, GB Deane, K Prather, TH Bertram, MJ Ruppel, OS Ryder, JM Brady, and D Zhao. A marine aerosol reference tank system as a breaking wave analogue for the production of foam and sea-spray aerosols. *Atmospheric measurement techniques*, 6(4):1085–1094, 2013. doi: 10.5194/amt-6-1085-2013.

[91] M Dale Stokes, Grant Deane, Douglas B Collins, Christopher Cappa, Timothy Bertram, Abigail Dommer, Steven Schill, Sara Forestieri, and Mathew Survilo. A miniature marine aerosol reference tank (minimart) as a compact breaking wave analogue. *Atmospheric Measurement Techniques*, 9(9):4257–4267, 2016. doi: 10.5194/amt-9-4257-2016.

[92] Grant B Deane and M Dale Stokes. Scale dependence of bubble creation mechanisms in breaking waves. *Nature*, 418(6900):839, 2002. doi: 10.1038/nature00967.

[93] C Li, J Miller, J Wang, SS Koley, and J Katz. Size distribution and dispersion of droplets generated by impingement of breaking waves on oil slicks. *Journal of Geophysical Research: Oceans*, 122(10):7938–7957, 2017. doi: 10.1002/2017JC013193.

[94] E Fuentes, H Coe, D Green, G de Leeuw, and G McFiggans. Laboratory-generated primary marine aerosol via bubble-bursting and atomization. *Atmospheric Measurement Techniques*, 3(1):141–162, 2010. doi: 10.5194/amt-3-141-2010.

[95] Kenneth T Kiger and James H Duncan. Air-entrainment mechanisms in plunging jets and breaking waves. *Annual Review of Fluid Mechanics*, 44:563–596, 2012. doi: 10.1146/annurev-fluid-122109-160724.

[96] William E Asher and Paul J Farley. Phase-doppler anemometer measurement of bubble concentrations in laboratory-simulated breaking waves. *Journal of Geophysical Research: Oceans*, 100(C4):7045–7056, 1995. doi: 10.1029/95JC00068.

[97] Caroline A Schneider, Wayne S Rasband, and Kevin W Eliceiri. Nih image to imagej: 25 years of image analysis. *Nature methods*, 9(7):671, 2012. doi: 10.1038/nmeth.2089.

[98] Kim AH Hultin, E Douglas Nilsson, Radovan Krejci, E Monica Mårtensson, Mikael Ehn, Åke Hagström, and Gerrit de Leeuw. In situ laboratory sea spray production during the marine aerosol production 2006 cruise on the northeastern atlantic ocean. *Journal of Geophysical Research: Atmospheres*, 115(D6), 2010. doi: 10.1029/2009JD012522.

[99] Xiaofei Wang, Grant B Deane, Kathryn A Moore, Olivia S Ryder, M Dale Stokes, Charlotte M Beall, Douglas B Collins, Mitchell V Santander, Susannah M Burrows, Camille M Sultana, et al. The role of jet and film drops in controlling the mixing state of submicron sea spray aerosol particles. *Proceedings of the National Academy of Sciences*, 114(27):6978–6983, 2017. doi: 10.1073/pnas.1702420114.

[100] Jin Wu. Bubbles in the near-surface ocean: A general description. *Journal of Geophysical Research: Oceans*, 93(C1):587–590, 1988. doi: 10.1029/JC093iC01p00587.

[101] Henri Lhuissier and Emmanuel Villermaux. Bursting bubble aerosols. *Journal of Fluid Mechanics*, 696:5–44, 2012. doi: 10.1017/jfm.2011.418.

[102] SA Thorpe, TR Osborn, DM Farmer, and S Vagle. Bubble clouds and langmuir circulation: observations and models. *Journal of Physical Oceanography*, 33(9):2013–2031, 2003. doi: 10.1175/1520-0485(2003)033⟨2013:BCALCO⟩2.0.CO;2.

[103] Emilie Forel, Benjamin Dollet, Dominique Langevin, and Emmanuelle Rio. Coalescence in two-dimensional foams: A purely statistical process dependent on film area. *Physical Review Letters*, 122(8):088002, 2019. doi: 10.1103/PhysRevLett.122.088002.

[104] Arnaud Saint-Jalmes. Physical chemistry in foam drainage and coarsening. *Soft Matter*, 2(10):836–849, 2006. doi: 10.1039/b606780h.

[105] DB Collins, DF Zhao, MJ Ruppel, O Laskina, JR Grandquist, RL Modini, MD Stokes, LM Russell, TH Bertram, VH Grassian, et al. Direct aerosol chemical composition measurements to evaluate the physicochemical differences between controlled sea spray aerosol generation schemes. *Atmospheric measurement techniques*, 7(11):3667–3683, 2014. doi: 10.5194/amt-7-3667-2014.

[106] Ira Leifer and Gerrit De Leeuw. Bubbles generated from wind-steepened breaking waves: 1. bubble plume bubbles. *Journal of Geophysical Research: Oceans*, 111(C6), 2006. doi: 10.1029/2004JC002673.

[107] Ira Leifer, Guillemette Caulliez, and Gerrit De Leeuw. Bubbles generated from wind-steepened breaking waves: 2. bubble plumes, bubbles, and wave characteristics. *Journal of Geophysical Research: Oceans*, 111(C6), 2006. doi: 10.1029/2004JC002676.

[108] HK Christenson, RE Bowen, JA Carlton, JRM Denne, and Y Lu. Electrolytes that show a transition to bubble coalescence inhibition at high concentrations. *The Journal of Physical Chemistry C*, 112(3):794–796, 2008. doi: 10.1021/jp075440s.

[109] Christine L Henry, Casuarina N Dalton, Lehoa Scruton, and Vincent SJ Craig. Ion-specific coalescence of bubbles in mixed electrolyte solutions. *The Journal of Physical Chemistry C*, 111(2):1015–1023, 2007. doi: 10.1021/jp066400b.

[110] Yonggang Zhu, Hasan N Oğuz, and Andrea Prosperetti. On the mechanism of air entrainment by liquid jets at a free surface. *Journal of Fluid Mechanics*, 404:151–177, 2000. doi: 10.1017/S0022112099007090.

[111] Emil D Manev and Anh V Nguyen. Critical thickness of microscopic thin liquid films. *Advances in Colloid and Interface Science*, 114:133–146, 2005. doi: 10.1016/j.cis.2004.07.013.

[112] JE Coons, PJ Halley, SA McGlashan, and T Tran-Cong. Bounding film drainage in common thin films. *Colloids and Surfaces A: Physicochemical and Engineering Aspects*, 263(1-3):197–204, 2005. doi: 10.1016/j.colsurfa.2005.01.009.

[113] S Poulain, E Villermaux, and L Bourouiba. Ageing and burst of surface bubbles. *Journal of Fluid Mechanics*, 851:636–671, 2018. doi: 10.1017/jfm.2018.471.

[114] Jessica L. Axson, Nathaniel W. May, Isabel D. Colón-Bernal, Kerri A. Pratt, and Andrew P. Ault. Lake spray aerosol: A chemical signature from individual ambient particles. *Environmental Science & Technology*, 50(18):9835–9845, 2016. doi: 10.1021/acs.est.6b01661. URL https://doi.org/10.1021/acs.est.6b01661. PMID: 27548099.

[115] Charbel Harb, Jin Pan, Stephen DeVilbiss, Brian Badgley, Linsey C. Marr, David G. Schmale, and Hosein Foroutan. Increasing freshwater salinity impacts aerosolized bacteria. *Environmental Science & Technology*, 55(9):5731–5741, 2021. doi: 10.1021/acs.est.0c08558. URL https://doi.org/10.1021/acs.est.0c08558. PMID: 33819033.

[116] Charbel Harb and Hosein Foroutan. A systematic analysis of the salinity effect on air bubbles evolution: Laboratory experiments in a breaking wave analog. *Journal of Geophysical Research: Oceans*, 124(11):7355–7374, 2019. doi: https://doi.org/10.1029/2019JC015337. URL https://agupubs.onlinelibrary.wiley.com/doi/abs/10.1029/2019JC015337.

[117] Stefan Barthel, Ina Tegen, and Ralf Wolke. Do new sea spray aerosol source functions improve the results of a regional aerosol model? *Atmospheric Environment*, 198:265–278, 2019. ISSN 1352-2310. doi: https://doi.org/10.1016/j.atmosenv.2018.10.016. URL https://www.sciencedirect.com/science/article/pii/S1352231018307064.

[118] H. Grythe, J. Ström, R. Krejci, P. Quinn, and A. Stohl. A review of sea-spray aerosol source functions using a large global set of sea salt aerosol concentration measurements. *Atmospheric Chemistry and Physics*, 14(3):1277–1297, 2014. doi: 10.5194/acp-14-1277-2014. URL https://acp.copernicus.org/articles/14/1277/2014/.

[119] M. E. Salter, P. Zieger, J. C. Acosta Navarro, H. Grythe, A. Kirkevåg, B. Rosati, I. Riipinen, and E. D. Nilsson. An empirically derived inorganic sea spray source

function incorporating sea surface temperature. *Atmospheric Chemistry and Physics*, 15(19):11047–11066, 2015. doi: 10.5194/acp-15-11047-2015. URL https://acp.copernicus.org/articles/15/11047/2015/.

[120] Mikhail Sofiev, Joana Soares, Marje Prank, Gerrit de Leeuw, and Jaakko Kukkonen. A regional-to-global model of emission and transport of sea salt particles in the atmosphere. *Journal of Geophysical Research: Atmospheres*, 116(D21), 2011. doi: https://doi.org/10.1029/2010JD014713. URL https://agupubs.onlinelibrary.wiley.com/doi/abs/10.1029/2010JD014713.

[121] J. Ovadnevaite, A. Manders, G. de Leeuw, D. Ceburnis, C. Monahan, A.-I. Partanen, H. Korhonen, and C. D. O'Dowd. A sea spray aerosol flux parameterization encapsulating wave state. *Atmospheric Chemistry and Physics*, 14(4):1837–1852, 2014. doi: 10.5194/acp-14-1837-2014. URL https://acp.copernicus.org/articles/14/1837/2014/.

[122] Kathryn J. Mayer, Jon S. Sauer, Julie Dinasquet, and Kimberly A. Prather. Caice studies: Insights from a decade of ocean–atmosphere experiments in the laboratory. *Accounts of Chemical Research*, 53(11):2510–2520, 2020. doi: 10.1021/acs.accounts.0c00504. URL https://doi.org/10.1021/acs.accounts.0c00504. PMID: 33086794.

[123] Andrew D. Gronewold, Vincent Fortin, Brent Lofgren, Anne Clites, Craig A. Stow, and Frank Quinn. Coasts, water levels, and climate change: A great lakes perspective. *Climatic Change*, 120(4):697–711, 2013. ISSN 1573-1480. doi: 10.1007/s10584-013-0840-2. URL https://doi.org/10.1007/s10584-013-0840-2.

[124] Josée Méthot, Xiyu Huang, and Himanshu Grover. Demographics and societal values as drivers of change in the great lakes–st. lawrence river basin. *Journal of Great Lakes Research*, 41:30–44, 2015. ISSN 0380-1330. doi: https://doi.org/10.1016/j.jglr.2014.11.001. URL https://www.sciencedirect.com/science/article/pii/S0380133014002123. The Great Lakes Futures Project: Using Scenario Analysis to Develop a Sustainable Socio-ecologic Vision for the Great Lakes-St. Lawrence River Basin.

[125] Donald Wuebbles, B Cardinale, K Cherkauer, R Davidson-Arnott, J Hellmann, D Infante, and A Ballinger. An assessment of the impacts of climate change on the great lakes. *Environmental Law & Policy Center*, 2019.

[126] Robert W. Sterner, Peggy Ostrom, Nathaniel E. Ostrom, J. Val Klump, Alan D. Steinman, Erin A. Dreelin, M. Jake Vander Zanden, and Aaron T. Fisk. Grand challenges for research in the laurentian great lakes. *Limnology and Oceanography*, 62(6):2510–2523, 2017. doi: https://doi.org/10.1002/lno.10585. URL https://aslopubs.onlinelibrary.wiley.com/doi/abs/10.1002/lno.10585.

[127] Kimberly A. Prather, Timothy H. Bertram, Vicki H. Grassian, Grant B. Deane, M. Dale Stokes, Paul J. DeMott, Lihini I. Aluwihare, Brian P. Palenik, Farooq Azam, John H. Seinfeld, Ryan C. Moffet, Mario J. Molina, Christopher D. Cappa, Franz M. Geiger, Gregory C. Roberts, Lynn M. Russell, Andrew P. Ault, Jonas Baltrusaitis, Douglas B. Collins, Craig E. Corrigan, Luis A. Cuadra-Rodriguez, Carlena J. Ebben, Sara D. Forestieri, Timothy L. Guasco, Scott P. Hersey, Michelle J. Kim, William F. Lambert, Robin L. Modini, Wilton Mui, Byron E. Pedler, Matthew J. Ruppel, Olivia S. Ryder, Nathan G. Schoepp, Ryan C. Sullivan, and Defeng Zhao. Bringing the ocean into the laboratory to probe the chemical complexity of sea spray aerosol. *Proceedings of the National Academy of Sciences*, 110(19):7550–7555, 2013. doi: 10.1073/pnas.1300262110. URL https://www.pnas.org/doi/abs/10.1073/pnas.1300262110.

[128] A. Khlystov, C. Stanier, and S. N. Pandis. An algorithm for combining electrical mobility and aerodynamic size distributions data when measuring ambient aerosol special issue of aerosol science and technology on findings from the fine particulate matter supersites program. *Aerosol Science and Technology*, 38(sup1):229–238, 2004. doi: 10.1080/02786820390229543. URL https://doi.org/10.1080/02786820390229543.

[129] Ryan C. Moffet, Xueying Qin, Thomas Rebotier, Hiroshi Furutani, and Kimberly A. Prather. Chemically segregated optical and microphysical properties of ambient aerosols measured in a single-particle mass spectrometer. *Journal of Geophysical Research: Atmospheres*, 113(D12), 2008. doi: https://doi.org/10.1029/2007JD009393. URL https://agupubs.onlinelibrary.wiley.com/doi/abs/10.1029/2007JD009393.

[130] Edward C Monahan and Adrian H Callaghan. The discrete whitecap method for estimating sea salt aerosol generation: A reassessment. In *17th conference on atmospheric chemistry*, 2015.

[131] Edward C. Monahan. Oceanic whitecaps. *Journal of Physical Oceanography*, 1(2):139 – 144, 1971. doi: 10.1175/1520-0485(1971)001⟨0139:OW⟩2.0.CO;2. URL https://journals.ametsoc.org/view/journals/phoc/1/2/1520-0485_1971_001_0139_ow_2_0_co_2.xml.

[132] Marina E. Quadros and Linsey C. Marr. Silver nanoparticles and total aerosols emitted by nanotechnology-related consumer spray products. *Environmental Science & Technology*, 45(24):10713–10719, 2011. doi: 10.1021/es202770m. URL https://doi.org/10.1021/es202770m. PMID: 22070550.

[133] Kaisen Lin and Linsey C. Marr. Aerosolization of ebola virus surrogates in wastewater systems. *Environmental Science & Technology*, 51(5):2669–2675, 2017. doi: 10.1021/acs.est.6b04846. URL https://doi.org/10.1021/acs.est.6b04846. PMID: 28125778.

[134] K. Max Zhang, Eladio M. Knipping, Anthony S. Wexler, Prakash V. Bhave, and Gail S. Tonnesen. Reply to comment on "size distribution of sea-salt emissions as a function of relative humidity". *Atmospheric Environment*, 40(3):591–592, 2006. ISSN 1352-2310. doi: https://doi.org/10.1016/j.atmosenv.2005.08.044. URL https://www.sciencedirect.com/science/article/pii/S1352231005009684.

[135] K. W. Appel, J. O. Bash, K. M. Fahey, K. M. Foley, R. C. Gilliam, C. Hogrefe, W. T. Hutzell, D. Kang, R. Mathur, B. N. Murphy, S. L. Napelenok, C. G. Nolte, J. E. Pleim, G. A. Pouliot, H. O. T. Pye, L. Ran, S. J. Roselle, G. Sarwar, D. B. Schwede, F. I. Sidi, T. L. Spero, and D. C. Wong. The community multiscale air quality (cmaq) model versions 5.3 and 5.3.1: system updates and evaluation. *Geoscientific Model Development*, 14(5):2867–2897, 2021. doi: 10.5194/gmd-14-2867-2021. URL https://gmd.copernicus.org/articles/14/2867/2021/.

[136] Jia Wang, Xuezhi Bai, Haoguo Hu, Anne Clites, Marie Colton, and Brent Lofgren. Temporal and spatial variability of great lakes ice cover, 1973–2010. *Journal of Climate*,

25(4):1318 – 1329, 2012. doi: 10.1175/2011JCLI4066.1. URL https://journals.ametsoc.org/view/journals/clim/25/4/2011jcli4066.1.xml.

[137] X. Li, S. Zhong, X. Bian, and W. E. Heilman. Climate and climate variability of the wind power resources in the great lakes region of the united states. *Journal of Geophysical Research: Atmospheres*, 115(D18), 2010. doi: https://doi.org/10.1029/2009JD013415. URL https://agupubs.onlinelibrary.wiley.com/doi/abs/10.1029/2009JD013415.

[138] US EPA. Cmaq model version 5.3 input data – 1/1/2016 - 12/31/2016 12km conus, 2019. URL https://dataverse.unc.edu/citation?persistentId=doi:10.15139/S3/MHNUNE.

[139] T. L. Otte and J. E. Pleim. The meteorology-chemistry interface processor (mcip) for the cmaq modeling system: updates through mcipv3.4.1. *Geoscientific Model Development*, 3(1):243–256, 2010. doi: 10.5194/gmd-3-243-2010. URL https://gmd.copernicus.org/articles/3/243/2010/.

[140] H. Morrison, G. Thompson, and V. Tatarskii. Impact of cloud microphysics on the development of trailing stratiform precipitation in a simulated squall line: Comparison of one- and two-moment schemes. *Monthly Weather Review*, 137(3):991 – 1007, 2009. doi: 10.1175/2008MWR2556.1. URL https://journals.ametsoc.org/view/journals/mwre/137/3/2008mwr2556.1.xml.

[141] Michael J. Iacono, Jennifer S. Delamere, Eli J. Mlawer, Mark W. Shephard, Shepard A. Clough, and William D. Collins. Radiative forcing by long-lived greenhouse gases: Calculations with the aer radiative transfer models. *Journal of Geophysical Research: Atmospheres*, 113(D13), 2008. doi: https://doi.org/10.1029/2008JD009944. URL https://agupubs.onlinelibrary.wiley.com/doi/abs/10.1029/2008JD009944.

[142] John S. Kain. The kain–fritsch convective parameterization: An update. *Journal of Applied Meteorology*, 43(1):170 – 181, 2004. doi: 10.1175/1520-0450(2004)043⟨0170:TKCPAU⟩2.0.CO;2. URL https://journals.ametsoc.org/view/journals/apme/43/1/1520-0450_2004_043_0170_tkcpau_2.0.co_2.xml.

[143] Jonathan E. Pleim and Aijun Xiu. Development of a land surface model. part ii: Data assimilation. *Journal of Applied Meteorology*, 42(12): 1811 – 1822, 2003. doi: 10.1175/1520-0450(2003)042⟨1811:DOALSM⟩2.0.CO; 2. URL https://journals.ametsoc.org/view/journals/apme/42/12/1520-0450_2003_042_1811_doalsm_2.0.co_2.xml.

[144] Aijun Xiu and Jonathan E. Pleim. Development of a land surface model. part i: Application in a mesoscale meteorological model. *Journal of Applied Meteorology*, 40(2):192 – 209, 2001. doi: 10.1175/1520-0450(2001)040⟨0192:DOALSM⟩2.0.CO; 2. URL https://journals.ametsoc.org/view/journals/apme/40/2/1520-0450_2001_040_0192_doalsm_2.0.co_2.xml.

[145] Jonathan E. Pleim. A combined local and nonlocal closure model for the atmospheric boundary layer. part i: Model description and testing. *Journal of Applied Meteorology and Climatology*, 46(9):1383 – 1395, 2007. doi: 10.1175/JAM2539.1. URL https://journals.ametsoc.org/view/journals/apme/46/9/jam2539.1.xml.

[146] S. L. Gong. A parameterization of sea-salt aerosol source function for sub- and super-micron particles. *Global Biogeochemical Cycles*, 17(4), 2003. doi: https://doi.org/10.1029/2003GB002079. URL https://agupubs.onlinelibrary.wiley.com/doi/abs/10.1029/2003GB002079.

[147] B. Gantt, J. T. Kelly, and J. O. Bash. Updating sea spray aerosol emissions in the community multiscale air quality (cmaq) model version 5.0.2. *Geoscientific Model Development*, 8(11):3733–3746, 2015. doi: 10.5194/gmd-8-3733-2015. URL https://gmd.copernicus.org/articles/8/3733/2015/.

[148] S.-L. von der Weiden, F. Drewnick, and S. Borrmann. Particle loss calculator – a new software tool for the assessment of the performance of aerosol inlet systems. *Atmospheric Measurement Techniques*, 2(2):479–494, 2009. doi: 10.5194/amt-2-479-2009. URL https://amt.copernicus.org/articles/2/479/2009/.

[149] Antony D. Clarke, Steven R. Owens, and Jingchuan Zhou. An ultrafine sea-salt flux from breaking waves: Implications for cloud condensation nuclei in the remote marine atmosphere. *Journal of Geophysical Research: Atmospheres*, 111(D6), 2006. doi: https:

//doi.org/10.1029/2005JD006565. URL https://agupubs.onlinelibrary.wiley.com/doi/abs/10.1029/2005JD006565.

[150] M. S. Long, W. C. Keene, D. J. Kieber, D. J. Erickson, and H. Maring. A sea-state based source function for size- and composition-resolved marine aerosol production. *Atmospheric Chemistry and Physics*, 11(3):1203–1216, 2011. doi: 10.5194/acp-11-1203-2011. URL https://acp.copernicus.org/articles/11/1203/2011/.

[151] Darius Ceburnis, Colin D. O'Dowd, Gerard S. Jennings, Maria Cristina Facchini, Lorenza Emblico, Stefano Decesari, Sandro Fuzzi, and Jonas Sakalys. Marine aerosol chemistry gradients: Elucidating primary and secondary processes and fluxes. *Geophysical Research Letters*, 35(7), 2008. doi: https://doi.org/10.1029/2008GL033462. URL https://agupubs.onlinelibrary.wiley.com/doi/abs/10.1029/2008GL033462.

[152] D. Ceburnis, M. Rinaldi, J. Ovadnevaite, G. Martucci, L. Giulianelli, and C. D. O'Dowd. Marine submicron aerosol gradients, sources and sinks. *Atmospheric Chemistry and Physics*, 16(19):12425–12439, 2016. doi: 10.5194/acp-16-12425-2016. URL https://acp.copernicus.org/articles/16/12425/2016/.

[153] Jurgita Ovadnevaite, Darius Ceburnis, Manjula Canagaratna, Harald Berresheim, Jakub Bialek, Giovanni Martucci, Douglas R. Worsnop, and Colin O'Dowd. On the effect of wind speed on submicron sea salt mass concentrations and source fluxes. *Journal of Geophysical Research: Atmospheres*, 117(D16), 2012. doi: https://doi.org/10.1029/2011JD017379. URL https://agupubs.onlinelibrary.wiley.com/doi/abs/10.1029/2011JD017379.

[154] Y. Zhang. Online-coupled meteorology and chemistry models: history, current status, and outlook. *Atmospheric Chemistry and Physics*, 8(11):2895–2932, 2008. doi: 10.5194/acp-8-2895-2008. URL https://acp.copernicus.org/articles/8/2895/2008/.

[155] J. M. Creamean, J. N. Cross, R. Pickart, L. McRaven, P. Lin, A. Pacini, R. Hanlon, D. G. Schmale, J. Ceniceros, T. Aydell, N. Colombi, E. Bolger, and P. J. DeMott. Ice nucleating particles carried from below a phytoplankton bloom to the arctic atmosphere. *Geophysical Research Letters*, 46(14):8572–8581, 2019. doi: https:

//doi.org/10.1029/2019GL083039. URL https://agupubs.onlinelibrary.wiley.com/doi/abs/10.1029/2019GL083039.

[156] Brock A. Mitts, Xiaofei Wang, Dolan D. Lucero, Charlotte M. Beall, Grant B. Deane, Paul J. DeMott, and Kimberly A. Prather. Importance of supermicron ice nucleating particles in nascent sea spray. *Geophysical Research Letters*, 48(3):e2020GL089633, 2021. doi: https://doi.org/10.1029/2020GL089633. URL https://agupubs.onlinelibrary.wiley.com/doi/abs/10.1029/2020GL089633. e2020GL089633 2020GL089633.

[157] Bruce F. Moffett, Tom C. J. Hill, and Paul J. DeMott. Abundance of biological ice nucleating particles in the mississippi and its major tributaries. *Atmosphere*, 9(8), 2018. ISSN 2073-4433. doi: 10.3390/atmos9080307. URL https://www.mdpi.com/2073-4433/9/8/307.

[158] Daniel Rosenfeld, Meinrat O. Andreae, Ari Asmi, Mian Chin, Gerrit de Leeuw, David P. Donovan, Ralph Kahn, Stefan Kinne, Niku Kivekäs, Markku Kulmala, William Lau, K. Sebastian Schmidt, Tanja Suni, Thomas Wagner, Martin Wild, and Johannes Quaas. Global observations of aerosol-cloud-precipitation-climate interactions. *Reviews of Geophysics*, 52(4):750–808, 2014. doi: https://doi.org/10.1002/2013RG000441. URL https://agupubs.onlinelibrary.wiley.com/doi/abs/10.1002/2013RG000441.

[159] Elizabeth C. Minor, Cody James Tennant, and Erik T. Brown. A seasonal to interannual view of inorganic and organic carbon and ph in western lake superior. *Journal of Geophysical Research: Biogeosciences*, 124(2):405–419, 2019. doi: https://doi.org/10.1029/2018JG004664. URL https://agupubs.onlinelibrary.wiley.com/doi/abs/10.1029/2018JG004664.

[160] Michael Notaro, Kathleen Holman, Azar Zarrin, Elody Fluck, Steve Vavrus, and Val Bennington. Influence of the laurentian great lakes on regional climate. *Journal of Climate*, 26(3):789 – 804, 2013. doi: 10.1175/JCLI-D-12-00140.1. URL https://journals.ametsoc.org/view/journals/clim/26/3/jcli-d-12-00140.1.xml.

[161] Thomas B. Bridgeman, Justin D. Chaffin, and Jesse E. Filbrun. A novel method for tracking western lake erie microcystis blooms, 2002–2011. *Journal of Great*

Lakes Research, 39(1):83–89, 2013. ISSN 0380-1330. doi: https://doi.org/10.1016/j.jglr.2012.11.004. URL https://www.sciencedirect.com/science/article/pii/S038013301200233X.

[162] Taikan Oki and Shinjiro Kanae. Global hydrological cycles and world water resources. *science*, 313(5790):1068–1072, 2006. ISSN 0036-8075.

[163] Robert B Jackson, Stephen R Carpenter, Clifford N Dahm, Diane M McKnight, Robert J Naiman, Sandra L Postel, and Steven W Running. Water in a changing world. *Ecological applications*, 11(4):1027–1045, 2001. ISSN 1939-5582.

[164] Eric V Novotny, Dan Murphy, and Heinz G Stefan. Increase of urban lake salinity by road deicing salt. *Science of the Total Environment*, 406(1-2):131–144, 2008. ISSN 0048-9697.

[165] WD Williams. *Anthropogenic salinisation of inland waters*, pages 329–337. Springer, 2001.

[166] Miguel Cañedo-Argüelles, Ben J Kefford, Christophe Piscart, Narcís Prat, Ralf B Schäfer, and Claus-Jürgen Schulz. Salinisation of rivers: an urgent ecological issue. *Environmental pollution*, 173:157–167, 2013. ISSN 0269-7491.

[167] Victoria R Kelly, Mary Ann Cunningham, Neil Curri, Stuart E Findlay, and Sean M Carroll. The distribution of road salt in private drinking water wells in a southeastern new york suburban township. *Journal of environmental quality*, 47(3):445–451, 2018. ISSN 0047-2425.

[168] Kelsey J Pieper, Min Tang, C Nathan Jones, Stephanie Weiss, Andrew Greene, Hisyam Mohsin, Jeffrey Parks, and Marc A Edwards. Impact of road salt on drinking water quality and infrastructure corrosion in private wells. *Environmental science & technology*, 52(24):14078–14087, 2018. ISSN 0013-936X.

[169] Steven R Corsi, David J Graczyk, Steven W Geis, Nathaniel L Booth, and Kevin D Richards. A fresh look at road salt: aquatic toxicity and water-quality impacts on local, regional, and national scales. *Environmental science & technology*, 44(19):7376–7382, 2010. ISSN 0013-936X.

[170] Barry T Hart, Paul Bailey, Rick Edwards, Kent Hortle, Kim James, Andrew McMahon, Charles Meredith, and Kerrie Swadling. A review of the salt sensitivity of the australian freshwater biota. *Hydrobiologia*, 210(1-2):105–144, 1991. ISSN 0018-8158.

[171] DL Nielsen, MA Brock, GN Rees, and Darren S Baldwin. Effects of increasing salinity on freshwater ecosystems in australia. *Australian Journal of Botany*, 51(6):655–665, 2003. ISSN 1444-9862.

[172] Ellen R Herbert, Paul Boon, Amy J Burgin, Scott C Neubauer, Rima B Franklin, Marcelo Ardón, Kristine N Hopfensperger, Leon PM Lamers, and Peter Gell. A global perspective on wetland salinization: ecological consequences of a growing threat to freshwater wetlands. *Ecosphere*, 6(10):1–43, 2015. ISSN 2150-8925.

[173] Lei Zhang, Guang Gao, Xiangming Tang, and Keqiang Shao. Can the freshwater bacterial communities shift to the "marine-like" taxa? *Journal of Basic Microbiology*, 54(11):1264–1272, 2014. ISSN 0233-111X.

[174] Heidi Bauer, Heinrich Giebl, Regina Hitzenberger, Anne Kasper-Giebl, Georg Reischl, Franziska Zibuschka, and Hans Puxbaum. Airborne bacteria as cloud condensation nuclei. *Journal of Geophysical Research: Atmospheres*, 108(D21), 2003. ISSN 0148-0227.

[175] Cindy E Morris, DG Georgakopoulos, and DC Sands. Ice nucleation active bacteria and their potential role in precipitation. In *Journal de Physique IV (Proceedings)*, volume 121, pages 87–103. EDP sciences, 2004. ISBN 1155-4339.

[176] Robert L Green and Gareth J Warren. Physical and functional repetition in a bacterial ice nucleation gene. *Nature*, 317(6038):645–648, 1985. ISSN 1476-4687.

[177] Bruce C Parker, Mary Ann Ford, Howard Gruft, and Joseph O Falkinham III. Epidemiology of infection by nontuberculous mycobacteria: Iv. preferential aerosolization of mycobacterium intracellulare from natural waters. *American Review of Respiratory Disease*, 128(4):652–656, 1983. ISSN 0003-0805.

[178] Aaron J Prussin II, David Otto Schwake, and Linsey C Marr. Ten questions concerning the aerosolization and transmission of legionella in the built environment. *Building and environment*, 123:684–695, 2017. ISSN 0360-1323.

[179] Renee B Pietsch, Hinrich Grothe, Regina Hanlon, Craig W Powers, Sunghwan Jung, Shane D Ross, and David G Schmale III. Wind-driven spume droplet production and the transport of pseudomonas syringae from aquatic environments. *PeerJ*, 6:e5663, 2018. ISSN 2167-8359.

[180] Camilla Fahlgren, Laura Gómez-Consarnau, Julia Zábori, Markus V Lindh, Radovan Krejci, E Monica Mårtensson, Douglas Nilsson, and Jarone Pinhassi. Seawater mesocosm experiments in the arctic uncover differential transfer of marine bacteria to aerosols. *Environmental Microbiology Reports*, 7(3):460–470, 2015. ISSN 1758-2229.

[181] Peter LL Walls and James C Bird. Enriching particles on a bubble through drainage: Measuring and modeling the concentration of microbial particles in a bubble film at rupture. *Elem Sci Anth*, 5:34, 2017. ISSN 2325-1026.

[182] Peter LL Walls, James C Bird, and Lydia Bourouiba. Moving with bubbles: a review of the interactions between bubbles and the microorganisms that surround them, 2014.

[183] Martin E Weber, Duncan C Blanchard, and Lawrence D Syzdek. The mechanism of scavenging of waterborne bacteria by a rising bubble. *Limnology and Oceanography*, 28(1):101–105, 1983. ISSN 0024-3590.

[184] Duncan C Blanchard, Lawrence D Syzdek, and Martin E Weber. Bubble scavenging of bacteria in freshwater quickly produces bacterial enrichment in airborne jet drops 1. *Limnology and oceanography*, 26(5):961–964, 1981. ISSN 0024-3590.

[185] Roman Marks, Ewa Górecka, Kevin McCartney, and Wojciech Borkowski. Rising bubbles as mechanism for scavenging and aerosolization of diatoms. *Journal of Aerosol Science*, 128:79–88, 2019. ISSN 0021-8502.

[186] Matthew T Cottrell and Kirchman L David. Contribution of major bacterial groups to bacterial biomass production (thymidine and leucine incorporation) in the delaware estuary. *Limnology and Oceanography*, 48(1):168–178, 2003. ISSN 0024-3590.

[187] Qinglong L Wu, Gabriel Zwart, Michael Schauer, Miranda P Kamst-van Agterveld, and Martin W Hahn. Bacterioplankton community composition along a salinity gradient of sixteen high-mountain lakes located on the tibetan plateau, china. *Applied and Environmental Microbiology*, 72(8):5478–5485, 2006. ISSN 0099-2240.

[188] Yao Zhang, Nianzhi Jiao, Matthew T Cottrell, and David L Kirchman. Contribution of major bacterial groups to bacterial biomass production along a salinity gradient in the south china sea. *Aquatic Microbial Ecology*, 43(3):233–241, 2006. ISSN 0948-3055.

[189] Daniel PR Herlemann, Matthias Labrenz, Klaus Jürgens, Stefan Bertilsson, Joanna J Waniek, and Anders F Andersson. Transitions in bacterial communities along the 2000 km salinity gradient of the baltic sea. *The ISME journal*, 5(10):1571–1579, 2011. ISSN 1751-7370.

[190] Thierry C Bouvier and Paul A del Giorgio. Compositional changes in free-living bacterial communities along a salinity gradient in two temperate estuaries. *Limnology and oceanography*, 47(2):453–470, 2002. ISSN 0024-3590.

[191] Silke Langenheder, Veljo Kisand, Johan Wikner, and Lars J Tranvik. Salinity as a structuring factor for the composition and performance of bacterioplankton degrading riverine doc. *FEMS Microbiology Ecology*, 45(2):189–202, 2003. ISSN 1574-6941.

[192] Jean Painchaud, J-C Therriault, and Louis Legendre. Assessment of salinity-related mortality of freshwater bacteria in the saint lawrence estuary. *Applied and environmental microbiology*, 61(1):205–208, 1995. ISSN 0099-2240.

[193] Byron C Crump, Charles S Hopkinson, Mitchell L Sogin, and John E Hobbie. Microbial biogeography along an estuarine salinity gradient: combined influences of bacterial growth and residence time. *Applied and environmental microbiology*, 70(3):1494–1505, 2004. ISSN 0099-2240.

[194] Eugenio Rastelli, Cinzia Corinaldesi, Antonio Dell'Anno, Marco Lo Martire, Silvestro Greco, Maria Cristina Facchini, Matteo Rinaldi, Colin O'Dowd, Darius Ceburnis, and Roberto Danovaro. Transfer of labile organic matter and microbes from the ocean surface to the marine aerosol: an experimental approach. *Scientific reports*, 7(1):1–10, 2017. ISSN 2045-2322.

[195] Josephine Y Aller, Marina R Kuznetsova, Christopher J Jahns, and Paul F Kemp. The sea surface microlayer as a source of viral and bacterial enrichment in marine aerosols. *Journal of aerosol science*, 36(5-6):801–812, 2005. ISSN 0021-8502.

[196] J Gregory Caporaso, Christian L Lauber, William A Walters, Donna Berg-Lyons, James Huntley, Noah Fierer, Sarah M Owens, Jason Betley, Louise Fraser, and Markus Bauer. Ultra-high-throughput microbial community analysis on the illumina hiseq and miseq platforms. *The ISME journal*, 6(8):1621–1624, 2012. ISSN 1751-7370.

[197] Katherine E Graham, Aaron J Prussin, Linsey C Marr, Lauren M Sassoubre, and Alexandria B Boehm. Microbial community structure of sea spray aerosols at three california beaches. *FEMS microbiology ecology*, 94(3):fiy005, 2018. ISSN 1574-6941.

[198] Craig W Powers, Regina Hanlon, Hinrich Grothe, Aaron J Prussin, Linsey C Marr, and David G Schmale III. Coordinated sampling of microorganisms over freshwater and saltwater environments using an unmanned surface vehicle (usv) and a small unmanned aircraft system (suas). *Frontiers in microbiology*, 9:1668, 2018. ISSN 1664-302X.

[199] Jessica V Trout-Haney, Ruth C Heindel, and Ross A Virginia. Picocyanobacterial cells in near-surface air above terrestrial and freshwater substrates in greenland and antarctica. *Environmental Microbiology Reports*, 12(3):296–305, 2020. ISSN 1758-2229.

[200] Jiaming Hu, Jiaqi Liu, Yi Zhu, Zoraida Diaz-Perez, Michael Sheridan, Haley Royer, Raymond Leibensperger, Daniela Maizel, Larry Brand, and Kimberly J Popendorf. Exposure to aerosolized algal toxins in south florida increases short-and long-term health risk in drosophila model of aging. *Toxins*, 12(12):787, 2020.

[201] Takashi ITO. The venice system for the classification of marine waters according to salinity: Symposium on the classification of brackish waters, venice, 8-14 april 1958. *Japanese Journal of Limnology (Rikusuigaku Zasshi)*, 20(3):119–120, 1959. ISSN 0021-5104.

[202] Yingying Wang, Frederik Hammes, Nico Boon, and Thomas Egli. Quantification of the filterability of freshwater bacteria through 0.45, 0.22, and 0.1 μm pore size filters and shape-dependent enrichment of filterable bacterial communities. *Environmental Science & Technology*, 41(20):7080–7086, 2007. ISSN 0013-936X.

[203] Nancy Clark Burton, Sergey A Grinshpun, and Tiina Reponen. Physical collection efficiency of filter materials for bacteria and viruses. *The Annals of occupational hygiene*, 51(2):143–151, 2007. ISSN 1475-3162.

[204] Alma E Parada, David M Needham, and Jed A Fuhrman. Every base matters: assessing small subunit rrna primers for marine microbiomes with mock communities, time series and global field samples. *Environmental microbiology*, 18(5):1403–1414, 2016. ISSN 1462-2912.

[205] Christopher Quince, Anders Lanzen, Russell J Davenport, and Peter J Turnbaugh. Removing noise from pyrosequenced amplicons. *BMC bioinformatics*, 12(1):38, 2011. ISSN 1471-2105.

[206] Evan Bolyen, Jai Ram Rideout, Matthew R Dillon, Nicholas A Bokulich, Christian Abnet, Gabriel A Al-Ghalith, Harriet Alexander, Eric J Alm, Manimozhiyan Arumugam, and Francesco Asnicar. Qiime 2: Reproducible, interactive, scalable, and extensible microbiome data science. Report 2167-9843, PeerJ Preprints, 2018.

[207] Benjamin J Callahan, Paul J McMurdie, Michael J Rosen, Andrew W Han, Amy Jo A Johnson, and Susan P Holmes. Dada2: high-resolution sample inference from illumina amplicon data. *Nature methods*, 13(7):581–583, 2016. ISSN 1548-7105.

[208] Fabian Pedregosa, Gaël Varoquaux, Alexandre Gramfort, Vincent Michel, Bertrand Thirion, Olivier Grisel, Mathieu Blondel, Peter Prettenhofer, Ron Weiss, and Vincent Dubourg. Scikit-learn: Machine learning in python. *the Journal of machine Learning research*, 12:2825–2830, 2011. ISSN 1532-4435.

[209] Christian Quast, Elmar Pruesse, Pelin Yilmaz, Jan Gerken, Timmy Schweer, Pablo Yarza, Jörg Peplies, and Frank Oliver Glöckner. The silva ribosomal rna gene database project: improved data processing and web-based tools. *Nucleic acids research*, 41(D1): D590–D596, 2012. ISSN 0305-1048.

[210] Paul J McMurdie and Susan Holmes. phyloseq: an r package for reproducible interactive analysis and graphics of microbiome census data. *PloS one*, 8(4):e61217, 2013. ISSN 1932-6203.

[211] R Core Team. R: A language and environment for statistical computing, 2019.

[212] Marti J Anderson, Kari E Ellingsen, and Brian H McArdle. Multivariate dispersion as a measure of beta diversity. *Ecology letters*, 9(6):683–693, 2006. ISSN 1461-023X.

[213] Marcelino T Suzuki, Lance T Taylor, and Edward F DeLong. Quantitative analysis of small-subunit rrna genes in mixed microbial populations via 5'-nuclease assays. *Applied and environmental microbiology*, 66(11):4605–4614, 2000. ISSN 0099-2240.

[214] Ching Jian, Panu Luukkonen, Hannele Yki-Järvinen, Anne Salonen, and Katri Korpela. Quantitative pcr provides a simple and accessible method for quantitative microbiota profiling. *PloS one*, 15(1):e0227285, 2020. ISSN 1932-6203.

[215] Paul A del Giorgio and Thierry C Bouvier. Linking the physiologic and phylogenetic successions in free-living bacterial communities along an estuarine salinity gradient. *Limnology and Oceanography*, 47(2):471–486, 2002. ISSN 0024-3590.

[216] Susannah M Burrows, Wolfgang Elbert, MG Lawrence, and Ulrich Pöschl. Bacteria in the global atmosphere-part 1: Review and synthesis of literature data for different ecosystems. *Atmospheric Chemistry & Physics*, 9(23):9263–9280, 2009. ISSN 1680-7316.

[217] AL Murby and James F Haney. Field and laboratory methods to monitor lake aerosols for cyanobacteria and microcystins. *Aerobiologia*, 32(3):395–403, 2016. ISSN 0393-5965.

[218] P Perrott, N Turgeon, L Gauthier-Levesque, and C Duchaine. Preferential aerosolization of bacteria in bioaerosols generated in vitro. *Journal of Applied Microbiology*, 123 (3):688–697, 2017. ISSN 1364-5072.

[219] Nirmalya Chatterjee and Markus Flury. Effect of particle shape on capillary forces acting on particles at the air–water interface. *Langmuir*, 29(25):7903–7911, 2013. ISSN 0743-7463.

[220] Mel Rosenberg and Staffan Kjelleberg. *Hydrophobic interactions: role in bacterial adhesion*, pages 353–393. Springer, 1986.

[221] E Fuentes, H Coe, D Green, G de Leeuw, and G McFiggans. On the impacts of phytoplankton-derived organic matter on the properties of the primary marine aerosol–part 1: Source fluxes. *Atmospheric Chemistry and Physics*, 10(19):9295–9317, 2010. ISSN 1680-7316.

[222] S Poulain and L Bourouiba. Biosurfactants change the thinning of contaminated bubbles at bacteria-laden water interfaces. *Physical Review Letters*, 121(20):204502, 2018.

[223] Wei Hu, Kotaro Murata, Shinichiro Fukuyama, Yoshimi Kawai, Eitarou Oka, Mitsuo Uematsu, and Daizhou Zhang. Concentration and viability of airborne bacteria over the kuroshio extension region in the northwestern pacific ocean: Data from three cruises. *Journal of Geophysical Research: Atmospheres*, 122(23):12,892–12,905, 2017. ISSN 2169-897X.

[224] Anke Schäfer, Hauke Harms, and Alexander JB Zehnder. Bacterial accumulation at the air-water interface. *Environmental science & technology*, 32(23):3704–3712, 1998. ISSN 0013-936X.

[225] Kevin D Young. The selective value of bacterial shape. *Microbiology and molecular biology reviews*, 70(3):660–703, 2006. ISSN 1092-2172.

[226] Jacob J Shephard, David M Savory, Phil J Bremer, and A James McQuillan. Salt modulates bacterial hydrophobicity and charge properties influencing adhesion of pseudomonas aeruginosa (pa01) in aqueous suspensions. *Langmuir*, 26(11):8659–8665, 2010. ISSN 0743-7463.

[227] Xin Cui, Chen Shi, Shuo Zhang, Lei Xie, Jing Liu, Dazhi Jiang, and Hongbo Zeng. Probing the effect of salinity and ph on surface interactions between air bubbles and hydrophobic solids: implications for colloidal assembly at air/water interfaces. *Chemistry–An Asian Journal*, 12(13):1568–1577, 2017. ISSN 1861-4728.

[228] Michael B Griffith. Natural variation and current reference for specific conductivity and major ions in wadeable streams of the conterminous usa. *Freshwater Science*, 33 (1):1–17, 2014. ISSN 2161-9549.

[229] Hilary A Dugan, Sarah L Bartlett, Samantha M Burke, Jonathan P Doubek, Flora E Krivak-Tetley, Nicholas K Skaff, Jamie C Summers, Kaitlin J Farrell, Ian M McCullough, and Ana M Morales-Williams. Salting our freshwater lakes. *Proceedings of the National Academy of Sciences*, 114(17):4453–4458, 2017. ISSN 0027-8424.

[230] Sujay S Kaushal, Gene E Likens, Michael L Pace, Ryan M Utz, Shahan Haq, Julia Gorman, and Melissa Grese. Freshwater salinization syndrome on a continental scale.

Proceedings of the National Academy of Sciences, 115(4):E574–E583, 2018. ISSN 0027-8424.

[231] David G Schmale III, Andrew P Ault, Walid Saad, Durelle T Scott, and Judy A Westrick. Perspectives on harmful algal blooms (habs) and the cyberbiosecurity of freshwater systems. *Frontiers in bioengineering and biotechnology*, 7:128, 2019. ISSN 2296-4185.

[232] Jeffrey Soller, Timothy Bartrand, John Ravenscroft, Marirosa Molina, Gene Whelan, Mary Schoen, and Nicholas Ashbolt. Estimated human health risks from recreational exposures to stormwater runoff containing animal faecal material. *Environmental modelling & software*, 72:21–32, 2015. ISSN 1364-8152.

[233] Stephen E. DeVilbiss, Meredith K. Steele, Leigh-Anne H. Krometis, and Brian D. Badgley. Freshwater salinization increases survival of escherichia coli and risk of bacterial impairment. *Water Research*, 191:116812, 2021. ISSN 0043-1354. doi: https://doi.org/10.1016/j.watres.2021.116812. URL https://www.sciencedirect.com/science/article/pii/S0043135421000105.

[234] Bruce F Moffett, Tom CJ Hill, and Paul J DeMott. Abundance of biological ice nucleating particles in the mississippi and its major tributaries. *Atmosphere*, 9(8):307, 2018.

[235] Bruce F Moffett. Fresh water ice nuclei. *Fundamental and Applied Limnology*, pages 19–23, 2016.

[236] Renée B. Pietsch, Boris A. Vinatzer, and David G. Schmale. Diversity and abundance of ice nucleating strains of pseudomonas syringae in a freshwater lake in virginia, usa. *Frontiers in Microbiology*, 8, 2017. ISSN 1664-302X. doi: 10.3389/fmicb.2017.00318. URL https://www.frontiersin.org/article/10.3389/fmicb.2017.00318.

[237] KC Failor, DG Schmale, BA Vinatzer, and Caroline L Monteil. Ice nucleation active bacteria in precipitation are genetically diverse and nucleate ice by employing different mechanisms. *The ISME journal*, 11(12):2740–2753, 2017. ISSN 1751-7370.

[238] Peter Kershaw. Sources, fate and effects of microplastics in the marine environment: a global assessment. Technical report, International Maritime Organization, 2015.

[239] Chloe Wayman and Helge Niemann. The fate of plastic in the ocean environment – a minireview. *Environ. Sci.: Processes Impacts*, 23:198–212, 2021. doi: 10.1039/D0EM00446D. URL http://dx.doi.org/10.1039/D0EM00446D.

[240] Jingyi Li, Huihui Liu, and J. Paul Chen. Microplastics in freshwater systems: A review on occurrence, environmental effects, and methods for microplastics detection. *Water Research*, 137:362–374, 2018. ISSN 0043-1354. doi: https://doi.org/10.1016/j.watres.2017.12.056. URL https://www.sciencedirect.com/science/article/pii/S0043135417310515.

[241] Chaoran Li, Rosa Busquets, and Luiza C. Campos. Assessment of microplastics in freshwater systems: A review. *Science of The Total Environment*, 707:135578, 2020. ISSN 0048-9697. doi: https://doi.org/10.1016/j.scitotenv.2019.135578. URL https://www.sciencedirect.com/science/article/pii/S0048969719355731.

[242] Lisbeth Van Cauwenberghe, Lisa Devriese, François Galgani, Johan Robbens, and Colin R. Janssen. Microplastics in sediments: A review of techniques, occurrence and effects. *Marine Environmental Research*, 111:5–17, 2015. ISSN 0141-1136. doi: https://doi.org/10.1016/j.marenvres.2015.06.007. URL https://www.sciencedirect.com/science/article/pii/S0141113615000938. Particles in the Oceans: Implication for a safe marine environment.

[243] Jing-Jie Guo, Xian-Pei Huang, Lei Xiang, Yi-Ze Wang, Yan-Wen Li, Hui Li, Quan-Ying Cai, Ce-Hui Mo, and Ming-Hung Wong. Source, migration and toxicology of microplastics in soil. *Environment International*, 137:105263, 2020. ISSN 0160-4120. doi: https://doi.org/10.1016/j.envint.2019.105263. URL https://www.sciencedirect.com/science/article/pii/S0160412019325097.

[244] Anderson Abel de Souza Machado, Werner Kloas, Christiane Zarfl, Stefan Hempel, and Matthias C. Rillig. Microplastics as an emerging threat to terrestrial ecosystems. *Global Change Biology*, 24(4):1405–1416, 2018. doi: https://doi.org/10.1111/gcb.14020. URL https://onlinelibrary.wiley.com/doi/abs/10.1111/gcb.14020.

[245] A. Dick Vethaak and Juliette Legler. Microplastics and human health. *Science*, 371 (6530):672–674, 2021. doi: 10.1126/science.abe5041. URL https://www.science.org/doi/abs/10.1126/science.abe5041.

[246] Heather A. Leslie, Martin J.M. van Velzen, Sicco H. Brandsma, A. Dick Vethaak, Juan J. Garcia-Vallejo, and Marja H. Lamoree. Discovery and quantification of plastic particle pollution in human blood. *Environment International*, 163:107199, 2022. ISSN 0160-4120. doi: https://doi.org/10.1016/j.envint.2022.107199. URL https://www.sciencedirect.com/science/article/pii/S0160412022001258.

[247] S.L. Wright, J. Ulke, A. Font, K.L.A. Chan, and F.J. Kelly. Atmospheric microplastic deposition in an urban environment and an evaluation of transport. *Environment International*, 136:105411, 2020. ISSN 0160-4120. doi: https://doi.org/10.1016/j.envint.2019.105411. URL https://www.sciencedirect.com/science/article/pii/S0160412019330351.

[248] Steve Allen, Deonie Allen, Vernon R Phoenix, Gaël Le Roux, Pilar Durántez Jiménez, Anaëlle Simonneau, Stéphane Binet, and Didier Galop. Atmospheric transport and deposition of microplastics in a remote mountain catchment. *Nature Geoscience*, 12 (5):339–344, 2019.

[249] Miri Trainic, J Michel Flores, Iddo Pinkas, Maria Luiza Pedrotti, Fabien Lombard, Guillaume Bourdin, Gabriel Gorsky, Emmanuel Boss, Yinon Rudich, Assaf Vardi, et al. Airborne microplastic particles detected in the remote marine atmosphere. *Communications Earth & Environment*, 1(1):1–9, 2020.

[250] Maria Masry, Stéphanie Rossignol, Brice Temime Roussel, David Bourgogne, Pierre-Olivier Bussière, Badr R'mili, and Pascal Wong-Wah-Chung. Experimental evidence of plastic particles transfer at the water-air interface through bubble bursting. *Environmental Pollution*, 280:116949, 2021. ISSN 0269-7491. doi: https://doi.org/10.1016/j.envpol.2021.116949. URL https://www.sciencedirect.com/science/article/pii/S0269749121005315.

[251] Shanye Yang, Tao Zhang, Yuqi Gan, Xiaohui Lu, Hong Chen, Jianmin Chen, Xin Yang, and Xiaofei Wang. Constraining microplastic particle emission flux from the ocean. *Environmental Science & Technology Letters*, 0(0):null, 0. doi: 10.1021/acs.estlett.2c00214. URL https://doi.org/10.1021/acs.estlett.2c00214.

[252] Jinping Peng, Jundong Wang, and Liqi Cai. Current understanding of microplastics in the environment: Occurrence, fate, risks, and what we should do. *Integrated En-*

vironmental Assessment and Management, 13(3):476–482, 2017. doi: https://doi.org/10.1002/ieam.1912. URL https://setac.onlinelibrary.wiley.com/doi/abs/10.1002/ieam.1912.

[253] Rachid Dris, Johnny Gasperi, Vincent Rocher, Mohamed Saad, Nicolas Renault, and Bruno Tassin. Microplastic contamination in an urban area: a case study in greater paris. *Environmental Chemistry*, 12(5):592–599, 2015.

[254] Austin K Baldwin, Kerensa King, Richard Damstra, Byron Karns, Lark Weller, Sherri A Mason, Timothy Hoellein, and Lisa H Kim. Microplastics are everywhere! Technical report, National Park Service, 2017.

[255] Austin K. Baldwin, Steven R. Corsi, and Sherri A. Mason. Plastic debris in 29 great lakes tributaries: Relations to watershed attributes and hydrology. *Environmental Science & Technology*, 50(19):10377–10385, 2016. doi: 10.1021/acs.est.6b02917. URL https://doi.org/10.1021/acs.est.6b02917. PMID: 27627676.

[256] Peter L. Lenaker, Austin K. Baldwin, Steven R. Corsi, Sherri A. Mason, Paul C. Reneau, and John W. Scott. Vertical distribution of microplastics in the water column and surficial sediment from the milwaukee river basin to lake michigan. *Environmental Science & Technology*, 53(21):12227–12237, 2019. doi: 10.1021/acs.est.9b03850. URL https://doi.org/10.1021/acs.est.9b03850. PMID: 31618011.

[257] Marcus Eriksen, Sherri Mason, Stiv Wilson, Carolyn Box, Ann Zellers, William Edwards, Hannah Farley, and Stephen Amato. Microplastic pollution in the surface waters of the laurentian great lakes. *Marine Pollution Bulletin*, 77(1):177–182, 2013. ISSN 0025-326X. doi: https://doi.org/10.1016/j.marpolbul.2013.10.007. URL https://www.sciencedirect.com/science/article/pii/S0025326X13006097.

[258] Paul A. Helm. *Occurrence, Sources, Transport, and Fate of Microplastics in the Great Lakes–St. Lawrence River Basin*, pages 15–47. Springer International Publishing, Cham, 2020. ISBN 978-3-030-57874-9. doi: 10.1007/698_2020_557. URL https://doi.org/10.1007/698_2020_557.

[259] Won Joon Shim, Sang Hee Hong, and Soeun Eo. Chapter 1 - marine microplastics: Abundance, distribution, and composition. In Eddy Y. Zeng, editor, *Microplastic*

Contamination in Aquatic Environments, pages 1–26. Elsevier, 2018. ISBN 978-0-12-813747-5. doi: https://doi.org/10.1016/B978-0-12-813747-5.00001-1. URL https://www.sciencedirect.com/science/article/pii/B9780128137475000011.

[260] Shanye Yang, Tao Zhang, Yuqi Gan, Xiaohui Lu, Hong Chen, Jianmin Chen, Xin Yang, and Xiaofei Wang. Constraining microplastic particle emission flux from the ocean. *Environmental Science & Technology Letters*, 9(6):513–519, 2022. doi: 10.1021/acs.estlett.2c00214. URL https://doi.org/10.1021/acs.estlett.2c00214.

[261] Janice Brahney, Natalie Mahowald, Marje Prank, Gavin Cornwell, Zbigniew Klimont, Hitoshi Matsui, and Kimberly Ann Prather. Constraining the atmospheric limb of the plastic cycle. *Proceedings of the National Academy of Sciences*, 118(16):e2020719118, 2021. doi: 10.1073/pnas.2020719118. URL https://www.pnas.org/doi/abs/10.1073/pnas.2020719118.

[262] Steve Allen, Dušan Materić, Deonie Allen, Anna MacDonald, Rupert Holzinger, Gael Le Roux, and Vernon R Phoenix. An early comparison of nano to microplastic mass in a remote catchment's atmospheric deposition. *Journal of Hazardous Materials Advances*, 7:100104, 2022. ISSN 2772-4166. doi: https://doi.org/10.1016/j.hazadv.2022.100104. URL https://www.sciencedirect.com/science/article/pii/S2772416622000602.

[263] Rachid Dris, Hannes Imhof, Wilfried Sanchez, Johnny Gasperi, François Galgani, Bruno Tassin, and Christian Laforsch. Beyond the ocean: contamination of freshwater ecosystems with (micro-) plastic particles. *Environmental chemistry*, 12(5):539–550, 2015.

[264] Rosina Girones, Maria Antonia Ferrús, José Luis Alonso, Jesus Rodriguez-Manzano, Byron Calgua, Adriana de Abreu Corrêa, Ayalkibet Hundesa, Anna Carratala, and Sílvia Bofill-Mas. Molecular detection of pathogens in water – the pros and cons of molecular techniques. *Water Research*, 44(15):4325–4339, 2010. ISSN 0043-1354. doi: https://doi.org/10.1016/j.watres.2010.06.030. URL https://www.sciencedirect.com/science/article/pii/S0043135410004173.

[265] A. Mark Ibekwe, Menu Leddy, and Shelton E. Murinda. Potential human pathogenic bacteria in a mixed urban watershed as revealed by pyrosequencing. *PLOS ONE*, 8

(11):1–9, 11 2013. doi: 10.1371/journal.pone.0079490. URL https://doi.org/10.1371/journal.pone.0079490.

[266] Luís Fernando Amato-Lourenço, Regiani Carvalho-Oliveira, Gabriel Ribeiro Júnior, Luciana dos Santos Galvão, Rômulo Augusto Ando, and Thais Mauad. Presence of airborne microplastics in human lung tissue. *Journal of Hazardous Materials*, 416:126124, 2021. ISSN 0304-3894. doi: https://doi.org/10.1016/j.jhazmat.2021.126124. URL https://www.sciencedirect.com/science/article/pii/S0304389421010888.

[267] Sadasivam Anbumani and Poonam Kakkar. Ecotoxicological effects of microplastics on biota: a review. *Environmental Science and Pollution Research*, 25(15):14373–14396, 2018.

[268] I. Steinke, P. J. DeMott, G. B. Deane, T. C. J. Hill, M. Maltrud, A. Raman, and S. M. Burrows. A numerical framework for simulating the atmospheric variability of supermicron marine biogenic ice nucleating particles. *Atmospheric Chemistry and Physics*, 22(2):847–859, 2022. doi: 10.5194/acp-22-847-2022. URL https://acp.copernicus.org/articles/22/847/2022/.

[269] C. S. McCluskey, T. C. J. Hill, R. S. Humphries, A. M. Rauker, S. Moreau, P. G. Strutton, S. D. Chambers, A. G. Williams, I. McRobert, J. Ward, M. D. Keywood, J. Harnwell, W. Ponsonby, Z. M. Loh, P. B. Krummel, A. Protat, S. M. Kreidenweis, and P. J. DeMott. Observations of ice nucleating particles over southern ocean waters. *Geophysical Research Letters*, 45(21):11,989–11,997, 2018. doi: https://doi.org/10.1029/2018GL079981. URL https://agupubs.onlinelibrary.wiley.com/doi/abs/10.1029/2018GL079981.

[270] Young Kyoung Song, Sang Hee Hong, Soeun Eo, Mi Jang, Gi Myung Han, Atsuhiko Isobe, and Won Joon Shim. Horizontal and vertical distribution of microplastics in korean coastal waters. *Environmental Science & Technology*, 52(21):12188–12197, 2018. doi: 10.1021/acs.est.8b04032. URL https://doi.org/10.1021/acs.est.8b04032. PMID: 30295469.

[271] A E Walsby. Gas vesicles. *Microbiological Reviews*, 58(1):94–144, 1994. doi: 10.1128/mr.58.1.94-144.1994. URL https://journals.asm.org/doi/abs/10.1128/mr.58.1.94-144.1994.

[272] Cayelan C. Carey, Bas W. Ibelings, Emily P. Hoffmann, David P. Hamilton, and Justin D. Brookes. Eco-physiological adaptations that favour freshwater cyanobacteria in a changing climate. *Water Research*, 46(5):1394–1407, 2012. ISSN 0043-1354. doi: https://doi.org/10.1016/j.watres.2011.12.016. URL https://www.sciencedirect.com/science/article/pii/S0043135411007883. Cyanobacteria: Impacts of climate change on occurrence, toxicity and water quality management.

[273] Jia Wang, Xuezhi Bai, Haoguo Hu, Anne Clites, Marie Colton, and Brent Lofgren. Temporal and spatial variability of great lakes ice cover, 1973–2010. *Journal of Climate*, 25(4):1318 – 1329, 2012. doi: 10.1175/2011JCLI4066.1. URL https://journals.ametsoc.org/view/journals/clim/25/4/2011jcli4066.1.xml.

[274] Meriam-Webster. *surf*. Merriam-Webster, 2022. URL https://www.merriam-webster.com/dictionary/surf.

[275] Gerrit de Leeuw, Filip P. Neele, Martin Hill, Michael H. Smith, and Elisabetta Vignati. Production of sea spray aerosol in the surf zone. *Journal of Geophysical Research: Atmospheres*, 105(D24):29397–29409, 2000. doi: https://doi.org/10.1029/2000JD900549. URL https://agupubs.onlinelibrary.wiley.com/doi/abs/10.1029/2000JD900549.

[276] Donald M. Anderson, Elizabeth Fensin, Christopher J. Gobler, Alicia E. Hoeglund, Katherine A. Hubbard, David M. Kulis, Jan H. Landsberg, Kathi A. Lefebvre, Pieter Provoost, Mindy L. Richlen, Juliette L. Smith, Andrew R. Solow, and Vera L. Trainer. Marine harmful algal blooms (habs) in the united states: History, current status and future trends. *Harmful Algae*, 102:101975, 2021. ISSN 1568-9883. doi: https://doi.org/10.1016/j.hal.2021.101975. URL https://www.sciencedirect.com/science/article/pii/S1568988321000020. Global Harmful Algal Bloom Status Reporting.

[277] Karen Sem, Myoseon Jang, Richard Pierce, Patricia Blum, and Zechen Yu. Characterization of atmospheric processes of brevetoxins in sea spray aerosols from red tide events. *Environmental Science & Technology*, 56(3):1811–1819, 2022. doi: 10.1021/acs.est.1c05740. URL https://doi.org/10.1021/acs.est.1c05740. PMID: 35050617.

[278] William M Abraham, Andrea J Bourdelais, Juan R Sabater, Ashfaq Ahmed, Troy A Lee, Irakli Serebriakov, and Daniel G Baden. Airway responses to aerosolized brevetoxins in an animal model of asthma. *American journal of respiratory and critical care medicine*, 171(1):26–34, 2005.

[279] R. O. Barnes and E. D. Goldberg. Methane production and consumption in anoxic marine sediments. *Geology*, 4(5):297–300, 05 1976. ISSN 0091-7613. doi: 10.1130/0091-7613(1976)4⟨297:MPACIA⟩2.0.CO;2. URL https://doi.org/10.1130/0091-7613(1976)4<297:MPACIA>2.0.CO;2.

[280] Mark A. Donelan and Rik Wanninkhof. *Gas Transfer at Water Surfaces—Concepts and Issues*, pages 1–10. American Geophysical Union (AGU), 2002. ISBN 9781118668634. doi: https://doi.org/10.1029/GM127p0001. URL https://agupubs.onlinelibrary.wiley.com/doi/abs/10.1029/GM127p0001.

[281] Lorraine C. Backer, Sandra V. McNeel, Terry Barber, Barbara Kirkpatrick, Christopher Williams, Mitch Irvin, Yue Zhou, Trisha B. Johnson, Kate Nierenberg, Mark Aubel, Rebecca LePrell, Andrew Chapman, Amanda Foss, Susan Corum, Vincent R. Hill, Stephanie M. Kieszak, and Yung-Sung Cheng. Recreational exposure to microcystins during algal blooms in two california lakes. *Toxicon*, 55(5):909–921, 2010. ISSN 0041-0101. doi: https://doi.org/10.1016/j.toxicon.2009.07.006. URL https://www.sciencedirect.com/science/article/pii/S0041010109003481. Harmful Algal Blooms and Natural Toxins in Fresh and Marine Waters – Exposure, occurrence, detection, toxicity, control, management and policy.

[282] C Hulbert, ME Dueker, A Maqbool, T Hamilton-Ward, A Russell, F Savulich, H Mathis, H Prudhomme, and R Smyth. Aerosolization from freshwater at the spillway of a small dam. In *AGU Fall Meeting Abstracts*, volume 2018, pages A11G–2308, 2018.

[283] Nabin Upadhyay, Qinyue Sun, Jonathan O Allen, Paul Westerhoff, and Pierre Herckes. Characterization of aerosol emissions from wastewater aeration basins. *Journal of the Air & Waste Management Association*, 63(1):20–26, 2013.

[284] Alexander Sutin, Alexander Benilov, Heui Seol Roh, and Yi Nah. Acoustic measurements of bubbles in the wake of ship models. In *Proceedings of the 3rd Interna-*

tional Conference on Underwater Acoustic Measurements: Technologies and Results, Napflion, Crete, pages 767–772, 2009.

[285] Pierre Soille and Luc M Vincent. Determining watersheds in digital pictures via flooding simulations. In *Visual Communications and Image Processing'90: Fifth in a Series*, volume 1360, pages 240–250. International Society for Optics and Photonics, 1990. doi: 10.1117/12.24211.

[286] David Legland, Ignacio Arganda-Carreras, and Philippe Andrey. MorphoLibJ: integrated library and plugins for mathematical morphology with ImageJ. *Bioinformatics*, 32(22):3532–3534, 07 2016. ISSN 1367-4803. doi: 10.1093/bioinformatics/btw413. URL https://doi.org/10.1093/bioinformatics/btw413.

[287] K. Max Zhang, Eladio M. Knipping, Anthony S. Wexler, Prakash V. Bhave, and Gail S. Tonnesen. Size distribution of sea-salt emissions as a function of relative humidity. *Atmospheric Environment*, 39(18):3373–3379, 2005. ISSN 1352-2310. doi: https://doi.org/10.1016/j.atmosenv.2005.02.032. URL https://www.sciencedirect.com/science/article/pii/S1352231005002219.

[288] Colin D. O'Dowd, Michael H. Smith, Ian E. Consterdine, and Jason A. Lowe. Marine aerosol, sea-salt, and the marine sulphur cycle: a short review. *Atmospheric Environment*, 31(1):73–80, 1997. ISSN 1352-2310. doi: https://doi.org/10.1016/S1352-2310(96)00106-9. URL https://www.sciencedirect.com/science/article/pii/S1352231096001069.

[289] Duncan C. Blanchard and Lawrence D. Syzdek. Concentration of bacteria in jet drops from bursting bubbles. *Journal of Geophysical Research (1896-1977)*, 77(27):5087–5099, 1972. doi: https://doi.org/10.1029/JC077i027p05087. URL https://agupubs.onlinelibrary.wiley.com/doi/abs/10.1029/JC077i027p05087.

Appendices

Appendix A

Supporting information for chapter 2

A.1 Image processing methodologies

Figure A.1 shows examples of the unprocessed and processed bubble plume and surface foam images. Subsurface bubbles were detected by generating a binary image from the raw image using a thresholding algorithm. Immediately after air entrainment cessation, the bubble plume is characterized by high void fractions which leads to bubble occlusion effects (see unprocessed image in Fig. A.1a). To mitigate this problem, we used the watershed segmentation option in ImageJ [285] to seperate overlapping bubbles (see binary image in Fig. A.1a). The foam area was also determined by applying a fixed thresold on the raw foam image (left panel of Fig. A.1b) to obtain a binary image (right panel of Fig. A.1b). Surface bubbles were manually detected by fitting a circle around the periphery of the bubbles resting on the water surface (see Fig. A.1c).

A.2 Salinity effect on bubbles and total air volume

Figure A.2 shows the effect of salinity on submillimeter bubbles (Fig. A.2a) and supramillimeter bubbles (Fig. A.1b) population in the bubble plume at the momment of active air entrainment cessation ($t = 0\ s$). The number of submillimeter bubbles in the observed bubble plume increases with salinity up to a value of 30 g/kg, after which a drop in the bubble count

occurs in the 30-40 g/kg range (Fig. A.2a). Unlike the submillimeter bubbles population, supramillimeter bubbles exhibit a less monotonic increase with salinity (Fig. A.1b).

Figure A.3 shows the temporal evolution of the total air volume in the first 1.67 s following active air entrainment cessation. The total air volume (V_{air}) is calculated from the subsurface bubble size distribution $D(r,t)$ by assuming that the bubbles have a spherical shape and by ignoring spatial occlusion effects:

$$V_{air}(t) = \int_{r_1}^{r_2} \frac{4}{3}\,\pi\, r^3\, D(r,t)\, dr \tag{A.1}$$

In Eq. (A.1), r is the subsurface bubble radius and r_1 and r_2 are the smallest and largest subsurface bubble radii detected by the plume camera, respectively.

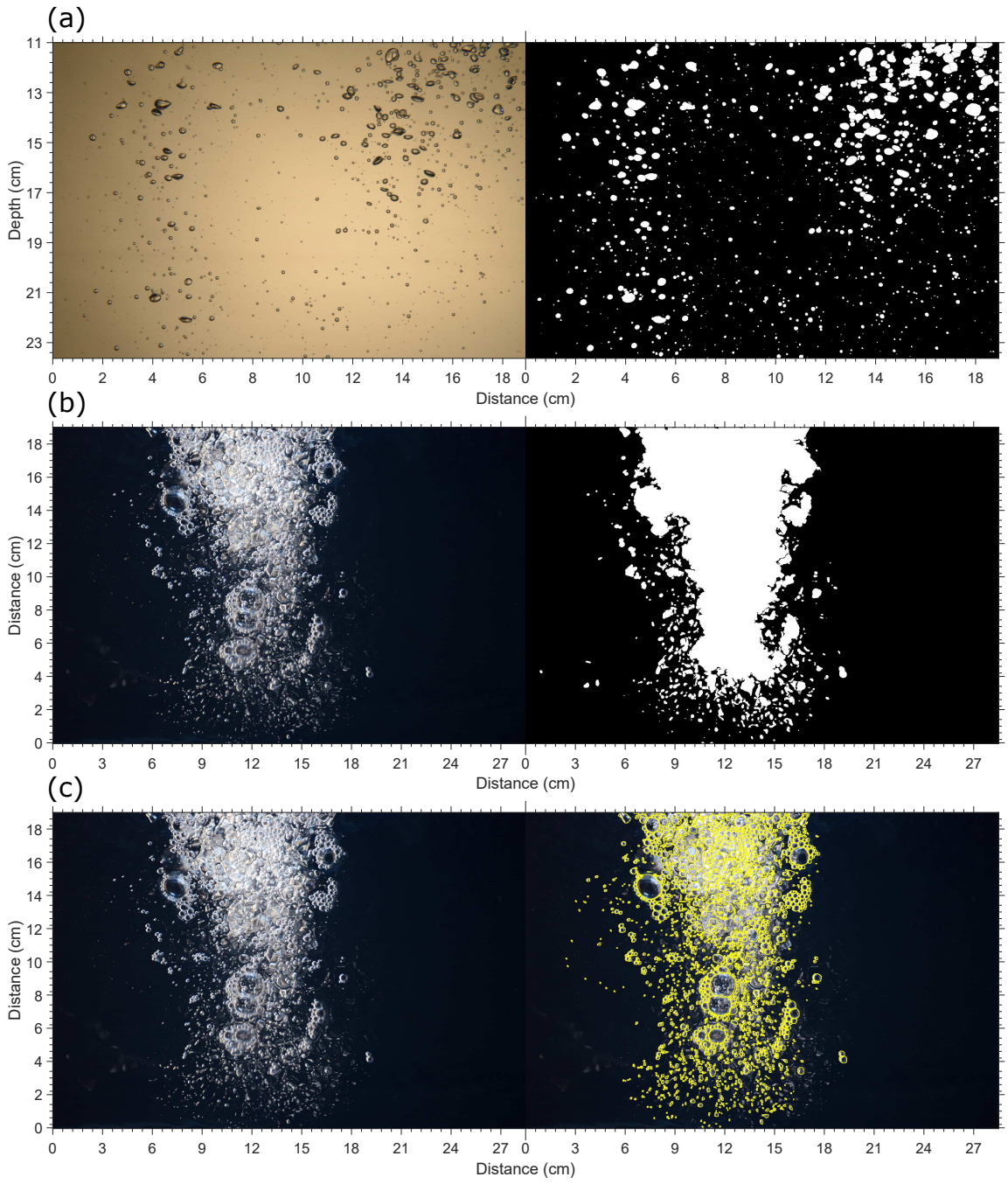

Figure A.1: **Images of subsurface bubbles and surface foam, and the corresponding binary images after thresholding and automated bubble detection.** **(a)** Image of subsurface bubbles taken at time $t = 0$ s for freshwater (0 g/kg) at 19 °C and the corresponding binary image after thresholding and automated bubble detection. **(b)** Surface foam image taken at time $t = 0$ s for saltwater (35 g/kg) at 20.3 °C and the corresponding binary image showing the thresholded total foam area. **(c)** Same foam image with the manually identified surface bubbles highlighted in yellow.

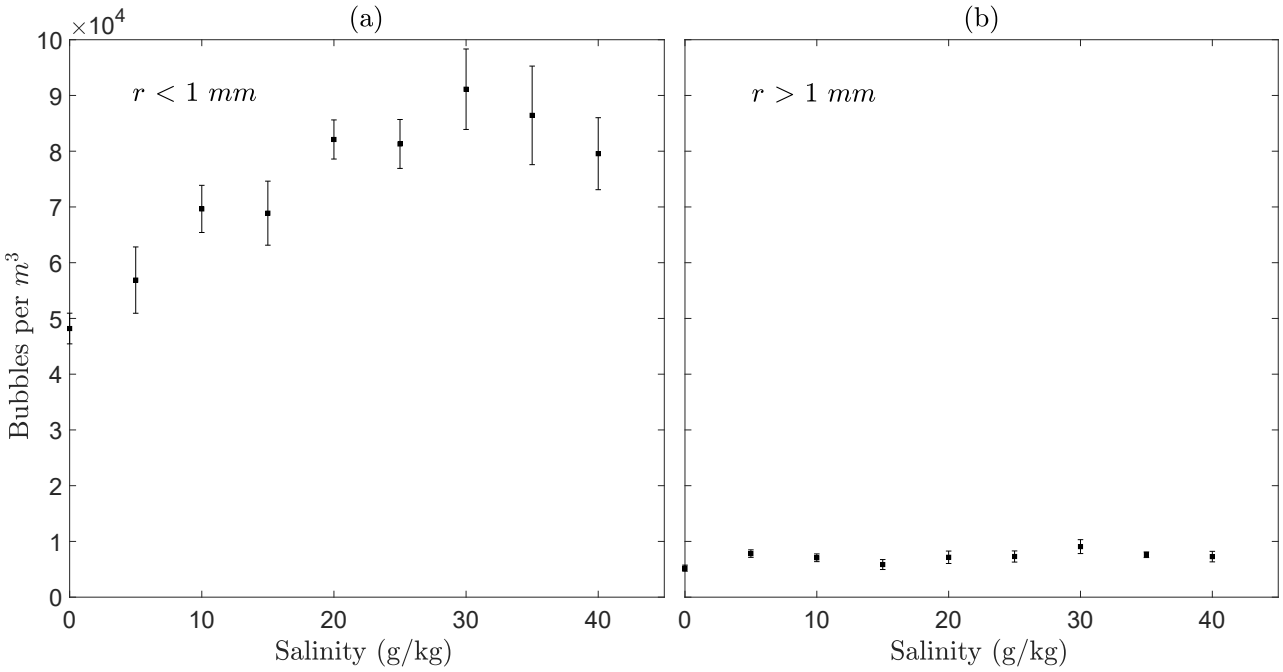

Figure A.2: **The variation in the population of submillimeter and supramillimeter subsurface bubbles with salinity.** The variation in the population of submillimeter **(a)** and supramillimeter **(b)** subsurface bubbles with salinity at time $t = 0\ s$. Each data point is the average of 10 indepenedent experimental runs and the error bars are ± 1 standard deviation.

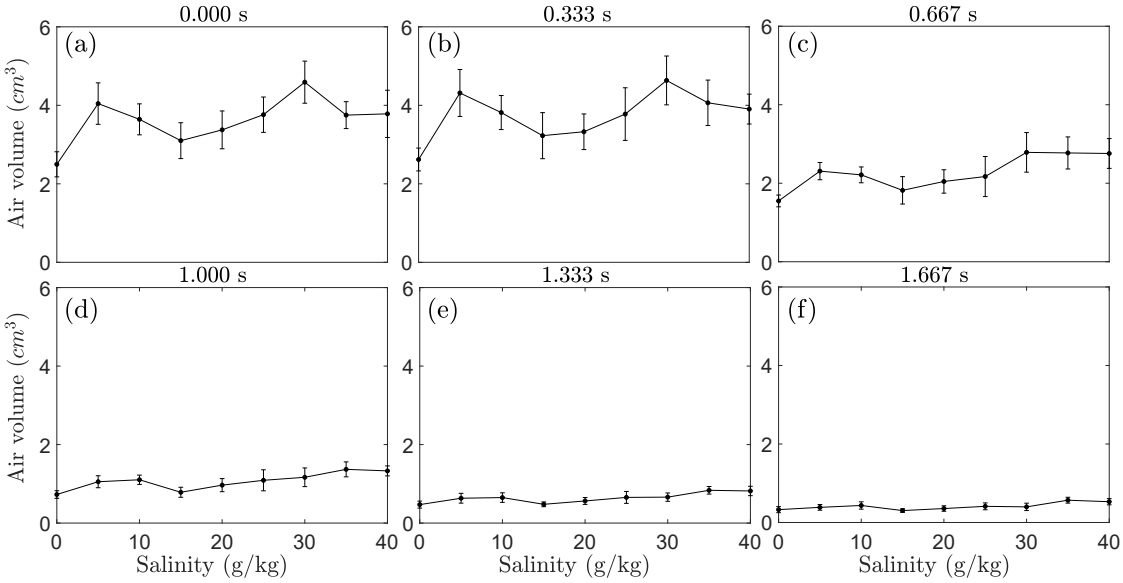

Figure A.3: **Time series of the total air volume in the imaging window following active air entrainment cessation.** Time series of the total air volume in the imaging window in the first 1.67 s following active air entrainment cessation. The data points are average values of 10 independent experimental runs at each salinity value and the error bars are ± 1 standard deviation.

Appendix B

Supporting information for chapter 3

B.1 Wall loss coefficient determination

To determine the wall loss coefficient k inside the MART, we arrest water flow (E=0) and measure the decay of aerosol number concentration [132, 133]. During this decay phase, the mass balance (Eq. (3.6)) reads:

$$\frac{\mathrm{d}C_{out}}{\mathrm{d}t} = -aC_{out} \tag{B.1}$$

In Eq. (B.1), the coefficient a is:

$$a = K + \frac{Q_{in}}{V} \tag{B.2}$$

Hence, Eq. (B.2) can be rearranged to obtain the wall loss coefficient k as follows:

$$K = a - \frac{Q_{in}}{V} \tag{B.3}$$

The coefficient a in Eq. (B.3) was determined by plotting the natural logarithm of the number concentration inside the MART ($\ln(C_{out})$) versus time (t) during the decay phase for submicron (Fig. B.3a) and supermicron particles (Fig. B.3b). In these plots, a is the slope of the linear fit to the data.

B.2 Estimate of particle losses in the diffusion dryer

We follow the procedure proposed by von der Weiden et al. [148] to estimate tubing losses in a simplified model of the TSI 3062 diffusion dryer consisting of a straight dryer tube with a length L equal to 53.5 cm and an inner diameter d equal to 12.7 mm, and two 90°-elbows on each side each having an inner diameter d equal to 12.7 mm and a length L equal to 6 cm (Fig. B.4a). The air flow rate in the dryer Q is set to 1.3 Lmin^{-1}, which is the combined sampling flow rate of the SMPS and APS. The estimated particle losses versus particle diameter are shown in Fig. B.4b. Particles were assumed to have a density of 1500 kgm^{-3} and to be spherical with a shape factor equal to 1.

Figure B.1: **Sampling location in Claytor Lake.**

Table B.1: Claytor Lake water samples metadata: collection date and time, water salinity, and water temperature at collection.

Sample	Collection date and time	Salinity* (ppt)	Temperature* (°C)
Claytor (October)	31-Oct-2020, 10:00-10:30 LT	0.05	14.4
Claytor (August)	9-Aug-2021, 10:00-10:30 LT	0.05	26.8

* As measured by an Extech EC170 salinity-temperature meter.

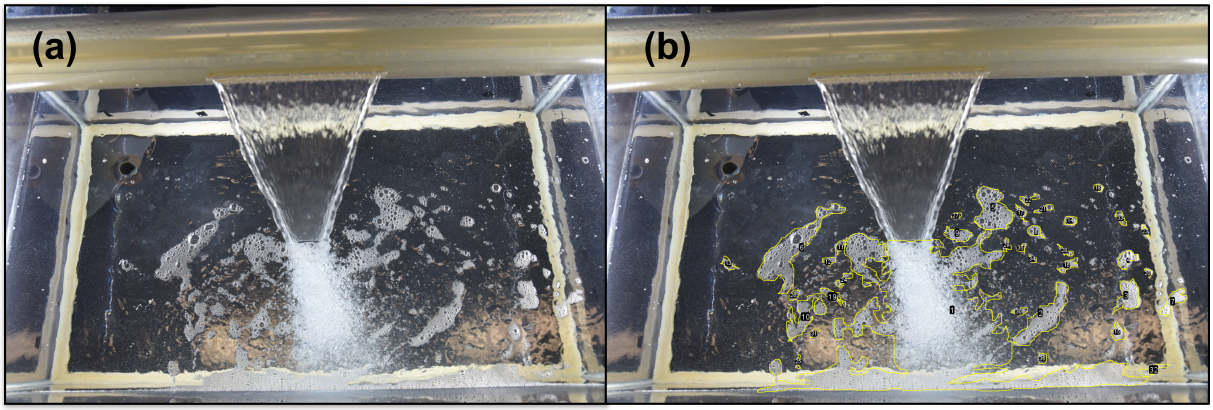

Figure B.2: **Surface foam and its corresponding area outlined manually using the ImageJ software. (a)** Surface foam generated by the MART using synthetic saltwater and **(b)** its corresponding outlined area produced manually using the ImageJ software.

Table B.2: Summary of the water and air properties in each experiment conducted in the MART.

Sample	Water temperature* (°C)	Water salinity* (ppt)	Air temperature** (°C)	Air RH** (%)
Freshwater (with dryer)	21.5/27.1	0.09/0.10	22.3	33
Freshwater (without dryer)	22.4/29.4	0.08/0.08	23.9	94
Saltwater (with dryer)	23.1/31.2	27.7/27.9	23.5	36
Saltwater (without dryer)	21.4/28.0	28.3/27.5	24.1	94
Claytor Lake (October)	19.5/27.7	0.09/0.10	23.3	90
Claytor Lake (August)	26.0/30.1	0.05/0.05	24.1	91

* As measured at the start/end of the experiment by an Extech EC170 salinity-temperature meter.

** As measured by a HOBO UX100-011 temperature-RH data logger.

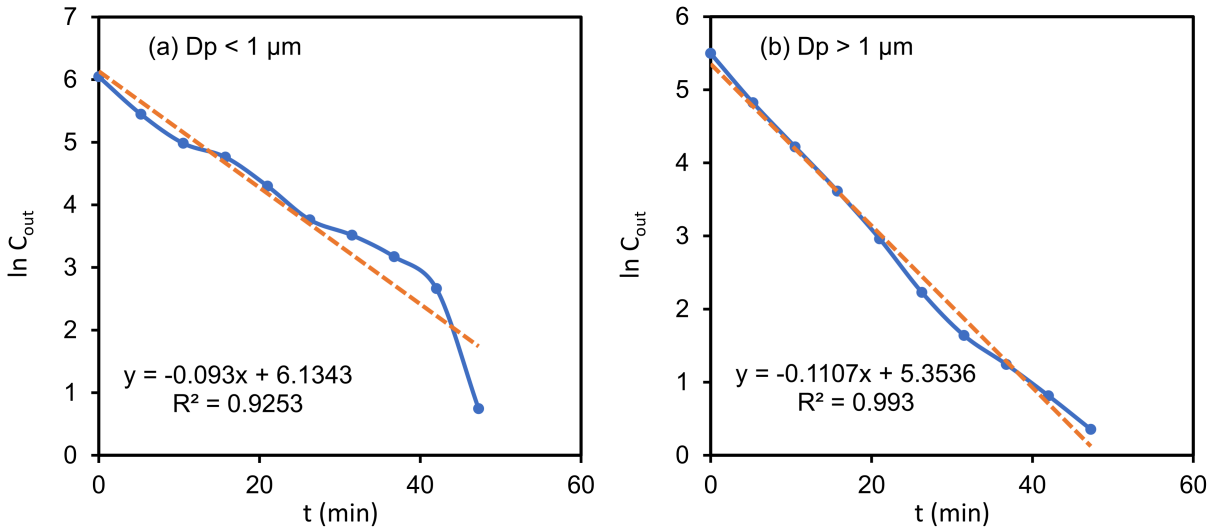

Figure B.3: **Submicron and supermicron aerosol number concentration decay following active air entrainment cessation.** The decay of ln C_{out} versus time t in the synthetic saltwater experiment (wet) for **(a)** submicron and **(b)** supermicron aerosols inside the MART. Also shown are the linear fits to the data for each size range.

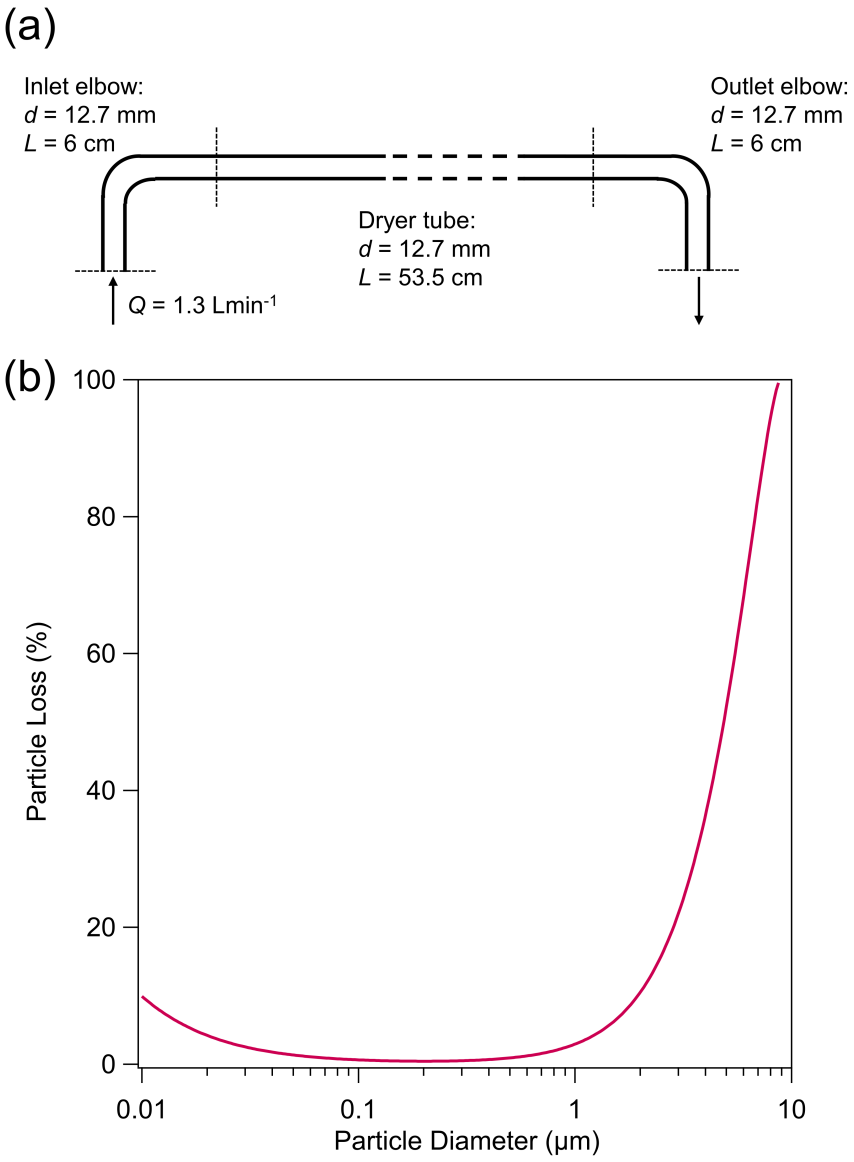

Figure B.4: **A simplified tubing configuration of the diffusion dryer and the corresponding particle loss. (a)** A simplified tubing configuration of the TSI 3062 diffusion dryer and **(b)** the corresponding particle loss in the dryer calculated using the procedure in von der Weiden et al. [148].

Appendix C

Supporting information for chapter 4

C.1 Salinity effect on surface foam and spray aerosols

C.1.1 Experimental design

Foam evolution experiments. To examine the effect of increasing salinity treatments on the size characteristics of surface foam, the tank was filled with 240 L of laboratory tap water providing a water depth, sheet fall height, and water flowrate of 44 cm, 10 cm, and 16 L/min, respectively. These water circulation conditions were chosen to match experimental conditions of a similar study conducted for salinity treatments extending beyond 5 g/kg [116]. A Nikon D750 DSLR camera (shutter speed 1/320 s, f-stop 6.3, ISO 800, and 86 mm focal length) was positioned 53 cm above the water surface facing downward towards the generated foam patch. The water sheet was turned on for 7 s followed by 30 s of surface foam decay by adjusting the knobs on the time delay relay. After 3 s of active air entrainment, the camera started recording (t= 0s) at 3 Hz for a period of 8 s, covering 4 s of active breaking and 4 s of foam decay (Fig. C.2). Freshwater (0, 0.25 g/kg) and oligohaline (0.50 ,0.75, 1, and 5 g/kg) salinity treatments were administered to the tap water sample using Instant Ocean Sea Salt. After each salt addition, water inside the tank was filtered using a MarineLand Polishing Internal Filter (Spectrum Brands, Blacksburg, VA, USA). Ten surface foam recordings (8 s, 3 Hz) were taken at each salinity treatment step.

Surface foam images were processed using the open-source software Fiji [97]. For foam area determination, the background was first subtracted from the unprocessed image (left panel of Fig. C.3A) to increase contrast between the foam patch and the surrounding still water. MorphoLibJ [286] plugin was used to detect foamy areas in the image. The detected foamy regions were then combined to create a binary image (right panel of Fig. C.3A) distinguishing the foam patch (white area) from the surrounding foam-free water (black area). The foam patch area was calculated by applying a scale determined from taking pictures of a precision ruler floating on the water surface. For surface bubbles size determination, a median filter was first applied to the unprocessed image (left panel of Fig. C.3B) to smoothen the image and facilitate subsequent bubble edge detection. MorphoLibJ [286] plugin was employed to detect individual bubbles in the image (right panel of Fig. C.3B). Some detected blobs did not accurately represent surface bubbles which necessitated some manual merging in the plugin output image. Surface bubbles radii were also calculated by applying a scale determined from taking pictures of a precision ruler floating on the water surface. It should be noted that surface bubbles with radii less than 0.4 mm were not reliably detected due to limitations in image resolution and image-processing algorithm.

Spray aerosol generation experiments. To examine the effect of increasing salinity treatments on the abundance and size distribution of ejected spray aerosols, the tank was filled with 147 L of laboratory tap water providing a water depth and sheet fall height both equal to 27 cm. These water circulation conditions were chosen to match corresponding conditions in the bacteria aerosolization experiment using Pandapas pond water (see Sect. 4.3 in Chapter 4). Salinity treatments spanning freshwater (0, 0.25 g/kg), oligohaline (0.50, 0.75, 1, 5 g/kg), polyhaline (15 g/kg) and euhaline (35 g/kg) conditions were applied to the water inside the tank by incremental addition of Instant Ocean Sea Salt. After each salt addition, water inside the tank was filtered using a MarineLand Polishing Internal Filter (Spectrum Brands, Blacksburg, VA, USA) and the headspace was flushed with HEPA-filtered air until the background particle concentration was <10 cm^{-3}. The water sheet was then operated in continuous mode at 24.5 L/min for a period of 3 hours during which the flow rate of HEPA-filtered air injected inside the headspace was maintained at 2 L/min using a mass flow controller (Model EW-32907-69, Cole-Parmer, Vernon Hills, Illinois, USA) (Fig. C.4). Nascent spray aerosols ejected from the generated foam patch were sampled 2 cm above the water surface, and then sampled by a scanning mobility particle sizer (SMPS 3936, TSI,

Shoreview, Minnesota, USA) and an aerodynamic particle size spectrometer (APS 3321, TSI, Shoreview, Minnesota, USA) (Fig. C.4) to determine the particle size distribution. The SMPS was operated at a sampling flow rate of 0.3 L/min and a scan rate of 5 min, providing a size distribution of particles with mobility diameter (d_m) between 14 and 700 nm. The APS was operated at a sampling flow rate of 1.0 L/min and a scan rate of 5 min, providing a size distribution of particles with aerodynamic diameter (d_a) between 0.5 and 20 μm. A vent in the tank's lid allowed excess air flow (0.7 L/min) to escape (Fig. C.4).

In order to obtain a single aerosol size distribution spanning the SMPS and APS measurement ranges, the d_m and d_a size distributions were merged [35, 90] into a single physical diameter (d_p) size distribution. To convert mobility diameters measured by the SMPS to physical diameters, the following relation was used under the assumption of spherical particle geometry:

$$d_m = d_p \tag{C.1}$$

Aerodynamic diameters measured by the APS were converted to physical diameters using the following relation:

$$d_p = \frac{d_a}{\sqrt{\frac{\rho_{eff}}{\rho_0}}} \tag{C.2}$$

where ρ_0 is equal to unit density (1 gcm^{-3}) and ρ_{eff} is an effective density of 1.1 gcm^{-3} assigned to particles sized by the APS. ρ_{eff} was assumed to be equal to the density of a sea salt particle at a measured relative humidity of ~92%, and was calculated using Eq. (4) in Zhang et al. [287]. When stitching, particle bins in the overlapping size region of the SMPS and APS were removed due to undercounting of particle concentrations in this size range by both instruments [90].

C.1.2 Results and discussion

The evolution of surface foam area during active air entrainment (0-4 s) and free surface decay (4-8 s) for salinity treatments corresponding to freshwater (0 and 0.25 g/kg) and oligohaline

water (0.5, 0.75, 1, and 5 g/kg) is shown in Fig. C.5A. Successive salt additions resulted in a monotonic increase in the generated foam area during active air entrainment (Figs. C.5A and C.5D). Average foam area during active air entrainment increased monotonically from 96.9 ($\pm$11.3) cm^2 for untreated water to 116.2 ($\pm$11.2) cm^2 at a salinity treatment of 1 g/kg, and to 129 ($\pm$11.7) cm^2 at a salinity treatment of 5 g/kg (Fig. C.5D). During free surface decay, average surface foam area also exhibited a monotonic increase from 16.1 ($\pm$7.7) cm^2 to 23.5 ($\pm$10) cm^2 in the 0-1 g/kg salinity treatment range, and it reached 37.7 ($\pm$16.4) cm^2 when salinity treatment was increased to 5 g/kg. The preceding result shows that surface foam persistence during free surface decay increased monotonically throughout limnic and oligohaline (i.e., $\leq$ 5 g/kg) salt additions. As for salinity treatments greater than 5 g/kg, surface foam persistence has also been shown to increase monotonically up to 40 g/kg (euhaline water) in a similar experiment [116]. Our results confirm that the addition of even small amounts of salt enhances foam generation during active air entrainment as well as foam persistence during free surface decay.

Besides surface foam area, surface bubble thickness and size at burst govern the number and size of ejected droplets [101] and may be related to the mechanism of droplet ejection (i.e., film or jet drops). It has been suggested that surface bubbles with a radius greater than 1-1.5 mm generate mostly film drops, whereas submillimeter surface bubbles generate predominately jet drops [27]. The size distributions of surface bubbles (Fig. C.5B), averaged during active air entrainment (0-4 s), show a discernible effect of salinity treatment on the sizes of surface bubbles. For limnic salinity treatments of 0 and 0.25 g/kg, surface bubbles size distributions were mostly similar (Fig. C.5B). Yet, once salinity treatments were increased to oligohaline conditions (0.5-5 g/kg), the population of smaller surface bubbles was enhanced. For instance, as salinity treatment was increased to 0.5 and up to 1 g/kg, there was a noticeable increase in the population of submillimeter surface bubbles. Increasing salinity treatment further to 5 g/kg led to a significant increase in the population of sub 3 mm bubbles (Fig. C.5B). Indeed, the mean surface bubble radius decreased slightly from 2.28 ($\pm$0.23) mm for untreated water down to 2.07 ($\pm$0.30) mm at a salinity treatment of 1 g/kg, and further down to 1.42 ($\pm$0.06) mm at a salinity treatment of 5 g/kg (Fig. C.5D). The preceding results indicate that increasing freshwater salinity to oligohaline conditions leads to smaller and more numerous surface bubbles during active wave breaking. This shift to smaller surface bubbles at higher salinities was attributed to an increase in tiny bubbles population

in the subsurface bubble plume [116] which feeds the surface foam without significant subsurface coalescence. The increase in the population of smaller surface bubbles with increasing salinity might enhance jet drop generation [116]. However, unequivocal conclusions about salinity effect on film and jet drops contribution to the spray aerosol population cannot be drawn without comprehensive measurements of the aerosol electrical mobility [99] at each salinity treatment.

The total number concentration of ejected spray aerosols (Fig. C.5D) increased with higher salinity treatments, rising from 139.30 ($\pm$26.37) cm^{-3} for untreated water up to 887.84 ($\pm$179.71) cm^{-3} for a salinity treatment of 35 g/kg. The size distributions of ejected spray aerosols exhibited two distinct modes at $\sim$100 and $\sim$2000-3000 nm (Fig. C.5C), which have been previously identified as film and jet drop modes, respectively [288]. The jet drop mode, which became more discernable at higher salinity treatments (Fig. C.5C), is particularly relevant to bacteria aerosolization as enrichment in biological material occurs mostly at supermicron particle diameters both in freshwater [37] and saltwater [105, 127]. Since biological material seems to increase in larger particles, it is believed that jet drop generation leads to enrichment of biological content both in marine [289] and freshwater [37] spray aerosols.

Table C.1: Waters samples metadata: salinity treatments, sampling times and sample volumes.

Sample	Salinity Treatment (g/kg)	Sampling time	Sample volume (mL)
WA-000-01	0	11/02/2019 13:25	500
WA-000-02	0	11/02/2019 18:00	500
WA-025-01	0.25	11/02/2019 19:25	500
WA-025-02	0.25	11/02/2019 23:10	500
WA-050-01	0.50	11/03/2019 09:35	500
WA-050-02	0.50	11/03/2019 13:35	500
WA-075-01	0.75	11/03/2019 14:05	250[a]
WA-075-02	0.75	11/03/2019 17:03	500
WA-100-01	1	11/03/2019 17:30	500
WA-100-02	1	11/03/2019 20:03	500
WA-500-01	5	11/04/2019 08:30	500
WA-500-02	5	11/04/2019 11:30	500
WA-1500-01	15	11/04/2019 15:50	500
WA-1500-02	15	11/04/2019 17:59	500
WA-3500-01	35	11/04/2019 19:31	500
WA-3500-02	35	11/04/2019 21:22	500

[a] Water was lost during the filtration process.

Table C.2: Air samples metadata: salinity treatments and sample volumes.

Sample	Salinity Treatment (g/kg)	Sample volume[b] (L)
AI-000	0	1800(±0)
AI-025	0.25	1500(±200)
AI-050	0.50	1350(±250)
AI-075	0.75	1200(±150)
AI-100	1	900(±50)
AI-500	5	1300(±100)
AI-1500	15	850(±150)
AI-3500	35	650(±150)

[b] Sample volume errors are shown between parentheses. Errors account for abrupt stops of the air pump due to clogging.

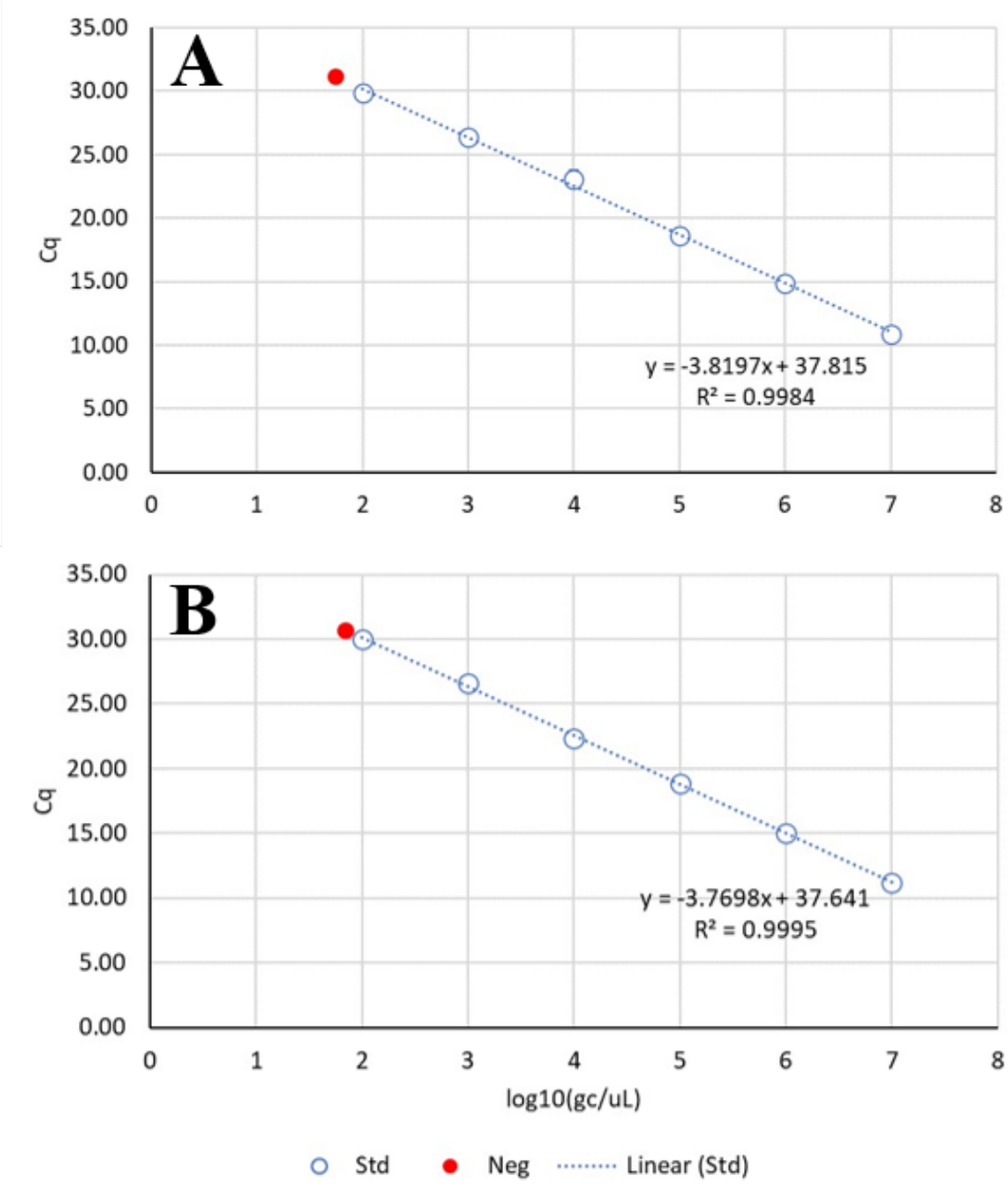

Figure C.1: **qPCR standard curves.** qPCR standard curve for **(A)** plate 1 and **(B)** plate 2.

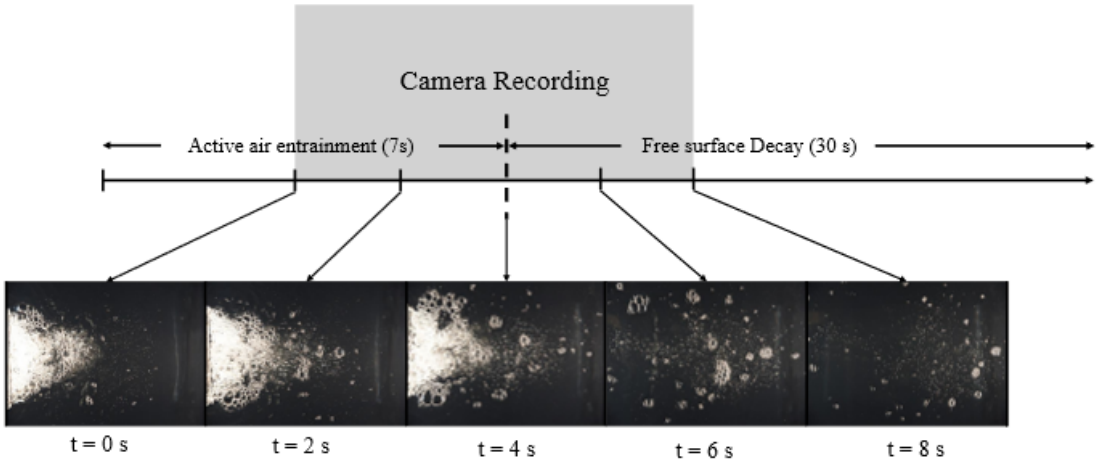

Figure C.2: **Timeline of active air entrainment and free surface decay and photos of the corresponding surface foam evolution.** Timeline showing active air entrainment and free surface decay durations. Surface foam camera starts recording 3 s into active air entrainment for a period of 8 s (grey shaded rectangle) covering 4 s of active air entrainment and 4 s of free surface decay. The collage of pictures at the bottom shows recordings of surface foam area at different instants during surface foam evolution at a salinity treatment of 5 g/kg.

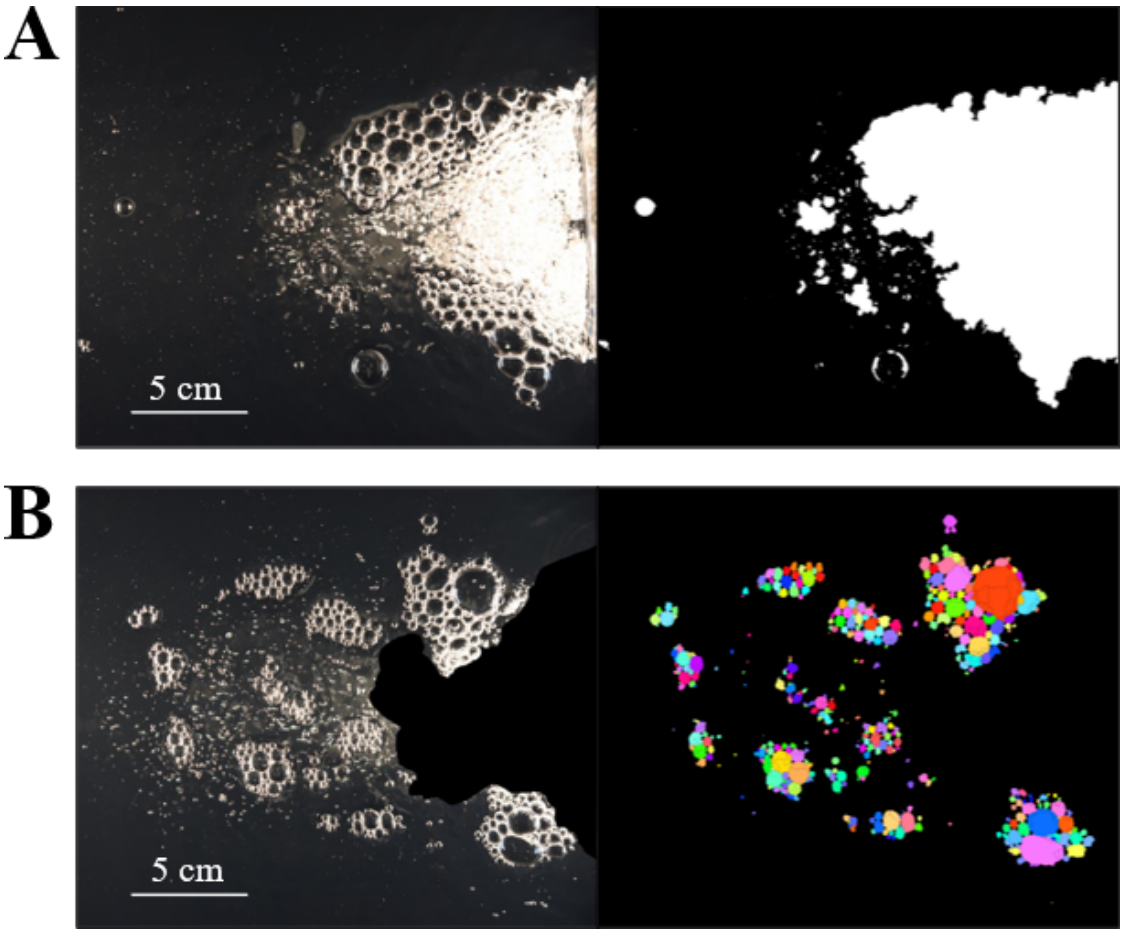

Figure C.3: **Surface foam and the corresponding area and surface bubbles detected by image processing.** **(A)** Left: Unprocessed image of surface foam area at a salinity treatment of 1 g/kg and time t=1s. Right: The corresponding binary image produced by the image-processing software (white area represents detected foam coverage). **(B)** Left: Unprocessed image of surface foam area at a salinity treatment of 5 g/kg and time t=2.67s (highly clustered foam patch was cropped from the image and omitted from subsequent surface bubbles detection). Right: The corresponding processed image showing detected surface bubbles.

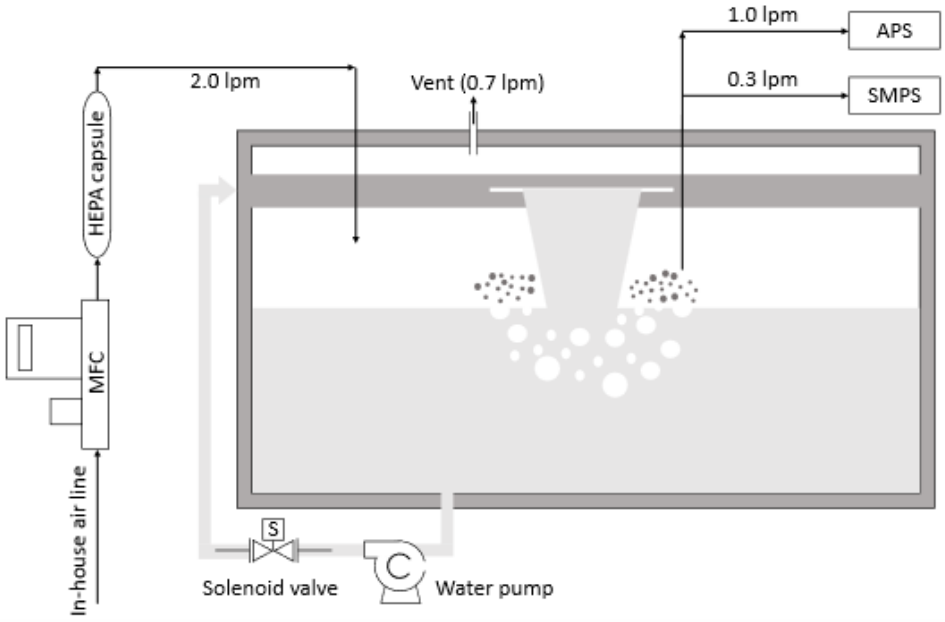

Figure C.4: **Experimental schematic of the tank setup for aerosol number size distribution measurements.**

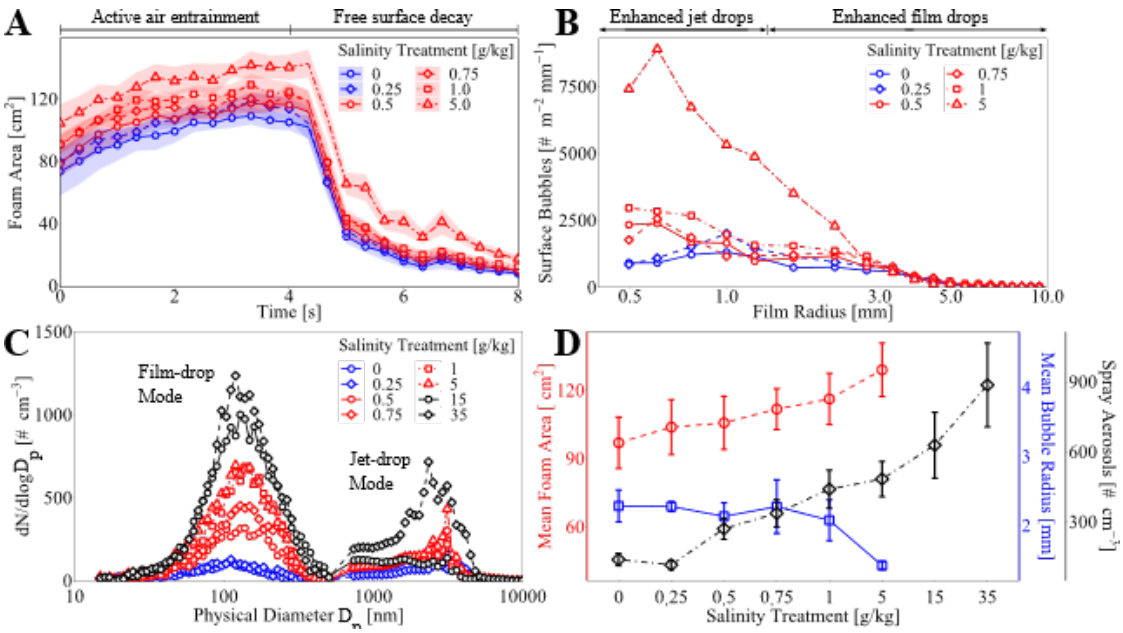

Figure C.5: **The change in surface foam area, surface bubbles size, and spray aerosols size distribution with salinity treatment. (A)** Mean (10 replicates) surface foam area evolution during active air entrainment (0-4 s) and free surface decay (4-8 s) for salinity treatments corresponding to freshwater (blue) and oligohaline (red) conditions. Shaded areas represent ± one standard deviation (n=10). **(B)** Corresponding mean (triplicates) surface bubbles size distributions during active air entrainment (0-4 s). Also shown are surface bubble size ranges with predominant jet and film drops generation. **(C)** Average (3 hours) aerosol number size distribution for salinity treatments corresponding to freshwater (blue), oligohaline (red), and mesohaline-euhaline (black) conditions. **(D)** Mean surface foam area (red), time-averaged during active air entrainment (0-4 s), versus salinity treatment. Error bars represent ± one standard deviation (n=25). Mean surface bubble radius (blue), averaged over 21 size bins during active air entrainment (0-4 s), versus salinity treatment. Error bars represent ± one standard deviation (n=21). Mean total spray aerosol number concentration (black), averaged over 3 hours of active air entrainment, versus salinity treatment. Error bars represent ± one standard deviation (n=35).

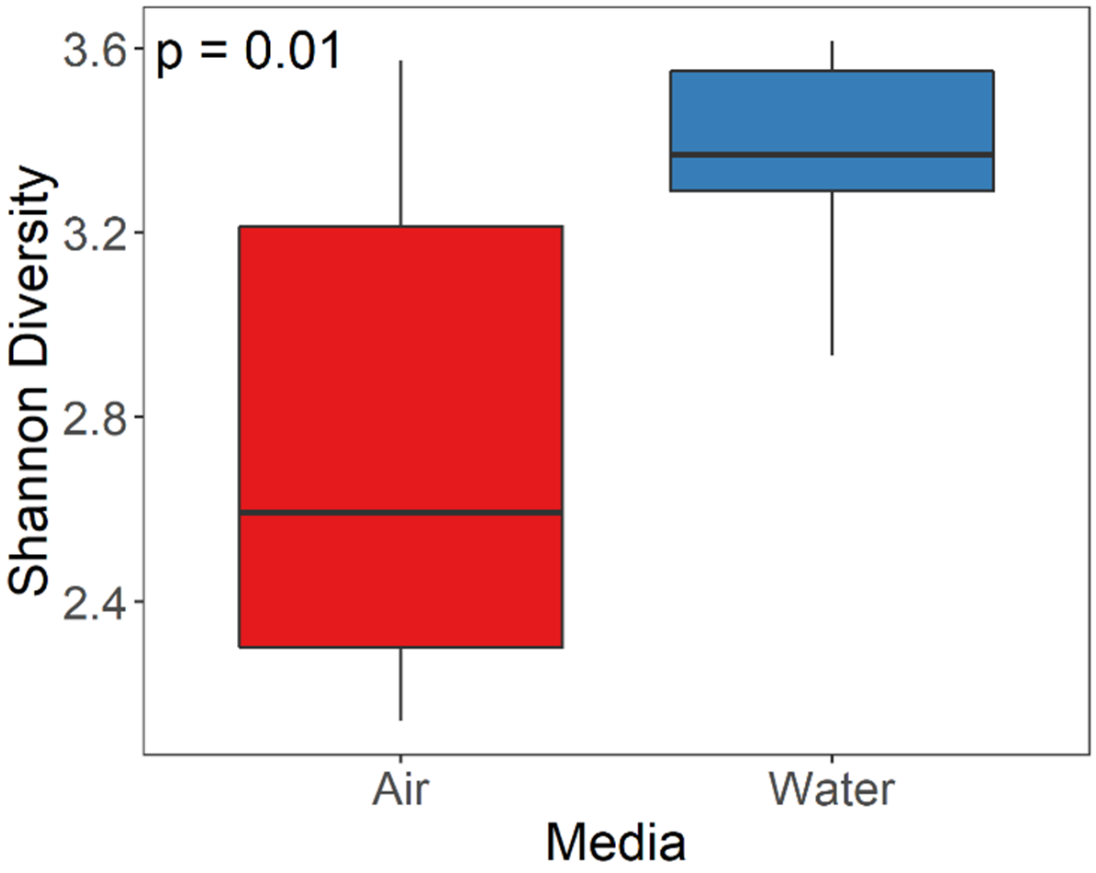

Figure C.6: **Shannon diversity of combined air and water samples.**